



HAL
open science

Characterization and modeling of porous bleed for boundary-layer control with and without shock-wave/boundary-layer Interaction

Julian Giehler

► **To cite this version:**

Julian Giehler. Characterization and modeling of porous bleed for boundary-layer control with and without shock-wave/boundary-layer Interaction. Fluid mechanics [physics.class-ph]. Institut Polytechnique de Paris, 2024. English. NNT : 2024IPPAX047 . tel-04757241

HAL Id: tel-04757241

<https://theses.hal.science/tel-04757241v1>

Submitted on 28 Oct 2024

HAL is a multi-disciplinary open access archive for the deposit and dissemination of scientific research documents, whether they are published or not. The documents may come from teaching and research institutions in France or abroad, or from public or private research centers.

L'archive ouverte pluridisciplinaire **HAL**, est destinée au dépôt et à la diffusion de documents scientifiques de niveau recherche, publiés ou non, émanant des établissements d'enseignement et de recherche français ou étrangers, des laboratoires publics ou privés.



INSTITUT
POLYTECHNIQUE
DE PARIS

NNT : 2024IPPAX047

Thèse de doctorat



Characterization & Modeling of Porous Bleed for Boundary-Layer Control with & without Shock-Wave Interaction

Thèse de doctorat de l'Institut Polytechnique de Paris
préparée à l'École polytechnique

École doctorale n°626 École doctorale de l'Institut Polytechnique de Paris (EDIPP)
Spécialité de doctorat : Mécanique des fluides et des solides, acoustique

Thèse présentée et soutenue à Meudon, le 19/03/2024, par

JULIAN GIEHLER

Composition du Jury :

Julien Weiss Professor, Technical University of Berlin (Chair of Aerodynamics)	Président
Holger Babinsky Professor, University of Cambridge (Energy, Fluid Mechanics and Turbomachinery)	Rapporteur
Piotr Doerffer Professor, Institute of Fluid Flow Machinery, Gdansk (Aerodynamics Department)	Rapporteur
Christian Tenaud Directeur de Recherche, CentraleSupélec (Laboratoire EM2C)	Examineur
Reynald Bur Directeur de recherche, ONERA (DAAA)	Directeur de thèse
Pierre Grenson Ingénieur de recherche, ONERA (DAAA)	Encadrant de thèse
Jean-Pierre Rosenblum Dassault Aviation	Invité
Christophe Nottin MBDA France	Invité

Acknowledgment

It never gets easier, you just get faster.

GREG LEMON

For some of you, this might be the most interesting part of this thesis. For me, it is clearly the most emotional. It marks the end of a journey that lasted a bit more than three years. I am grateful for the opportunity I received and even more grateful for all the people who supported me. First, I thank the European Union for partly funding my work as part of the TEAMAero project, and ONERA for funding me and providing an excellent working environment within the Département Aérodynamique, Aéroélasticité, Acoustique.

A big thanks to my thesis committee for reading and evaluating my thesis. Thanks to Holger Babinsky and Piotr Doerffer for reviewing my thesis and for all the fruitful discussions during the TEAMAero meetings. A special thanks to Holger for the significant effort in providing me with comprehensive feedback, which (hopefully) made this thesis more readable and understandable. I also wish to thank Julien Weiss and Christian Tenaud for evaluating my work again after the mid-term defense, and Julien for supervising me earlier as a student research assistant in Berlin, which prepared me for my Ph.D. journey. Finally, I want to thank Jean-Pierre Rosenblum and Christophe Nottin for being part of the jury. It was a pleasure to be challenged with more industry-related questions.

Merci beaucoup to my supervisor Pierre Grenson and my thesis director Reynald Bur. It was a great pleasure to work with both of you. Thank you for all your academic and administrative support, and all the discussions and conversations we had. I am very grateful to have had such a great supervision team and thank you both for welcoming me!

Also, many thanks to Thibault for all the support with the wind tunnel measurements, and the excursions into French music, art, and culture. Merci, Robert, pour tout le temps et le travail que tu as consacré aux mesures LDV. Et merci, Tanya, for all your support in administrative topics, which made my working life much easier. Moreover, I wish to thank all the MASH team.

I thank all my friends and (ex-)colleagues at the ONERA, starting with Pierre N. for welcoming me into the office and becoming one of my best friends. Thank you for all the support, and for being there all the time, et ne pas m'apprendre le français !¹ A big thanks to Markus

¹Je rigole !

and Jaime for helping me to arrive in France, and surviving the short days limited by the couvre-feu (during the COVID pandemic). Thank you, Mathieu, Alex, and Vianney, for the funny times that we had in our office together. Without you, it would not have been the same. Xavier and Clément, merci for many sunny moments with nice music in the background (or foreground), long nights, and the lost days that followed. Carmen, gracias for always having a sympathetic ear for me and supporting me so much. Loïc, thanks for many hours on the bike together, and for rescuing me in the Pyrenees. Thanks for all the after-lunch coffee or ping-pong breaks to Arthur, Romain, Michele, and Aron. And of course, thank you, Camille, Ilyès, Simon, Lucas, and Julien, for many evenings at Rosi's or the After.

Moreover, I want to thank all the other TEAMAero ESRs (and project members) for an incredible time together all around Europe. Wherever we met, it was a pleasure to work and laugh with you. I will miss this feeling of going on "school trips". Also, a big thanks to the Aeros in Berlin, who prepared me for the thesis work, and shared many unforgettable conference moments with me. I will never forget the week in Chicago at the AIAA Aviation conference!

Outside of work, I thank Zuzanna for many long afternoons or evenings of talking and philosophizing about so many different topics. It is always a big pleasure! Also, a big thanks to my friends in Germany: Anne and Max, Ilona and Mathis, and of course Marvin. I enjoyed it every time I saw you in the last three years, no matter if it was for just a short dinner during a visit, or during some of the holidays we spent together. Also, I'm grateful for two people who made me discover more about this beautiful country, and also made the last year (often) more enjoyable and easier for me: Hannah and Léa.

Am Schluss möchte ich noch meiner Familie danken. Allen voran meiner Mutter für die lebenslange Unterstützung, ohne die ich nie so weit gekommen wäre. Auch meinen Schwestern möchte ich danken. Insbesondere Rita für die Präsenz und den mentalen Support während meiner Verteidigung und in zahlreichen Momenten während der letzten Jahre. Zuallerletzt: Danke Kim, für deine Unterstützung in den ersten, so schwierigen Monaten, ohne die ich vielleicht nicht an diesen Punkt gelangt wäre.

As a passionate cyclist, I had to start this part of my thesis with a quote from a former *Tour de France* winner. I am glad that you were all part of my personal *Tour de France*. You all helped me to become faster (or maybe sometimes not, but then – to turn the statement on its head – you made it easier for me). In other words, you were all part of this work, and these two pages are not enough to express my gratitude for it.

Thank you so much! – Merci beaucoup ! – Vielen Dank! – ¡Muchas gracias! – Dziękuję! – Grazie mille!

Publications and Communications

Publications

- J. Giehler, P. Grenson, and R. Bur. Porous Bleed Boundary Conditions for Supersonic Flows With & Without Shock-Boundary Layer Interaction. *Flow, Turbulence and Combustion*, 2023. [46]
- J. Giehler, P. Grenson, and R. Bur. Parameter Influence on Porous Bleed Performance for Supersonic Turbulent Flows. *Journal of Propulsion and Power*, 2024. [48]
- J. Giehler, T. Leudiere, R. Soares Morgadinho, P. Grenson, and R. Bur. Experimental and Numerical Investigation of Porous Bleed Control for Supersonic/Subsonic Flows, and Shock-Wave/Boundary-Layer Interactions. *Aerospace Science and Technology*, 2024. [50]
- J. Giehler, P. Grenson, and R. Bur. A Novel Bleed Model for Supersonic & Subsonic Boundary-Layer Control by Suction Through Perforated Plates. *AIAA Journal*, submitted in 2024.

Communications

- J. Giehler, P. Grenson, and R. Bur. Porous Bleed Boundary Conditions for Shock-Induced Boundary Layer Separation Control. *56th 3AF International Conference on Applied Aerodynamics*, 2022. [44]
- J. Giehler, P. Grenson, and R. Bur. Parameter Influence on the Porous Bleed Performance with & without Shock-Boundary Layer Interaction. *AIAA AVIATION 2022 Forum*, 2022. [45]
- J. Giehler, P. Grenson, and R. Bur. A New Approach of Using Porous Bleed Boundary Conditions - Application of Local Porosity. *23. DGLR-Fachsymposium der STAB*, 2022. [49]
- J. Giehler, T. Leudiere, R. Soares Morgadinho, P. Grenson, and R. Bur. Experimental and Numerical Investigation of Supersonic Turbulent Boundary Layer Bleeding. *57th 3AF International Conference on Applied Aerodynamics*, 2023. [47]

Contents

Nomenclature	VII
List of Figures	XIII
List of Tables	XXIII
Introduction	1
1 Literature Review	5
1.1 Shock-Wave/Boundary-Layer Interactions	7
1.1.1 Presence in Supersonic Air Intakes	7
1.1.2 Types of Shock Waves and their Interactions with Walls	7
1.1.3 Flow Structure for Shock Reflections with Flow Separation	8
1.1.4 Influence of the Boundary Layer on the Interaction	10
1.1.5 Control of Shock-Wave/Boundary-Layer Interactions	13
1.2 Bleed Systems	15
1.2.1 History of Technological Studies	15
1.2.2 The Steps to Basic Academic Research	16
1.2.3 To the Understanding of the Flow Physics using CFD	27
1.2.4 Modeling the Effect of Porous Bleed as a Boundary Condition	31
2 Computational Setup	45
2.1 Problem Description	47
2.1.1 Flow Inside the Wind Tunnel with & without SBLI	47
2.1.2 Boundary-Layer Bleed on a Flat Plate	48
2.2 Governing Fluid Equations and Flow Solver	50
2.3 Meshing for the Three-Dimensional Simulations	51
2.4 Extraction and Evaluation of the Bleed Efficiency and Control Effectiveness	53
2.5 Implementation of State-of-the-Art Bleed Models	55
2.6 Implementation of the Local Porosity Variation	58

3	Experimental Setup	65
3.1	Supersonic Wind Tunnel	67
3.2	Porous Bleed System	68
3.3	Laser Doppler Velocimetry Measurements	69
3.4	Flow Visualizations	70
3.5	Wall Pressure Measurements	71
4	Description of the Flow Cases	75
4.1	Uncontrolled Shock-Wave/Boundary-Layer Interaction	77
4.1.1	Influence of the Shock Intensity on the Interaction	77
4.1.2	Impact of the Three-Dimensionality on the Center-Plane Flow	78
4.1.3	Selected Base Flow Case	80
4.2	Control of the Shock-Wave/Boundary-Layer Interaction	82
4.3	Boundary-Layer Control	83
4.3.1	Supersonic External Flow	83
4.3.2	Subsonic External Flow	85
5	Comparison of Experiments and Simulations	89
5.1	Existing Experimental Data	91
5.1.1	Experiments of Eichorn et al.	91
5.1.2	Experiments of Willis et al.	92
5.2	New ONERA Experiments	93
5.2.1	Supersonic Boundary-Layer Bleed	93
5.2.2	Subsonic Boundary-Layer Bleed	104
5.2.3	Shock-Wave/Boundary-Layer Interaction Control	106
6	Numerical Study of the Parameter Influences	117
6.1	Influence of the Inflow Conditions	120
6.1.1	Mach Number	120
6.1.2	Displacement-Thickness-to-Diameter Ratio	123
6.2	Geometry Influence on Supersonic Boundary-Layer Bleed	126
6.2.1	Plate Length	126
6.2.2	Hole Diameter	131
6.2.3	Porosity Level	136
6.2.4	Thickness-to-Diameter Ratio	139
6.2.5	Stagger Angle	142
6.2.6	Comparison of all Geometrical Parameters	144
6.3	Geometry Influence on Subsonic Boundary-Layer Bleed	146
6.3.1	Plate Length	146
6.3.2	Hole Diameter	148
6.3.3	Porosity Level	150
6.3.4	Thickness-to-Diameter Ratio	152
6.3.5	Stagger Angle	152
6.3.6	Comparison of all Geometrical Parameters	153
6.4	Geometry Influence on Shock-Wave/Boundary-Layer Interaction Control	155
6.4.1	Hole Diameter	155
6.4.2	Porosity Level	160
6.4.3	Thickness-to-Diameter Ratio	161
6.4.4	Stagger Angle	162
6.4.5	Comparison of all Geometrical Parameters	164

7	Benchmark of State-of-the-Art Bleed Models	171
7.1	Supersonic Boundary-Layer Bleed	173
7.1.1	A Posteriori Comparison	173
7.1.2	Implementation as a Boundary Condition	174
7.2	Subsonic Boundary-Layer Bleed	178
7.2.1	A Posteriori Comparison	178
7.2.2	Implementation as a Boundary Condition	179
7.3	Shock-Wave/Boundary-Layer Interaction Control	182
7.3.1	A Posteriori Comparison	182
7.3.2	Implementation as a Boundary Condition	183
8	Derivation of a Novel Bleed Model	189
8.1	Numerical Aims and Requirements for a Novel Model	191
8.2	Computation of the Bleed Rate	191
8.3	Validation of the New Model	196
8.3.1	Supersonic Boundary-Layer Bleed	196
8.3.2	Subsonic Boundary-Layer Bleed	200
8.3.3	Shock-Wave/Boundary-Layer Interaction Control	202
	Conclusions and Perspectives	207
	Appendices	213
	A Implementation of the New Model Using Python	215
	B Turbulent Shear Stress in Experiments and Simulations	221
	Résumé en Français	223
	References	227

Nomenclature

Acronyms

BC	: Boundary condition
BOS	: Background Oriented Schlieren
CFD	: Computational Fluid Dynamics
LDV	: Laser Doppler Velocimetry
LES	: Large Eddy Simulation
MAE	: Mean absolute error
PIV	: Particle Image Velocimetry
QCR	: Quadratic constitutive relation
RANS	: Reynolds-Averaged Navier-Stokes
RMSE	: Root-mean-square error
SA	: Spalart-Allmaras
SBLI	: Shock-wave/boundary-layer interaction
SST	: Shear stress transport

Latin symbols

A	: Area
A_o	: (Circular) extraction area
$A_{pl,ex}$: Plenum exit throat area
a, b, c	: Constants
C_D	: Discharge coefficient
c_v, c_p	: Specific heat capacity at constant volume, pressure
D	: Hole diameter
\mathcal{D}	: Diagnostic function
d	: Displacement
H	: (Incompressible) boundary-layer shape factor
L	: Length
M	: Mach number

\dot{m}	: Mass flow rate
Pr	: Prandtl number
p	: Static pressure
p_t	: Stagnation pressure
Q	: Flow coefficient
q	: Mass flux
R_s	: Specific gas constant (air)
Re	: Reynolds number
T	: Static temperature
T_t	: Stagnation temperature
T/D	: Thickness-to-diameter ratio
TR	: Throat ratio
\mathbf{u}	: Velocity vector
u, v, w	: Streamwise, transpiration, spanwise velocity
$u'v'$: Turbulent shear stress
x, y, z	: Cartesian coordinates in streamwise, wall-normal, and spanwise direction
\hat{x}, \tilde{x}	: Streamwise position from start/end of bleed region

Greek symbols

α	: Wedge angle
α_R	: Relaxation factor
β	: Stagger angle
δ	: Boundary-layer thickness
δ_1	: Boundary-layer displacement thickness
$\delta_{1,c}$: Compressible boundary-layer displacement thickness
δ_2	: Boundary-layer momentum thickness
ε_τ	: Rise in wall-shear stress
γ	: Heat capacity ratio
μ	: Dynamic viscosity
Ω	: Vorticity
ϕ	: Porosity level
φ	: Heat flux vector
φ_t	: Turbulent heat flux
ψ	: Extraction weighting factor
ρ	: Density
τ	: Shear stress
τ_t	: Reynolds tensor
τ_v	: Stress tensor
θ	: Deflection angle

Subscripts

$2D, 3D$: Two-/Three-dimensional
bl	: Bleed
c	: Cell

<i>h</i>	:	Hole
<i>e</i>	:	Boundary-layer edge
<i>o</i>	:	Circular extraction
<i>pl</i>	:	Cavity plenum
<i>sonic</i>	:	Sonic
<i>subsonic</i>	:	Subsonic
<i>supersonic</i>	:	Supersonic
<i>t, n</i>	:	Tangential and normal components
<i>w</i>	:	External wall
∞	:	Free-stream
99	:	99 % boundary-layer thickness

Superscripts

+ : Wall units

List of Figures

1	Porous bleed systems applied in supersonic air intakes.	1
2	Schlieren photograph showing terminal shock controlled by bleed, from Chen et al. [20].	2
1.1	Shock interactions in a mixed compression air intake, from Babinsky and Ogawa [5].	7
1.2	Basic shock-wave/boundary-layer interactions, from Détery and Dussauge [37].	8
1.3	Schematic of oblique shock-wave reflections, from Ben-Dor [8].	8
1.4	Schematic of an oblique SBLI with flow separation, from Babinsky and Harvey [4].	9
1.5	Wall pressure distribution along the SBLI, from Babinsky and Harvey [4].	9
1.6	Schematic of an oblique SBLI with flow separation, from Babinsky and Harvey [4].	10
1.7	Laminar (left) and turbulent (right) boundary-layer profiles on a flat plate for $M = 2.0$, from Babinsky and Harvey [4].	11
1.8	Velocity distributions by Coles [25] for different shape factors, from Babinsky and Harvey [4].	11
1.9	Supersonic interaction length as a function of the Mach number, from Delery [35].	12
1.10	skin friction coefficient for a boundary layer on a flat plate as a function of the Reynolds and Mach number, from Babinsky and Harvey [4].	12
1.11	Theoretical incipient separation limit of Inger [63] compared to experimental data, from Delery [35].	13
1.12	Schlieren photographs showing SBLI control on a transonic wing. (a) baseline, (b) vortex generators, (c) vortex generators, (d) tangential blowing, from Delery [35].	14
1.13	Schematic of the flow through a porous plate in supersonic flow.	14
1.14	Experimental setup with a bleed slot of Oswatitsch [79] to investigate the pressure recovery of shock diffusers.	15
1.15	Experimental setup of Simon et al. [97] to investigate a bump-intake with several porous bleed regions.	15
1.16	Experimental setup of Smeltzer and Sorensen [100] to investigate the effectiveness of porous bleed in mixed compression air intakes.	16
1.17	Experimental setup of Willis et al. [117].	17
1.18	Bleed mass flow recovery curves, from Willis et al. [117].	18
1.19	Schematic of bleed holes, from Eichorn et al. [40].	18

1.20	Investigated plate configurations from Davis et al. [33] with the characteristics of the C1 plate from Willis et al. [117].	19
1.21	Surface sonic flow coefficient for all 21 plates investigated by Eichorn et al. [40].	19
1.22	Pitot-pressure profiles downstream of the bleed for $M = 1.58$, from Willis and Davis [115].	20
1.23	Evaluation of the shape factor from Willis and Davis [115] as a function of the bleed rate normalized by the boundary-layer mass flow rate, from Oorebeek et al. [76].	20
1.24	Velocity profiles for $M = 1.27$, from Davis et al. [33].	21
1.25	Evaluation of the shape factor for microporous bleed, from Davis et al. [33].	21
1.26	Bleed rate measured by Doerffer and Bohning [38].	22
1.27	Velocity field on wall-normal plane acquired with LDV and CFD, from Oorebeek et al. [77].	22
1.28	Pressure field around a bleed hole, from Bodner et al. [12].	23
1.29	Oil flow visualization of flow over the bleed region, from Oorebeek and Babinsky [75].	23
1.30	PIV measurements performed by Polivanov [83].	24
1.31	Experimental setup of Hingst and Tanji [62].	24
1.32	Experimental results of Hingst and Tanji [62].	25
1.33	Experimental setup of Willis et al. [116].	26
1.34	Experimental results of Willis et al. [116] for several bleed rates.	26
1.35	Experimental setup of Akatsuka et al. [3].	27
1.36	Schlieren photograph from Akatsuka et al. [3].	27
1.37	Sonic flow coefficient measured by Akatsuka et al. [3].	27
1.38	Mach number contours inside a bleed slot, from Hamed and Lehnig [55].	28
1.39	Flow topology inside the bleed holes, from Chyu et al. [23].	28
1.40	Pitot-pressure profiles by Rimlinger et al. [87] compared to the experiments of Willis and Davis [115].	29
1.41	Computational flow field by Schwartz et al. [92]; isocontours of the Q-criterion are colored by the streamwise velocity, and the contours show the static temperature.	29
1.42	Mach number contours around the bleed hole, from Hamed et al. [60].	30
1.43	Schematic of a porous bleed below a shock foot.	31
1.44	Decrease of the sonic discharge coefficient with the Mach number, from Harloff and Smith [61].	32
1.45	Mach number contours of the applied models of Choe et al. [21].	33
1.46	Mach contour field (top) and transpiration velocity (bottom) for reference simulation (left), pressure boundary condition (center), and model of Slater [98] (right), from Orkwis et al. [78].	33
1.47	Grid topology of Wang et al. [114].	34
2.1	Computational domain for the SBLI.	47
2.2	Computational domain for the supersonic boundary-layer bleed.	48
2.3	Variation of the porosity level.	49
2.4	Influence of the turbulence modeling.	51
2.5	Computed error in sonic flow coefficient and pressure ratio as a function of the mesh size.	52
2.6	Mesh resolution comparison; different meshes inside the hole are illustrated in zoom-in views.	52
2.7	View on mesh around the holes.	53

2.8	Positions for the local extractions.	53
2.9	Schematic of boundary-layer mass flow rate and displacement mass flow rate (mass deficit); darkened area highlights deviations due to determination method of the boundary-layer thickness.	55
2.10	Application approaches for bleed models compared to three-dimensional reference simulations; blue patches illustrate areas where suction is applied.	55
2.11	Extraction locations in the mesh.	56
2.12	Influence of the mesh resolution.	58
2.13	Schematic of local porosity: red cells illustrate suction cells; all cells within the dashed lines ($A_o = \pi D^2/(4\phi)$) are used for the extraction of the physical quantities.	59
2.14	Influence of the mesh on the bleed rate.	60
2.15	Envelope of boundary-layer profile for different meshes compared to the reference simulation (gray); dashed lines highlight mean profiles and the dotted lines the envelope of the reference simulation.	60
3.1	Experimental setup.	67
3.2	Characteristics of perforated plates.	68
3.3	Orientation of the Laser beams.	69
3.4	Reproducibility in the inflow measurement.	70
3.5	Schematic of BOS setup.	71
4.1	Contour of Mach number for varying wedge angles in the three-dimensional simulation; dotted line visualizes the sonic line.	77
4.2	Contour of wall shear stress for varying angles of attack.	78
4.3	Conversion from three-dimensional (center plane) to two-dimensional simulation using the streamwise position of the upper triple point.	79
4.4	Comparison between three-dimensional and two-dimensional simulations.	80
4.5	Uncontrolled base flow in the wind tunnel for a wedge angle of $\alpha = 9.5^\circ$; contours on bottom and back wall showing wall shear stress; isocontour $u = 0$ m/s highlighted in yellow; shock pattern illustrated by isocontour of the density gradient and colored by the spanwise position.	81
4.6	Mach number contours for the uncontrolled case with SBLI.	81
4.7	Mach number field for an SBLI control; gray patches illustrate the out-of-plane holes ($TR = 0.7$).	82
4.8	Mach number field for a supersonic turbulent boundary bleed; gray patches illustrate the out-of-plane holes.	84
4.9	Mach number field for a subsonic turbulent boundary bleed; gray patches illustrate the out-of-plane holes.	85
5.1	Experimentally and numerically determined surface sonic flow coefficient for the plates of Eichorn et al. [40] compared to the regression of Slater [98]; plates 101 and 1501 are shifted upwards to increase the readability of the graph; gray area illustrates 5% range around the experimental data.	92
5.2	Experimentally and numerically determined sonic flow coefficient for the C1 plate of Willis et al. [117].	93
5.3	Mach contour fields; white areas illustrate holes of the second column.	94
5.4	BOS visualization of the flow around the perforated plate.	95
5.5	Comparison of flow field from LDV measurements and simulations.	96
5.6	Wall pressure distributions along the bleed region for the two plates; contours at top and bottom from CFD.	97

5.7	Illustration of the effect of the porous bleed system on the boundary layer based on numerical results.	98
5.8	Comparison of boundary-layer profiles for low-porosity plate AR from experiments and simulations.	98
5.9	Boundary-layer profiles 15 mm downstream of the bleed region for low-porosity plate AR.	99
5.10	Boundary-layer profiles 15 mm downstream of the bleed region for high-porosity plate HR.	100
5.11	Flow topology inside the wind tunnel for supersonic boundary-layer bleed from simulation ($p_{pl}/p_t = 0.073$).	101
5.12	Velocity contours at a wall-normal distance of $y/D = 0.25$ ($y/\delta_{99} \approx 0.12$) for experiments ($p_{pl}/p_t = 0.072$) and simulations ($p_{pl}/p_t = 0.073$); plots in (c) and (d) show zoom-view to area highlights by dashed lines.	103
5.13	Variations in the boundary-layer profiles 15 mm downstream of the bleed region along the span.	103
5.14	Illustration of the velocity profiles along the span for experiments ($p_{pl}/p_t = 0.072$) and simulations ($p_{pl}/p_t = 0.073$).	104
5.15	Mach contour field for plate HR ($p_{pl}/p_t = 0.651$); white areas illustrate holes of the second column.	105
5.16	Boundary-layer profiles 15 mm downstream of the bleed region for subsonic conditions.	105
5.17	CFD Mach contours for SBLI in controlled and uncontrolled case; dotted lines highlight sonic line.	107
5.18	Wall pressure distributions along the bleed region for the two plates; contours at top and bottom from CFD; last row shows pressure contours from wind tunnel half-span simulations.	108
5.19	Velocity profiles along the bleed region for low-porosity plate AR.	109
5.20	Flow topology with SBLI inside the wind tunnel from simulation ($p_{pl}/p_t = 0.095$).	110
5.21	BOS visualization of the SBLI control for $p_{pl}/p_t = 0.094$	111
6.1	Contours of the wall-normal velocity component in the bleed holes for different Mach numbers at $\hat{x} = 0$ mm, 8 mm, and 32 mm (top to bottom) for $TR = 0.7$; dashed lines highlight zero wall-normal velocity contour; dotted magenta lines illustrate sonic lines.	121
6.2	Stream tube captured by porous bleed for different Mach numbers.	122
6.3	Surface sonic flow coefficient for different Mach numbers; right triangle (\blacktriangleright) symbolizes the first hole, left triangle (\blacktriangleleft) the last hole, and circle (\bullet) the mean value.	123
6.4	Surface sonic flow coefficient for both plates with equal $\delta_{1,c}/D$ and different Mach numbers; right triangle (\blacktriangleright) symbolizes the first hole, left triangle (\blacktriangleleft) the last hole, and circle (\bullet) the mean value.	124
6.5	Surface sonic flow coefficient as a function of the Mach number for two plates with different hole diameters and $\delta_{1,c}/D = const.$ ($TR = 0.7$ and 2.5); patches illustrate the envelope of local values and dashed lines illustrate the global trend.	124
6.6	Mach number contours for different plate lengths ($TR = 0.7$); dotted line refers to the wall distance of a streamline outside the boundary layer at the beginning of the plate.	126
6.7	Static external wall and plenum pressure for different plate lengths ($TR = 0.7$); the dotted line highlights the isentropic pressure ratio for $M = 1.6$	127

6.8	Surface sonic flow coefficient for different plate lengths; right triangle (►) symbolizes the first hole, left triangle (◄) the last hole, and circle (●) the mean value.	128
6.9	Comparison of the wall shear stress downstream of the bleed region for different plate lengths; yellow areas in (a) visualize regions with negative streamwise component and gray areas indicate supersonic hole entry flow; (b) wall shear stress 10 mm ($20D$) downstream of the last hole compared to its value 10 mm upstream of the first hole; dotted line illustrates averaged value along the spanwise direction and gray curves illustrate trends for other values.	129
6.10	Rise in the wall shear stress as a function of the bleed rate \dot{m}_{bl} and the pressure ratio p_{pl}/p_w for varying plate lengths; dashed lines in (b) pinpoint lines of constant bleed rate.	130
6.11	Mach number contours of the flow in the bleed holes for different hole diameters at $\hat{x} = 0$ mm, 8 mm, and 32 mm (top to bottom) for $TR = 0.7$; dotted line illustrates sonic line; brightened areas outlined by dashed lines illustrate regions with positive wall-normal flow momentum.	131
6.12	Surface sonic flow coefficient for different hole diameters; right triangle (►) symbolizes the first hole, left triangle (◄) the last hole, and circle (●) the mean value.	133
6.13	Boundary layer 10 mm downstream of the bleed region for $D = 0.25$ mm, 1.00 mm, and 4.00 mm (left to right); gray patch illustrates the envelope of the boundary-layer profiles along the spanwise direction; red area details the compressible displacement thickness and green area the difference to the inflow.	134
6.14	Comparison of the wall shear stress downstream of the bleed region for different hole diameters; yellow areas in (a) visualize regions with negative streamwise component and gray areas indicate supersonic hole entry flow; (b) wall shear stress 10 mm downstream of the last hole compared to its value 10 mm upstream of the first hole; dotted line illustrates averaged value along the spanwise direction and gray curves illustrate trends for other values.	135
6.15	Rise in the wall shear stress as a function of the bleed rate \dot{m}_{bl} and the pressure ratio p_{pl}/p_w for varying hole diameters; dashed lines in (b) pinpoint lines of constant bleed rate.	135
6.16	Mach number contours of the flow in the bleed holes for different porosity levels at $\hat{x} \approx 0$ mm, 8 mm, and 32 mm (top to bottom) for $TR = 0.7$; dotted line illustrates sonic line; brightened areas outlined by dashed lines illustrate regions with positive wall-normal flow momentum; red dash-dotted line in the first row highlights the sonic line for $\phi = 5.67\%$	136
6.17	Surface sonic flow coefficient for different porosity levels; right triangle (►) symbolizes the first hole, left triangle (◄) the last hole, and circle (●) the mean value.	137
6.18	Comparison of the wall shear stress downstream of the bleed region for different porosities; yellow areas in (a) visualize regions with negative streamwise component and gray areas indicate supersonic hole entry flow; (b) wall shear stress 10 mm ($20D$) downstream of the last hole compared to its value 10 mm upstream of the first hole; dotted line illustrates averaged value along the spanwise direction and gray curves illustrate trends for other values.	138
6.19	Rise in the wall shear stress as a function of the bleed rate \dot{m}_{bl} and the pressure ratio p_{pl}/p_w for varying porosities; dashed lines in (b) pinpoint lines of constant bleed rate.	139

6.20	Surface sonic flow coefficient for different thickness-to-diameter ratios; right triangle (▶) symbolizes the first hole, left triangle (◀) the last hole, and circle (●) the mean value.	140
6.21	Wall shear stress inside the holes at $\hat{x} = 8 \text{ mm}$ ($16D$); dashed lines illustrate $\tau_{w,y} = 0 \text{ Pa}$ isolines; blue patches visualize areas with upward-directed momentum on the hole-cutting plane.	141
6.22	Surface sonic flow coefficient for different stagger angles; right triangle (▶) symbolizes the first hole, left triangle (◀) the last hole, and circle (●) the mean value.	142
6.23	Comparison of the wall shear stress downstream of the bleed region for different stagger angles; yellow areas in (a) visualize regions with negative streamwise component; (b) wall shear stress 10 mm ($20D$) downstream of the last hole compared to its value 10 mm upstream of the first hole; dotted line illustrates averaged value along the spanwise direction and gray curves illustrate trends for other values.	143
6.24	Surface sonic flow coefficient for all parameters for supersonic conditions; right triangle (▶) symbolizes the first hole, left triangle (◀) the last hole, and circle (●) the mean value.	144
6.25	Rise in the wall shear stress for all parameters for supersonic conditions.	145
6.26	Static external wall and plenum pressure for different plate lengths ($TR = 0.7$); the dotted line highlights the isentropic pressure ratio for $M = 0.6$	146
6.27	Surface sonic flow coefficient for different plate lengths; right triangle (▶) symbolizes the first hole, left triangle (◀) the last hole, and circle (●) the mean value.	147
6.28	Rise in the wall shear stress as a function of the bleed rate \dot{m}_{bl} and the pressure ratio p_{pl}/p_w for varying plate lengths; dashed lines in (b) pinpoint lines of constant bleed rate.	147
6.29	Surface sonic flow coefficient for different hole diameters; right triangle (▶) symbolizes the first hole, left triangle (◀) the last hole, and circle (●) the mean value.	148
6.30	Boundary layer 10 mm downstream of the bleed region for $D = 0.25 \text{ mm}$, 0.50 mm , 1.00 mm , and 2.00 mm (left to right); gray patch illustrates the envelope of the boundary-layer profiles along the spanwise direction; red area represents the compressible displacement thickness and green area the difference to the inflow.	148
6.31	Comparison of the wall shear stress downstream of the bleed region for different hole diameters; yellow areas in (a) visualize regions with negative streamwise component and gray areas indicate supersonic hole entry flow; (b) wall shear stress 10 mm downstream of the last hole compared to its value 10 mm upstream of the first hole; dotted line illustrates averaged value along the spanwise direction and gray curves illustrate trends for other values.	149
6.32	Rise in the wall shear stress as a function of the bleed rate \dot{m}_{bl} and the pressure ratio p_{pl}/p_w for varying hole diameter; dashed lines in (b) pinpoint lines of constant bleed rate.	150
6.33	Surface sonic flow coefficient for different porosity ratios; right triangle (▶) symbolizes the first hole, left triangle (◀) the last hole, and circle (●) the mean value.	151
6.34	Rise in the wall shear stress as a function of the bleed rate \dot{m}_{bl} and the pressure ratio p_{pl}/p_w for varying porosity levels; dashed lines in (b) pinpoint lines of constant bleed rate.	151

6.35	Surface sonic flow coefficient for different thickness-to-diameter ratios; right triangle (▶) symbolizes the first hole, left triangle (◀) the last hole, and circle (●) the mean value.	152
6.36	Surface sonic flow coefficient for different stagger angles; right triangle (▶) symbolizes the first hole, left triangle (◀) the last hole, and circle (●) the mean value.	153
6.37	Surface sonic flow coefficient for all parameters for subsonic conditions.	153
6.38	Mach number contours for different hole diameters; gray patches illustrate the second row hole positions; dotted line highlights shock location for $D = 0.25$ mm.	155
6.39	Comparison of the flow quantities for different hole diameters along the bleed region.	156
6.40	Variation of the surface sonic flow coefficient for different hole diameters for the SBLI; right triangle (▶) symbolizes the first hole, left triangle (◀) the last hole, and circle (●) the mean value.	157
6.41	Streamwise wall shear stress below the shock foot for different hole diameters; dashed lines mark $\tau_{w,x} = 0$ contour line.	158
6.42	Boundary layer 10 mm downstream of the bleed region for $D = 0.25$ mm, 1.00 mm, and 4.00 mm (left to right); gray patch illustrates the envelope of the boundary-layer profiles along the spanwise direction; red area details the compressible displacement thickness and green area the difference to the inflow.	159
6.43	Rise in the wall shear stress as a function of the bleed rate \dot{m}_{bl} and the pressure ratio p_{pl}/p_t for varying hole diameters; dotted line in (b) highlights isentropic pressure ratio for $M = 1.62$	160
6.44	Variation of the surface sonic flow coefficient for different porosity levels for the SBLI; right triangle (▶) symbolizes the first hole, left triangle (◀) the last hole, and circle (●) the mean value.	160
6.45	Rise in the wall shear stress as a function of the bleed rate \dot{m}_{bl} and the pressure ratio p_{pl}/p_t for varying hole diameters; dotted line in (b) highlights isentropic pressure ratio for $M = 1.62$	161
6.46	Variation of the surface sonic flow coefficient for different thickness-to-diameter ratios for the SBLI; right triangle (▶) symbolizes the first hole, left triangle (◀) the last hole, and circle (●) the mean value.	162
6.47	Variation of the surface sonic flow coefficient for different stagger angles for the SBLI; right triangle (▶) symbolizes the first hole, left triangle (◀) the last hole, and circle (●) the mean value.	163
6.48	Streamwise wall shear stress below the shock foot for different stagger angles; dashed lines mark $\tau_{w,x} = 0$ contour line.	163
6.49	Rise in the wall shear stress as a function of the bleed rate \dot{m}_{bl} and the pressure ratio p_{pl}/p_t for varying stagger angles; dotted line in (b) highlights isentropic pressure ratio for $M = 1.62$	164
7.1	Predicted surface sonic flow coefficient $Q_{sonic,w}$ of the selected bleed models as a function of the pressure ratio p_{pl}/p_w a posteriori compared to the reference simulations.	173
7.2	Prediction of the bleed mass fluxes based on physical quantities for various bleed models ($TR = 0.7$).	174
7.3	Mach number contour fields for the applied bleed boundary condition compared to the reference simulation.	175
7.4	Applied boundary condition compared to the reference simulations.	176

7.5	Comparison of the boundary layers downstream of the plate in dimensionless numbers.	176
7.6	Comparison of the different bleed options for the models of Slater [98] and Grzelak et al. [54].	177
7.7	Predicted surface sonic flow coefficient $Q_{sonic,w}$ of the selected bleed models as a function of the pressure ratio p_{pl}/p_w a posteriori compared to the reference simulations.	179
7.8	Prediction of the bleed mass fluxes based on physical quantities for various bleed models ($TR = 0.7$).	179
7.9	Mach number contour fields for the applied bleed boundary condition compared to the reference simulation.	180
7.10	Applied boundary condition compared to the reference simulations.	181
7.11	Comparison of the boundary layers downstream of the plate in dimensionless numbers.	181
7.12	Prediction of the bleed mass fluxes based on physical quantities for various bleed models ($TR = 0.7$).	182
7.13	Mach number contour fields for the applied bleed boundary condition compared to the reference simulation.	183
7.14	Applied boundary condition compared to the reference simulations with SBLI.	184
7.15	Comparison of the different bleed options for the models of Slater [98] and Grzelak et al. [54].	185
8.1	Schematic of the tangential hole Mach number.	192
8.2	Surface sonic flow coefficient as a function of the pressure ratio p_{pl}/p_w and the tangential hole Mach number $M_{h,t}$	193
8.3	New model compared to the reference data.	195
8.4	Flow field of the reference simulation with $D = 2.0$ mm compared to the model of Slater [98] and the new model.	196
8.5	Applied boundary condition compared to the reference simulations.	197
8.6	Relative deviation in the Mach number between coarse and fine mesh.	198
8.7	Influence of bleed models on Spalart-Allmaras non-dimensional turbulent viscosity.	198
8.8	Flow field for new model compared to reference simulation and model of Poll et al. [85] for $D = 2.0$ mm.	200
8.9	Applied boundary condition compared to the reference simulations.	201
8.10	Relative deviation in the Mach number between coarse and fine mesh.	201
8.11	Flow field of the reference simulation with $D = 2.0$ mm compared to the model of Harloff and Smith [61] and the new model.	202
8.12	Relative deviation in the Mach number between coarse and fine mesh.	203
8.13	Influence of the mesh refinement on the flow field.	204
A.1	Implementation of the new bleed model using 4×4 cells per hole; the location of outflow boundary conditions ($\phi > 0$) is shown at the top; ϕ (center) and ψ (bottom) are illustrated for two holes; dotted lines surround the hole area and dashed lines the extraction area.	217
A.2	Implementation of the new bleed model using 12×12 cells per hole; the location of outflow boundary conditions ($\phi > 0$) is shown at the top, ϕ (center) and ψ (bottom) are illustrated for two holes; dotted lines surround the hole area and dashed lines the extraction area.	218

A.3	Implementation of the new bleed model using 4 x 4 cells per hole unaligned with the bleed holes; the location of outflow boundary conditions ($\phi > 0$) is shown at the top, ϕ (center) and ψ (bottom) are illustrated for two holes; dotted lines surround the hole area and dashed lines the extraction area.	219
B.1	Turbulent shear stress profiles normalized with free-stream (streamwise) velocity for the high-porosity plate HR.	221
B.2	Turbulent shear stress contours for low-porosity plate AR.	222

List of Tables

1.1	Validated scope of application for the different models.	40
2.1	Total conditions and range of investigated bleed parameters.	49
2.2	Mesh sensitivity study.	52
3.1	Stagnation pressure and temperature in experiments (range during all measurements).	67
3.2	Investigated perforated plates.	68
3.3	Positions of wall pressure taps.	71
5.1	Simulated plates from Eichorn et al. [40].	91
6.1	Incompressible boundary-layer shape factor, compressible displacement thickness, and rise in the wall shear stress for the boundary-layer profiles shown in Figure 6.13.	134
6.2	Trends on bleed efficiency and control effectiveness and recommendations for all investigated parameters for supersonic conditions.	145
6.3	Incompressible boundary-layer shape factor, compressible displacement thickness, and rise in the wall shear stress for the boundary-layer profiles shown in Figure 6.30.	149
6.4	Trends on bleed efficiency and control effectiveness and recommendations for all investigated parameters for subsonic conditions.	154
6.5	Incompressible boundary-layer shape factor, compressible displacement thickness, and rise in the wall shear stress for the boundary-layer profiles shown in Figure 6.42.	159
6.6	Trends on bleed efficiency and control effectiveness and recommendations for all investigated parameters for the SBLI control.	164
8.1	Error of the new model compared to state-of-the-art models.	195

Introduction

Ibergekumene zoress is gut zu derzajln.

YIDDISH SAYING

Motivation and Approach

The presence of shock-wave/boundary-layer interactions (SBLI) may have detrimental effects on high-speed vehicles. These interactions can cause separation or distortion of the boundary layer, affecting the airflow for example inside air intakes, and disrupting the compression effects. Consequences are performance and efficiency losses or unsteady effects as shock oscillations (e.g., supersonic intake buzz), leading to the need for flow control techniques. One promising technique is the application of distributed suction, so-called porous bleed systems.



(a) Eurofighter Typhoon (Airbus)



(b) Lockheed Martin F-22 (United States Air Force)

Figure 1: Porous bleed systems applied in supersonic air intakes.

The application of porous bleed is a proven technology to mitigate boundary-layer separation caused by SBLIs. Typical bleed systems consist of a vast number of small holes (see Figure 1) that cover the area around or upstream of the shock foot, as shown in Figure 2. The principle is to suck the low-momentum flow near the wall in a cavity plenum and, as a result, generate

a boundary-layer profile that is less susceptible to separation for adverse pressure gradients. However, bleed systems are also a source of losses caused by the removal of mass from the air intake. Optimization is required to obtain the maximum control effect by keeping the costs, i.e., the removed mass, at a minimum. A major problem in the design process is the vast number of bleed holes of the size of the boundary-layer displacement thickness, leading to high computational costs, which makes a parametric design even with Reynolds-Averaged Navier-Stokes (RANS) simulations too expensive.



Figure 2: Schlieren photograph showing terminal shock controlled by bleed, from Chen et al. [20].

With the aim to simplify the design process, several bleed models have been proposed in the last decades, which can be applied as a boundary condition in Computational Fluid Dynamics (CFD) solvers and mimic the effect of the porous bleed system without including the complex geometry to the numerical setup. However, their accuracy is not always guaranteed, especially when used out of the validation range. Many models are validated for supersonic flows, which makes the application downstream of a normal shock uncertain. Others do not consider choking of the holes, or any external (tangential) flow. Moreover, most geometrical characteristics of the perforated plates are not considered in the models, since only a few experimental and numerical datasets exist. Also, two-dimensional approaches do not capture compressible flow phenomena, like compression and expansion waves induced by the hole contours, which may influence the effect of the system.

The main goal of this thesis is the derivation of a novel bleed model applicable to SBLI control. Therefore, a better understanding of the working principle of porous bleed is required, including the influence of geometrical parameters and inflow conditions. For the application below a normal SBLI, the model is required to work for both supersonic and subsonic conditions, which requires an understanding of the impact of tangential flow. Also, existing numerical approaches need to be evaluated concerning their applicability. In contrast to many existing studies, the complex problem of controlling an SBLI will be simplified by considering separately supersonic and subsonic flow control before heading to SBLI control. Moreover, a distinction is made between bleed efficiency and control effectiveness. The bleed efficiency describes the capability of removing the highest possible bleed rate for a given pressure drop from the external wall to the bleed plenum. On the contrary, the control effectiveness is unlinked to the bleed efficiency and describes the ability to achieve the maximum effect on the boundary layer, i.e., the increase of the momentum in the near-wall region, for a given bleed rate.

To sum up, several objectives are defined for this thesis. These objectives are ordered chronologically in the order to proceed:

- ① Understanding the underlying flow physics of porous bleed for:
 - ▶ Supersonic and subsonic inflow conditions
 - ▶ Different geometrical plate characteristics
- ② Comprehensive evaluation and comparison of existing bleed modeling approaches

- ③ Derivation of a novel bleed model, which is validated for a broad range of flow conditions and geometrical characteristics, and suitable for the control of SBLIs in industrial cases

In the first step of the thesis, comprehensive literature research is conducted to localize gaps in the research. In the following, supersonic and subsonic experiments in the ONERA S8Ch wind tunnel are performed to validate the numerical setup. Additionally, a shock generator is used to generate an oblique SBLI that is irregularly reflected at the wall to investigate the SBLI control. The validated setup is then used for a numerical parametric study on the control of a flat-plate boundary layer is performed. Both inflow conditions and bleed geometry are investigated with the aim of achieving a deeper understanding of the underlying physics and performance-influencing parameters. Also, the interaction of the porous bleed with an incident oblique shock wave is investigated. The comprehensive database generated through the parametric study is then used for the evaluation of state-of-the-art bleed models. Moreover, the database forms the basis for deriving a novel bleed model, which is validated over a broad range of inflow and geometrical characteristics. In the end, this new model is benchmarked against the data from the numerical database and the best state-of-the-art models.

Organization of the Manuscript

The present manuscript is organized into eight chapters associated with the steps in the proposed strategy.

► Chapter 1

The first chapter is dedicated to the literature review. The physical problem of SBLI is introduced before porous bleed systems and their development are described. Moreover, conclusions from the literature review for the current work are drawn.

► Chapter 2

The chapter introduces the computational setup for numerical investigations. It outlines the description of bleed efficiency and control effectiveness and their extraction from simulations, followed by the introduction of the implementation approaches for the state-of-the-art bleed models and the new bleed model.

► Chapter 3

The third chapter is dedicated to the experiments performed in the ONERA S8Ch wind tunnel in Meudon. The wind tunnel and the bleed system are presented before the experimental methods are introduced.

► Chapter 4

In the next chapter, the investigated flow cases are presented. First, the uncontrolled SBLI is presented before heading to the operation principle of the control with porous bleed. Supersonic and subsonic boundary-layer bleed are presented, as well as the control of an SBLI.

► Chapter 5

Chapter 5 is dedicated to the comparison of RANS simulations and experiments. First, the prediction of the bleed rate is evaluated based on existing experimental data. Afterward, the experiments performed in the ONERA S8Ch wind tunnel are compared to simulations using two different perforated plates. This chapter was partly presented at the *57th 3AF International Conference on Applied Aerodynamics* [47] and is part of the paper published in *Aerospace Science and Technology* [50].

► Chapter 6

In this chapter, the influence of the inflow properties and the geometrical characteristics are numerically investigated. All geometrical parameters are studied separately for supersonic and subsonic conditions before heading to the SBLI control. Both bleed efficiency and control effectiveness are evaluated. The sections dedicated to supersonic inflow conditions and SBLI control were partly presented at the *AIAA Aviation Forum 2022* [45] and the study on supersonic boundary-layer bleed was published in the *Journal of Propulsion and Power* [48].

► Chapter 7

The chapter deals with the prediction accuracy of the implemented state-of-the-art bleed models. First, they are compared a posteriori to reference simulations from the numerical database. Afterwards, the models are applied as a boundary condition and their predictions are evaluated. Some of the results presented in this chapter were presented at the *56th 3AF International Conference on Applied Aerodynamics* [44] and are part of the publication in *Flow, Turbulence and Combustion* [46].

► Chapter 8

In the final Chapter, a novel bleed model is introduced. The model is compared to the same reference simulations as in the previous Chapter. The results presented in this chapter are submitted as a paper to the *AIAA Journal*.

Literature Review

Everything is complicated if no one explains it to you.

FREDRIK BACKMAN

Chapter Introduction

The first chapter of the thesis is dedicated to the literature research. First, the physical problem of an SBLI in supersonic air intakes is introduced. Afterward, we focus on the influence of the incoming boundary layer on the SBLI and techniques to control the interaction. In the second step, porous bleed systems are reviewed. The history of experimental and numerical research on this control technique is described, as well as approaches to modeling these systems. Finally, selected state-of-the-art bleed models are presented in more detail as they are evaluated in Chapter 7 of this thesis.

1.1 Shock-Wave/Boundary-Layer Interactions	7
1.1.1 Presence in Supersonic Air Intakes	7
1.1.2 Types of Shock Waves and their Interactions with Walls	7
1.1.3 Flow Structure for Shock Reflections with Flow Separation	8
1.1.4 Influence of the Boundary Layer on the Interaction	10
1.1.5 Control of Shock-Wave/Boundary-Layer Interactions	13
1.2 Bleed Systems	15
1.2.1 History of Technological Studies	15
1.2.2 The Steps to Basic Academic Research	16
1.2.2.1 Studies without SBLI	16
1.2.2.2 Interaction with an SBLI	24
1.2.3 To the Understanding of the Flow Physics using CFD	27
1.2.4 Modeling the Effect of Porous Bleed as a Boundary Condition	31
1.2.4.1 History of Modeling Work	31
1.2.4.2 Implementation Approaches for the Boundary Condition	33
1.2.4.3 Models in Focus	34
Abrahamson and Brower (1988)	35
Poll et al. (1992)	35
Harloff and Smith (1996)	36
Doerffer and Bohning (2000)	37
Frink et al. (2003)	38
Slater (2012)	39
Choe et al. (2020)	39
Grzelak et al. (2021)	40
1.2.4.4 Scope of Application	40

1.1 Shock-Wave/Boundary-Layer Interactions

Shock waves are present for all vehicles flying at transonic, supersonic, and hypersonic speeds. The existence of these discontinuities results in high gradients, activating the viscous terms that are responsible for the production of entropy. Consequently, they are a source of drag and lead to drastic stagnation pressure losses [36].

Additionally, shock waves interact with the boundary layer at the wall, resulting in a thickening of the boundary layer caused by the adverse pressure gradient, or even a flow separation. Thus, shock-wave/boundary-layer interactions (SBLI) may result in the occurrence of large-scale unsteadiness with hazardous consequences such as air intake buzz or buffet [36].

1.1.1 Presence in Supersonic Air Intakes

In supersonic air intakes for air-breathing engines, the flow is gradually decelerated from supersonic to subsonic conditions. A series of shock waves is present, which leads to the gradual compression of the air. Figure 1.1 sketches the shock pattern in a supersonic mixed compression air intake. The contour of the air intake generates a row of oblique shock waves, which are reflected at the wall further downstream. Finally, the flow passes a normal shock, called terminal shock, which finally decelerates the flow to subsonic conditions.

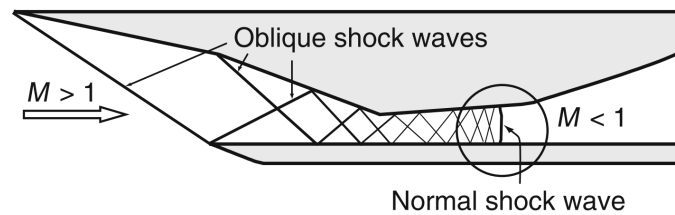


Figure 1.1: Shock interactions in a mixed compression air intake, from Babinsky and Ogawa [5].

The presence of oblique shock waves upstream of the normal shock is beneficial, as the stagnation pressure losses are smaller compared to a single normal shock. Thus, the efficiency of the air intake is increased. However, every shock wave interacts with the boundary layer at the wall, leading to a boundary-layer thickening due to the adverse pressure gradient, or even to a flow separation. The consequence is the formation of a virtual nozzle throat, which reduces the effective mass flow rate through the duct [52]. Moreover, the shock-wave/boundary-layer interactions in air intakes can lead to nonuniformity in the flow, and potential unstart conditions, which can disrupt the efficient operation of the engine [4, 82].

1.1.2 Types of Shock Waves and their Interactions with Walls

As previously described, oblique and normal shock waves are found in supersonic air intakes and interact with the boundary layers. The sharp-edged intake lip and/or the contour of the compression ramp generate oblique shock waves. In mixed compression air intakes, these shock waves impinge on the walls and are reflected. Figure 1.2a shows a basic (two-dimensional) oblique shock reflection at the wall. The incident shock decelerates the flow and deflects it towards the wall with a deflection angle θ_1 . The presence of the wall entails the formation of a shock reflection to deflect the flow in the wall-parallel direction. Thus, the deflection angle of the reflected shock is $\theta_2 = -\theta_1$ [37].

Another basic SBLI, which is found in supersonic air intakes, is the normal SBLI. In contrast to the oblique SBLI, the normal SBLI is caused by a back pressure that forces the flow to

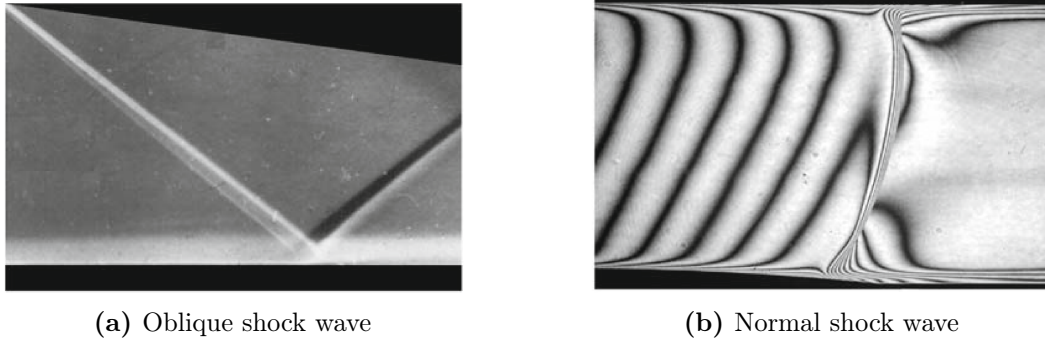


Figure 1.2: Basic shock-wave/boundary-layer interactions, from Déleroy and Dussauge [37].

decelerate to subsonic conditions. In channel flows like in supersonic air intakes, downstream choking is the reason for the back pressure that requires stagnation pressure losses to fulfill mass conservation. As visible in Figure 1.2b, the shock is usually not perfectly normal and corresponds to a strong oblique shock. However, the deflection of the flow is small and the shock can be assumed as normal [37].

As described before, an oblique incident shock is reflected at the wall to obtain a wall-parallel flow downstream of the reflected shock. This is called regular reflection and is shown for inviscid flow in Figure 1.3a with i being the incident shock wave, and r being the reflected shock wave.

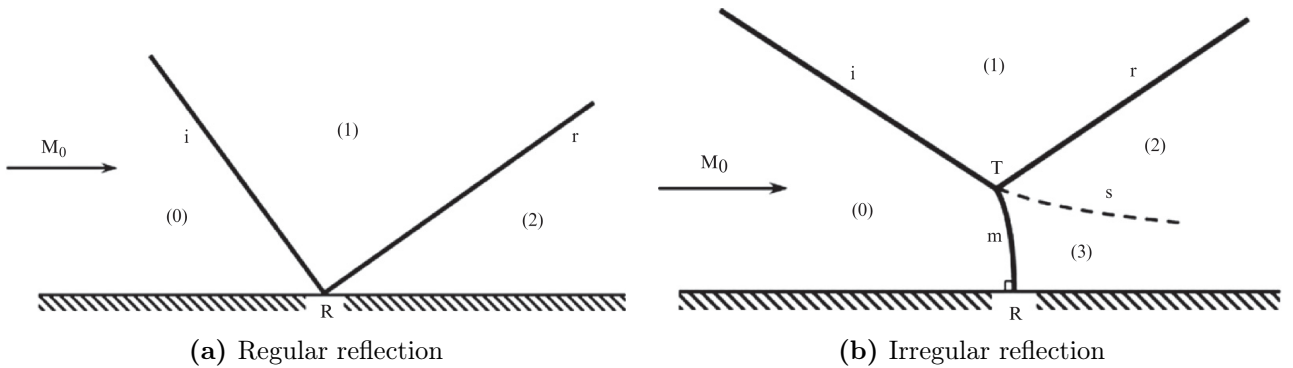


Figure 1.3: Schematic of oblique shock-wave reflections, from Ben-Dor [8].

In particular cases, the deflection caused by the incident shock is too high to obtain a regular reflection. Since the Mach number downstream of the incident shock (region (1)) is lower than upstream (region (0)), the maximum possible deflection angle of the reflected shock r is lower. In this case, the deflection angles are not of the same magnitude $\theta_2 \neq -\theta_1$, and the flow in region (2) is not wall-parallel. As a consequence, a third (normal) shock wave is formed in the vicinity of the wall, which is called Mach stem m . In region (3) downstream of the Mach stem, the flow is subsonic.

Mach stem m , incident shock i , and reflected shock r intersect in the so-called triple point T . Downstream of the triple point, a boundary called slip line s is found between regions (1) and (2), which is a consequence of different entropies because of higher stagnation pressure losses due to the normal shock.

1.1.3 Flow Structure for Shock Reflections with Flow Separation

Now, we focus on the viscous case, where the incident oblique shock interacts with the boundary layer and causes flow separation, as shown in Figure 1.4. The shock pattern in the

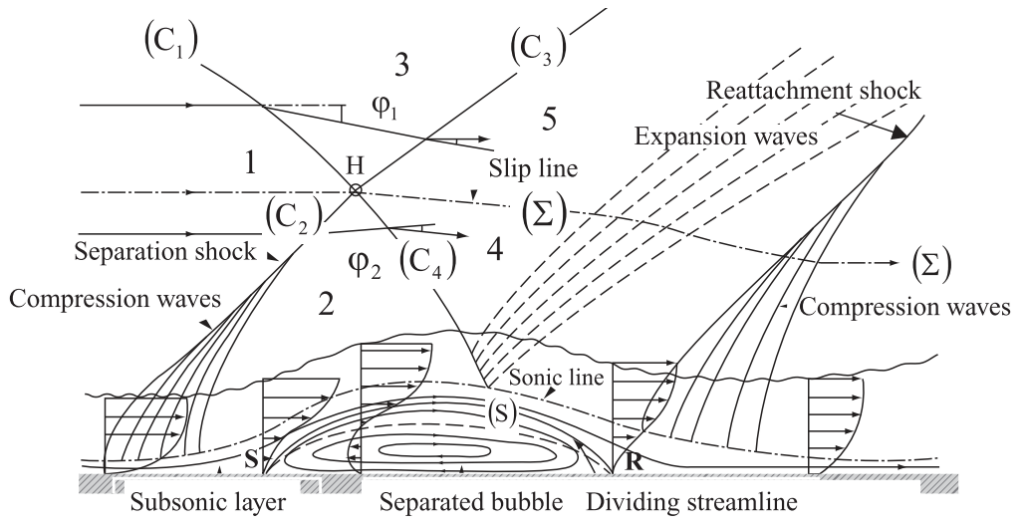


Figure 1.4: Schematic of an oblique SBLI with flow separation, from Babinsky and Harvey [4].

outer flow field, consisting of the incident shock (C_1) and reflected shock (C_3), is equal to the inviscid case with the difference that the shock is not reflected at the wall but in point H . Below this point, a more complex flow field is observed because of the effect of the adverse pressure gradient on the boundary layer. In the subsonic part of the boundary layer, the pressure propagates in the upstream direction, leading to a thickening of the boundary layer, or in the worst case to a flow separation, as shown in Figure 1.4. Thus, the so-called separation shock (C_2) is induced by the flow deflection at the separation point S . This shock intersects the incident shock (C_1) at point H , causing a bend of shock (C_1), resulting in shock (C_4), while the separation shock (C_2) becomes the reflected shock (C_3).

Downstream of the separation point S , a circulating 'bubble' flow is present, which is enclosed by a streamline (S). This line starts at S and goes to reattachment point R . The mixing

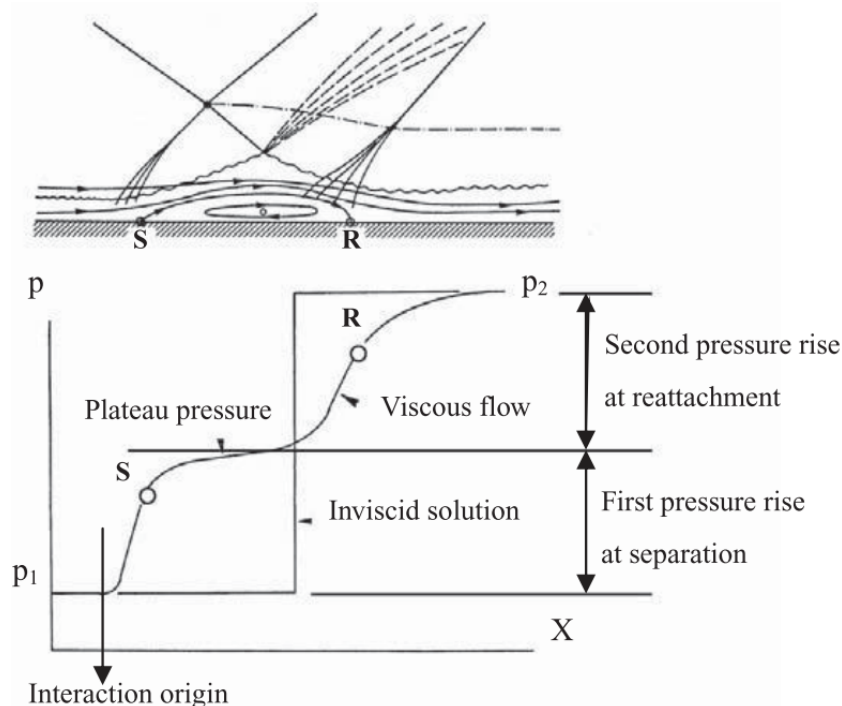


Figure 1.5: Wall pressure distribution along the SBLI, from Babinsky and Harvey [4].

of the shear layer starting from S causes a transfer of energy from the outer high-speed flow to the separated zone. Thus, the velocity u_S on streamline (S) increases until it decelerates approaching the reattachment point R .

A shock (C_4) penetrates the separated viscous flow and reflects as an expansion wave because of the near-constant pressure in the separation bubble. This makes the shear layer shift towards the wall, eventually reattaching at R . At this point, the separation bubble disappears, and the flow on (S) decelerates until stagnation at point R . This process comes with a series of compression waves forming a reattachment shock in the outer stream, explained in more detail later. In Figure 1.5, the wall pressure distribution along the interaction is shown. A steep pressure rise occurs along the compression waves at the beginning of the interaction. Due to the separation, a kind of plateau follows as typical for separated flows, and finally, a gradual pressure rise during reattachment is present. Thus, the pressure rise occurs in two parts contrary to the inviscid solution.

If the strength of the incident shock (C_1) is increased for a fixed upstream Mach number, a point is reached where the shock cannot be regularly reflected at the wall. Instead, a near-normal shock, or a Mach stem, forms between the triple points T_1 and T_2 , as shown in Figure 1.6. Downstream of the Mach stem (C_5), a subsonic channel occurs, and its flow accelerates due to the supersonic flows around. The occurrence of the Mach phenomenon may be problematic in air intakes because the stagnation-pressure loss behind the normal shock is significantly greater than behind an oblique shock.

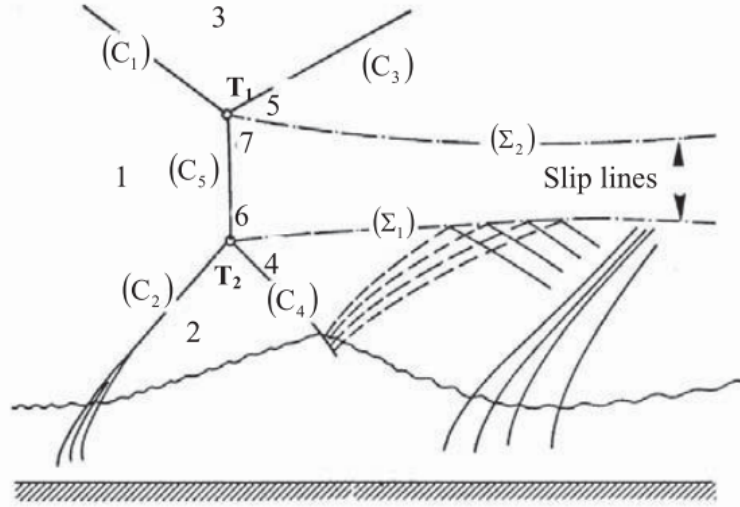


Figure 1.6: Schematic of an oblique SBLI with flow separation, from Babinsky and Harvey [4].

1.1.4 Influence of the Boundary Layer on the Interaction

The boundary-layer profile affects the response of the boundary layer to an adverse pressure gradient as induced by an incident shock wave. The interaction mechanism strongly depends on the thickness of the subsonic part. In Figure 1.7, the supersonic profiles for laminar flow using a Blasius profile and turbulent flow using the velocity distribution by Coles [25] are illustrated. For both profiles, the sonic point, which limits the subsonic part of the profile, is highlighted. A significantly lower thickness of subsonic height is found for turbulent flows.

However, the sonic point is not the only measure to describe the velocity distribution. Another convenient measure is the (incompressible) shape factor

$$H = \frac{\delta_1}{\delta_2}, \quad (1.1)$$

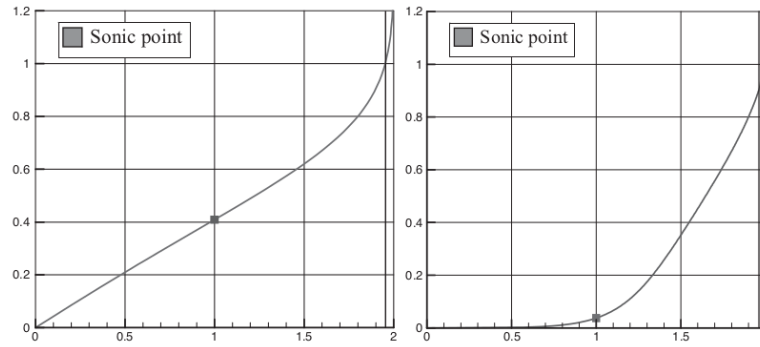


Figure 1.7: Laminar (left) and turbulent (right) boundary-layer profiles on a flat plate for $M = 2.0$, from Babinsky and Harvey [4].

which defines the ratio of the incompressible displacement and momentum thicknesses, which in turn are defined as follows:

$$\delta_1 = \int_0^\delta \left(1 - \frac{u}{u_e}\right) dy \quad (1.2)$$

$$\delta_2 = \int_0^\delta \frac{u}{u_e} \left(1 - \frac{u}{u_e}\right) dy \quad (1.3)$$

The shape factor describes the velocity distribution inside the boundary layer. The smaller its value, the fuller the boundary-layer profile, resulting in more momentum and lower reactivity to adverse pressure gradients. Figure 1.8 details velocity profiles for various shape factors. For the plate boundary layer without pressure gradient, the shape factor is $H = 2.59$ in laminar flows and $H \approx 1.4$ in turbulent flows [90]. In turn, a low shape factor goes along with low sonic line heights for an equal external Mach number. If adverse pressure gradients are present, the momentum inside the boundary layer decreases, resulting in an increase in the shape factor.

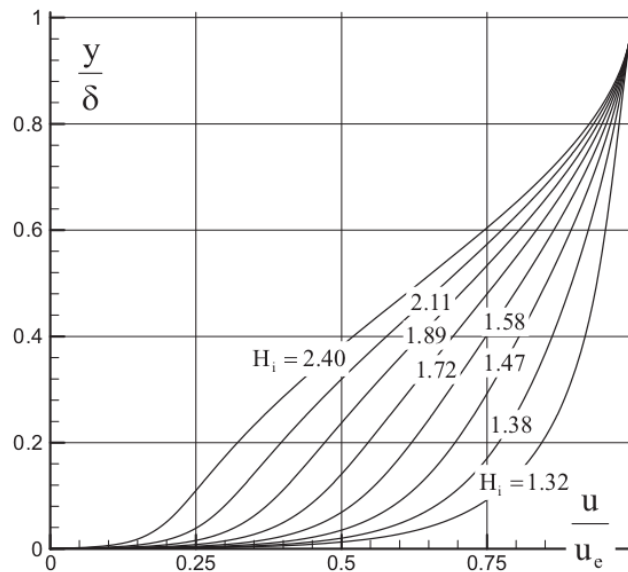


Figure 1.8: Velocity distributions by Coles [25] for different shape factors, from Babinsky and Harvey [4].

The influence of the shape factor on the interaction length is illustrated in Figure 1.9b for transonic interactions with turbulent boundary layers. The higher the shape factor, the larger

the interaction length. An increase of the shape factor from $H = 1.20$ to $H = 1.41$ results in roughly doubling the interaction length. Interestingly, the interaction length does not increase with the Mach number, which is a consequence of the thinner subsonic part in the boundary layer for higher Mach numbers.

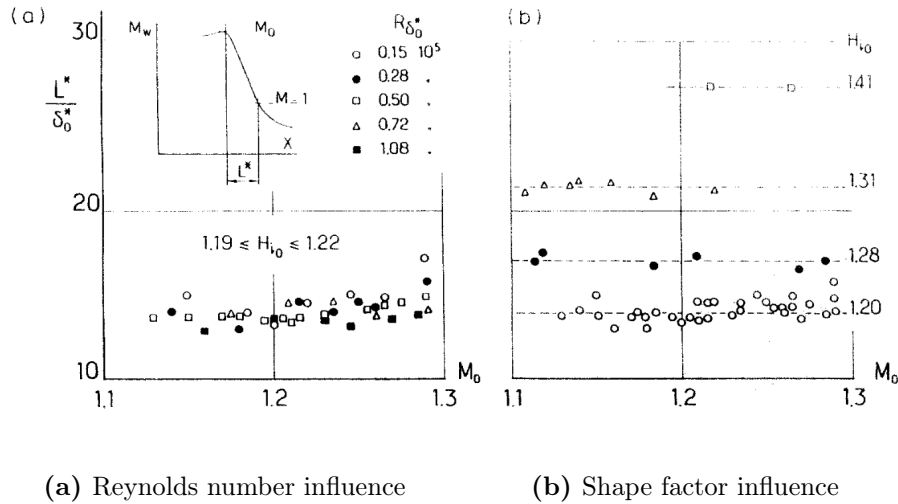


Figure 1.9: Supersonic interaction length as a function of the Mach number, from Delery [35].

Moreover, Figure 1.9a shows the influence of the Reynolds number on the interaction length. Compared to the shape factor, its influence is small. The main reason is the normalization with the boundary-layer displacement thickness. The thinner the boundary-layer displacement thickness, the higher the Reynolds number $Re_{\delta_{1,c}}$ if the other parameters are kept constant.

Another factor influencing the response of the boundary layer to an adverse pressure gradient is wall shear stress or skin friction coefficient. The skin friction coefficient is dependent on the Reynolds number Re_x and the external Mach number, as shown in Figure 1.10 for laminar and turbulent flat-plate boundary layers. The lower the Reynolds number, the higher the skin friction coefficient. Thus, the boundary layer is more resistant to adverse pressure gradients since the high shear forces counteract the retardation effect of the shock. For turbulent flows, the skin friction coefficient also significantly depends on the external Mach number, which is more subtle for laminar flows.

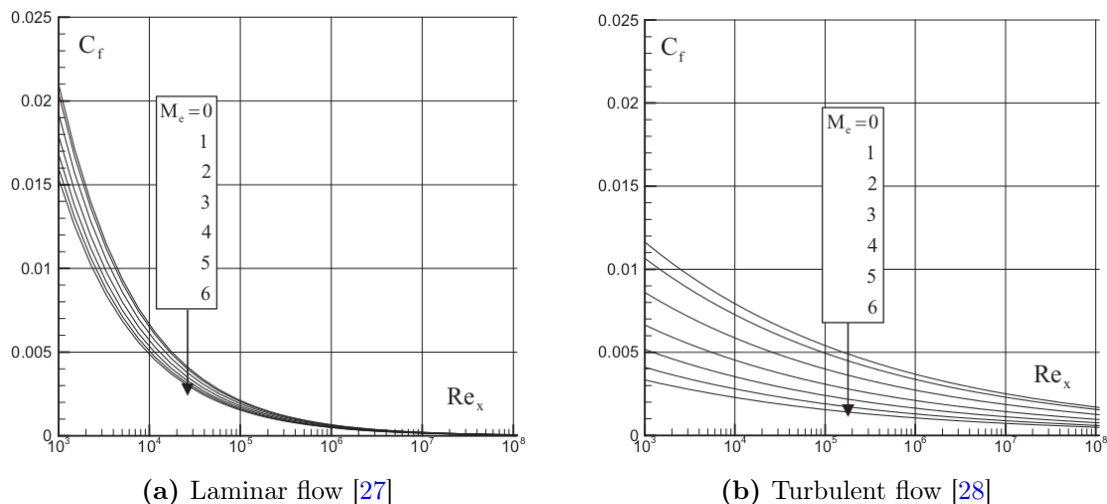


Figure 1.10: skin friction coefficient for a boundary layer on a flat plate as a function of the Reynolds and Mach number, from Babinsky and Harvey [4].

As discussed, there are multiple parameters affecting the response of the boundary layer to an adverse pressure gradient. However, another important factor for flow control is the occurrence of flow separation. Nussdorfer [73] observed a separation onset for $M = 1.33$ if a normal shock interacts with a turbulent boundary layer or a static-pressure-rise ratio of approximately 1.89. Delery [35] compared transonic experimental data to find the onset of separation, as shown in Figure 1.11. He found a slight increase in the Mach number for incipient separation with a decrease in the shape factor. Thus, higher momentum inside the boundary layer results in greater resistance against adverse pressure gradients. However, this influence is low, and even for full boundary-layer profiles, the onset was observed at approximately $M = 1.3$.

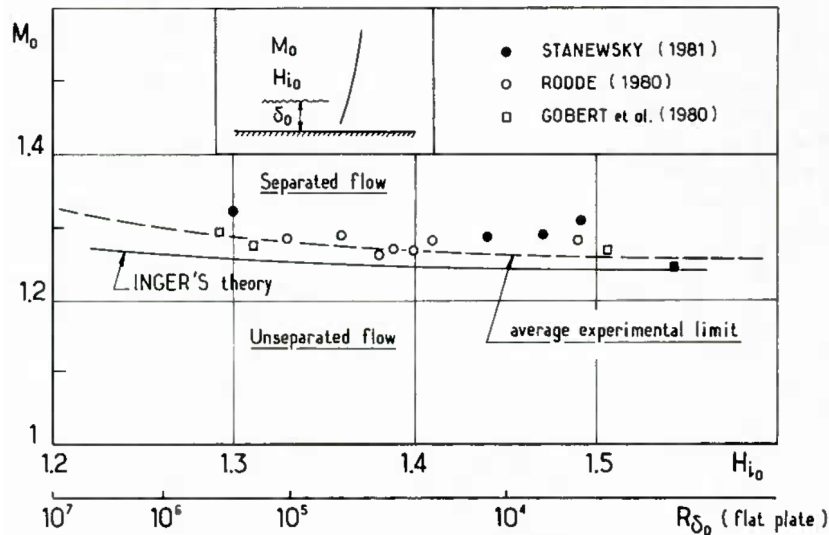


Figure 1.11: Theoretical incipient separation limit of Inger [63] compared to experimental data, from Delery [35].

Two antagonistic effects are present for full boundary-layer profiles with low shape factors: on the one hand, the boundary layer becomes more resistant against adverse pressure gradients. On the other hand, as seen in Figure 1.9b, the interaction length decreases. Consequently, the compression is spread over a short distance, resulting in a higher adverse pressure gradient. Thus, even though full boundary layers separate, the interaction length is shortened.

1.1.5 Control of Shock-Wave/Boundary-Layer Interactions

SBLI control involves strategies to manage and mitigate the effect of the adverse pressure gradient of the incident shock on the boundary layer. As previously described, the boundary-layer momentum affects the upstream influence of the shock and the resistance of the boundary layer to adverse pressure gradients. Therefore, multiple approaches to manipulate the boundary layer are employed, such as blowing, suction, or the use of vortex generators [35, 36, 81].

Blowing can be applied in a distributed manner, which leads to an increase in the shape factor with the result of a boundary layer that is more sensible to the shock. Consequently, the shock intensity decreases as well as the wave drag. Moreover, tangential blowing can be applied to increase the flow momentum in the near-wall region, as shown in Figure 1.12.

Vortex generators induce, as the name implies, vortices inside the boundary layer. They can be applied in the classical way as physical devices, or by using air jets. These devices disrupt the boundary layer and alter its characteristics, reducing the likelihood of separation induced by shock waves. The application of vortex generators is illustrated in Figure 1.12.

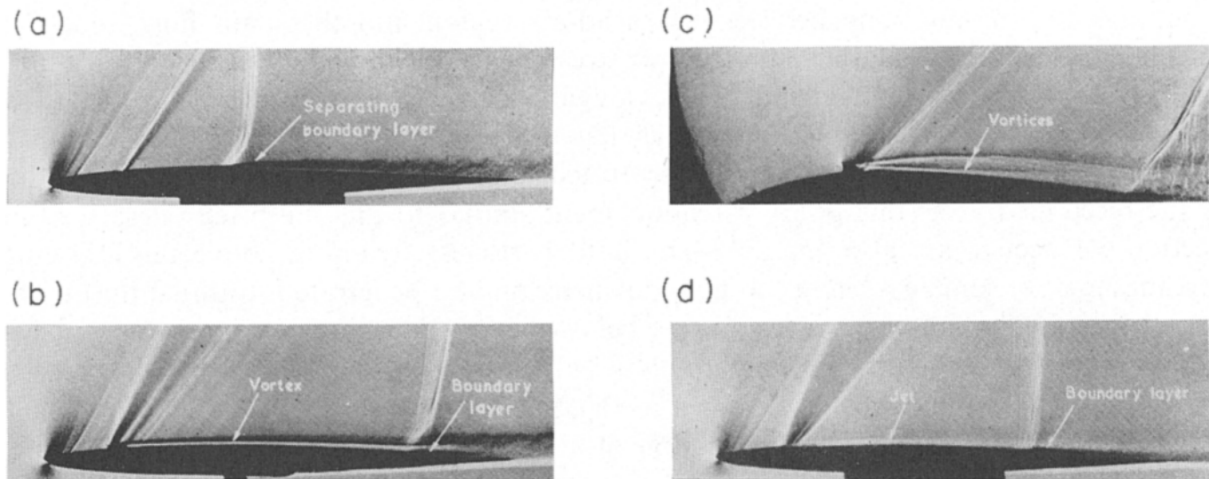


Figure 1.12: Schlieren photographs showing SBLI control on a transonic wing. (a) baseline, (b) vortex generators, (c) vortex generators, (d) tangential blowing, from Delery [35].

Also, suction can be applied distributed over the wall, the so-called porous bleed, or only localized through a slot bleed. A porous bleed is generally applied below the shock foot as a "shock trap" with different effects upstream and downstream of the shock. Upstream of the shock, the low momentum flow in the wall vicinity is sucked away (see Figure 1.13) to remove the part of the flow that is susceptible to separating. However, shock waves generated by the suction contradict the effect. Thus, flow separation may still occur, but the separated flow is removed by the part of the porous bleed that is placed downstream of the shock. In contrast, the bleed slot is placed directly below the shock foot to remove the separated flow, which requires a very careful placement.

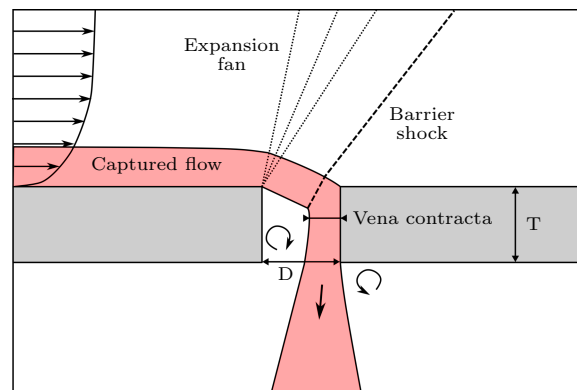


Figure 1.13: Schematic of the flow through a porous plate in supersonic flow.

1.2 Bleed Systems

Bleed systems are a proven technology to control SBLIs. They can be applied as a slot, or a so-called porous bleed using a perforated plate to obtain a distribution of the suction. In the following, the history of its research is sketched.

1.2.1 History of Technological Studies

In 1944, the first experimental investigations on the boundary-layer suction were conducted during the Second World War in Germany to increase the pressure recovery in air intakes of missiles [79]. A suction slot has been implemented in these experiments to avoid "disturbing" boundary-layer effects. Figure 1.14 shows the used experimental setup.

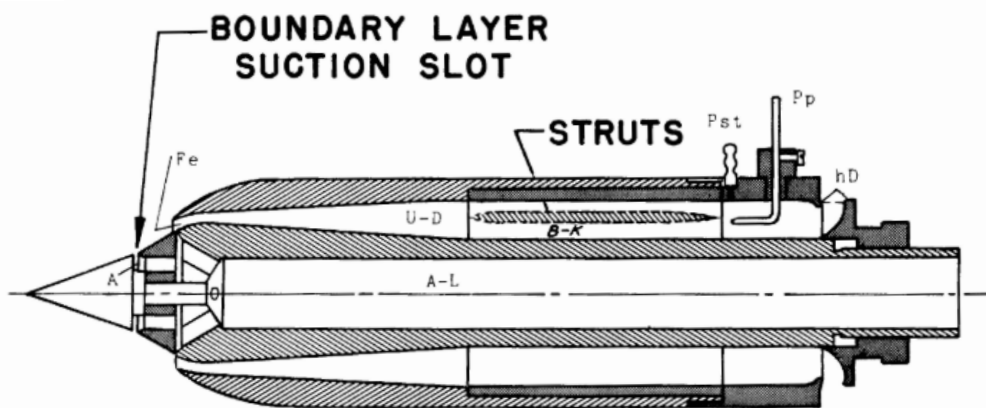


Figure 1.14: Experimental setup with a bleed slot of Oswatitsch [79] to investigate the pressure recovery of shock diffusers.

The first experimental investigations on the application of porous bleed systems were performed at the NACA in the 1950s on the compression ramps of supersonic air intakes [74, 97],

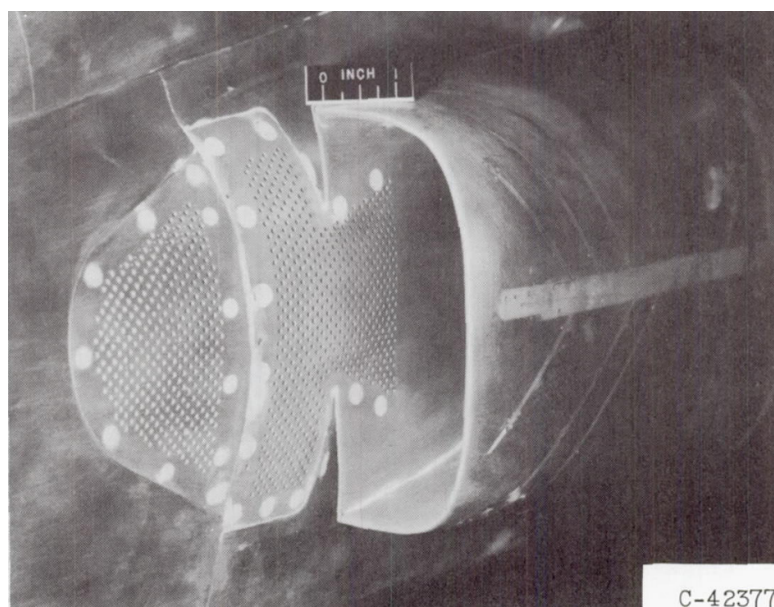


Figure 1.15: Experimental setup of Simon et al. [97] to investigate a bump-intake with several porous bleed regions.

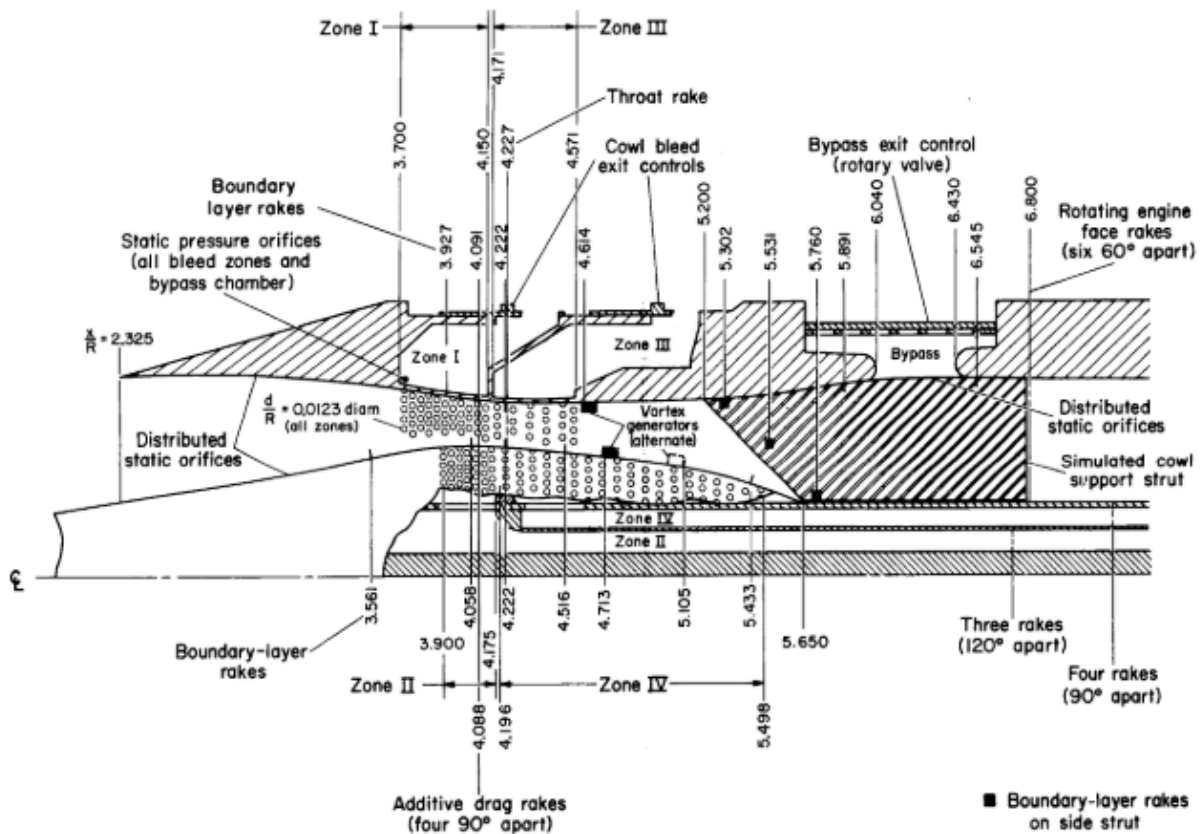


Figure 1.16: Experimental setup of Smeltzer and Sorensen [100] to investigate the effectiveness of porous bleed in mixed compression air intakes.

resulting in an increased total pressure recovery. Figure 1.15 shows a photograph of an investigated air intake, including a bump and a bleed system. The installed perforated plates upstream and inside the duct are visible. In total, the bleed surface was arbitrarily divided into five different regions to test different configurations of plate geometries. All regions entered in the same cavity plenum. One outlet of the bleed chamber is faintly visible at the top of the photo (right next to the scale), while a second one is located at the bottom. While the positive effect of the bleed was investigated, the bleed rate was not measured.

In the late 1960s and 1970s, several experimental investigations on supersonic mixed compression air intakes were conducted with the aim to obtain inviscid pressure distributions [29, 42, 89, 100, 108, 110]. Bleed systems were successfully applied to prevent unstart conditions in supersonic air intakes. High porosities (i.e., high percentages of open areas to wall areas) were found to be more effective [89]. Bleed positions downstream of the incident shock were observed to be more effective in increasing the margin to unstart [29, 100]. Figure 1.16 shows the investigated air intake of Smeltzer and Sorensen [100] with several bleed regions.

1.2.2 The Steps to Basic Academic Research

Besides the applied studies on supersonic air intakes, also fundamental studies on basic flow cases were performed as introduced in the following.

1.2.2.1 Studies without SBLI

From 1994 to 1997, the NASA Lewis Research Center had an active bleed research program in the 1 x 1 ft and the 15 x 15 cm supersonic wind tunnels. Part of this program was investigating

the effect of perforated plates with different geometrical characteristics on supersonic turbulent boundary layers for Mach numbers ranging from 1.27 to 2.46. Thereby, bleed rate [117] and boundary-layer profiles [115] have been evaluated. Also, the effect of a single hole [12], the interaction between holes, as well as the hole misalignment [32], and the effect of microporous holes [33] have been investigated.

The study performed by Willis et al. [117] forms an important database for characterizing porous bleed for a wide range of supersonic Mach numbers. The boundary-layer thickness in their experiment was $\delta = 2.10$ cm to 2.63 cm depending on the Mach number, while the hole diameter of the here shown results was $D = 0.635$ cm. The general experimental setup, which was also used in subsequent studies, is shown in Figure 1.17. Mass was removed through a perforated plate located on the wind tunnel floor. An ASME-calibrated Venturi nozzle was used to measure the bleed rate, which was fixed by a mass-flow plug installed downstream of the nozzle. Fences were installed alongside the perforated plate to suppress any three-dimensional effects.

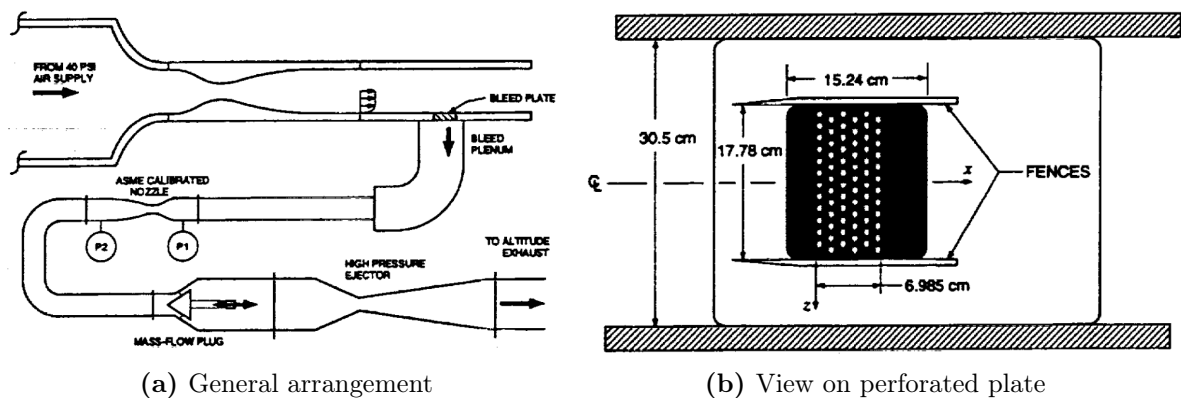


Figure 1.17: Experimental setup of Willis et al. [117].

The bleed rate is represented using the sonic flow coefficient

$$Q = \frac{\dot{m}_{bl}}{\dot{m}_{sonic}}, \quad (1.4)$$

as the ratio of the bleed rate \dot{m}_{bl} and the sonic mass flow rate \dot{m}_{sonic} , which is the maximum achievable mass flow rate for fully choked holes. Typically, the sonic flow coefficient is presented as a function of the pressure ratio p_{pl}/p_t , as schematically illustrated in Figure 1.18a. The higher the Mach number, the lower the sonic flow coefficient, because of the decreasing (static) density that leads to a decrease of the bleed rate. On the contrary, the sonic mass flow rate is calculated based on total quantities. The working regime is distinguished into three different states:

1. Subcritical operation: the flow through the holes is unchoked. Any decrease in the plenum pressure leads to an increase in the bleed rate.
2. Supercritical operation: the hole flow is choked and saturated. A decrease in the plenum pressure increases entropy because of the presence of shocks, but not in an increase of the bleed rate.
3. Critical operation: choking of the holes. This regime is the border between subcritical and supercritical operations.

Measured values of the sonic flow coefficient are presented in Figure 1.18b. Here, two different plates are investigated: one plate with 90-degree holes (open symbols), as investigated

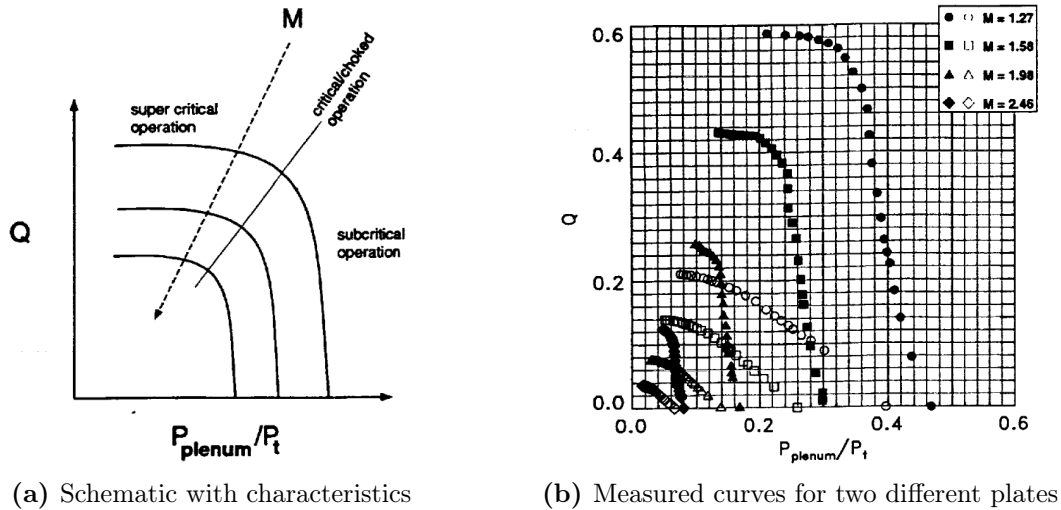


Figure 1.18: Bleed mass flow recovery curves, from Willis et al. [117].

in this thesis, and a second one with 20-degree (slanted) holes (solid symbols). The hole inclination angle α is illustrated in Figure 1.19. The acquired recovery curves for the slanted holes show a good agreement with the theoretical curves from Figure 1.18a. All three regimes can be detected, and the influence of the Mach number is visible. The optimum working regime is around the critical operation, as the bleed rate is the highest keeping simultaneously the pressure losses low.

On the contrary, the working regimes are challenging to detect in the case of 90-degree holes. The bleed seems to perform in the subcritical regime over almost the entire range of pressure ratios. However, a decrease in the sonic flow coefficient for very low pressure ratios is apparent. Moreover, the sonic flow coefficient is significantly lower. This is a consequence of the lower ram effect because of the hole misalignment with the boundary-layer flow [117].

Bodner et al. [12] performed the same kind of experiments with a single-hole setup to investigate the effects of the interaction between the holes. No major differences were found for 90-degree holes. Only for slanted holes, a positive effect of multiple rows was observed in the critical and supercritical regime. It was expected to be a consequence of the change in the flow field along the bleed, leading to different conditions at the bleed hole inlet.

Porous bleed with microporous skins and holes were investigated by Davis et al. [33] (see Figure 1.20). In this study, the sonic flow coefficient was approximately 75% higher than for the reference setup of Willis et al. [117] by using microporous holes with a low porosity level of 9%, while the sonic flow coefficient was similar to those of Willis et al. [117] for higher porosity

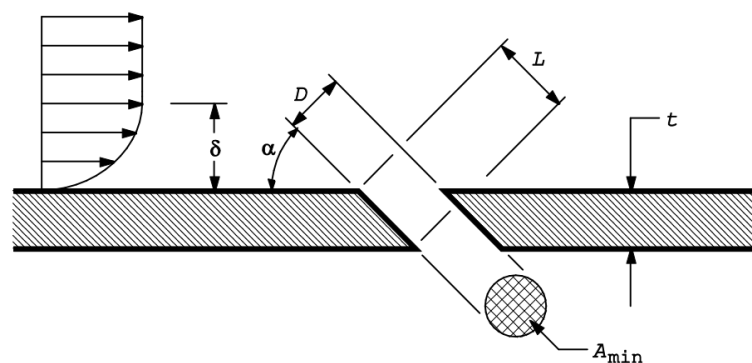


Figure 1.19: Schematic of bleed holes, from Eichorn et al. [40].

levels. Moreover, using a porous honeycomb configuration with a microporous skin decreases the sonic flow coefficient by 21 % compared to the reference data of Willis et al. [117] even though the hole diameter was equal. However, the reason was expected to be the honeycomb structure below the skin that guaranteed the solidity of the plate. Thus, the interaction between the jets exiting in the plenum chamber was prevented, and additional losses were expected due to the honeycomb geometry.

Plate	C1	HC1	HC2	MP1	MP2	MP3
D (mm)	6.350	6.350	3.175	0.203	0.368	0.239
L/D	1	0.1	0.2	1	1	1
L_{HC}/D	N/A	1.75	3.5	47	26	40
N	75	87	348	85,000	43,000	173,000
A_{total} (mm ²)	2375.0	2755.0	2755.0	2076.0	4844.0	7150.0
Porosity (%)	19.64	35.06	35.06	9.0	21.0	31.0
S_r (mm)	69.85	50.4	50.4	139.7	139.7	139.7
S_c (mm)	152.4	148.6	148.6	165.1	165.1	165.1

Figure 1.20: Investigated plate configurations from Davis et al. [33] with the characteristics of the C1 plate from Willis et al. [117].

In 2013, Eichorn et al. [40] presented a new database consisting of 21 perforated plate configurations. In this study, the hole inclination, the hole diameter, and the plate-thickness-to-diameter ratio were varied in the steps $\alpha = 20^\circ, 55^\circ, \text{ and } 90^\circ$; $D = 0.794 \text{ mm}, 3.572 \text{ mm}, \text{ and } 6.350 \text{ mm}$; $T/D = 0.250, 1.125, \text{ and } 2.000$. The boundary-layer thickness varied from $\delta = 12.1 \text{ mm}$ to 13.2 mm depending on the inflow Mach number. For the largest holes, only a single hole was investigated, while the hole number was increased to 3 and 15 holes for the smaller hole diameter to keep to overall bleed rate in the same order of magnitude.

Figure 1.21 shows the surface sonic flow coefficient for all investigated plates. In contrast to

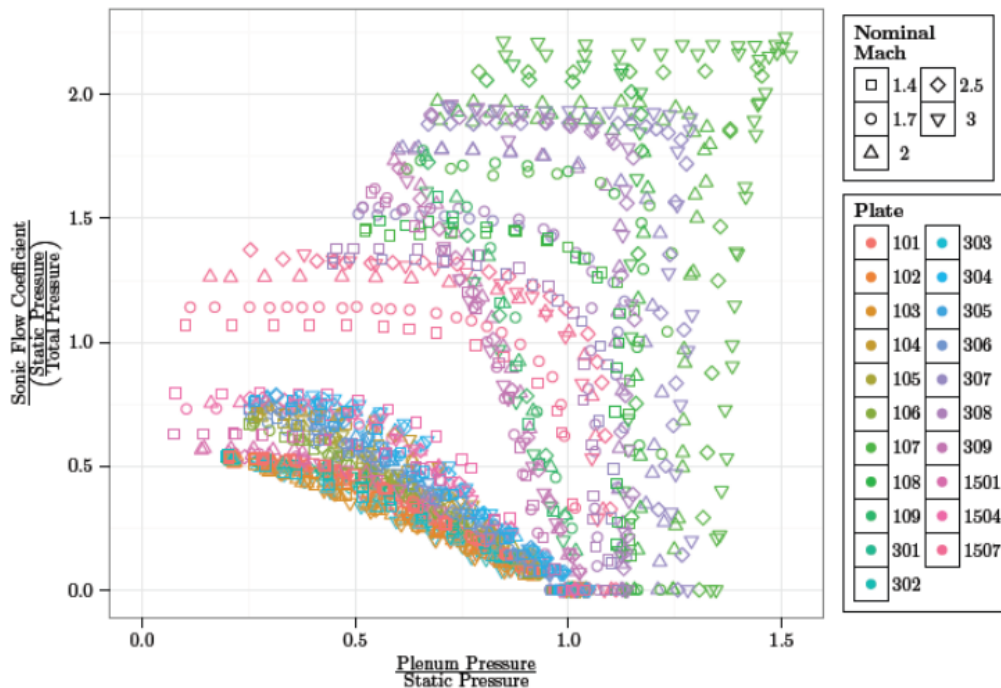


Figure 1.21: Surface sonic flow coefficient for all 21 plates investigated by Eichorn et al. [40].

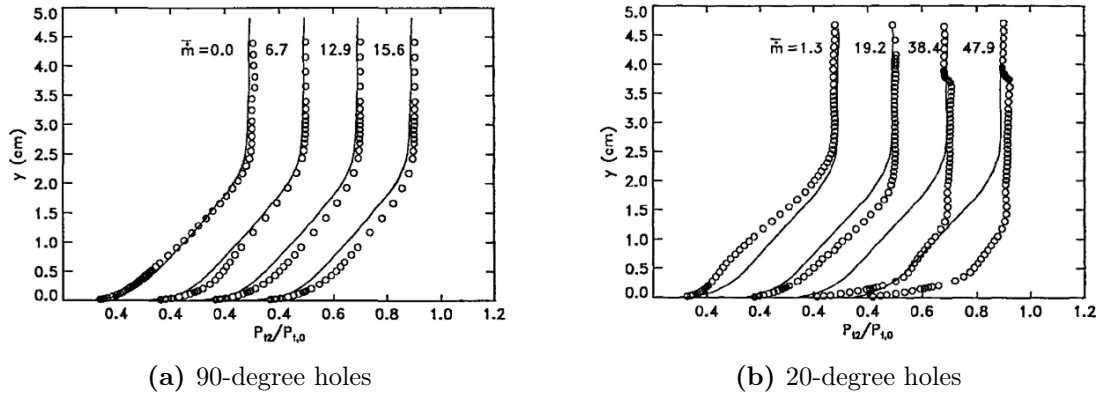


Figure 1.22: Pitot-pressure profiles downstream of the bleed for $M = 1.58$, from Willis and Davis [115].

Figure 1.18, the sonic flow coefficient was computed based on the static wall quantities and not using the total quantities. This scaling was introduced by Slater [98] and was discussed in more detail in Section 1.2.4.3. However, the Figure shows a large spreading of the data. The most significant impact is the hole inclination angle α . The lower the inclination angle, the higher the surface sonic flow coefficient. The plate thickness affects the size of the subcritical regime. The thinner the plate, the more extended the subcritical regime, which means that choking occurs for lower pressure ratios. Furthermore, a positive effect of the smallest hole diameter is found, leading to higher surface sonic flow coefficients.

While the sonic flow coefficient can be seen as a measure of bleed efficiency, it is also important to consider the control effectiveness of the flow control device. Therefore, Willis and Davis [115] measured the boundary-layer Pitot profiles downstream of the bleed region for different bleed rates using the same experimental setup as shown in Figure 1.17. Again, 90-degree holes and 20-degree (slanted) holes were compared. For a zero bleed rate, a degradation was found, meaning that the momentum inside the boundary layer was lower with respect to the inflow upstream of the bleed region, resulting in a lower shape factor. This effect is called the bleed roughness effect and was introduced by Paynter et al. [80]. Due to the hole contour, adverse pressure gradients and mixing effects are present, resulting in a decrease in the near-wall

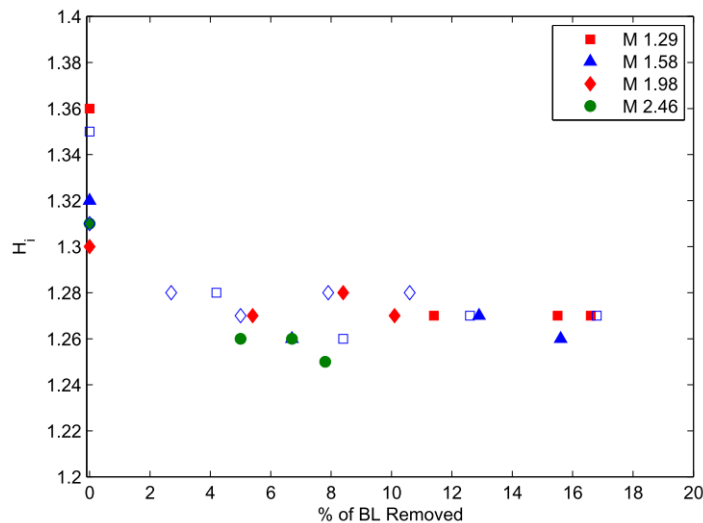


Figure 1.23: Evaluation of the shape factor from Willis and Davis [115] as a function of the bleed rate normalized by the boundary-layer mass flow rate, from Oorebeek et al. [76].

velocity. Willis and Davis [115] observed a higher roughness effect for slanted holes compared to the 90-degree holes, as visible in the Pitot-pressure profiles in Figure 1.22.

Any increase in the bleed rate resulted in the achievement of fuller profiles downstream of the bleed region. Similar to the sonic flow coefficient, slanted holes were found to be advantageous. Moreover, a quick saturation in the effect of the bleed was observed. Figure 1.23 clearly shows the saturation in the shape factor for 90-degree holes, as analyzed by Oorebeek et al. [76].

Davis et al. [33] also acquired the boundary-layer profiles downstream of the bleed region in their study about microporous bleed. Figure 1.24 shows the comparison between the C1 plate used by Willis and Davis [115] and a microporous plate with a porosity level of 9%. Significantly fuller profiles were achieved with the micro-holes, even for low bleed rates.

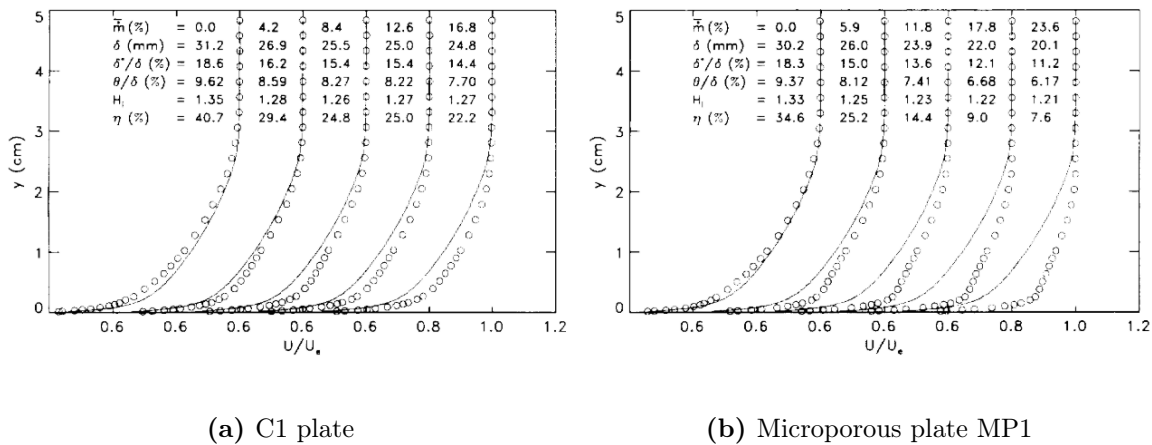


Figure 1.24: Velocity profiles for $M = 1.27$, from Davis et al. [33].

Additionally, they analyzed the influence of the bleed rate on the incompressible shape factor for the investigated plates compared to the C1 plate of Willis and Davis [115], as shown in Figure 1.25. Fuller boundary-layer profiles, resulting in lower shape factors, were observed for microporous plates (MP1, MP2, and MP3) compared to the measurements with larger holes. Moreover, a later saturation in the shape factor was found for these plates independently of the Mach number.

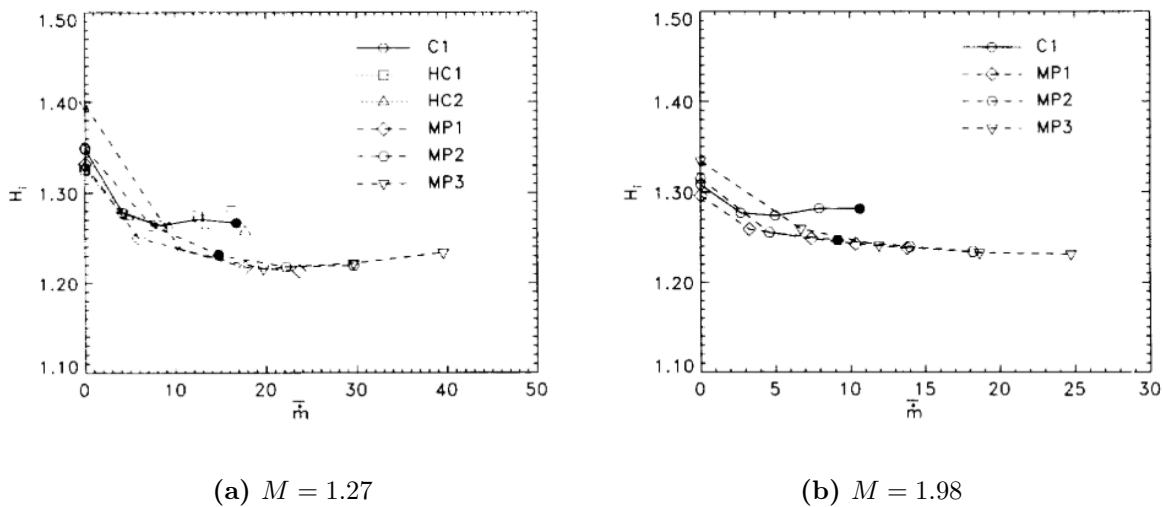


Figure 1.25: Evaluation of the shape factor for microporous bleed, from Davis et al. [33].

In Europe, several studies on porous bleed have been performed within the EUROSCHOCK project [104]. Doerffer and Bohning [38] used 22 different plates to characterize the transpiration

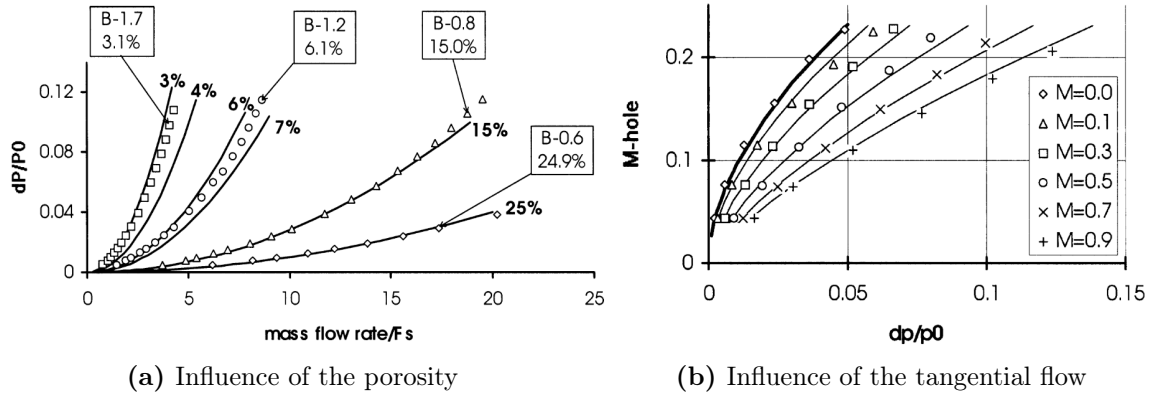


Figure 1.26: Bleed rate measured by Doerffer and Bohning [38].

flow as a function of the pressure drop. In contrast to the American studies, the hole diameter was low with values from $D = 0.085$ mm to 0.325 mm, as well as the porosity level, which was for the majority of the plates in the order of $\phi \sim 5\%$. The authors characterized the bleed rate as a function of the pressure drop through the plate, and the porosity ratio, and the influence of tangential flow over the perforated plate.

Figure 1.26a illustrates the impact of the porosity level on the bleed rate. The higher the porosity, the higher the bleed rate, because of the higher open area. Moreover, a rise in the

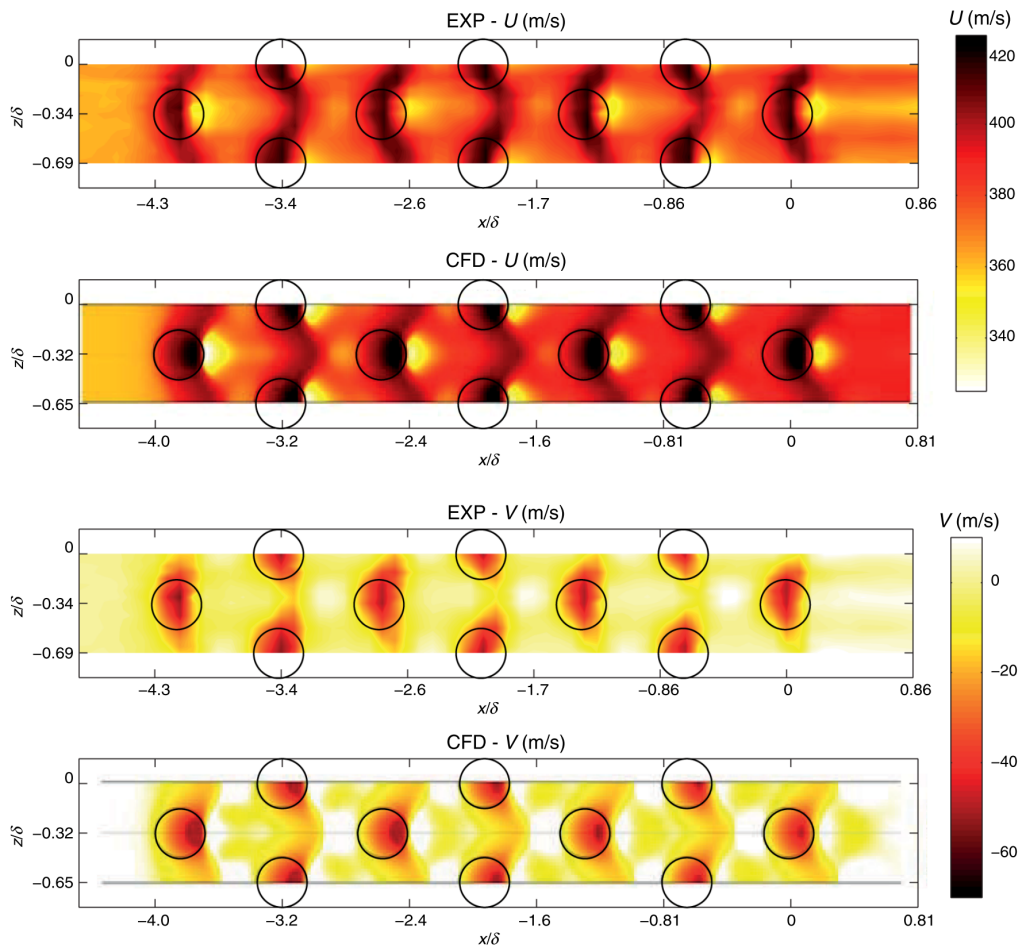


Figure 1.27: Velocity field on wall-normal plane acquired with LDV and CFD, from Oorebeek et al. [77].

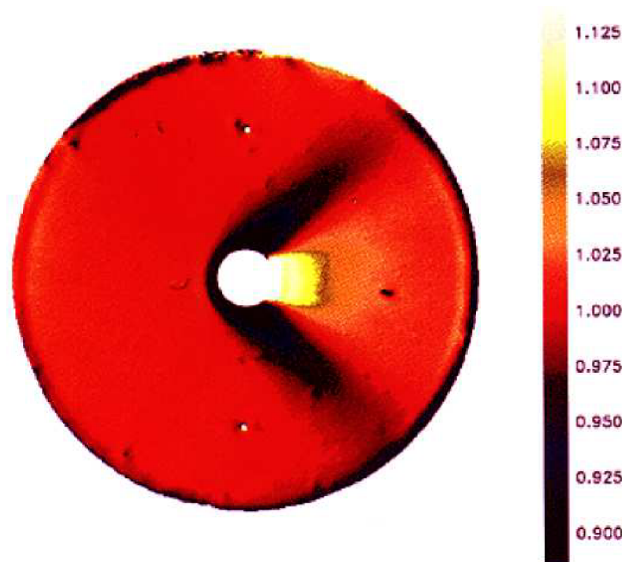


Figure 1.28: Pressure field around a bleed hole, from Bodner et al. [12].

pressure drop for increasing (subsonic) Mach numbers was found, as shown in Figure 1.26b. In this Figure, the (average) Mach number inside the hole is shown, which is proportional to the bleed rate.

Oorebeek et al. [76] characterized the effect of a porous bleed with $D = 2$ mm holes on a turbulent boundary layer for supersonic Mach numbers $M = 1.3$ and 1.8 with boundary-layer thicknesses of $\delta = 6.3$ mm and 7.0 mm ($\delta_{1,c} = 1.10$ mm and 1.42 mm). In particular, they observed its effect on the shape factor, which has a strong influence on the resistance of the boundary layer against adverse pressure gradients. As observed from the data of Willis and Davis [115], no more improvement was found after a certain bleed rate. Moreover, the acquired profiles were used to compute the skin friction coefficient by fitting a Van Driest-transformed boundary-layer profile to a log law. Thus, an increase in the skin friction coefficient with regard to the uncontrolled baseline flow was observed, which was higher for higher bleed rates.

Moreover, Oorebeek et al. [77] also performed LDV measurements on a wall-normal plane with a wall distance of $y/\delta = 0.086$ and compared it with CFD results. Figure 1.27 shows the obtained flow field for a free-stream Mach number of $M = 1.8$. In this figure, the traces of the expansion fans and barrier shocks generated by the bleed holes are apparent and showcase tree-dimensional effects provoked by the bleed holes. Already Bodner et al. [12] performed

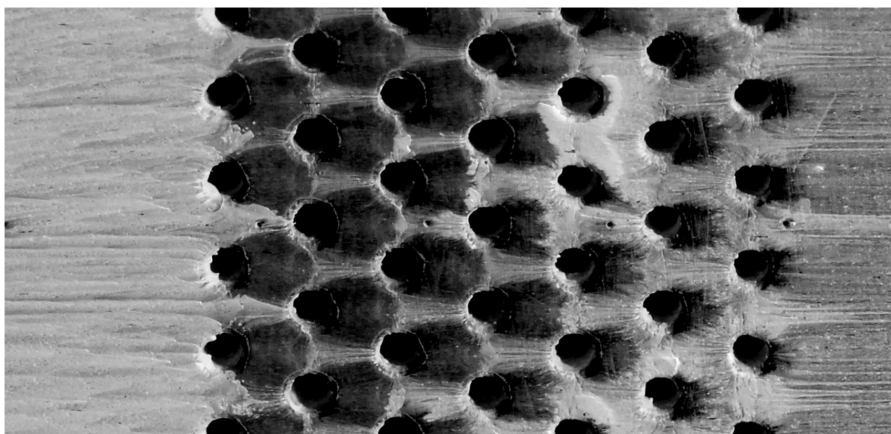


Figure 1.29: Oil flow visualization of flow over the bleed region, from Oorebeek and Babinsky [75].

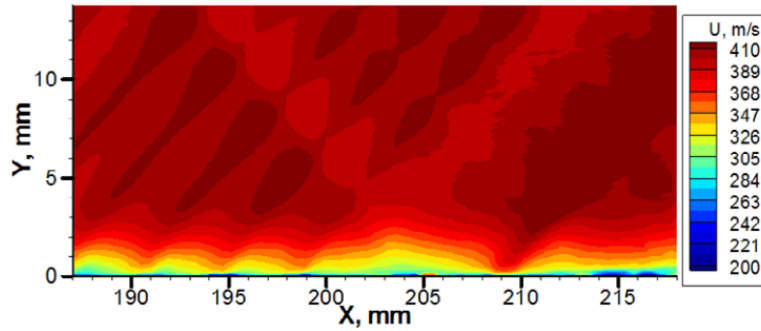


Figure 1.30: PIV measurements performed by Polivanov [83].

measurements with pressure-sensitive paint around the holes to highlight compressible flow features. Figure 1.28 shows one of the measurements for a Mach number of $M = 2.46$. A high-pressure area is located downstream of the bleed hole caused by the barrier shock. Oblique regions of low pressure can be seen alongside of the hole, induced by the expansion fan.

In an earlier study, Oorebeek and Babinsky [75] performed also oil flow visualization of the flow over the bleed region, as illustrated in Figure 1.29. Thus, three-dimensional flow structures become visible, caused by vortices that are generated by the bleed flow. Moreover, it visualizes variations of the flow downstream of the bleed region along the spanwise direction, as seen by the accumulation of oil between the last holes and further downstream.

In 2015, Polivanov et al. [84] investigated the influence of porous blowing and suction on a turbulent boundary layer at a Mach number of $M = 1.4$ with a boundary-layer thickness $\delta = 3$ mm. For the first time, Particle Image Velocimetry (PIV) was used to investigate the effect of a bleed on the boundary layer. Figure 1.30 shows one of these measurements for a hole diameter of $D = 2$ mm. The strong effect of the bleed holes on the streamwise velocity component is apparent.

1.2.2.2 Interaction with an SBLI

With the aim of controlling SBLIs, experiments have been performed by applying bleed below a shock foot. Hingst and Tanji [62] conducted the first fundamental study on perforated plates for the control of an oblique SBLI for Mach numbers of $M = 2.0$ and 2.5 in 1983. The bleed rate was evaluated using hot-wire measurements at the hole exit inside the cavity plenum. Moreover, the velocity profiles have been acquired along the bleed region by Pitot probe measurements. Figure 1.31 illustrates both the experimental setup and the instrumentation used for the measurements.

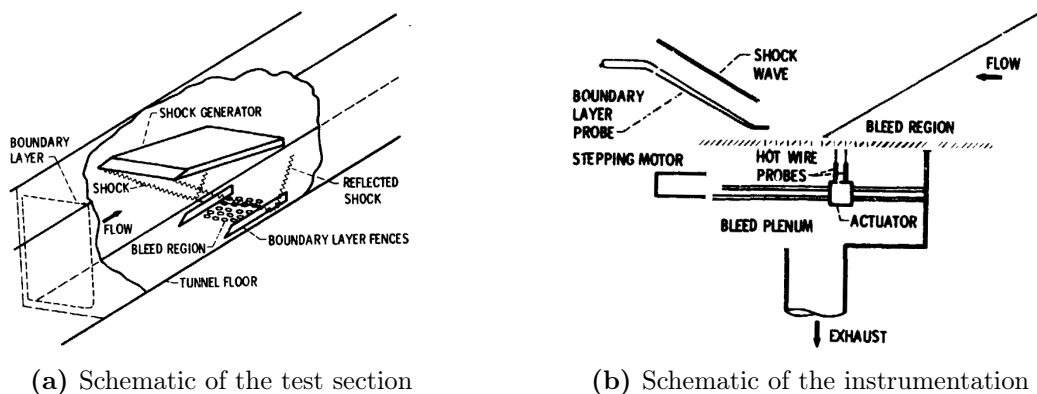


Figure 1.31: Experimental setup of Hingst and Tanji [62].

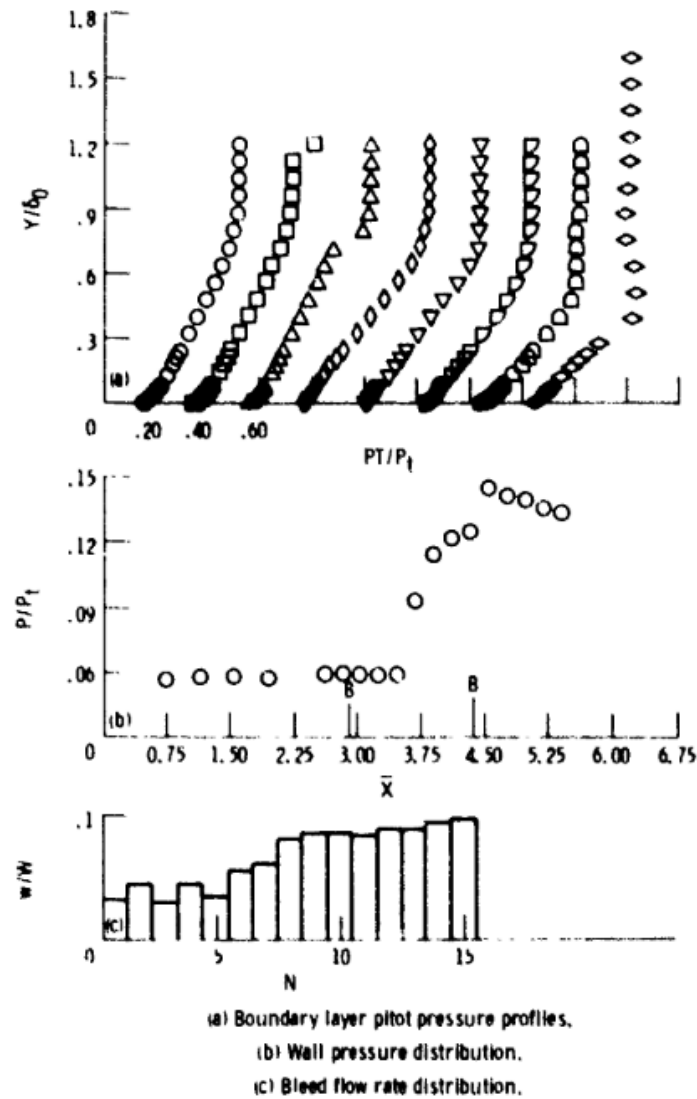


Figure 1.32: Experimental results of Hingst and Tanji [62].

It has shown that the bleed positively affected the boundary layer as the separation in the interaction region was eliminated, and the turbulent boundary layer downstream of the interaction was fuller compared to the uncontrolled case. Figure 1.32 details the Pitot-pressure profiles, the wall pressure distribution, and the bleed rate along the bleed region. The pressure rise due to the incident shock is observed at approximately 50% of the perforated plate length. A change in the slope of the pressure was found associated with the high bleed rates downstream of the shock. Thus, high bleed rates were noticed to reduce the interaction length.

The bleed rate distribution shows the bleed rate for all 15 bleed holes along the plate at the center. Fences were used alongside the perforated plate to guarantee the two-dimensionality of the flow, which was proven by employing oil-flow visualizations. Thus, the bleed rate can be assumed to be equal over the entire span of the plate. The plot demonstrates the increase of the bleed rate due to the pressure rise downstream of the shock. For the measurements, hot-wire measurements were performed at several streamwise positions along the bleed hole.

A subsequent study by Benhachmi et al. [9] showed similar results for the variation in the shock intensity. In all investigated cases, an improvement of the downstream boundary-layer profile in terms of the shape factor was found by applying suction.

Willis et al. [116] used the same setup as in their earlier study [117] to investigate the

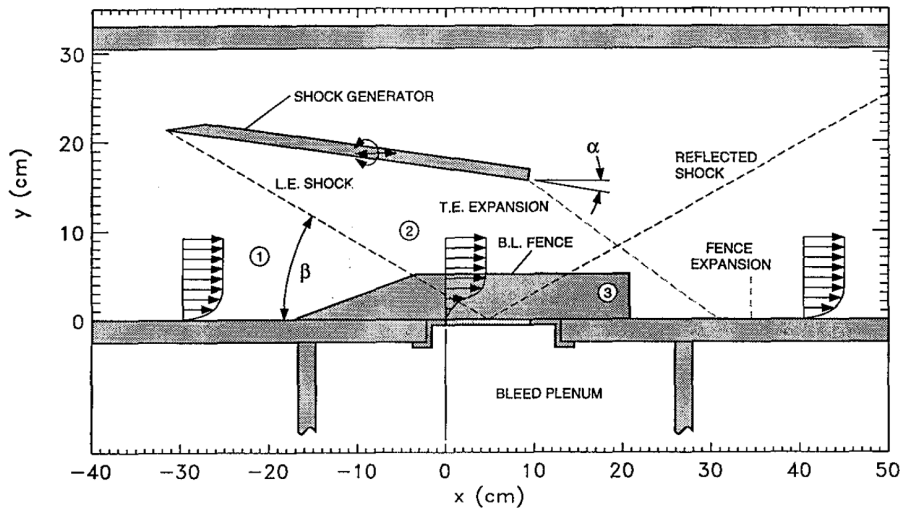


Figure 1.33: Experimental setup of Willis et al. [116].

control effect on an oblique SBLI at a Mach number of $M = 2.46$. Therefore, they added a shock generator with a wedge angle of $\alpha = 8^\circ$ to the test section, as shown in Figure 1.33.

Three different bleed rates have been investigated and compared to the uncontrolled baseline case. Figure 1.34 shows this comparison. The centerline pressure distribution, as presented in Figure 1.34a, demonstrates the impact of the bleed rate. For a zero bleed rate, the interaction length is found to be longer than in the reference case. With an increasing bleed rate, the effectiveness of the bleed in reducing the interaction length was proven. Moreover, the Pitot profiles were acquired along the bleed. Figure 1.34b shows the profiles downstream of the region. No significant difference in the boundary-layer profiles between the zero bleed case and the baseline was found, implying a low roughness effect of the holes. The higher the bleed rate, the fuller the boundary layer downstream of the bleed region. Thus, for the maximum bleed rate, only a small degradation compared to the reference profile upstream of the bleed region and incident shock was observed.

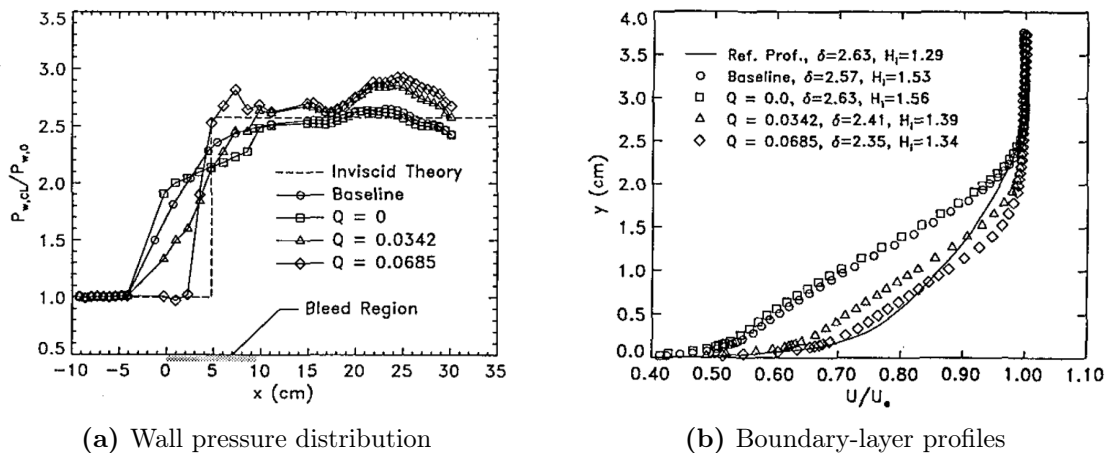


Figure 1.34: Experimental results of Willis et al. [116] for several bleed rates.

In 2006, experiments at the JAXA were performed to evaluate an existing bleed model [3]. Therefore, supersonic and subsonic boundary-layer bleed was investigated in a continuous-running wind tunnel. The bleed was applied in a diffuser-shaped test section (see Figure 1.35) meaning that the Mach number was not constant. Moreover, depending on the exit area, a normal shock wave was present inside the section.

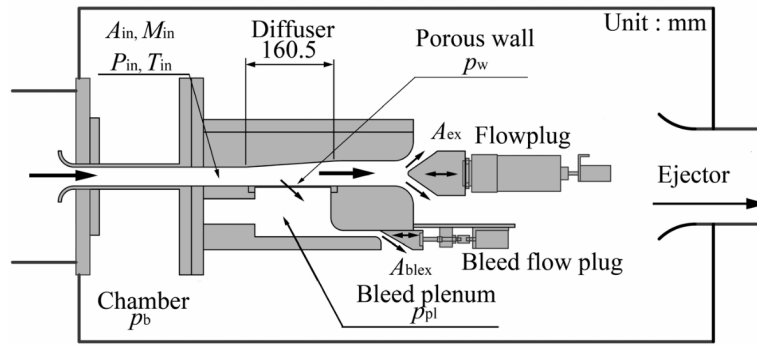


Figure 1.35: Experimental setup of Akatsuka et al. [3].

Two different plate characteristics with hole diameters of $D = 1.5$ mm and 7.0 mm ($D/\delta_1 = 0.38$ and 8.30) were investigated. By changing the plenum's exit area, the bleed rate was varied. Figure 1.36 shows a Schlieren photograph of the case with a normal SBLI and the smaller holes.

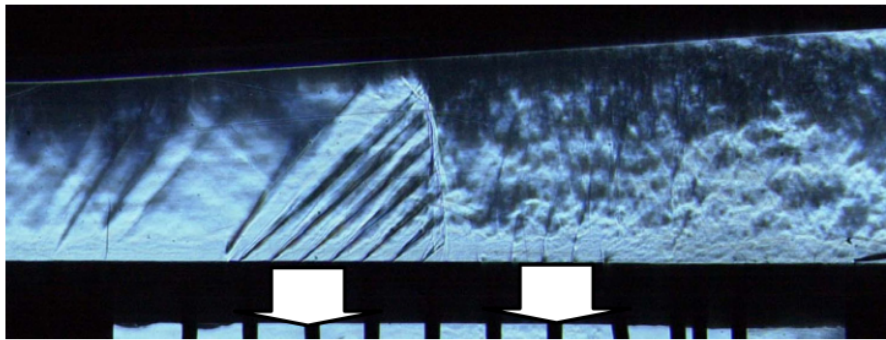


Figure 1.36: Schlieren photograph from Akatsuka et al. [3].

Moreover, the bleed rate was measured, and thus, the sonic flow coefficient was determined. Figure 1.37 presents all the points acquired in their study compared to the bleed model of Harloff and Smith [61], which are introduced later.

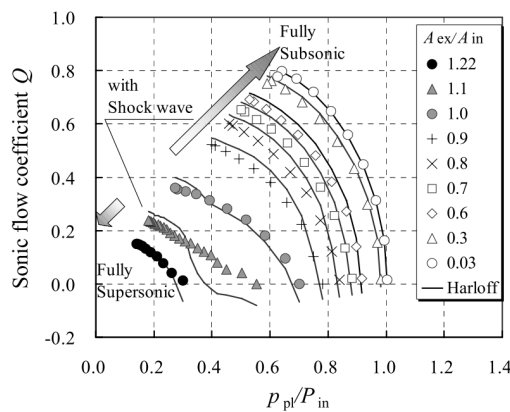


Figure 1.37: Sonic flow coefficient measured by Akatsuka et al. [3].

1.2.3 To the Understanding of the Flow Physics using CFD

The small size of the bleed holes makes it challenging, if not impossible to investigate the flow inside the bleed holes with state-of-the-art measurement techniques. However, also numerical

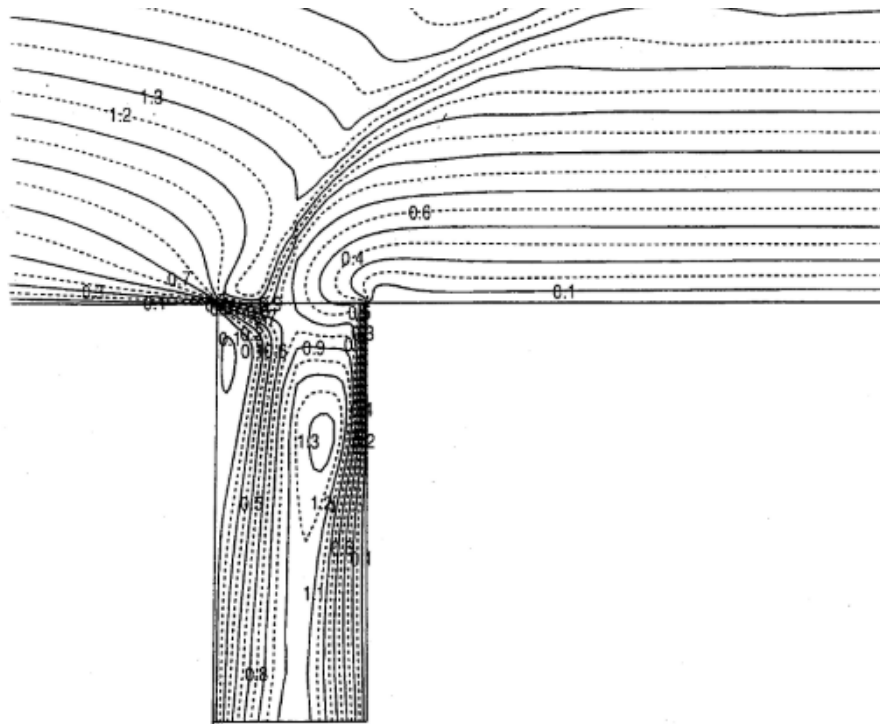


Figure 1.38: Mach number contours inside a bleed slot, from Hamed and Lehnig [55].

research on porous bleed systems is a challenging task since the computational costs are intense. The small size of the holes results in large meshes, which made numerical simulations for a long time too expensive in terms of computational costs.

The first two-dimensional RANS simulations on bleed slots were conducted in the early 1990s [55, 57, 58], investigating the interaction between the bleed and an incident oblique shock wave. These studies gained an insight into the flow structure inside a bleed including the separated region at the front of the bleed slot, an expansion fan, and a bow shock further downstream. Figure 1.38 shows the flow field obtained by the simulations of Hamed and Lehnig [55].

The first three-dimensional simulations, including a meshed bleed hole, were published at the same time [23, 86, 95] using a chimera overlapping grid to examine the SBLI controlled by the bleed for an external Mach number of $M = 2.5$. These studies enabled the investigation of the flow field inside the holes. Thus, the typical flow structure including a Prandtl-Meyer

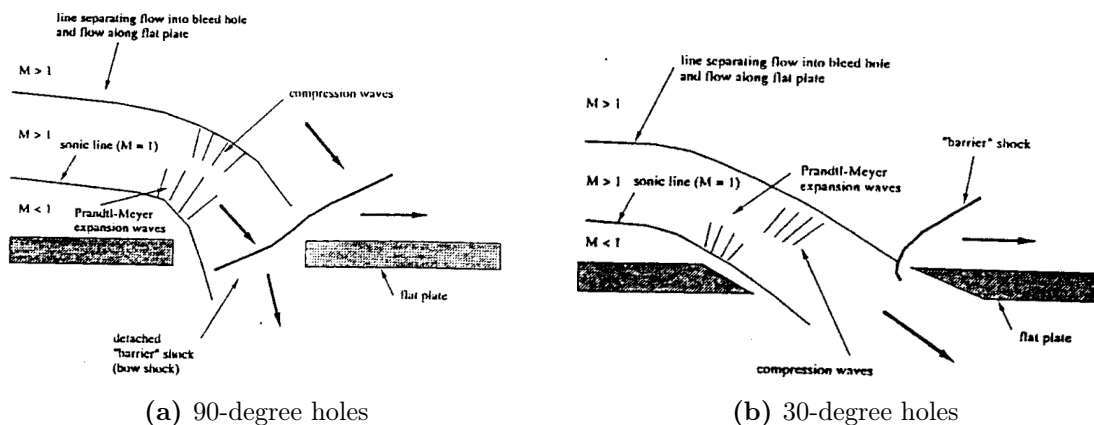


Figure 1.39: Flow topology inside the bleed holes, from Chyu et al. [23].

expansion at the front of the hole and the so-called barrier shock further downstream could be described. Moreover, differences between slanted holes and 90-degree holes were described, as shown in Figure 1.39. Subsequent studies further deepened the knowledge about the flow physics inside the holes [24, 96].

Rimlinger et al. [87] performed simulations intending to replicate the experiments of Willis et al. [116]. Extracted Pitot-pressure profiles downstream of the bleed region showed a very good agreement with the experiments, as shown in Figure 1.40.

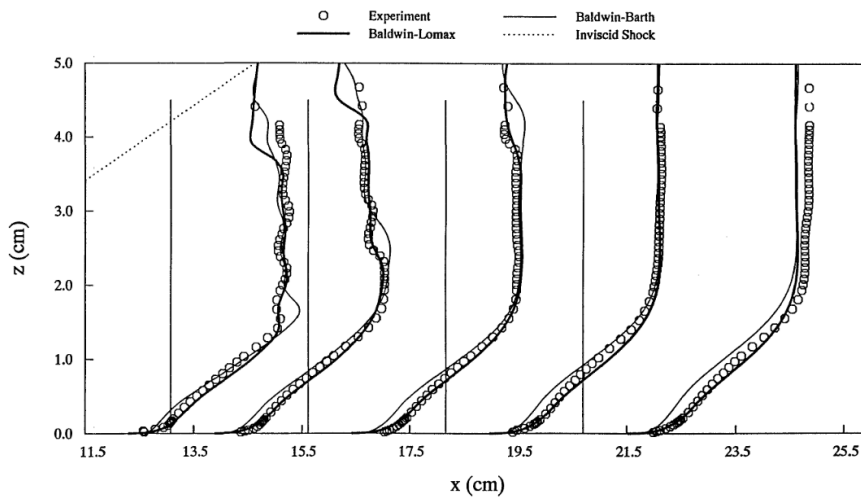


Figure 1.40: Pitot-pressure profiles by Rimlinger et al. [87] compared to the experiments of Willis and Davis [115].

Later studies [2, 43, 66, 92, 93] also focused on the replication of the study of Willis et al. [116]. Ghosh et al. [43] used an immersed-boundary method with Large Eddy Simulations (LES)/RANS and RANS turbulence modeling. Using this approach, but also with a pure RANS simulation, they obtained very good predictions of the Pitot-pressure profiles along the bleed region. Schwartz et al. [92] published the first study using LES simulations. Figure 1.41 illustrates a snapshot of the flow field. They observed the removal of the low-frequency unsteadiness that is typical for turbulent SBLIs. Moreover, a spanwise periodic vortex structure in the wake of the bleed was revealed, generating high-frequency behavior.

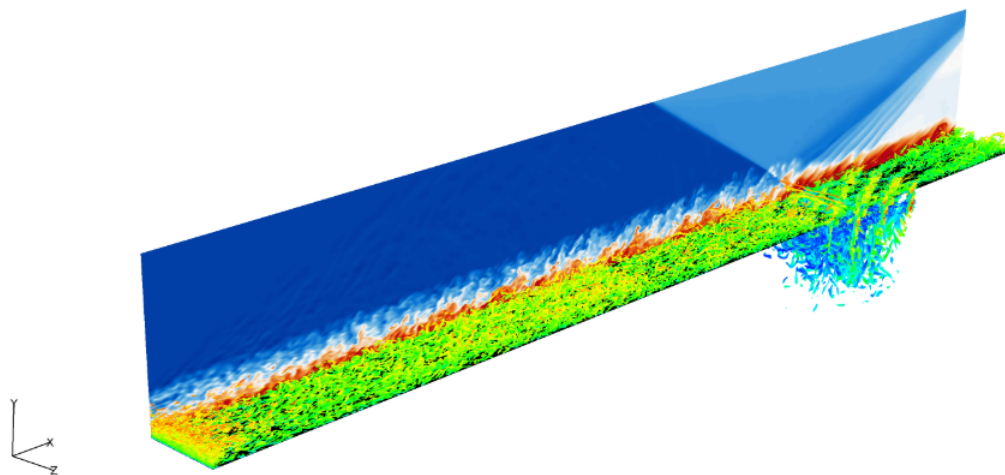


Figure 1.41: Computational flow field by Schwartz et al. [92]; isocontours of the Q-criterion are colored by the streamwise velocity, and the contours show the static temperature.

The experiments on the supersonic turbulent boundary-layer bleed performed by NASA in the 90s [115, 117] were also simulated in several studies [2, 43, 56, 59, 91, 98]. These investigations proved the applicability of numerical tools to predict the boundary-layer profiles along and downstream of the bleed region, as well as the sonic flow coefficient.

Moreover, several groups investigated single-hole setups [3, 34, 40, 60, 118]. Hamed et al. [60] focused on the effect of Reynolds number and boundary-layer thickness. Both parameters have a notable effect on the flow field behind the bleed. However, no significant influence on the sonic flow coefficient was found. Figure 1.42 illustrates the flow field inside a hole of a boundary-layer bleed for a free-stream Mach number of $M = 1.27$. Akatsuka et al. [3] and Eichorn et al. [40] used the simulations in addition to the performed experiments. Both studies investigated the influence of the inclination angle of the hole, finding a degradation in the bleed rate caused by the separation inside the holes in the case of 90-degree bleed holes.

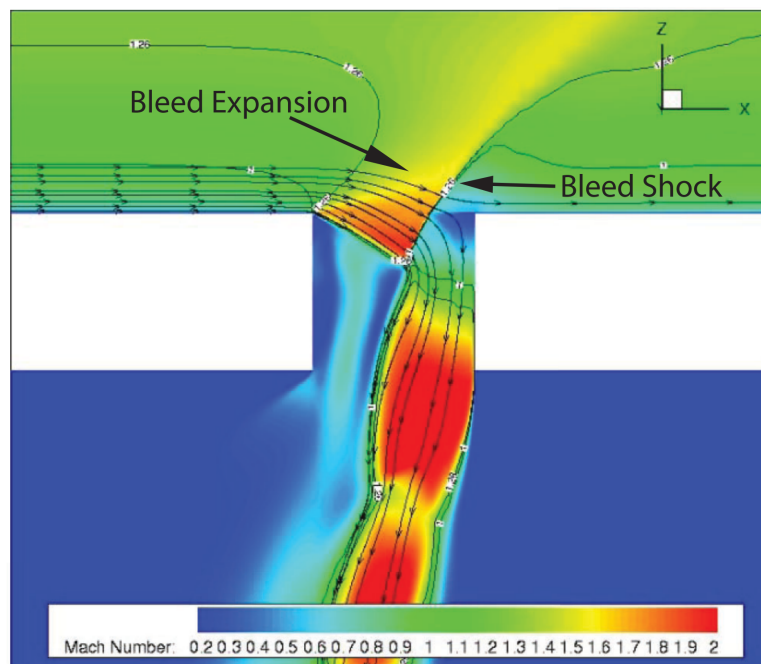


Figure 1.42: Mach number contours around the bleed hole, from Hamed et al. [60].

Also, Oorebeek et al. [77] used RANS simulations in addition to experiments for qualitative comparisons, finding a good agreement in the observed flow patterns.

The influence of the turbulence modeling using RANS simulations was investigated by Teh and Shih [111] using four different turbulence models. The simulations were conducted on bleed controlling an oblique SBLI for Mach numbers of 1.6, 2.0, and 2.4. While bleed rates and flow structure inside the holes were similarly predicted, significant differences in the boundary-layer profiles downstream of the bleed region were observed. However, the results were not compared to experimental data, which makes any assessment of the accuracy of the turbulence models challenging.

Altogether, CFD simulations have played a major role in understanding the flow physics within the bleed holes, which are challenging if not impossible to investigate experimentally. Flow phenomena such as barrier shocks and the separated region inside the holes became only visible with the help of numerical simulations. However, many studies only focused on the replication of experimental studies, while the power of numerical tools has been barely used to define the effects of the external flow characteristics or the geometrical parameters.

of Hingst and Tanji [62]. In 1992, Chyu et al. [22] tested nine different boundary conditions to simulate the flow in an axisymmetric air intake, which was experimentally investigated by Smeltzer and Sorensen [100]. They found three boundary conditions that stabilized the terminal shock in the air intake's throat in an unsteady RANS simulation. Two of these boundary conditions were adapted from Abrahamson and Brower [1]. Other early models are the model of Mayer and Paynter [67], which uses lookup tables from the experiments of Syberg and Hickcox [108] to interpolate the sonic mass flow coefficient for a given pressure ratio and Mach number, and the model of Dambara et al. [30], which is similar to that of Abrahamson and Brower [1]. The model of Harloff and Smith [61] semi-empirically computes the sonic flow coefficient. Remarkable is the classification of the flow topology inside the holes as a function of the external Mach number, as shown in Figure 1.44. Thus, the model is applicable to supersonic and subsonic conditions.

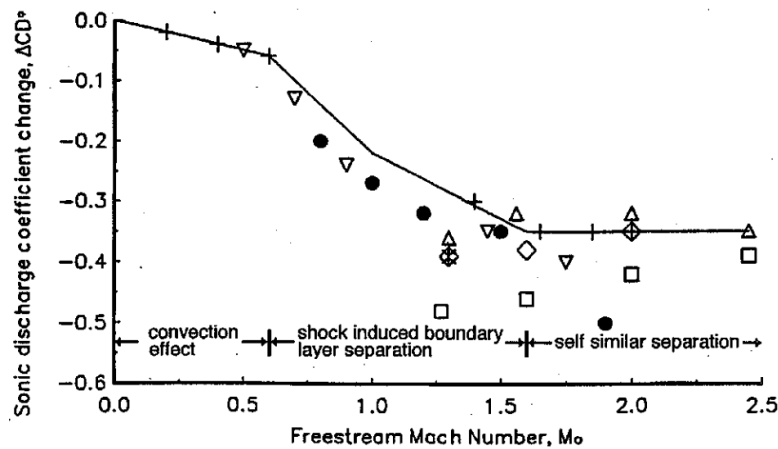


Figure 1.44: Decrease of the sonic discharge coefficient with the Mach number, from Harloff and Smith [61].

In the last two decades, more bleed models have been introduced. Akatsuka et al. [3] extended the model of Harloff and Smith [61] based on their experiments and numerical simulations. They improved the model for the case of blowing, where the bleed rate is overestimated. Moreover, they added a term to model the effect of the incoming boundary layer for ratios of boundary-layer (displacement) thickness to hole diameter. However, a coefficient needs to be determined to fit experimental data, which makes this model challenging to apply. Slater [98] found a correlation to fit the data of Willis et al. [117] by using a quadratic relation. Thus, the bleed rate can be computed using wall quantities only. Choe et al. [21] improved this model by considering the pressure change at the beginning of the plate caused by the Prandtl-Meyer expansion. Moreover, they added a porosity variation applicable to two-dimensional simulations. Morell and Hamed [70], Zhang et al. [120], and Wang et al. [114] introduced physics-based bleed models for supersonic flow. These models compute the bleed rate based on the free-stream Mach number and pressure ratio by assuming a two-dimensional Prandtl-Meyer expansion redirecting the flow into the bleed hole opening to calculate the deflection angle and the downstream Mach number. Thus, the mass flow rate passing the lower part of the barrier shock is computed. However, these models are inapplicable for subsonic flows and, consequently, for SBLIs.

Besides the application for supersonic air intakes, other bleed models have been introduced. Poll et al. [85] and Inger and Babinsky [64] proposed transpiration flow models based on the assumption of a fully developed (laminar) pipe flow. For these models, no external flow was taken into account. Doerffer and Bohning [38] found a relationship between the pressure ratio, the average transpiration Mach number inside the hole, and the wall shear stress at the external

wall. This model is validated using experimental data of different plates without external flow and measurements of one plate for external Mach numbers up to $M = 0.9$. Another transpiration flow model was introduced by Grzelak et al. [54], modeling the efficiency of the hole flow based on a comprehensive dataset of single-hole simulations. However, this model is not validated with external flow.

1.2.4.2 Implementation Approaches for the Boundary Condition

The modeling part is not only limited to the computation of the bleed rate but also consists of the application of models. Typically, bleed models are applied homogeneously, meaning that suction is applied on all cell faces. However, suction can be also applied in a distributed way similar to reality. Figure 1.45 shows two different approaches applied by Choe et al. [21]: on the left, we see the classical homogeneous application of their bleed models, while the bleed rate is varied as a function of the streamwise location on the right. In their approach, the porosity is calculated for every cell. However, this approach works only in a two-dimensional environment, where holes are not staggered or overlapping.

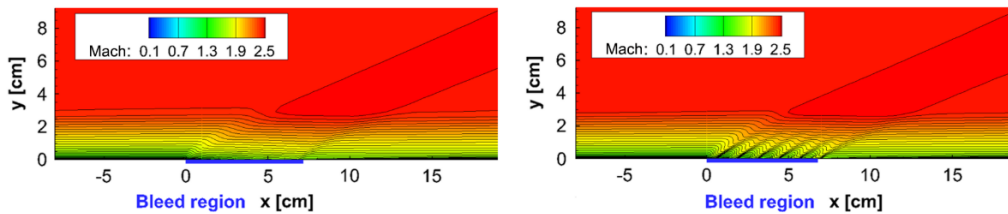


Figure 1.45: Mach number contours of the applied models of Choe et al. [21].

In 2000, Benson et al. [11] applied different approaches to use bleed boundary conditions in three-dimensional simulations. First, the computed reference simulations with the holes are taken into account. In the next step, the hole was closed, and the outflow profile from the preliminary simulations was applied. The next simplification was the application of a continuous bleed rate over the whole hole, and finally, only one cell was used to model the hole. With every step, some information got lost. However, the boundary-layer profiles downstream



Figure 1.46: Mach contour field (top) and transpiration velocity (bottom) for reference simulation (left), pressure boundary condition (center), and model of Slater [98] (right), from Orkwis et al. [78].

of the bleed have shown a good agreement with the reference case since the barrier shocks were modeled. Orkwis et al. [78] and Wukie et al. [118] worked on a similar approach showing significant improvement in the prediction of the flow field downstream of the bleed region. However, all these approaches are challenging to apply as the hole contour is still meshed, which results in heavy and complex computational meshes. Figure 1.46 compares a resolved reference simulation (left) with their approach of applying a pressure boundary condition at only the hole location (center), and the approach of Slater [98] (right).

Wang et al. [114] discretely modeled the hole using structured mesh grids (see Figure 1.47). Thus, the number of cells is reduced. However, their model is based on supersonic flow physics, as stated before. Moreover, the modeling of the barrier shock location might lead to very heavy meshes in case of small bleed holes.

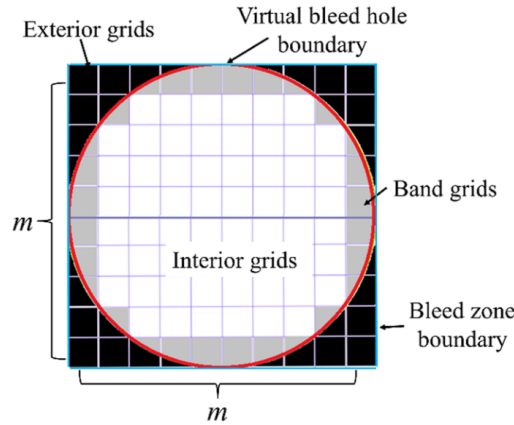


Figure 1.47: Grid topology of Wang et al. [114].

An entirely different approach to modeling the effect of a porous bleed on the boundary layer was used by Laurendeau et al. [65]. In their approach, the velocity scale in the turbulence model is manipulated. Therefore, the bleed roughness (Nikuradse's roughness k_s) at zero bleed is measured for a bleed geometry in subsonic flow. Afterwards, the zero bleed velocity profile is measured at the desired Mach number and a constant is varied to match the profile numerically. Finally, the model is applicable for all bleed rates for this Mach number since the bleed roughness is assumed to be constant independently of the bleed rate. Suction is applied by defining the transpiration velocity at the wall.

1.2.4.3 Models in Focus

In the following, eight models are presented in the order of their publication date. All selected bleed models are applicable in two-dimensional simulations, using the same approach as shown at the left side of Figure 1.45, and are therefore directly comparable. Moreover, the models are applicable for subsonic flows in contrast to the physics-based bleed models for supersonic flow (Morell and Hamed [70], Zhang et al. [120], and Wang et al. [114]).

All equations have been transcribed in the notation shown in Figure 1.43 to facilitate the comparison. For the application of the models, the holes are not modeled, but a suction/blowing boundary condition is applied on all cell faces, defined as the bleed region. Thus, the suction is homogeneously applied and not in a distributed manner. All quantities extracted or computed on these faces are denoted as wall quantities (subscript w). By contrast, the subscript bl designates the bleed flow properties inside the bleed holes. An important step is the conversion

of the bleed quantities into wall quantities using the porosity level ϕ . Thus, the bleed area

$$A_{bl} = \underbrace{\phi A_w}_{\text{Boundary condition}} = \underbrace{\sum A_h}_{\text{Reality}} \quad (1.6)$$

can be computed by correcting the wall area A_w using the porosity level. While the bleed rate [kg/s] equals the mass flow rate passing the wall $\dot{m}_{bl} = \dot{m}_w$, the wall mass flux [kg s/m²] given by

$$q_w = \phi q_{bl} \quad (1.7)$$

is lower than the bleed mass flux q_{bl} . This correction is required as the blowing and suction are applied on the whole patch and not locally distributed as in reality, where the bleed area corresponds to the sum of all holes areas A_h .

Only the final equations, as implemented in our solver, are shown for the presentation of the bleed models. See the corresponding reference for more details regarding the models and their derivations. Typically, bleed models have a wall transpiration flow velocity v_w or wall mass rate \dot{m}_w as the outcome. In this paper, all model outputs are converted into the wall mass flux for later application in the boundary condition.

$$q_w = \dot{m}_w / A_w = v_w \rho_w \quad (1.8)$$

Abrahamson and Brower (1988) The bleed model introduced by Abrahamson and Brower [1] is an analytical approach to compute the transpiration flow velocity across the plate based on the isentropic mass flow rate. The transpiration velocity is expressed as

$$v_w = \frac{c_b p_{pl} \phi}{\rho_w T_w} \sqrt{\left(\frac{p_w}{p_{pl}}\right)^{\frac{\gamma-1}{\gamma}} \left[\left(\frac{p_w}{p_{pl}}\right)^{\frac{\gamma-1}{\gamma}} - 1 \right] \frac{2\gamma}{R_s(\gamma-1)}} \quad (1.9)$$

for unchoked holes or as

$$v_w = \frac{c_b p_{pl} \phi}{\rho_w T_w} \sqrt{\frac{\gamma}{R_s} \left(\frac{\gamma+1}{2}\right)^{\frac{-(\gamma+1)}{2(\gamma-1)}}} \quad (1.10)$$

for choked flow with a pressure ratio $p_{pl}/p_w < 0.528$. The variable c_b is an empirically derived constant required to obtain agreement with the experiments of Hingst and Tanji [62]. Those experiments have been carried out for free-stream Mach numbers $M = 2.47$ and $M = 1.98$ and an oblique SBLI with a hole diameter of $D = 3.17$ mm and a porosity level of $\phi = 34.8\%$.

Poll et al. (1992) The bleed model of Poll et al. [85] is also an analytical model to compute the transpiration flow, which does not consider external flow. Here, the flow through the individual holes is assumed to be laminar and incompressible. The relation between pressure drop $\Delta p = p_w - p_{pl}$ and bleed rate is expressed as

$$\frac{\Delta p D^2}{\rho \nu^2} \left(\frac{D}{L}\right)^2 = 40.7 \frac{\dot{m}_{bl}}{\mu t} \left(1 + 0.05 \frac{\dot{m}_{bl}}{\mu L}\right). \quad (1.11)$$

Finally, we obtain the bleed rate by finding the root of (quadratic) equation 1.11.

Harloff and Smith (1996) The model of Harloff and Smith [61] is an approach to model the flow through a single hole or slot using the conservation of mass, momentum, and energy as well as empirical relations. Here, only the equations for a 90-degree hole are presented. The idea is to model the discharge coefficient of the hole for different geometries depending on the local flow conditions. Therefore, discharge coefficient correctors for the pressure effect ΔC_D^P , the effect of flow separation ΔC_D^S , and the length-to-diameter effect $\Delta C_D^{L/D}$ are added to the initial discharge coefficient.

$$C_D = C_{D,i} + \Delta C_D^P + \Delta C_D^S + \Delta C_D^{L/D} \quad (1.12)$$

The discharge coefficient depends on the Mach number at the boundary-layer edge M_e (see Figure 1.43).

$$C_D = C_{D,i} + \Delta C_D^{L/D} \quad \text{if } M_e = 0 \quad (1.13)$$

$$C_D = \frac{C_{D,i} + C_D^B}{2} \quad \text{if } 0 < M_e < 0.6 \quad (1.14)$$

$$C_D = C_D^B \quad \text{if } M_e \geq 0.6 \quad (1.15)$$

Without external flow, the incompressible discharge coefficient $C_{D,i} = 0.82$ is considered and corrected according to the length-to-diameter ratio. For Mach numbers $M_e < 0.6$, the discharge coefficient is based on the incompressible discharge coefficient and the discharge coefficient of Bragg [13], which in turn is a function of the pressure ratio and the incompressible discharge coefficient $C_D^B = CD(C_{D,i}, p_{pl}/p_w)$. For higher Mach numbers, only the discharge coefficient of Bragg [13] is applied.

The correction of the pressure effect is only taken into account for high Mach numbers $M_e > 0.84$ and pressure ratios $p_{pl}/p_w > 0.5$ when the presence of internal flow separation is assumed:

$$\Delta C_D^P = -0.46 \left(\frac{p_{pl}}{p_w} - 0.5 \right) \quad \text{if } \begin{cases} M_e > 0.84 \\ \frac{p_{pl}}{p_w} > 0.5 \end{cases} \quad (1.16)$$

$$\Delta C_D^P = 0 \quad \text{else} \quad (1.17)$$

Moreover, depending on the Mach number M_e , flow separation in the holes is considered with the trend of a lower corrector ΔC_D^S for higher Mach numbers.

$$\Delta C_D^S = -0.1M_e \quad \text{if } M_e \leq 0.6 \quad (1.18)$$

$$\Delta C_D^S = -0.06 - 0.4(M_e - 0.6) \quad \text{if } 0.6 < M_e \leq 1.0 \quad (1.19)$$

$$\Delta C_D^S = -0.22 - 0.217(M_e - 1.0) \quad \text{if } 1.0 < M_e \leq 1.6 \quad (1.20)$$

$$\Delta C_D^S = -0.35 \quad \text{if } M_e > 1.6 \quad (1.21)$$

The last considered effect is the length-to-diameter ratio effect. For long holes, the friction losses are assumed to be higher, leading to an increased discharge coefficient for lower ratios:

$$\Delta C_D^{L/D} = 0.08 \quad \text{if } L/D < 3 \quad (1.22)$$

$$\Delta C_D^{L/D} = 0 \quad \text{if } L/D \geq 3 \quad (1.23)$$

For the computation of the bleed rate \dot{m}_{bl} , the sonic mass flow rate \dot{m}_{sonic} needs to be determined first. Therefore, the sonic area

$$A_{sonic,w} = \phi A_w \frac{216}{125} M_{bl} (1 + 0.2M_{bl}^2)^{-3} \quad (1.24)$$

is computed with the hole exit Mach number

$$M_{bl} = \sqrt{5 \left(\frac{p_{pl}}{p_w} \right)^{-2/7} - 5}. \quad (1.25)$$

By knowing the sonic area, the sonic mass flow rate is calculated as follows:

$$\dot{m}_{sonic,w} = A_{sonic,w} p_w \left(\frac{\gamma}{R_s T_w} \right)^{\frac{1}{2}} \left(\frac{\gamma + 1}{2} \right)^{\frac{-\gamma+1}{2(\gamma-1)}}. \quad (1.26)$$

Finally, the bleed rate can be computed.

$$\dot{m}_w = C_D \dot{m}_{sonic,w} \quad (1.27)$$

The model of Harloff and Smith [61] has been calibrated and validated on different experimental datasets [109, 117].

Doerffer and Bohning (2000) Doerffer and Bohning [38] provide a porous bleed model based on the experimental data generated in the EUROSHOCK project [105]. The tested perforated plates have small hole diameters from 0.085 mm to 0.325 mm and porosity levels ranging from 2.27% to 24.9%. It should be noted that the porosity stated by Doerffer and Bohning [38] is an aerodynamic (measured) porosity, which is used because of manufacturing tolerances resulting in slightly differing hole sizes and hence, porosity levels. Therefore, a dependency between aerodynamic porosity and pressure drop without external flow was found, and all plates were calibrated using this relation. Moreover, the validation of the model with an external flow was performed using a plate with a hole diameter of $D = 0.185$ mm and a low porosity level of $\phi = 5.05\%$ or $\phi = 5.30\%$ depending on the installation direction. They found a relation between the pressure difference Δp across the plate and the effective (bleed) Mach number in the holes. Suction and blowing are distinguished because the suction rate was observed to be reduced for increasing external flow velocities.

In the case of suction, the following relation is applied:

$$\frac{p_w - p_{pl}}{p_w} = M_{bl}^{\frac{1}{0.55}} \left[\left(\frac{1}{1.2} \right)^{\frac{1}{0.55}} + 25 \left(\frac{|\tau_w|}{\frac{\rho_h v_{bl}^2}{2}} M_{bl} \right)^{\frac{1}{1.52}} \right]. \quad (1.28)$$

Here, the wall shear stress τ_w is used to quantify the external flow velocity. Its value is normalized by the dynamic pressure of the flow in the hole. In contrast, the external flow is not considered in the case of blowing. Hence, the pressure difference is only a function of the effective (bleed) Mach number:

$$\frac{p_{pl} - p_w}{p_{pl}} = M_{bl}^{\frac{1}{0.55}} \left[\left(\frac{1}{1.2} \right)^{\frac{1}{0.55}} \right] \quad (1.29)$$

The holes are assumed choked for a Mach number of $M_{bl} \geq 0.57$. This value is set as a limiter in the model.

Finally, with the knowledge about the hole Mach number, the mass flow rate is computed

$$\dot{m}_w = \phi A \rho_h \frac{M_{bl} \sqrt{\gamma R_s T_0}}{\sqrt{1 + \frac{\gamma-1}{2} M_{bl}^2}} \quad (1.30)$$

with T_0 being T_w for suction and T_{pl} for blowing.

Frink et al. (2003) The boundary condition introduced by Frink et al. [41] uses the porous surface model of Bush [16] for screen losses to simulate the transpiration flow through a porous wall in the case of passive control. However, its definition also enables the use in an active mode by setting a different plenum pressure. Three different states are defined in the equations, with the first state located upstream of the hole corresponding to the wall properties (subscript w), the second state associated with the throat inside the hole where the stream tube is the most contracted (subscript h), and the third state being downstream inside the cavity plenum corresponding to the subscript pl in the current nomenclature. The throat area inside the hole (A_h) is calculated

$$A_h = A_{pl} \underbrace{\varphi}_{\phi} (1 - s) \quad (1.31)$$

with the contraction factor φ and the solidity $s = 1 - \phi$. The contraction factor is based on an empirical relationship found by Bush [16] in the experimental data of Cornell [26]:

$$\varphi = \varphi_0 + 0.185(1 - \phi)^{1/4} \left(\frac{p_{t,h}}{p_h} - 1 \right) \quad (1.32)$$

$$\varphi_0 = \frac{0.04137}{1.0982 - \phi} + 0.57293 + 0.005786\phi \quad (1.33)$$

Thus, the contraction factor is purely based on the porosity ϕ and the reciprocal of the isentropic pressure ratio inside the holes, a function of the Mach number M_h .

In the following, only the equations considering flow from the external wall into the cavity plenum are regarded where the plenum pressure is smaller than the external wall pressure $p_{pl} < p_w$. In case of blowing, the plenum and wall states need to be swapped to obtain a flow into the domain. In the first step, the flow inside the hole throat is assumed to be choked ($M_h = 1$) to compute the maximum achievable mass flux through the holes. Therefore, the Mach number inside the plenum M_{pl} is iteratively calculated using the Newton approach:

$$\frac{\gamma + 1}{2} \left[\frac{1 + \gamma M_{pl}^2}{1 + \gamma \varphi \phi} \right]^2 \varphi^2 \phi^2 - M_{pl}^2 \left(1 + \frac{\gamma - 1}{2} M_{pl}^2 \right) = 0 \quad (1.34)$$

Subsequently, the maximum mass flux in the plenum is computed using the static pressure and the total temperature T_t :

$$(\rho u)_{max} = \left(\sqrt{\gamma / (R_s T_t)} \right) p_{pl} M_{pl} \left[1 + \frac{\gamma - 1}{2} M_{pl}^2 \right]^{1/2} \quad (1.35)$$

If the flow is choked, $(\rho u)_w \geq (\rho u)_{max}$, the Mach number in the hole is set to $M_h = 1$, and the mass flux at the wall to $(\rho u)_w = (\rho u)_{max}$. If not, M_h is iteratively calculated.

$$M_h^2 \left(1 + \frac{\gamma - 1}{2} M_h^2 \right) \left[\frac{1 + \gamma M_{pl}^2}{1 + \gamma M_h^2 \varphi \phi} \right]^2 \varphi^2 \phi^2 - \frac{R_s T_t (\rho u)_w^2}{\gamma p_{pl}^2} = 0 \quad (1.36)$$

It is essential to know that the contraction factor is a function of M_h , which is, in turn, computed using the contraction factor. Therefore, multiple iterations are required to converge to the final Mach numbers M_h and M_{pl} .

In the next step, the physical quantities at the wall are computed, starting with the total pressure $p_{t,w}$:

$$p_{t,w} = p_{pl} \frac{1 + \gamma M_{pl}^2}{1 + \gamma M_h^2 \varphi \phi} \left[1 + \frac{\gamma - 1}{2} M_h^2 \right]^{\gamma / (\gamma - 1)} \quad (1.37)$$

The Mach number at the wall is iteratively solved as follows.

$$M_w^2 \left[1 + \frac{\gamma - 1}{2} M_w^2 \right]^{-\frac{\gamma+1}{\gamma-1}} - \frac{R_s T_t (\rho u)_w^2}{\gamma p_{t,w}^2} = 0 \quad (1.38)$$

The static wall pressure is finally computed by knowing the total conditions and the Mach number:

$$p_w = p_{t,w} \left[1 + \frac{\gamma - 1}{2} M_w^2 \right]^{-\frac{\gamma}{\gamma-1}} \quad (1.39)$$

Since the wall pressure is directly extracted from the boundary interface inside the domain during the numerical computation, and the wall mass flux $q_w = (\rho u)_w$ is required, a further iterative calculation using the Newton method is needed to obtain the desired output. Please note that Equations 1.34, 1.36, and 1.38 are stated differently in the original publication because of an error in the isentropic flow relation. Non-consideration of these corrections increases the estimated mass flux by approximately one order of magnitude.

Slater (2012) The bleed model of Slater [98] is an empirical model based on the supersonic experiments of Willis et al. [117] for the (C1) plate with a hole diameter of $D = 6.35$ mm and a porosity level of $\phi = 19.1$ %. The sonic flow coefficient, defined as

$$Q_{sonic,w} = \frac{\dot{m}_w}{\dot{m}_{sonic,w}} \quad (1.40)$$

is scaled with respect to wall conditions using the bleed rate \dot{m}_w and the sonic mass flow rate for wall conditions:

$$\dot{m}_{sonic,w} = p_w \phi A_w \left(\frac{\gamma}{R_s T_w} \right)^{\frac{1}{2}} \left(\frac{\gamma + 1}{2} \right)^{\frac{-\gamma+1}{2(\gamma-1)}} \quad (1.41)$$

This scaling is applied to eliminate the dependency of the Mach number at the boundary-layer edge from the equations. Otherwise, the extraction at the boundary-layer edge would be required, which is complex and almost impossible for separated or distorted flows. The sonic flow coefficient for wall conditions quantifies the efficiency of the bleed device. The author proposed a quadratic curve fit to model the sonic flow coefficient

$$Q_{sonic,w} = -0.57 \left(\frac{p_{pl}}{p_w} \right)^2 + 0.6 \quad (1.42)$$

as a function of the pressure ratio of plenum pressure and external wall pressure.

Choe et al. (2020) The model of Choe et al. [21] is a variation of the boundary condition of Slater [98]. Slater [98] assumes a wall pressure equal to the pressure on the boundary-layer edge. By contrast, Choe et al. [21] take the effect of the flow expansion above the porous bleed region into account. Baurle and Norris [7] have already found an underestimation of the sonic flow coefficient using the bleed model of Slater [98] due to the missing consideration of the local flow expansion in the bleed region.

The new scaling of Choe et al. [21] leads to the new quadratic curve fit

$$Q_{sonic,w} = 0.6756 - 0.8086 \left(\frac{p_{pl}}{p_w} \right)^2 + 0.1846 \frac{p_{pl}}{p_w} \quad \text{if } \frac{p_{pl}}{p_w} \geq 0.2634 \quad (1.43)$$

$$Q_{sonic,w} = 0.6681 \quad \text{else} \quad (1.44)$$

by using the same validation data [117] as Slater [98].

Grzelak et al. (2021) Grzelak et al. [54] defined the first bleed model based on a numerical database. Therefore, single-hole simulations without external flow were conducted. The simulations were validated against experiments by measuring the bleed rate for three different perforated plates up to choking conditions. The authors introduced the concept of modeling the flow efficiency η , which describes the flow losses across the plate. Using the flow efficiency, the Mach number at the hole outlet is computed

$$M_{bl} = \sqrt{\frac{2}{\gamma - 1} \left[\left(1 + \eta \left(\frac{p_w}{p_{pl}} - 1 \right) \right)^{\frac{\gamma-1}{\gamma}} - 1 \right]} \quad (1.45)$$

as a function of the pressure ratio from stagnation hole inlet pressure, which is equal to the wall pressure p_w for no external flow, to the static hole outlet pressure, here described by the plenum pressure p_{pl} .

By knowing the hole exit Mach number, the bleed rate of the boundary condition is computed as:

$$\dot{m}_w = \phi A_w [p_{pl} + \eta(p_w + p_{pl})] \sqrt{\frac{\gamma M_{bl}^2}{R_s T_w (1 + \frac{\gamma-1}{2} M_{bl}^2)^{\frac{\gamma+1}{\gamma-1}}}} \quad (1.46)$$

The flow efficiency is expressed as

$$\eta = 0.429\phi - 0.01803 \frac{L}{D} + 0.64472, \quad (1.47)$$

which is a function of the porosity level ϕ and the length-to-diameter ratio L/D . The validation range goes from 4% to 10% for the porosity level and 1.5 to 8 for the length-to-diameter ratio.

1.2.4.4 Scope of Application

For the control of SBLIs in supersonic air intakes (see Figure 1.43), various aspects must be considered in modeling the porous bleed to guarantee an accurate prediction. For normal SBLIs or SBLIs with flow separation, both subsonic and supersonic flows must be controlled. Moreover, local blowing may occur due to the intense pressure gradient and shock instabilities, causing a higher static pressure in the plenum than in the supersonic region, which should be considered in the modeling. Besides, low pressure ratios p_{pl}/p_w can lead to the choking of the holes.

Model	External flow		Choked holes	Blowing	Extra inputs
	Subsonic	Supersonic			
Abrahamson and Brower [1]	-	✓	✓	-	-
Poll et al. [85]	-	-	-	o	L/D
Harloff and Smith [61]	✓	✓	✓	-	$L/D, M_e$
Doerffer and Bohning [38]	✓	-	✓	✓	τ_w
Frink et al. [41]	-	-	✓	o	-
Slater [98]	-	✓	✓	-	-
Choe et al. [21]	-	✓	✓	-	-
Grzelak et al. [54]	-	-	✓	o	L/D

Table 1.1: Validated scope of application for the different models.

Table 1.1 gives an overview of the range of validity for the previously introduced models. Furthermore, the table shows the additional input data required to compute the bleed mass flux. If no extra input is stated, the model only uses the static external wall pressure and plenum pressure, as well as the wall temperature and porosity level. These four quantities are required for each of these models.

Three of the selected models (Abrahamson and Brower [1], Slater [98], Choe et al. [21]) are based on supersonic data only, which results in the consideration of compressible effects that are not necessarily present for subsonic flows. It is expected that the accuracy of the models is reduced for subsonic conditions. However, the governing equations of the models enable their use even for subsonic conditions, which is different from other models (e.g., Zhang et al. [120]) that are purely based on supersonic flow phenomena. On the contrary, the models of Poll et al. [85], Frink et al. [41], and Grzelak et al. [54] are validated without external flow. Consequently, flow separation in the front of the hole induced by any external flow is not considered. Harloff and Smith [61] introduced the only model relying on both supersonic and subsonic data. However, extracting the Mach number at the boundary-layer edge M_e is required, complicating the implementation. The model of Doerffer and Bohning [38] is validated up to $M = 0.9$ by using the wall shear stress as an indicator of the external flow magnitude.

Moreover, the model of Doerffer and Bohning [38] is the only model with a separate relation for blowing. For the models of Poll et al. [85], Frink et al. [41], and Grzelak et al. [54], no differentiation between blowing and suction (o) is made. Since the models of Slater [98] and Choe et al. [21] are based on a quadratic regression, pressure ratios $p_{pl}/p_w > 1$ lead to relatively high blowing rates.

Besides this theoretical comparison of the bleed models, comprehensive studies evaluating their performance are missing. Baurle and Norris [7] compared the implemented models of Doerffer and Bohning [38] and Slater [98] with the experimental results of Willis et al. [117], Willis and Davis [115], and Willis et al. [116]. Both models have shown qualitatively good agreement with the reference cases. However, they stated the necessity of a larger sample to fully validate the models. Moreover, the experimental results of Willis et al. [117] were used to derive the model of Slater [98]. Nevertheless, a significant underestimation of the sonic flow coefficient by the applied model compared to the experimental results was observed. Also, for both models, the boundary-layer profiles downstream of the bleed region were fuller compared to both experimental results and fully resolved three-dimensional reference simulations. The same effect is found in the results of Choe et al. [21], who compared their model with the model of Slater [98] and the same experimental reference data.

In summary, none of the presented bleed models cover all possible situations that may appear in an SBLI, which justifies the present study. Moreover, a comprehensive evaluation of the models is missing, which is mainly a consequence of insufficient reference data to compare.

Chapter Summary

In this chapter, the physical principles of SBLIs and the state of the art on the research of flow control by porous bleed were introduced. First, the different kinds of SBLIs, which are found in supersonic air intakes, were presented. After, the flow and boundary-layer characteristics that influence the shock-induced flow separation were detailed. These are essential for any flow control technique. In the second step, the history of experimental and numerical research on porous bleed was presented, as well as modeling work to simplify the design of bleed systems.

In supersonic air intakes, both oblique and normal SBLIs are found, and flow separation may occur. Thus, flow control is often required and applied. Different parameters were found to influence the flow separation in the case of oblique SBLIs, namely the (incompressible) boundary-layer shape factor and the skin friction coefficient. The lower the shape factor, the lower the interaction length. Moreover, high skin friction coefficients counteract the retardation effect of the incident shock. Both parameters are linked to the subsonic part of the boundary layer. The lower the shape factor or the higher the skin friction coefficient, the smaller the subsonic region in the boundary layer. Thus, the upstream influence of the adverse pressure gradient decreases, and a smaller part of the boundary layer is susceptible to separation. For the final terminal shock, the shape factor has no significant effect on the onset of flow separation, which is at $M \approx 1.3$ or a static-pressure-rise ratio of approximately 1.89.

Porous bleed flow control was successfully applied in supersonic air intakes, resulting in an increased total pressure recovery and the prevention of unstart conditions. High porosities and an application downstream of the shock were found to be advantageous. More fundamental experimental studies have proven a positive effect on the boundary layer, i.e., fuller boundary-layer profiles with a lower (incompressible) shape factor downstream of the bleed region. Small and slanted holes increased this effect, but saturation was observed with increasing bleed rates. Also, both parameters improved the bleed rate for a given pressure ratio from cavity plenum pressure to stagnation pressure. Moreover, the bleed rate depends on the inflow Mach number and differs significantly, especially for subsonic conditions.

Even though experiments showed parameter effects, numerical research was required to understand the flow physics inside the holes, which are not resolved by experimental studies. RANS simulations are proven to show a good agreement with experimental results. However, the numerical costs are high because of the large mesh sizes to model all the bleed holes. Unfortunately, most numerical works focused only on the reproduction of experiments without extending the knowledge of geometrical or flow influences on the bleed performance.

Bleed modeling is an approach to reduce the numerical costs by applying an outflow boundary condition in the CFD solver. Different approaches for the computation of the bleed rate, but also on the implementation in the numerical setup have been introduced. The major problem of the existing bleed models is the limited validation range, which results in almost every case in an application being out of the validation range. Moreover, the implementation approach affects the effect of the boundary condition on the flow field. Usually, bleed models are homogeneously applied, and thus, compressible phenomena such as barrier shocks are not modeled.

Chapter Conclusions

The literature research gives valuable insights that are used to draw conclusions considered in this work. Numerical simulations are found to be the best way to investigate porous bleed, as experimental work cannot resolve the flow physics inside the bleed holes, and parametric studies are too expensive to perform experimentally. Previous studies have proven a good agreement between numerical and experimental work.

The literature research is used to define a representative flow case to investigate the control effect of porous bleed systems. In this study, an oblique SBLI, which is irregularly reflected at the wall, is examined, which is a flow pattern that may appear in supersonic air intakes. Thus, the effect of porous bleed on supersonic and subsonic flow can be determined, as the flow downstream of the Mach stem is decelerated to subsonic conditions. In contrast to a normal SBLI, the SBLI is geometrically induced and no second throat is required to generate the required back pressure, simplifying both numerical and experimental studies. The selected inflow Mach number is $M = 1.6$ to guarantee a sufficient shock intensity to obtain shock-induced flow separation. Moreover, boundary-layer bleed is investigated separately for supersonic and subsonic conditions as an influence of the external Mach number on the bleed performance was observed. The flow cases are presented in Chapter 4.

An important step is extending the understanding of flow physics for different inflow characteristics and the influences of geometrical parameters. Even though numerical simulations are the main tool used in this study, experiments play a major role in validating the numerical setup for different bleed configurations. Two different plate geometries are used to experimentally characterize the control on three different flow cases. The generated data is compared to the numerical findings in Chapter 5.

After the validation with a relatively small number of samples, the numerical setup can be used to generate a big database, highlighting the influences of geometry and external flow on the bleed performance (see Chapter 6). This database is used to evaluate the bleed performance in two respects. First, the parameter influences on the bleed efficiency are examined, showcasing the impact of geometry and external flow conditions on the bleed rate for a given pressure ratio. In the second step, the control effectiveness is investigated. As stated before, the boundary-layer state upstream of the shock affects the interaction length. Thus, simulations with a fixed bleed rate are conducted to determine the effect of the bleed on the boundary layer.

The database is used to evaluate state-of-the-art bleed models in Chapter 7. The application of the models in the same setup is used to highlight the advantages and disadvantages of the different models, but also to investigate the accuracy of the models for a wide range. In contrast to previous studies, the applied models are compared to numerical reference data to highlight the drawbacks of the bleed modeling clearly and to neglect deviations caused by measurement uncertainties and numerical approaches (turbulence modeling, RANS approach, etc.). Moreover, the implementation of the models is used to find drawbacks that complicate the application or increase numerical costs.

Key Points:

Shock-wave/boundary-layer interactions

- ❑ Low (incompressible) **shape factor** decreases interaction length
- ❑ High **skin friction coefficient** (wall shear stress) leads to higher resistance of the boundary layer against adverse pressure gradients
- ❑ **Reynolds number effects** are low on interaction length and flow separation onset
- ❑ **Flow separation onset** for normal SBLI at $M \approx 1.3$ or static-pressure-rise ratio of approximately 1.89
- Mach number of $M = 1.6$ selected in this study to guarantee flow separation in case of an SBLI → Chapter 4
- Wall shear stress suitable quantity to evaluate the control effectiveness of a porous bleed

Experimental work on porous bleed

- ❑ Successfully applied in **supersonic air intakes**
- ❑ Effects on bleed rate → **bleed efficiency**
 - Higher bleed rates for **small holes** (microporous holes)
 - Higher bleed rate for **slanted holes**
 - Differences between **supersonic** and **subsonic** inflow conditions
 - Investigation of the **geometrical parameters** required, especially on the hole diameter → Chapters 6
 - Distinction between **supersonic** and **subsonic** regimes required → Chapter 4
- ❑ Effects on boundary layer → **control effectiveness**
 - Fuller boundary-layer profiles for **small holes** (microporous holes)
 - Higher roughness effect for **slanted holes**, but fuller boundary-layer profiles in the case of suction
 - Quick **saturation** in the improvement of the shape factor

Numerical work on porous bleed

- ❑ **Flow topology inside the holes** only observable by means of CFD
- ❑ **Good agreement** between RANS simulations and experiments
- **RANS simulations** a priori suitable for investigation of porous bleed

Bleed modeling

- ❑ Bleed models do not consider all **geometrical parameters**
- ❑ Models are **validated for small ranges** only (specific Mach number, porosity level, hole diameter, etc.)
- ❑ Model of Harloff and Smith [61] is the only model applicable for both **supersonic and subsonic** conditions but requires flow field quantities that are challenging to extract
- Eight models selected for **benchmarking** in Chapter 7
- **New model** required that is suitable for the application in SBLI control → Chapter 8

Computational Setup

*Regardless of how complex a simulation is, the reality is
always more complex.*

MARC-UWE KLING

Chapter Introduction

RANS simulations were selected as the main tool for investigating porous bleed flow control in this work. The following chapter is dedicated to the computational setup used for the numerical investigations. First, the domains and parameters for the investigated physical problems are introduced before heading to the numerical settings. Afterward, the mesh of the three-dimensional (reference) simulations is detailed, before describing the evaluation of bleed efficiency and control effectiveness. In the last step, the approach to implement state-of-the-art bleed models is introduced, as well as the implementation procedure for the new model.

2.1	Problem Description	47
2.1.1	Flow Inside the Wind Tunnel with & without SBLI	47
2.1.2	Boundary-Layer Bleed on a Flat Plate	48
2.2	Governing Fluid Equations and Flow Solver	50
2.3	Meshing for the Three-Dimensional Simulations	51
2.4	Extraction and Evaluation of the Bleed Efficiency and Control Effectiveness	53
2.5	Implementation of State-of-the-Art Bleed Models	55
2.6	Implementation of the Local Porosity Variation	58

2.1 Problem Description

In the current work, we simplify the complex flow case of an SBLI by separately investigating supersonic and subsonic bleed. In this section, the domains and parameters of the investigated physical problems are explained.

2.1.1 Flow Inside the Wind Tunnel with & without SBLI

For the comparison with the experiments performed later, the flow within the ONERA S8Ch supersonic wind tunnel is investigated. The incoming Mach number is $M = 1.62$, and the bleed system is integrated into a flat plate. This Mach number is selected to ensure the presence of flow separation. The stagnation pressure is $p_t = 93\,000$ kPa and the stagnation temperature is $T_t = 300$ K. The free-stream flow is generated using a convergent-divergent nozzle with its shape being equal to that of the S8Ch wind tunnel at ONERA in Meudon for a later comparison of the numerical results with experiments. With the aim of investigating the interaction of the porous bleed with an incident shock, a shock generator can be added to the domain. In that case, the shock generator provokes an oblique shock which is in the uncontrolled case non-regularly reflected at the wall, leading to a strong shock near the wall. Its presence allows us to investigate the bleed in supersonic and subsonic regimes.

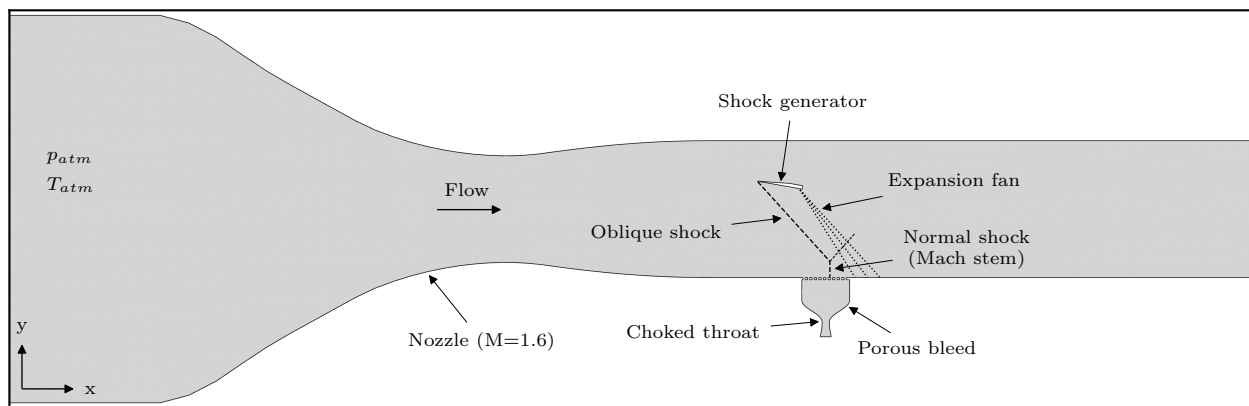


Figure 2.1: Computational domain for the SBLI.

The domain, including the shock generator, is schematically shown in Figure 2.1. As explained in the previous paragraph, the shock generator can be added and its position and wedge angle can be varied to match the setup of the later conducted experiments. For the investigation of the interaction of the bleed with the incident shock, also the position of the bleed region can be varied to examine the impact of the bleed below the shock foot, as well as the effect of a bleed located upstream of the shock. Moreover, the bleed system can be removed to obtain the flow topology of the uncontrolled SBLI.

With the aim of examining the interaction of the porous bleed with the corner flow, the size of the domain can be varied in the spanwise direction. In the classical setup, only two columns of holes are modeled, and symmetry boundary conditions are applied on the front and back of the domain like in the previous case. Moreover, the half-span of the wind tunnel can be simulated with the wind tunnel sidewall taken into account. Thus, the spanwise extent of the bleed region can be examined. In this case, only the center plane is treated as a symmetry boundary condition, and the wind tunnel sidewall is a viscous wall.

The inflow profile is generated by the convergent-divergent nozzle. Only the total conditions are defined at the inlet. The main outlet is defined as a supersonic outlet boundary condition.

Again, all walls except the plenum sidewalls are treated as viscous walls. The plenum outlet is a supersonic outlet boundary condition like in the previous flow case.

The geometrical characteristics of the perforated plates can be varied for a parametric study of the effect on the SBLI control. Therefore, the length of the plate is kept constant with a length of $L_w = 40$ mm. The hole diameter D , the thickness-to-diameter ratio T/D , the porosity ratio ϕ , and the stagger angle β can be varied in the ranges stated in Table 2.1. More details about the geometrical characteristics are introduced in the following subsection.

2.1.2 Boundary-Layer Bleed on a Flat Plate

The second investigated phenomenon in this study is turbulent boundary-layer bleed for varying Mach numbers in the range from $M = 0.0$ to 2.0. The porous bleed system is installed on a flat plate, where it controls a turbulent boundary layer. Thus, the influence of the bleed parameters for supersonic and subsonic conditions is investigated.

Figure 2.2 illustrates the basic computational domain for the case of supersonic flow, where its size is smaller compared to the domain for the subsonic flow case. The investigated bleed region starts with an offset of 40 mm from the inlet, and its length L_w is up to 80 mm. In the spanwise direction, three bleed holes are included in the domain, cutting the first and the third one in the center, as shown in Figure 2.2a. Thus, the width of the perforated plate corresponds to twice the spanwise distance between the hole columns. The staggering of the hole columns (see Figure 2.2b) is altered in the steps $\beta = 30^\circ$, 45° , 60° , and 90° with $\beta = 90^\circ$ being an orthogonal hole pattern. The thickness of the porous wall is varied with respect to the hole diameter from $T/D = 0.5$ to 8.

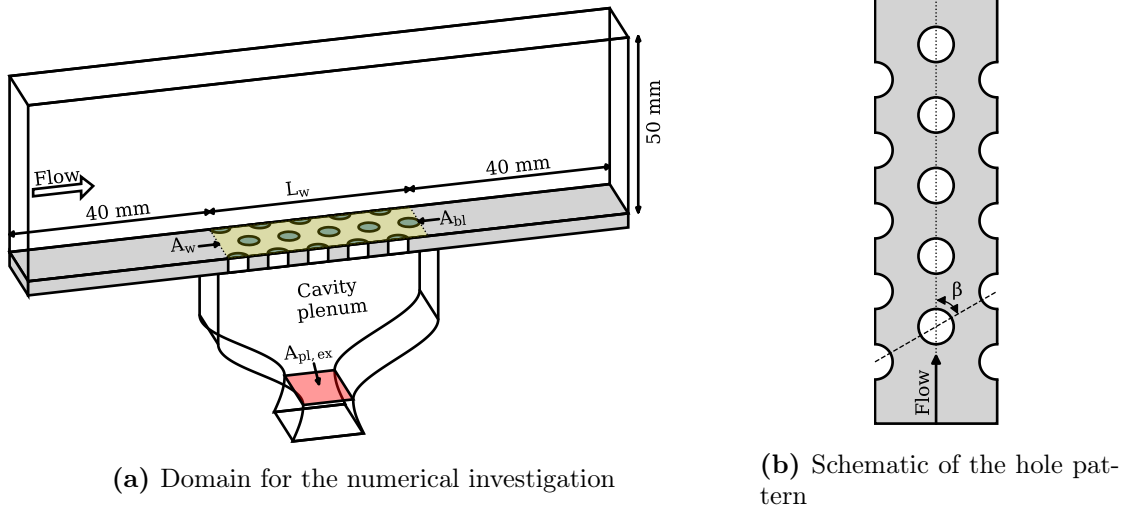


Figure 2.2: Computational domain for the supersonic boundary-layer bleed.

The domain extends 50 mm in height for supersonic flow, and 400 mm for subsonic (and sonic) flows. A larger domain is chosen for subsonic conditions as the pressure propagation increases the influence of the boundary conditions on the flow field for domains that are too small. The main outlet of the domain is located 40 mm and 400 mm downstream of the bleed region, respectively. The base area of the plenum is equal to the bleed region's area, with its depth being 20 mm. Below the plenum, a choked convergent-divergent nozzle is added to fix the plenum exit mass flow rate. The throat ratio

$$TR = \frac{A_{pl,ex}}{A_{bl}} = \frac{A_{pl,ex}}{\phi A_w} \quad (2.1)$$

is introduced to compare different bleed parameters for identical working conditions. It is the ratio of the areas of the exit nozzle throat $A_{pl,ex}$ and the bleed region A_{bl} , which is, in turn, a function of the porosity level ϕ and the plate area A_w .

The range of investigated parameters, as well as the total conditions, are listed in Table 2.1. All parameters can be varied independently to isolate the parameter influences and avoid parameter interactions. Only the plate length L_w cannot be kept constant in all cases as it depends on the hole diameter and the porosity level. However, the plate length is not uniformly defined in the literature. In this study, the maximum streamwise distance between the edges of the first and the last hole is measured, as illustrated in Figure 2.2a. The definition of the porosity level ϕ is visualized in Figure 2.3 using a triangle drawn from the hole center points. Thus, the fraction of open to closed area can be calculated. A doubling of the spacing between two holes divides the porosity level by a factor of four.

p_t	T_t	M	$\delta_{1,c}$	L_w	D	T/D	ϕ	β
		0.0	0.89 mm	2.0 mm	0.25 mm	0.5	5.67%	30°
93 000 Pa	300 K	-	-	-	-	-	-	-
		3.0	3.56 mm	80.0 mm	4.00 mm	8.0	40.31%	90°

Table 2.1: Total conditions and range of investigated bleed parameters.

The inflow profiles have been extracted from preliminary simulations on a flat plate with a length of 5 m. Thus, the turbulent boundary-layer profile can be varied in the displacement thickness depending on the extraction position from the flat plate simulation. The top of the domain is set as a far-field boundary condition, while the main outlet is treated as a supersonic outlet condition if the inflow Mach number is supersonic ($M > 1.0$), and as an outlet pressure boundary condition for lower Mach numbers. The application of a choked nozzle to fix the bleed rate enables the use of a supersonic outlet boundary condition for the plenum exit. The front and back of the domain are treated as symmetry boundary conditions. All walls are handled as viscous walls except the plenum sidewalls, which are defined as inviscid walls to reduce the computational costs.

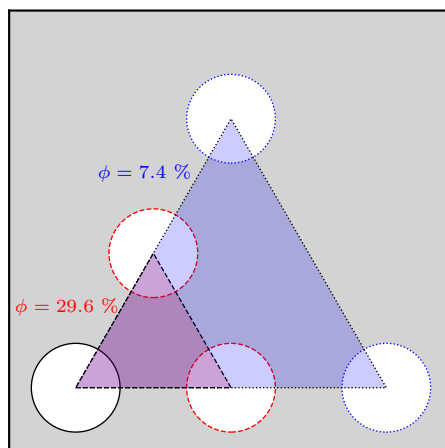


Figure 2.3: Variation of the porosity level.

2.2 Governing Fluid Equations and Flow Solver

We consider the compressible Reynolds-averaged Navier-Stokes equations for ideal gas flowing with \mathbf{u} being the velocity vector $[u, v, w]$:

$$\text{Continuity:} \quad \frac{\partial \rho}{\partial t} + \nabla \cdot (\rho \mathbf{u}) = 0 \quad (2.2)$$

$$\text{Momentum:} \quad \frac{\partial(\rho u)}{\partial t} + \nabla \cdot (\rho \mathbf{u} \otimes \mathbf{u}) = -\nabla p + \nabla \cdot \tau_\nu + \nabla \cdot \tau_t \quad (2.3)$$

$$\text{Total energy:} \quad \frac{\partial \rho E}{\partial t} + \nabla \cdot [(\rho E + p)\mathbf{u}] = \nabla \cdot [(\tau_\nu + \tau_t) \cdot \mathbf{u}] - \nabla \cdot \varphi - \nabla \cdot \varphi_t \quad (2.4)$$

The total energy E is equal to the sum of the internal energy e and the kinetic energy $\frac{\|\mathbf{u}\|^2}{2}$. By supposing a calorically perfect gas, the internal energy $e = c_v T$ is computed from the specific heat of a gas at constant volume $c_v = 717.63 \text{ J kg}^{-1} \text{ K}^{-1}$ and the temperature T . For Newtonian fluids, the stress tensor τ_ν can be expressed as a function of the velocity gradient $\nabla \mathbf{u}$ and the dynamic viscosity μ :

$$\tau_\nu = \mu [\nabla \mathbf{u} + \nabla \mathbf{u}^T - 2/3(\nabla \cdot \mathbf{u})\mathbb{I}] \quad (2.5)$$

The dynamic viscosity is computed via Sutherland's law [107] from the static temperature computed by the ideal gas law $T = p/(R_s \rho)$ with $R_s = 287.058 \text{ J kg}^{-1} \text{ K}^{-1}$. The heat flux vector φ is given by the Fourier law as $\varphi = -\lambda_f \nabla T$, where λ_f indicates the thermal conductivity coefficient. The Reynolds tensor τ_t and the turbulent heat flux φ_t are computed using a turbulence model according to the Boussinesq hypothesis with the turbulent Prandtl number $Pr_t = 0.9$ and the turbulent viscosity coefficient μ_t modeled.

The compressible Navier-Stokes equations are numerically solved using the ONERA-Safran finite-volume solver *elsA* [17]. The second-order-accurate Roe upwind scheme together with the minmod limiter and the Harten entropic correction is used for the spatial derivative with a backward-Euler implicit local time-stepping scheme.

For the evaluation of the bleed efficiency, the bleed flow is fixed by setting a throat ratio. With this method, the plenum-to-external-wall pressure ratio is found to be similar for all plates. In contrast, a constant bleed rate is required to quantify the control effectiveness. In this case, the throat ratio is automatically adjusted to obtain equal bleed rates for all hole configurations.

The influence of the turbulence modeling on the predictions is evaluated by applying the Spalart-Allmaras (SA) turbulence model [103], the Spalart-Allmaras model with quadratic constitutive relation (QCR) [102], and the Menter shear stress transport (SST) turbulence model [69]. Figure 2.4 illustrates the impact of the turbulence model on the sonic flow coefficient, the boundary-layer profiles, and the pressure field inside the hole. A look at the sonic flow coefficient in Figure 2.4a proves a low influence on the removed bleed rate. However, differences in the pressure ratio from the plenum to the external wall are significant. The Menter SST model predicts a lower pressure inside the cavity plenum, which is a result of higher pressure losses inside the hole. The impact of the QCR is small, and slightly increases the pressure ratio compared to the standard Spalart-Allmaras model.

In contrast, the differences in the boundary-layer profiles downstream of the bleed region are negligible (see Figure 2.4b). The Spalart-Allmaras model predicts the same downstream profiles with and without the QCR. Using the Menter SST model leads to a minimally fuller boundary-layer profile. Finally, a view on the pressure field, as shown in Figure 2.4c, confirms higher pressure losses in the simulations with the Menter SST turbulence model. The pressure in the stagnation point downstream of the shock is higher, which is a consequence of a higher shock

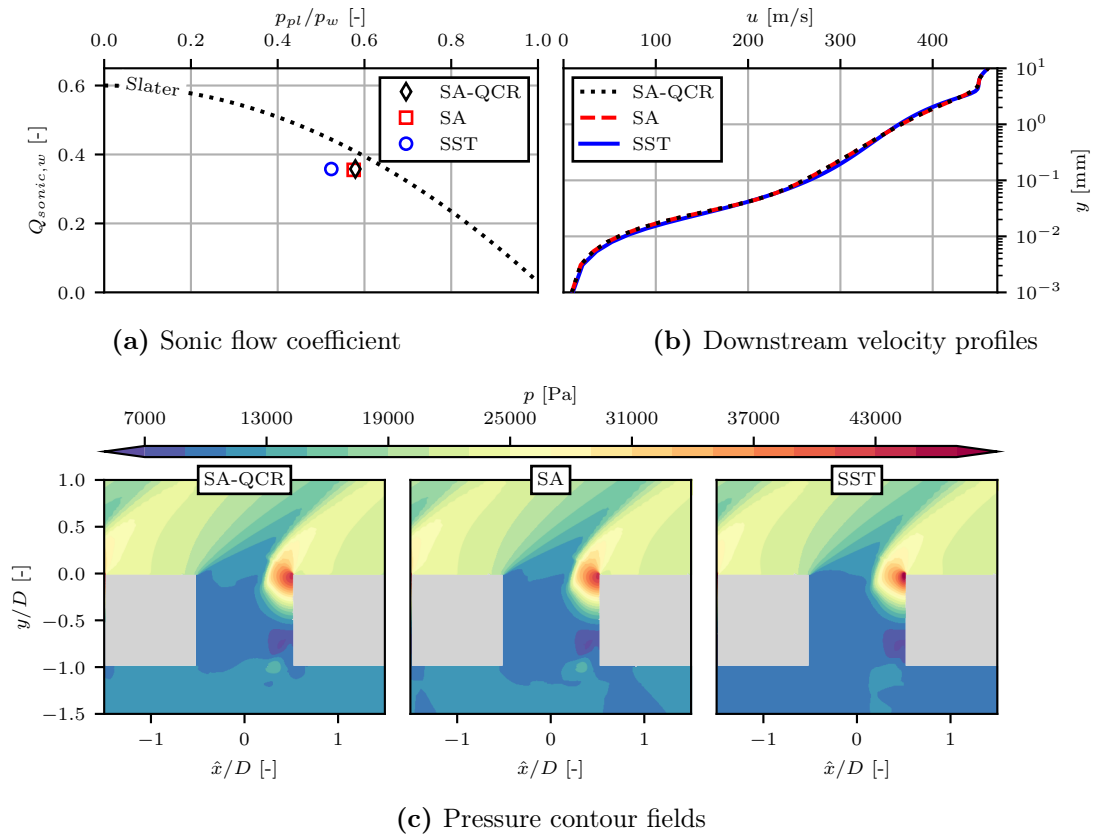


Figure 2.4: Influence of the turbulence modeling.

intensity resulting in higher pressure losses. Again, applying the QCR in the Spalart-Allmaras model has no essential impact on the results.

Similar to the illustrated case, the assessment of the turbulence models is also carried out for another configuration with a smaller hole diameter, resulting in the same trend of higher pressure losses applying the Menter SST model. Finally, the Spalart-Allmaras turbulence model with QCR is selected for the parametric study since it delivers the closest results to the regression of Slater [98]. Thus, the prediction of the pressure losses is assumed to be accurate. Moreover, previous studies have shown a very good fit of simulations using this turbulence model with experiments of the SBLI with flow separation [19].

2.3 Meshing for the Three-Dimensional Simulations

The structured mesh is generated using the in-house pre-processing tool and mesh-generator *Cassiopee* [10]. A fully parameterized mesh allows the variation of the bleed parameters. Therefore, each hole is modeled out of five blocks using a butterfly mesh. The four other blocks are part of a C-grid, including the wall boundary layer on the plate and plenum sides (see Figure 2.7). For a proper resolution of the boundary layer, the minimum wall-normal cell size is $y^+ \approx 1$ (0.2×10^{-3} mm). The cell-to-cell growth ratio inside the boundary layer is 1.1, as well as inside the holes. Around the shock generator, the same minimal mesh size is applied, with an increased cell-to-cell growth ratio of 1.3 to decrease the mesh size.

A mesh sensitivity study is performed on four different meshes for a 12 mm long perforated plate with the maximum hole diameter of $D = 4$ mm. The size of the different meshes as well as the computed sonic flow coefficient and the pressure ratio, are listed in Table 2.2. The mesh dependence on the sonic flow coefficient is very low even for the coarse mesh. However,

Mesh	Number of cells	$Q_{sonic,w}$	$\Delta Q_{sonic,w}$	p_{pl}/p_w	$\Delta(p_{pl}/p_w)$
Coarse	149 056	0.3590	-0.44 %	0.5394	-2.83 %
Medium	412 664	0.3581	-0.69 %	0.5501	-0.81 %
Regular	1 376 000	0.3599	-0.19 %	0.5546	-0.09 %
Fine	3 958 624	0.3606	-	0.5551	-

Table 2.2: Mesh sensitivity study.

the plenum pressure is slightly underpredicted in the case of the lowest mesh resolution. The difference between medium, regular, and fine mesh is minor. Both errors in the sonic flow coefficient and pressure ratio compared to the fine mesh are shown in Figure 2.5.

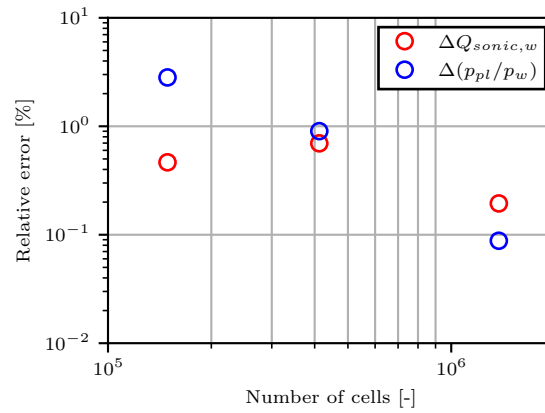
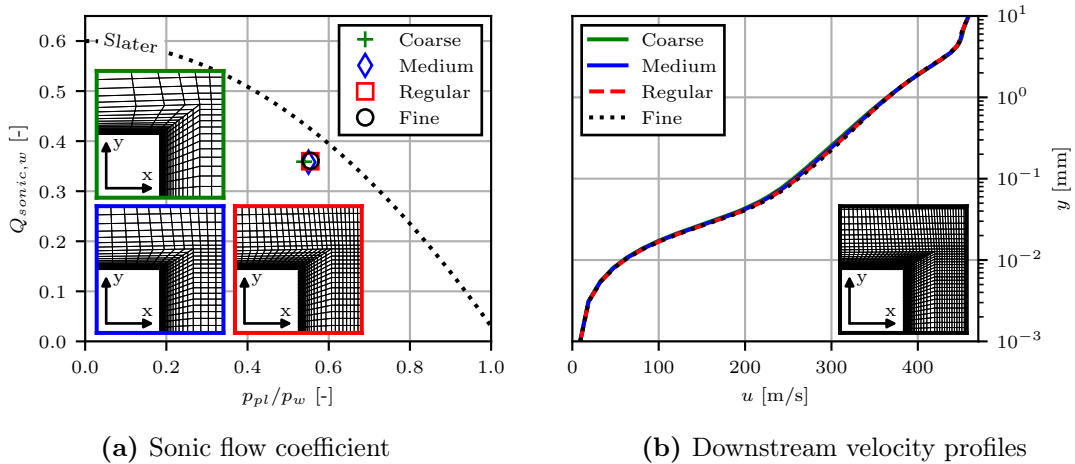


Figure 2.5: Computed error in sonic flow coefficient and pressure ratio as a function of the mesh size.

Moreover, the sonic flow coefficient is shown as a function of the pressure ratio in Figure 2.6a, where no difference between the three finest meshes is notable. The same applies to the boundary-layer profiles extracted downstream of the bleed region, as shown in Figure 2.6b. Even though the medium mesh is, in this case, sufficient, the regular mesh topology is chosen for the parametric study as a high mesh quality is ensured even in cases of varying hole sizes.



(a) Sonic flow coefficient

(b) Downstream velocity profiles

Figure 2.6: Mesh resolution comparison; different meshes inside the hole are illustrated in zoom-in views.

2.4 Extraction and Evaluation of the Bleed Efficiency and Control Effectiveness

The **bleed efficiency** of porous bleed systems is typically quantified by the sonic flow coefficient. In this study, the scaling of Slater [98] is used to compute the surface sonic flow coefficient

$$Q_{sonic,w} = \frac{\dot{m}_{bl}}{\dot{m}_{sonic,w}}, \quad (2.6)$$

where the surface sonic mass flow rate $\dot{m}_{sonic,w}$ normalizes the bleed rate \dot{m}_{bl} . The surface sonic mass flow rate can be computed using the static flow quantities at the wall as follows:

$$\dot{m}_{sonic,w} = p_w A_{bl} \left(\frac{\gamma}{RT_w} \right)^{1/2} \left(\frac{\gamma + 1}{2} \right)^{-\frac{\gamma+1}{2(\gamma-1)}} \quad (2.7)$$

With the aim to analyze the local mass flow rate for each hole, the local extraction of the hole mass flow rate $\dot{m}_{bl,i}$ and the local wall pressure is required. In the current study, the mass flow rate is extracted locally in each hole instead of using the bleed rate extracted at the plenum exit. Therefore the flow momentum in the plate's normal direction is integrated

$$\dot{m}_{bl,i} = \int_S \rho v dS \quad (2.8)$$

at the hole center corresponding to half the plate thickness, as illustrated in Figure 2.8. The (global) bleed rate can be easily computed by summing all hole mass flow rates:

$$\dot{m}_{bl} = \sum_{i=1}^N \dot{m}_{bl,i} \quad (2.9)$$

The static wall pressure and temperature cannot be extracted at the hole position since its value is disturbed by the local velocity caused by the flow into the holes. Therefore, a circular

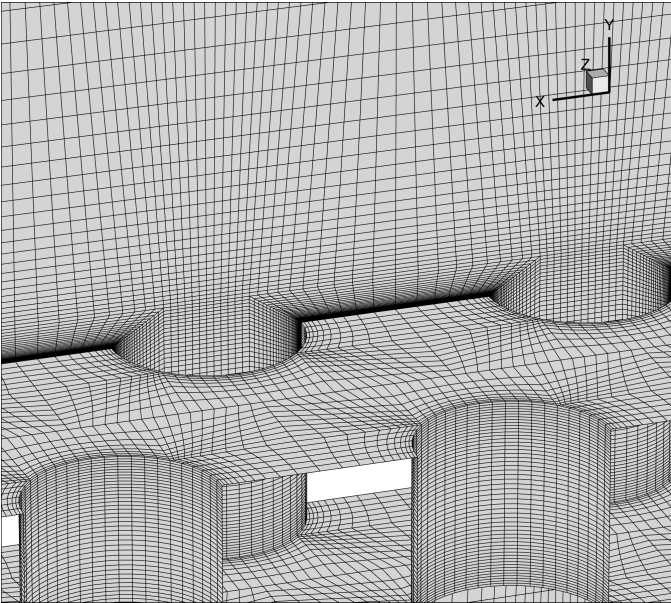


Figure 2.7: View on mesh around the holes.

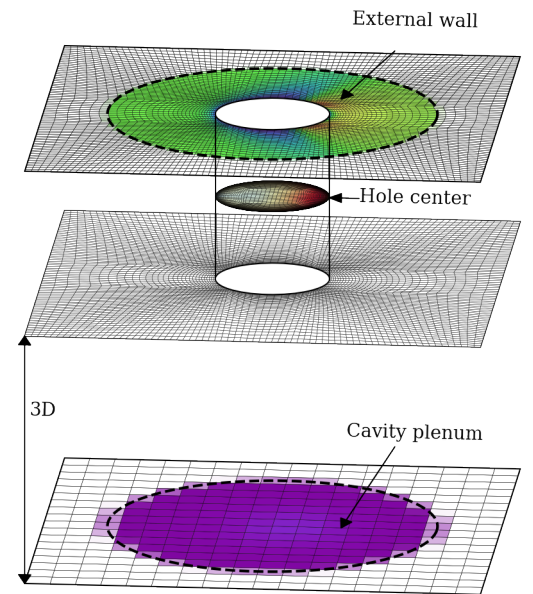


Figure 2.8: Positions for the local extractions.

patch around the hole is defined with its size A_o fitting the porosity ϕ concerning the hole area A_h :

$$A_o = \frac{A_{bl,i}}{\phi} = \pi \frac{D^2}{4\phi} \quad (2.10)$$

The external wall quantities are then extracted by averaging their values above the patch size (see Figure 2.8). Cells that partially lie within the circular patch are weighted using the areal fraction inside the circle. A similar method is applied to the plenum pressure, where the patch is equal in size but placed three hole diameters (3D) below the wall instead of using the wall pressure, which can be highly affected by the under-expanded jet at the hole exit. Higher patch distances lead to local information losses as the plenum pressure becomes more uniform with further distance from the holes.

The **control effectiveness** describes the ability of the bleed system to control the flow. The aim of the porous bleed is the increase of the flow momentum in the wall vicinity. Therefore, characteristic quantities of the boundary layer are required, which are challenging to extract even in this relatively simple case of a flat plate because shock waves and expansion fans induced by the suction holes profoundly modify the boundary layer downstream of the region. As a result, we selected the wall shear stress to evaluate the control effectiveness of the bleed system. The fuller and/or thinner the boundary layer, the higher the wall shear stress. Thus, comparing the wall shear stress upstream and downstream of the bleed regions enables the evaluation of the control effectiveness. Therefore, the wall shear stress along the span is extracted on a line 10 mm upstream of the leading edge of the first hole and 10 mm downstream of the rear edge of the last hole. Using these quantities, we define the rise in the wall shear stress as

$$\varepsilon_\tau = \frac{\tau_{w,d} - \tau_{w,u}}{\tau_{w,u}}, \quad (2.11)$$

quantifying the relative increase of the wall shear stress along the bleed region. However, it is essential to note that this value is case-sensitive and dependent on the inflow conditions, which are kept constant in this study.

Moreover, the bleed rate must be constant relative to the inflow to evaluate the control effectiveness. Hence, the displacement mass flow rate

$$\dot{m}_{\delta_{1,c}} = \int \delta_{1,c} \rho_\infty u_\infty dz, \quad (2.12)$$

which describes the theoretical mass deficit required to obtain an inviscid flow, is computed. The ratio of bleed rate and displacement mass flow rate, i.e., the mass deficit is kept constant ($\dot{m}_{bl}/\dot{m}_{\delta_{1,c}} = const.$). In contrast to earlier studies [33, 77], the mass deficit is used in this study instead of the boundary-layer mass flow rate since the boundary-layer thickness is often ill-defined and may result in large errors. On the contrary, the integral boundary-layer quantities as the displacement thickness are less sensitive to the method of determining the boundary-layer thickness. For the same reason, Delery [35] used the displacement thickness to normalize the interaction length in Figure 1.9. Figure 2.9 sketches the boundary-layer mass flow rate \dot{m}_δ and the mass deficit $\dot{m}_{\delta_{1,c}}$ determined for the 99% boundary-layer thickness δ_{99} . Moreover, the deviation is illustrated by using the 99.9% boundary-layer thickness $\delta_{99.9}$ instead. Because of the low gradient $\partial \rho u / \partial y$ around δ , the error in determining the displacement thickness is significantly lower. The significantly lower influence of the determination method is showcased in Figure 2.9b, where the mass deficit is illustrated for ideal flow.

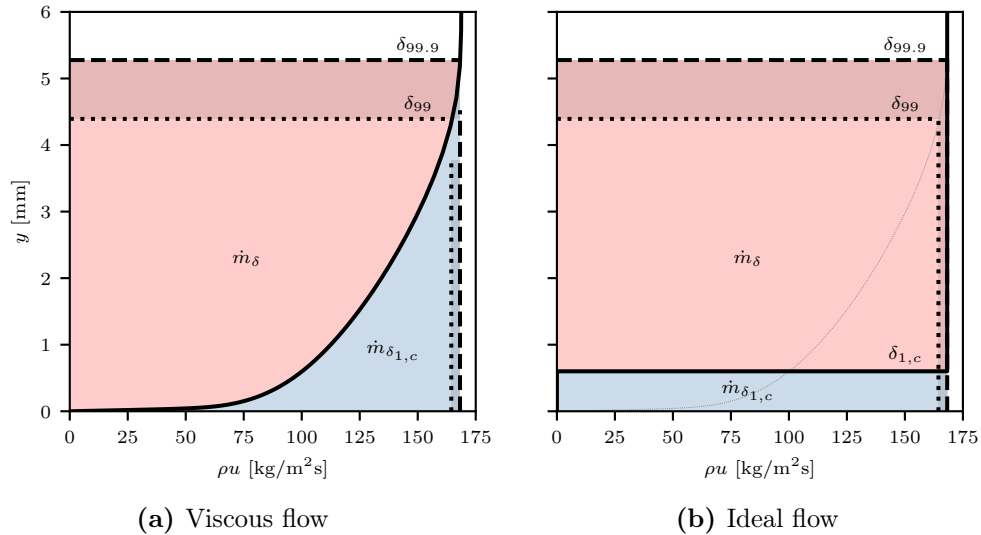


Figure 2.9: Schematic of boundary-layer mass flow rate and displacement mass flow rate (mass deficit); darkened area highlights deviations due to determination method of the boundary-layer thickness.

2.5 Implementation of State-of-the-Art Bleed Models

The application of the bleed models as a boundary condition allows a significant reduction of the mesh size by ignoring the real geometry of the bleed system, including the bleed holes and the cavity plenum. Instead, the porous bleed is applied as a suction/blowing boundary condition on the wall, as sketched in Figure 2.10b. The finite-volume solver *elsA* enables the use of the model of Poll et al. [85], which is implemented as a transpiration wall. The tangential wall velocity components are set to zero using this boundary condition, and only a wall-normal component is permitted. Since the boundary condition is not easily manipulable, an approach using source terms has been applied, as explained in the following. This approach is validated with the implemented boundary condition of Poll et al. [85].

The solver *elsA* has an integrated interface that enables the run of *Python* codes with full access to the simulation data after (or before) a specific number of iterations, which allows the manipulation of the simulation. Thus, the bleed boundary condition is computed in *Python* and updated regularly. Therefore, several flow variables are extracted from the latest flow solution.

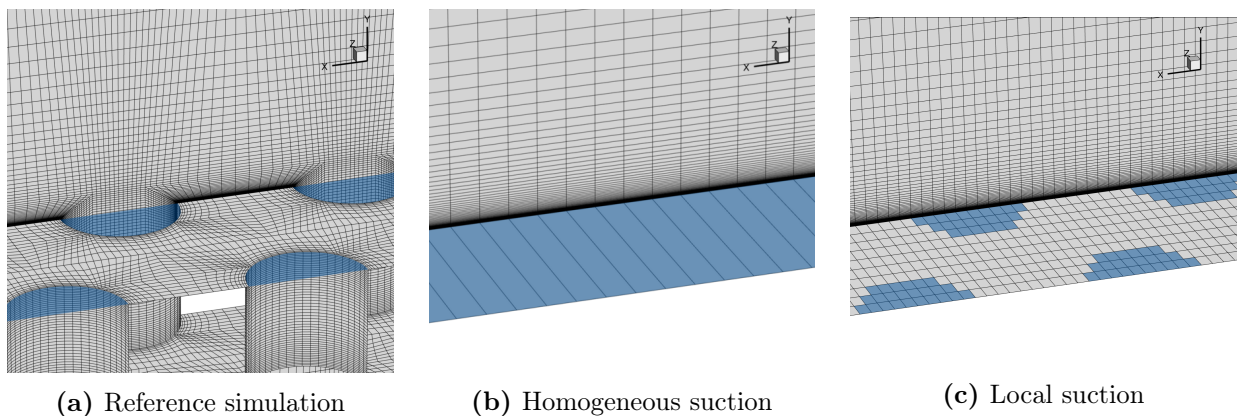


Figure 2.10: Application approaches for bleed models compared to three-dimensional reference simulations; blue patches illustrate areas where suction is applied.

The *Python* routine has access to all flow variables at all cell centers within the mesh and the values at the cell faces that are defined as bleed regions.

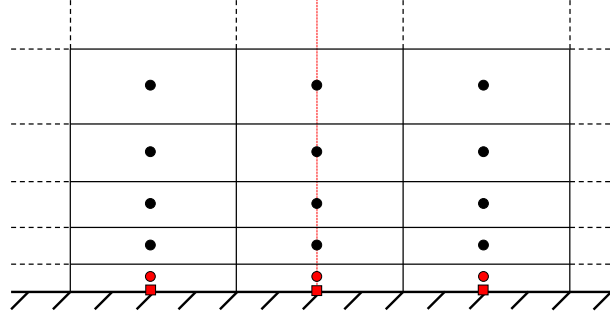


Figure 2.11: Extraction locations in the mesh.

Figure 2.11 gives an overview of the extraction locations. The circles illustrate the cell centers, and the squares are the interfaces on the boundary condition. All positions where variables are extracted are marked in red. The red vertical line symbolizes the extraction of the Mach number on the boundary edge required for the bleed model of Harloff and Smith [61]. The RANS-solver *elsA* offers multiple options to define the boundary-layer edge to extract variables. Here, a diagnostic function

$$\mathcal{D} = d^a \|\Omega\|^b \quad (2.13)$$

with d being the wall distance and $\|\Omega\|$ the vorticity vector modulus is used [106]. The boundary-layer thickness

$$\delta = \varepsilon d_{max} \quad (2.14)$$

is proportional to the wall distance where $D|_{d_{max}} = \max(D)$. The coefficients $a = 3.9$, $b = 1.0$, and $\varepsilon = 1.294$ are determined by Stock and Haase [106] for laminar flow. Even though Stock and Haase [106] also defined coefficients for turbulent velocity profiles, the laminar solution is applied as it is more robust than the turbulent and, thus, has a lower error in the case of suction or blowing.

The static wall pressure and temperature applied for the bleed models are extracted at the interfaces of the boundary condition (■). The wall shear stress required for the model of Doerffer and Bohning [38] is calculated using the flow properties in the first cell center (●) and the wall distance Δy :

$$\tau_w = \mu_c \frac{u_c}{\Delta y}. \quad (2.15)$$

Equation 2.15 is applied since the wall is defined as a viscous wall, and the dimensionless wall distance is $y^+ \approx 1$. The tangential velocity is assumed to be zero at the wall since the porosity level is relatively low.

The blowing and suction are applied to the first row of cells using source terms. The following source terms are adapted from Baurle and Norris [7] and added to the compressible

Navier-Stokes equations.

$$\text{Continuity:} \quad \frac{q_w A_c}{V_c} \quad (2.16)$$

$$\text{Momentum:} \quad \frac{\mathbf{u} q_w A_c}{V_c} \quad (2.17)$$

$$\text{Energy:} \quad \frac{q_w c_p T_w A_c}{V_c} \quad (2.18)$$

The physical values applied in the source terms are directly extracted from the first cell centers (●). All bleed model outputs are converted to a wall mass flux q_w . The local bleed rate is computed using the surface mass flux and the projected cell area A_c . All source terms are normalized using the local cell volume V_c .

A relaxation factor α_R is added to the computation of the wall mass flux

$$q_w^t = (1 - \alpha_R)q_w^{t-n} + \alpha_R q_w^t \quad (2.19)$$

to ensure robustness and to accelerate the simulation by updating the boundary condition only every n iterations.

Three options to set the working regime of the porous bleed for the computation of the bleed models are possible:

- ① Fixed plenum pressure p_{pl}
- ② Fixed bleed rate \dot{m}_{bl}
- ③ Fixed throat ratio TR .

① The fixation of plenum pressure is the classical way to define the working regime used by all existing models. ② The second option is the setting of a desired bleed rate. Therefore, the plenum pressure is iteratively updated until the used bleed model reaches the correct mass flow rate. The obtained plenum pressure is then used in the simulation. As the wall pressure varies with the computational iterations, this step has to be repeated with every update of the boundary condition. ③ The last option is setting the throat ratio

$$TR = \frac{A_{pl,ex}}{A_{bl}}, \quad (2.20)$$

which is the ratio of the plenum exit area $A_{pl,ex}$ and the bleed area A_{bl} . The flow in the plenum exit throat is supposed to be choked. With the assumption of a large cavity plenum and, consequently, very low flow speed, the plenum pressure is assumed to be equal to the total pressure inside the cavity plenum. Thus, the mass flow rate passing the choked nozzle

$$\dot{m}_{pl,ex} = \frac{p_{pl} A_{pl,ex}}{\sqrt{T_w}} \sqrt{\frac{\gamma}{R_s}} \left(\frac{\gamma + 1}{2} \right)^{-\frac{\gamma+1}{2(\gamma-1)}} \quad (2.21)$$

is computed using the external wall temperature T_w . Hence, the mass flow rate leaving the cavity plenum and the mass flow rate passing the perforated plate can be determined as a function of the plenum pressure. Again, the plenum pressure is iteratively adjusted until the balance between these two flow rates is achieved [99]. The definition of a throat ratio facilitates the comparison between the three-dimensional simulation, where a choked nozzle fixes the mass flow rate and the simulations with the bleed boundary condition. For this reason, the third option ③ is the default option used in this study.

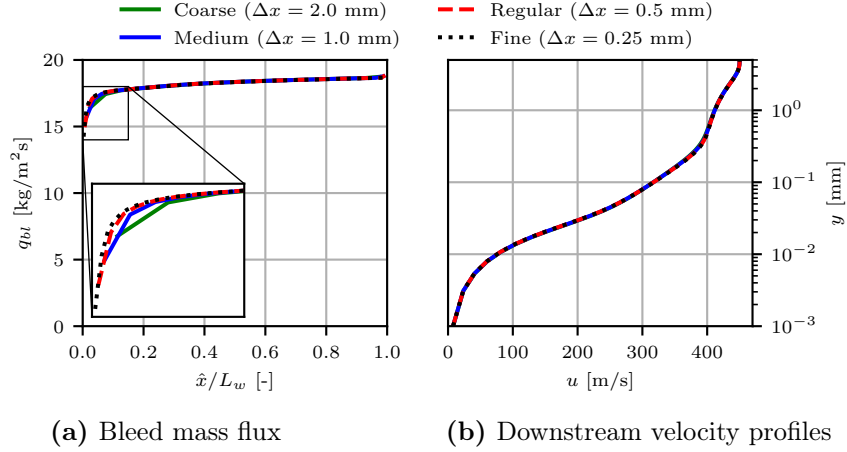


Figure 2.12: Influence of the mesh resolution.

For the simulation with the porous bleed boundary condition, the mesh is simplified and consists only of one cell in the spanwise direction, as illustrated in Figure 2.10b. A mesh convergence study is performed to determine the influence on the mass flux along the bleed region and the downstream velocity profiles. The mesh spacing is varied from $\Delta x = 0.25$ mm to $\Delta x = 2.00$ mm. As shown in Figure 2.12, the influence of the spatial resolution is small in the case of the supersonic boundary-layer bleed. Only at the beginning of the plate (see Figure 2.12a) minor differences in the bleed mass flux are notable as pressure gradients are smeared with lower mesh resolutions. However, the nominal mesh with a spacing of $\Delta x = 0.5$ mm (80 cells along the porous bleed region) overlays almost perfectly with the fine grid and is considered converged.

2.6 Implementation of the Local Porosity Variation

The principle of the local porosity is the discrete modeling of the hole contour with a pre-defined number of cells as schematically illustrated in Figure 2.13, and compared to the classical approach in Figure 2.10. The advantage of this approach is the direct modeling of the hole pattern. Thus, the modeling of the bleed rate as a function of flow properties extracted on the patch of the boundary condition is simplified as no complex regression is expected, considering all parameters are required. Moreover, the flow topology around the bleed holes with the barrier shocks and expansion fans is partially modeled. Wang et al. [114] modeled the bleed holes using the same methodology. However, their method required a large amount of cells to resolve the hole caused by the complexity of their model. A similar method is used by Orkwis et al. [78] with the difference that they meshed the hole contour, which requires a higher amount of cells, a more complex mesh, and is less flexible. Also, Benson et al. [11] used a boundary condition at the location of the holes using a fine mesh with the hole contours resolved, and a coarse mesh consisting of one cell per hole.

Similar to Wang et al. [114], a weight coefficient is calculated. Here, we call this factor (local) porosity level ϕ as it describes the fraction of porous area for each cell. All cells lying entirely inside the hole geometry have a porosity of $\phi = 1$ and cells outside the hole contour have $\phi = 0$. For the cells overlaying the hole contour, the porosity $\phi = A_{c,h}/A_c$ is the fraction of the hole area overlapping the cell $A_{c,h}$ and the cell area A_c . An array is computed with the local porosity level for every patch cell. This array is defined for every bleed hole to correct the bleed mass flux $q_{w,c} = \phi q_w$ in the cells that model the hole contour. Hence, the bleed mass flux in cells with a small porosity, which corresponds to cells on the hole edge, is reduced.

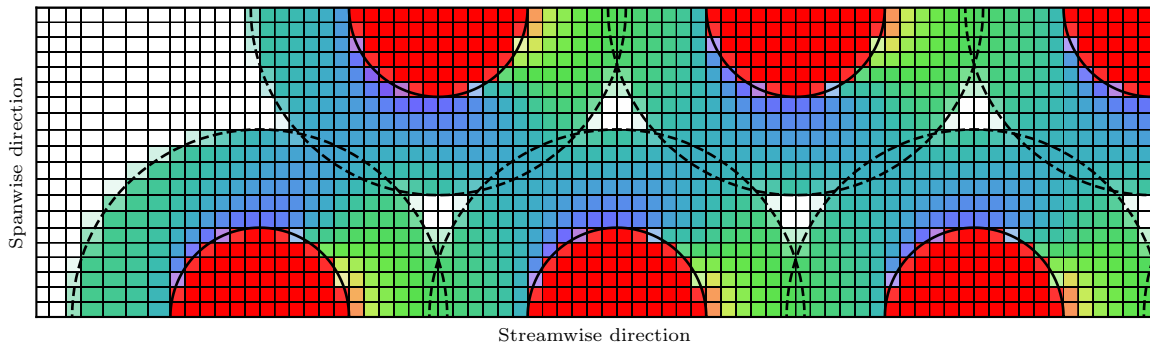


Figure 2.13: Schematic of local porosity: red cells illustrate suction cells; all cells within the dashed lines ($A_o = \pi D^2/(4\phi)$) are used for the extraction of the physical quantities.

For the computation of the local porosity level, the hole geometry is simplified as a polygon with 120 points, resulting in an error of less than 0.1%. In contrast, Wang et al. [114] used a Monte-Carlo method, which might be manageable for small amounts of cells and holes, but leads to a significant increase in the computational time for large mesh sizes, while the current method requires even for the largest applied resolution less than 10s of pre-processing time. Please refer to Appendix A for more information on the method.

Another difference to earlier approaches is the local extraction of the wall quantities for every hole by averaging their amount over the extraction area defined by Equation 2.10. Therefore, the weighting factor $\psi = A_{c,o}/A_c - \phi$ is defined analogously to the porosity level. However, its value becomes zero if the cell lies inside the hole contour as the wall quantities shall not be extracted at the outlet. The wall quantities are computed as follows (here for the wall pressure):

$$p_w = \frac{\sum p_{w,c} \psi A_c}{\sum \psi A_c}. \quad (2.22)$$

Moreover, the value of ψ is set to zero if $\phi > 0.5$ to prevent an underestimation in the wall pressure, which significantly decreases at the outlet.

For the application of the approach of local porosity, the *collect* boundary condition in the in-house solver *elsA* is applied. This boundary condition enables the application of multiple boundary conditions on one patch. Therefore, all porous cells are handled as mass outflow boundary conditions, while the other cells are defined as viscous walls. For the computation of the bleed mass flux, the same options as in the previous section are implemented (fixed plenum pressure, bleed rate, or throat ratio).

More details on the implementation approach are provided in Appendix A, where the implementation in Python is presented. Moreover, the application of the different boundary conditions, the local porosity level ϕ , and the weighting factor ψ are illustrated.

Since the new model requires the discrete modeling of the hole contour, a mesh convergence study is performed. The mesh resolution is altered in both streamwise and spanwise directions to investigate its influence on both the bleed rate and the boundary-layer profiles. Similar to the mesh convergence study for the resolved simulations, a plate with a large diameter ($D = 4$ mm) is chosen as the effects on the flow are the largest. Consequently, this case is assumed to be the hardest to mirror.

The influence of the mesh on the bleed rate is demonstrated in Figure 2.14 by simulating a 40 mm plate for $M = 1.6$ with various mesh resolutions and comparing the total bleed rate. On the left side, the mesh is schematically shown for three different mesh resolutions. On the right side, the bleed rate is compared to the bleed rate of the finest grid with 24 x 24 cells per

hole. Simulations were performed for even higher resolutions up to 40 x 40 cells without any further improvement. The blue, red, and green squares on the right side highlight the meshes shown on the left.

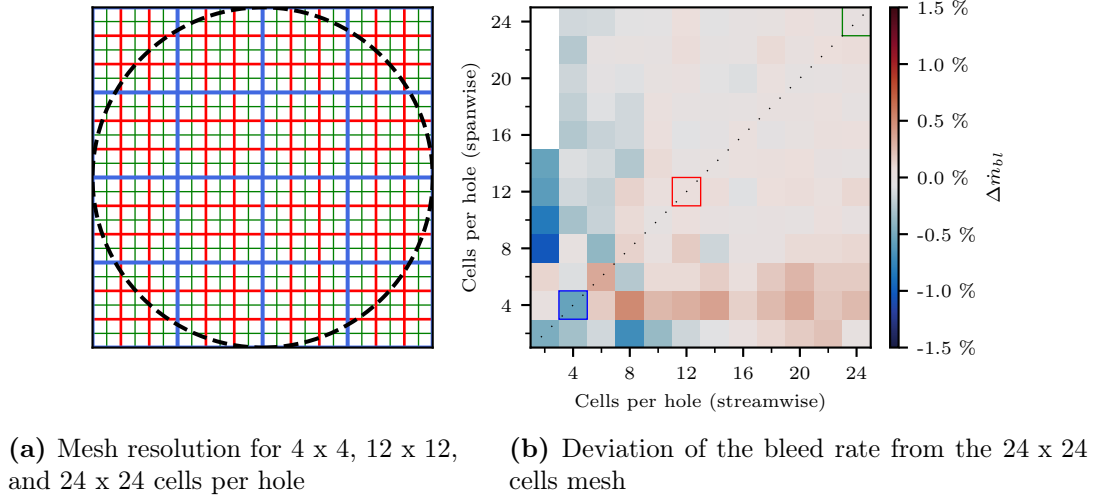


Figure 2.14: Influence of the mesh on the bleed rate.

The mesh resolution has a very low impact on the computed bleed rate. The highest deviation from the converged mesh is around $\Delta\dot{m}_{bl} = -1.04\%$ for the 2 x 8 cells mesh. Generally, a low number of cells in the spanwise direction leads to a slight overestimation of the bleed rate while the opposite is the case in the case of low streamwise mesh resolutions. The highlighted meshes with 4 x 4 cells (blue) and 12 x 12 cells (red) have an error of -0.55% and 0.06% , respectively. Consequently, even very low mesh resolutions are sufficient to accurately predict the bleed rate.

The influence of the mesh resolution on the boundary-layer profiles is shown in Figure 2.15. Here, the number of cells in spanwise and streamwise directions is identical. From the left to the right, the mesh resolution increases. The blue, red, and black profiles correspond to the sketched grids from Figure 2.14a. At first glance, the variation of the boundary-layer profiles along the span is observed. The new approach enables the simulation of three-dimensional effects induced by the hole geometry (shown by the envelope), even though the effect is weaker

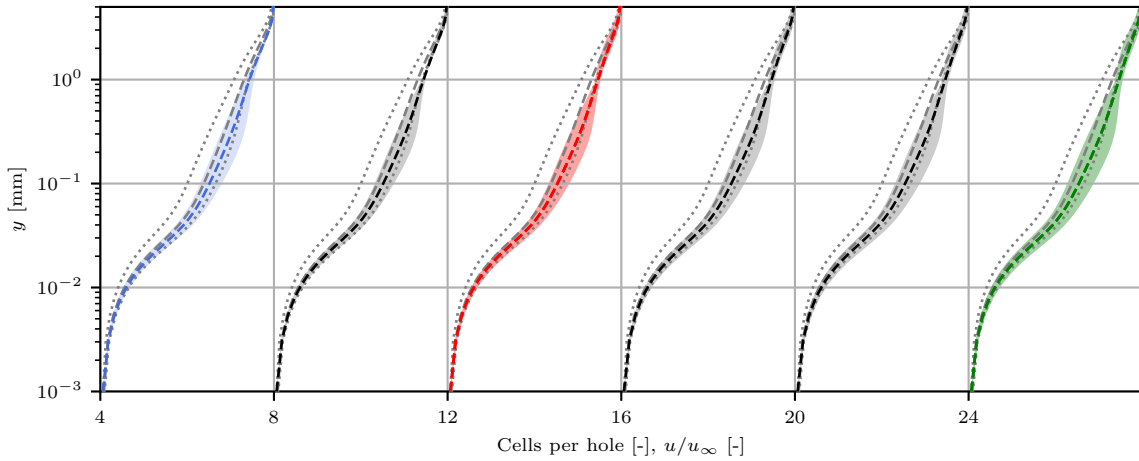


Figure 2.15: Envelope of boundary-layer profile for different meshes compared to the reference simulation (gray); dashed lines highlight mean profiles and the dotted lines the envelope of the reference simulation.

than in the reference simulation (shown in gray). The average profiles along the span (dashed) are still slightly fuller than in the reference simulation. However, any further increase in the mesh resolution does not increase the variability in the profiles.

Chapter Summary

The numerical setup for the three-dimensional simulations, the simulations with the state-of-the-art bleed models, and the new model were presented. Two different numerical domains are used to investigate flow control with porous bleed, and the bleed performance is evaluated defining bleed efficiency and control effectiveness.

Two setups are investigated: the control of the flow in the ONERA S8Ch wind tunnel with and without an oblique SBLI, and the turbulent boundary-layer bleed on a flat plate. For the flow inside the ONERA S8Ch wind tunnel, a convergent-divergent nozzle is modeled to generate the same inflow conditions as in the experiments. A shock generator can be added to the domain to observe the control of an oblique SBLI. The simulations of the wind tunnel are first applied for the validation of the numerical setup in Chapter 5, and for the parametric study on the SBLI control in Chapter 6. The boundary-layer bleed is investigated for both supersonic and subsonic conditions, using a larger domain for subsonic conditions to prevent influences of the boundary conditions as the pressure can propagate in the upstream direction. This setup enables the variation of inflow conditions and the plate geometry and is used for the parametric study in Chapter 6.

The CFD solver *elsA* is used for all RANS simulations. Three-dimensional simulations with the bleed system included in the domain are the base of this study. The sensitivity to the turbulence model was very low regarding the boundary-layer profiles downstream of the bleed region and the bleed rate. However, lower pressure inside the cavity plenum was predicted using the Menter SST model compared to Spalart-Allmaras. Finally, the Spalart-Allmaras model with QCR was selected in this work. Moreover, the influence of the mesh was even lower than for the turbulence model.

For the evaluation of the bleed efficiency, an extraction area around the hole is defined for the local extraction of the physical quantities. The bleed rate is calculated for every bleed hole by integrating the momentum at the center of the holes. Using these extractions, the surface sonic coefficient is computed. The control effectiveness is computed using the wall shear stress upstream and downstream of the bleed region, and the relative increase in the wall shear stress is calculated. In Chapter 6, these definitions of bleed efficiency and control effectiveness will be used.

The state-of-the-art bleed models are homogeneously applied on a simplified, two-dimensional mesh using source terms in the first layer of cells. Below, a no-slip boundary condition is applied. Three different options for computing the bleed rate were implemented. The influence of the mesh refinement was very low and only observed in the areas where gradients in the bleed mass flux are apparent. In Chapter 7, the state-of-the-art bleed models are applied using the approach with source terms.

The new model, which is introduced in Chapter 8, is applied using a locally distributed outflow boundary condition on a simplified, three-dimensional mesh. Between the discretely modeled holes, a no-slip wall boundary condition is applied. Again, the mesh influence was low and mainly observed in the variations of the boundary-layer profiles along the spanwise direction.

Key Points:

Investigated physical problems

- ❑ **Turbulent boundary-layer bleed** is examined for supersonic and subsonic conditions
- ❑ **Flow inside the S8Ch wind tunnel** is investigated without and with SBLI

Numerical settings

- ❑ **RANS simulations** using *elsA* flow solver
- ❑ **Turbulence models** have a negligible influence on the boundary-layer profiles downstream of the bleed; Spalart-Allmaras model predicts lower pressure losses
- **Spalart-Allmaras with QCR** selected turbulence model for this study
- ❑ Low sensitivity of the **mesh resolution** on predicted bleed rate and boundary-layer profiles

Evaluation of the bleed performance

- ❑ Derivation of **bleed efficiency** and **control effectiveness** based on the extracted physical quantities
- ❑ **New extraction approach** for physical quantities locally around the holes considering the porosity level
- Approach used in Chapter 6

Implementation of boundary condition for bleed models

- ❑ **Homogeneous suction/blowing boundary condition** for state-of-the-art models from Section 1.2.4.3
 - Use of **source terms** for mass removal in the first layer of cells
 - **No-slip** boundary condition to suppress tangential velocity at the wall
 - Three options for computation of bleed rate implemented
 - Low sensitivity of the **mesh resolution** on predicted bleed rate and boundary-layer profiles
 - Approach used in Chapter 7
- ❑ **Local suction boundary condition** for the novel model from Chapter 8
 - Combination of **outflow** and **no-slip** boundary conditions
 - **Discrete modeling** of hole contour
 - **Local extraction** of wall quantities equally to reference simulations
 - Low sensitivity of the **mesh resolution** on predicted bleed rate and boundary-layer profiles
 - Approach used in Chapter 8

Experimental Setup

The true method of knowledge is experiment.

WILLIAM BLAKE

Chapter Introduction

This chapter focuses on the experiments performed in the ONERA S8Ch wind tunnel in Meudon. The wind tunnel and the bleed system are presented before the experimental methods are introduced. Moreover, measurement uncertainties because of system errors, calibration, and wind tunnel operation are stated.

3.1	Supersonic Wind Tunnel	67
3.2	Porous Bleed System	68
3.3	Laser Doppler Velocimetry Measurements	69
3.4	Flow Visualizations	70
3.5	Wall Pressure Measurements	71

3.1 Supersonic Wind Tunnel

The experiments are performed in the continuous-running S8Ch supersonic wind tunnel of ONERA in Meudon, supplied with dried atmospheric air. Figure 3.1 shows a photograph of the test section. The convergent-divergent nozzle is designed to generate a supersonic flow with a Mach number of $M = 1.62$. The size of the test section is 120 mm in width and 120 mm in height. The porous bleed system is installed 50 mm downstream from the nozzle. Windows on the sidewalls allow optical access to the entire region of interest around the bleed region at the lower wall. In addition, a shock generator can be mounted at the upper wall of the test section. Its position and wedge angle are adjustable so that the impingement of the incident shock wave is located on the porous bleed system.

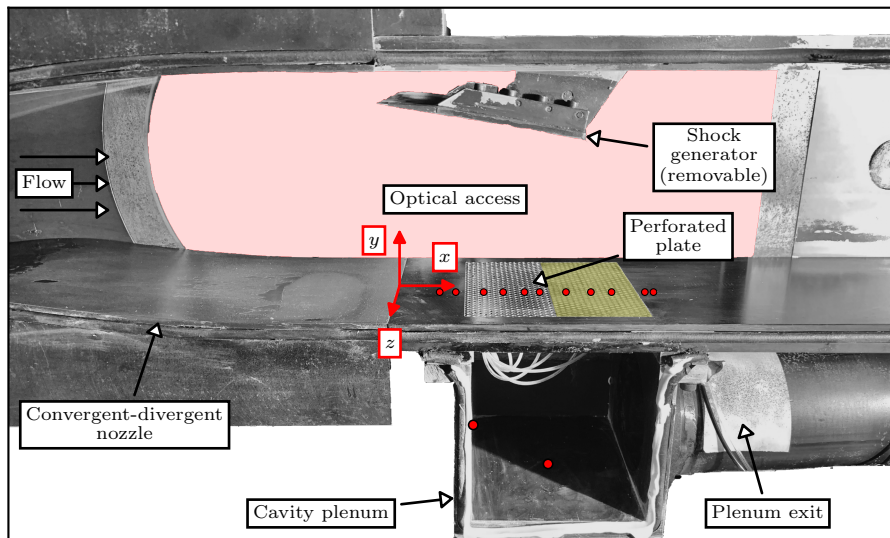


Figure 3.1: Experimental setup.

The experiments are performed over several months, resulting in variations in the atmospheric conditions, as presented in Tab. 3.1. Thus, the total conditions inside the test section can not be kept constant. Please note that the total conditions listed in Tab. 3.1 are independent of the Mach number. Moreover, the temperature increased on some days during the measurement by approximately 20 K within the first running hour.

	p_t	T_t
Minimum	97 370 Pa	290.6 K
	-	-
Maximum	101 960 Pa	317.6 K

Table 3.1: Stagnation pressure and temperature in experiments (range during all measurements).

A valve upstream of the compressor allows the suction of air from a bypass channel, and thus, the reduction of mass flow rate passing the test section. Hence, the Mach number can be varied for subsonic conditions, which is used in this study to also perform measurements for a fully subsonic flow inside the wind tunnel. A Mach number of $M = 0.5$ is selected to avoid the appearance of a normal shock inside the divergent part of the nozzle due to choking of the nozzle throat and an under-expanded working regime. The Mach number is monitored in real-time using the isentropic pressure ratio from wall pressure to total pressure in the settling chamber and controlled manually for each bleed rate by adjusting the valve opening until the

desired value is obtained. Thus, an uncertainty in the inflow Mach number of up to 5% is estimated for the subsonic operation.

3.2 Porous Bleed System

The perforated plate has a length of 40 mm and a span of 80 mm, corresponding to 2/3 of the channel span. The plate length can be increased to up to 80 mm, which is not used in this study to guarantee a choking of the holes for the highest bleed rate. As a consequence, the second half of the plate is filled with plaster, as highlighted by the grey-filled holes in Figure 3.2. Preliminary numerical investigations have shown that wider plates do not affect the center-plane flow but require higher bleed rates as the suction area is increased. Two perforated plates with 90-degree holes from *Mevaco* are utilized in this study with their hole diameters being $D = 0.5$ mm and 2.0 mm. The plate with the smaller holes has a porosity of $\phi = 14.5\%$, whereas the second plate has a porosity of $\phi = 29.6\%$.

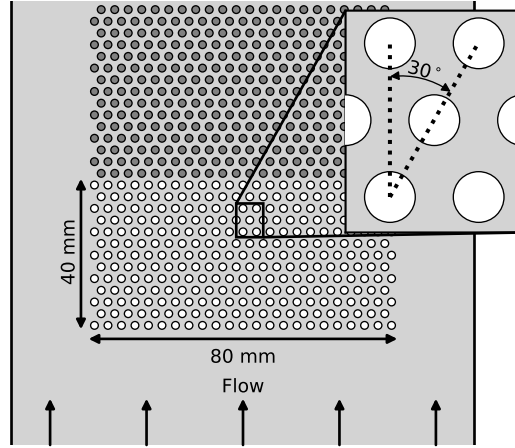


Figure 3.2: Characteristics of perforated plates.

Porosity levels and hole diameters are selected concerning the application in supersonic air intakes. The smaller holes are close to the typical ratio of $D/\delta_{1,c} = 1$ [61], while the second plate has significantly larger holes to observe negative effects induced by the bleed roughness. Independent of the hole size, the thickness-to-diameter ratio is kept constant at $T/D = 1$. The holes are distributed in a triangular shape, resulting in different streamwise positions for every second column of the holes. The stagger angle between the columns is $\beta = 30^\circ$ for both plates. Table 3.2 summarizes the geometric parameters of the perforated plates.

Plate	D [mm]	ϕ [%]	β [°]	T/D [-]
AR	0.5	14.5	30	1
HR	2.0	29.6	30	1

Table 3.2: Investigated perforated plates.

The bleed rate can be varied by using a choked throat at the plenum exit. The throat diameter varies from $D_{pl,ex} = 10$ mm to 50 mm, while the inner pipe diameter is 76.2 mm (3 inches).

Please note that the throat is only applied to fix the bleed rate. No bleed rate measurements are conducted in this study. A stiffening system is installed inside the cavity plenum to avoid plate bending caused by high pressure differences from the external wall to the cavity plenum. The maximum bending at the plate center of less than 0.1 mm is optically measured with the LDV and traverse system for the maximum bleed rate compared to the static case (i.e., the wind tunnel is turned off).

3.3 Laser Doppler Velocimetry Measurements

A two-component Laser Doppler Velocimetry (LDV) system is used in a forward scatter mode to describe the flow field around the bleed region. Two lasers from the *Coherent Genesis MX SLM-series* with wavelengths 514.5 nm and 488 nm are utilized to measure both streamwise and wall-normal velocity components of the flow. Both fringe patterns are tilted by 45° with respect to the wind tunnel floor to obtain the closest possible measurements to the wall (see Figure 3.3). The first reliable point of measurement is at a wall-normal distance $y = 0.2$ mm ($y^+ = \mathcal{O}(100)$). A 40 MHz frequency shift is provided by a Bragg cell to one of the beams using the *FiberFlow* system from *Dantec* to resolve negative velocities. A *TOPAS Aerosolgenerator ATM 210* is used to seed DEHS droplets into the air.

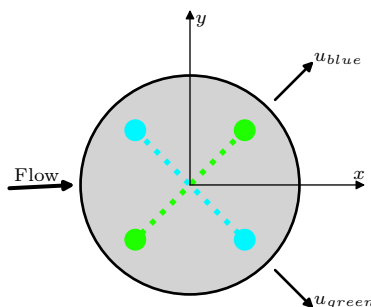


Figure 3.3: Orientation of the Laser beams.

Both the emitted beams have a waist diameter of 4.3 mm. The distance between the beams is set to 35 mm, a beam expander with a ratio of 1.95 and a converging lens with a focal length of 230 mm are used. The measurement volume characteristics can be calculated using classical relations [39], resulting in diameters of $35.04 \mu\text{m}/33.23 \mu\text{m}$, lengths of 0.46 mm/0.44 mm, and fringe spacing of $3.39 \mu\text{m}/3.22 \mu\text{m}$. With the given characteristics, sampling rates on the order of $\mathcal{O}(1 \text{ kHz})$ are achieved.

The entire LDV system is mounted on a three-axis traverse system, using stepper motors with a resolution of 0.01 mm. A pinhole is placed at the center of the wind tunnel to check the beam crossing and the correct spanwise position. The streamwise position is optically verified against the exit of the convergent-divergent nozzle. The exact angle of the beams with respect to the test section is measured using a theodolite. Before each run, the vertical position is checked on the floor by moving the system toward the wall until a reflection is seen.

The relatively complex setup of LDV systems coincides with several sources of uncertainty. The manufacturer of the system quotes a system error of less than 0.2%. However, other errors and uncertainties must be taken into account. For the optical calibration, the error is estimated to be less than 0.5%. As stated before, the LDV system is mounted on a traverse system, which is not linked to the actual test section. The pumps for the bleed system generate vibrations during the wind tunnel operation, which is noted to lead to a slight oscillation

of the measurement volume. Another error source is velocity biasing, which is according to McLaughlin and Tiederman [68] 10% of the local fluctuation intensity, and thus up to 4% in the velocity inside the boundary layer. Also, the lengths of the measurement volumes are with 0.46 mm and 0.44 mm of almost the same size as the bleed holes for plate AR. Thus, the spanwise resolution is significantly lower than in the wall-normal direction. Moreover, particle drag leads to an overestimation of the velocity downstream of shock waves, i.e., a smearing of the shock.

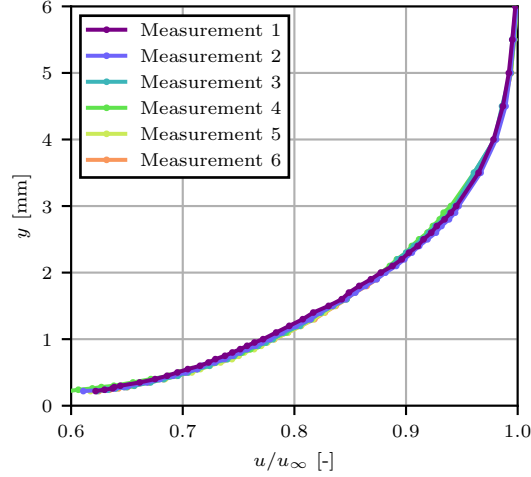


Figure 3.4: Reproducibility in the inflow measurement.

For the evaluation of the measurement uncertainty, six measurements of the inflow profile are compared in Figure 3.4. These measurements are conducted over several days with repeated optical calibrations. The differences between the measurements are very low, leading us to the conclusion of high reproducibility in measuring the mean velocity profiles.

3.4 Flow Visualizations

A Background Oriented Schlieren (BOS) system [72] is installed to monitor the flow in real-time using a 2.3 MP camera. Using the BOS method, the deviation of the light rays induced by density gradients is measured by cross-correlating one image of a random pattern without flow and one with flow. The deflections in the streamwise and wall-normal directions are estimated using the in-house *FOLKI* algorithm [18].

Figure 3.5 illustrates the installation of the BOS system. The camera is placed to focus the field of view on the open bleed holes only. Important to note is the nonparallel passing of the light rays through the test section contrary to a classical Schlieren setup. Thus, the integration of the density gradient is not in all points aligned with the spanwise coordinate. As a consequence, the shock waves induced by the bleed holes are smeared if they are not in the center of the field of view. However, this system can be applied parallel to LDV measurements because of its simple setup and the small size of the camera. On the contrary, a classical Schlieren setup cannot be arranged in combination with the LDV system.

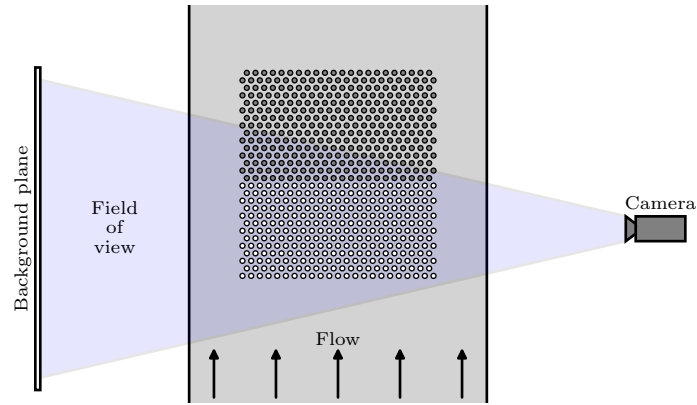


Figure 3.5: Schematic of BOS setup.

3.5 Wall Pressure Measurements

Static pressure measurements are performed to monitor the flow using *ESP-32HD* pressure scanners with a range of ± 15 PSI (103 421 Pa) and a $\pm 0.03\%$ full-scale accuracy (31 Pa). Pressure taps on the top wall inside the convergent-divergent nozzle and test section are used to check the correct starting of the test section. Moreover, pressure taps are located on the bottom wall and the perforated plate to acquire the wall pressure changes induced by boundary-layer bleed. Inside the cavity plenum, pressure taps on the side and bottom walls are used to measure the plenum pressure, while pressure taps upstream and downstream of the sonic throat are used to prove choking conditions.

The streamwise positions of the pressure taps on the bottom wall are presented in Table 3.3 for both perforated plates. The positions are also highlighted by the red dots in Figure 3.1 for plate HR. Moreover, the pressure tap locations inside the cavity plenum are illustrated.

Plate	Position x [mm]											
AR	25	35	55	65	75	85	95	105	115	125	145	150
HR			50	62	76	86	98	110	122	-		

Table 3.3: Positions of wall pressure taps.

With a hole diameter of 0.4 mm, the size of the pressure taps is in the same order of magnitude as the bleed holes for plate AR with 0.5 mm holes. Thus, some bleed holes are blocked, which may affect the thinning effect in this region. Therefore, the taps are located with an offset of 10 mm from the center plane to neglect the influence on the LDV measurements. For the plate with the large holes, no bleed holes are blocked, and no significant effect on the flow field is expected to be induced by the roughness of the pressure taps.

Chapter Summary

The experimental setup for the validation of the numerical setup in Chapter 5 was presented. Supersonic and subsonic experiments are performed in the ONERA S8Ch wind tunnel. A porous bleed system with the option to use two different perforated plates is installed in the wind tunnel and the bleed rate is adjustable.

The flow field is qualitatively observed using BOS visualizations and measured with LDV. The two-component LDV measurements allow the measurements of the boundary-layer profiles with high reproducibility of the mean velocity components. Flow visualizations are performed using a BOS setup instead of the classical Schlieren as it can be used parallel with the LDV measurements. Moreover, static wall pressure measurements are utilized to obtain the pressure ratio from the external wall to the cavity plenum to compare with the numerical simulations. The pressure taps are not installed on the center plane to prevent any influence on the flow field measured with LDV.

Key Points:**Experimental installations**

- ❑ **S8Ch supersonic wind tunnel**
 - **Supersonic** ($M = 1.62$) and **subsonic** ($M = 0.50$) investigations of the turbulent boundary-layer bleed
 - Investigation of **oblique SBLI** for $M = 1.62$
- ❑ **Bleed systems**
 - Two perforated plates with **different geometrical characteristics**
 - **Bleed rate variation** by using a choked throat

Metrology

- ❑ **LDV measurements** to acquire boundary-layer profiles along the bleed region
- ❑ Real-time **BOS visualizations** of the flow field
- ❑ **Wall pressure measurements** along the porous bleed

Description of the Flow Cases

Hab's aans g'sehn?

ERNST MACH

Chapter Introduction

The following chapter is dedicated to the presentation of the investigated flow cases. With the main goal of a porous bleed in a supersonic air intake being the SBLI control, a base flow case including an SBLI needs to be defined. First, preliminary studies to determine the base flow case for the experimental and numerical investigations are presented. The three-dimensionality of the flow in the later experiments requires a focus on the comparison from the simulations of the wind tunnel center segment with symmetry planes on the front and the back of the domain to the three-dimensional flow field including the sidewalls. After introducing the uncontrolled case, the flow case showing the SBLI control is illustrated, showcasing the differences in the flow field inside the holes upstream and downstream of the incident shock. Finally, the same perforated plate is used to show the effect of porous bleed control on a turbulent supersonic and subsonic boundary layer separately. The perforated plate used in this chapter represents one of the two plates used for the later benchmark of the state-of-the-art bleed models in Chapter 7 and the new model in Chapter 8.

4.1	Uncontrolled Shock-Wave/Boundary-Layer Interaction . . .	77
4.1.1	Influence of the Shock Intensity on the Interaction	77
4.1.2	Impact of the Three-Dimensionality on the Center-Plane Flow	78
4.1.3	Selected Base Flow Case	80
4.2	Control of the Shock-Wave/Boundary-Layer Interaction . .	82
4.3	Boundary-Layer Control	83
4.3.1	Supersonic External Flow	83
4.3.2	Subsonic External Flow	85

4.1 Uncontrolled Shock-Wave/Boundary-Layer Interaction

Before controlling an SBLI, the base flow without any control is investigated. First, the influence of the shock intensity is observed before evaluating the three-dimensionality of the flow field and introducing the selected base flow case.

4.1.1 Influence of the Shock Intensity on the Interaction

In the first step, simulations of the wind tunnel half span (see Chapter 2) are conducted and the Mach contours on the centerline are shown in Figure 4.1. The wedge angle is varied from 6° (Figure 4.1a) to 11° (Figure 4.1f). The shock intensity increases with the wedge angle. Thus, the transition from a regular oblique SBLI (Figures 4.1a & 4.1b) to a Mach reflection (Figures 4.1c to 4.1f) occurs. Higher angles of attack are not shown as a further increase leads to a detachment of the shock from the leading edge of the shock generator.

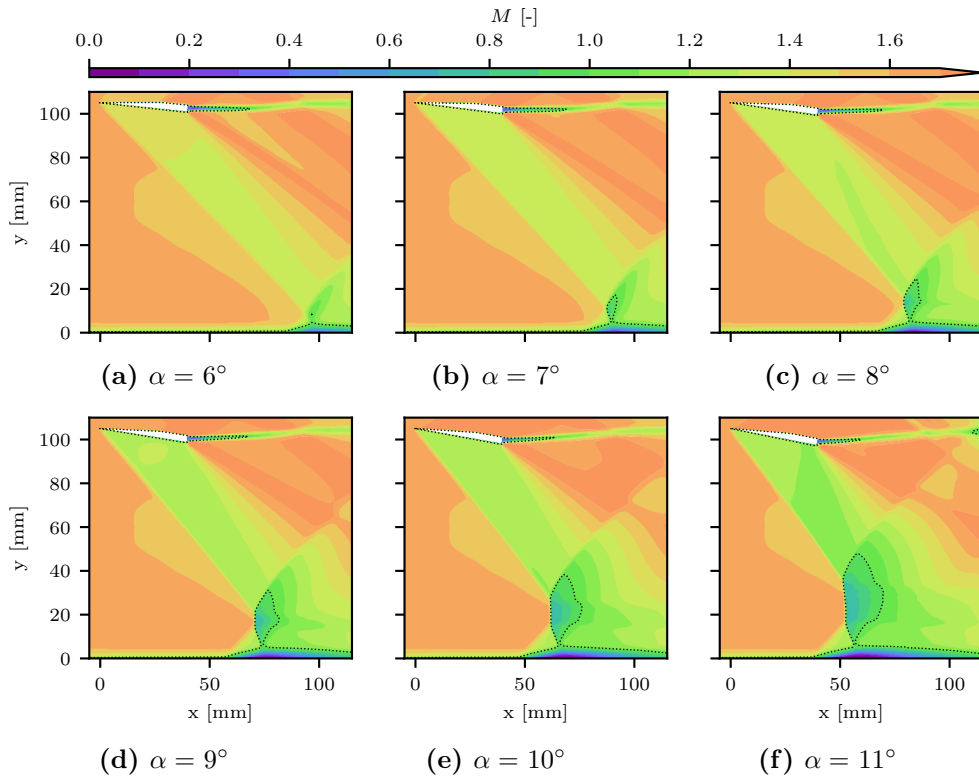


Figure 4.1: Contour of Mach number for varying wedge angles in the three-dimensional simulation; dotted line visualizes the sonic line.

From a wedge angle of $\alpha = 8^\circ$ (Figure 4.1c), the deflection angle is high enough to observe a Mach stem. The presence of a normal shock results in higher losses downstream of the Mach stem. Thus, the Mach number is lower in the region downstream of the Mach stem, highlighted by the bump in the sonic line (dotted line).

For higher angles of attack, the Mach stem is growing in size, and the shock position moves upstream. While the position of the Mach stem is at $x = 79$ mm for a wedge angle of $\alpha = 8^\circ$, the Mach stem is located at $x = 53$ mm for $\alpha = 11^\circ$ (see Figure 4.1f).

Details about the size of the separated region can be highlighted utilizing the streamwise wall shear stress and friction lines (Figure 4.2). We can see that flow separation is apparent for all angles of attack. The higher the wedge angle, the larger the separation bubble. This

is a consequence of the higher shock intensity provoked by the higher deflection angle. The separated region moves upstream with higher angles of attack, similar to the shock foot.

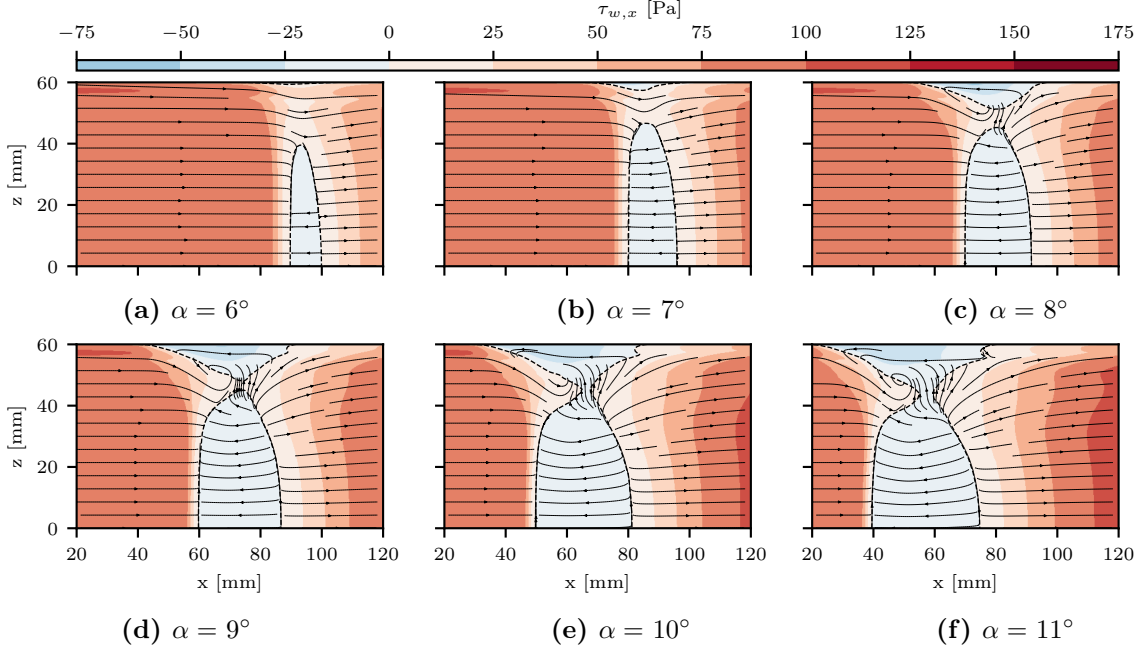


Figure 4.2: Contour of wall shear stress for varying angles of attack.

Figure 4.2 also indicates a growth of the corner separation. The corner flow starts to separate for a low wedge angle of $\alpha = 6^\circ$ (see Figure 4.2a), and a recirculating flow can be observed for higher angles of attack. In this case, a secondary flow streaming from the center to the corner is apparent.

4.1.2 Impact of the Three-Dimensionality on the Center-Plane Flow

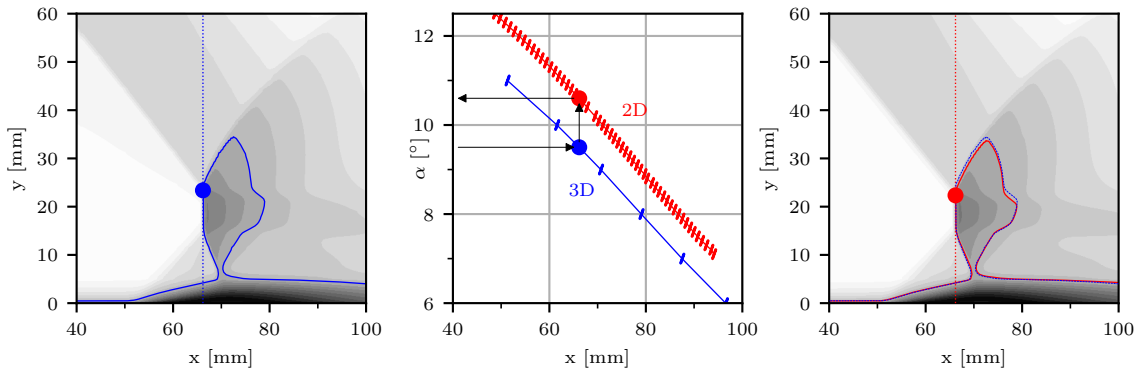
As stated in Chapter 2, wind tunnel half-span simulations are more expensive in terms of number of cells and computational time. For the later application of flow control, simulations of the center segment are preferable as meshes containing a porous bleed and the half-span of the wind tunnel are too large to perform a large number of simulations. Therefore, two-dimensional simulations of the reference flow are conducted to analyze the impact of the three-dimensionality on the center-plane flow.

The comparison of the shock pattern for the three-dimensional and two-dimensional simulations is necessary for the later comparison between experiments and simulations. In both cases, the porous bleed is installed at the same streamwise position, and its location concerning the incident shock might essentially change the flow field. However, the sidewalls in the wind tunnel cause three-dimensional effects influencing the flow at the center plane [14]. In contrast, symmetry boundary conditions on the front and the back of the numerical domain prevent the presence of sidewall effects.

In the following, the flow fields on the center plane of the wind tunnel half-span simulations are compared to the two-dimensional simulations. A displacement of the shock in the downstream direction is observed for the two-dimensional simulations. With the aim of finding a comparable two-dimensional case, the streamwise position of the upper triple point – the position where the oblique shock is reflected – is extracted as highlighted in Figure 4.3. In Figure 4.3a, the extraction is shown for a three-dimensional simulation with a wedge angle of $\alpha = 9.5^\circ$ by using the sonic line to determine the shock position. Knowing about the curvature

of the strong shock near the triple point, the minimum of the streamwise coordinate outside the boundary layer is assumed as the position of the triple point.

The upper triple point is extracted for several three-dimensional and two-dimensional simulations with varying shock intensities. Figure 4.3b shows the position of the upper triple point versus the wedge angle of the shock generator. The markers highlight the performed computations. This graph shows an offset between the trend curves for three-dimensional and two-dimensional simulations. Higher angles of attack are required for two-dimensional computations to obtain the same streamwise position of the upper triple point. However, the almost linear trend enables conversion from a three-dimensional to a two-dimensional simulation by adjusting the wedge angle, as represented by the black arrows.



(a) Upper triple point in three-dimensional simulation (b) Triple point position as a function of the wedge angle (c) Upper triple point in two-dimensional simulation

Figure 4.3: Conversion from three-dimensional (center plane) to two-dimensional simulation using the streamwise position of the upper triple point.

Figure 4.3c shows the corresponding two-dimensional simulation with an equal streamwise position of the upper triple point as for the three-dimensional simulation from Figure 4.3a. The sonic line is highlighted in red and laid on top of those from the three-dimensional simulation (in blue), showing a good agreement between both simulations. An increase in the wedge angle by approximately 1° is required in this case to obtain the same shock pattern, even though the position of the expansion fan caused by the rear edge of the shock generator is different. The different shock position is a consequence of the corner separation shock waves, which affect the size and shape of the separation of the center-plane flow [6, 88, 119]. In the present case, the interaction length increases, leading to an upstream movement of the Lambda shock and the upper triple point.

A more detailed comparison of the two simulations is shown in Figure 4.4 for the difference of the Mach number (Figure 4.4a) and the curves of the wall pressure (Figure 4.4b). A slight deviation of the incoming flow field can be observed, with a higher Mach number in the two-dimensional simulation. The deviation is thought to be a consequence of confinement effects due to the sidewall boundary layer in the three-dimensional simulations. Thus, the effective cross-sectional area of the channel is smaller and the Mach number at the exit of the convergent-divergent nozzle is reduced compared to the two-dimensional case without boundary-layer growth at the sidewalls. However, the difference is negligibly small ($(M_{2D} - M_{3D})_{upstream} \approx 0.02$). Downstream of the SBLI, the differences are small and only notable close to the wall and around the slip line.

A good fit of the wall pressure curves can be seen in Figure 4.4b. The curve for the three-dimensional simulations starts at a lower position as the free-stream Mach number is slightly

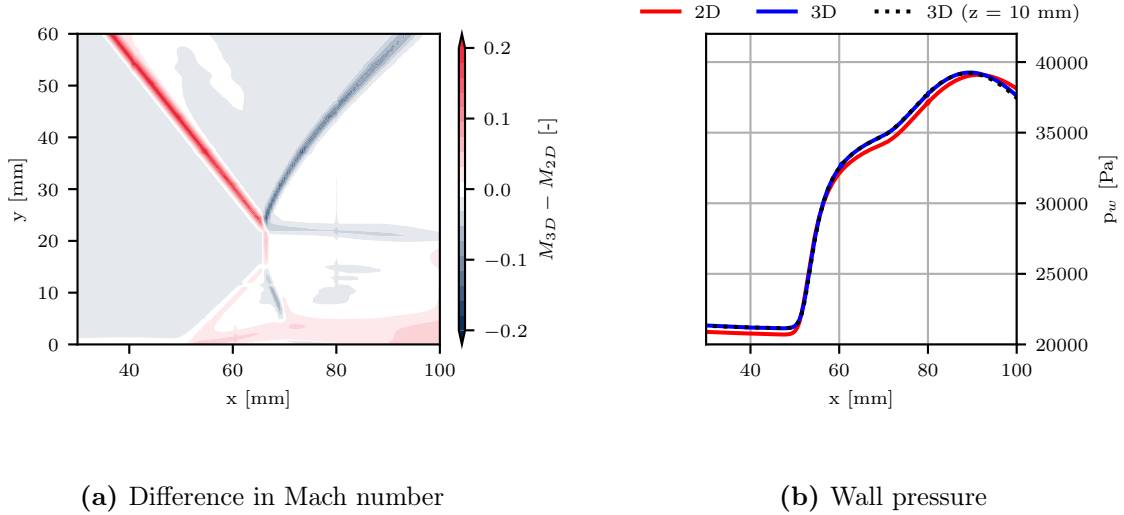


Figure 4.4: Comparison between three-dimensional and two-dimensional simulations.

higher. However, the curves for both computations are very similar and the main difference is the lower wall pressure for the two-dimensional case due to the higher Mach number upstream of the incident shock.

Moreover, the wall pressure for the three-dimensional simulation with an offset of 10 mm from the center plane is illustrated. The curve fits the curve from the center plane very well, which underlines the two-dimensionality of the flow in the center of the wind tunnel. Thus, the wall pressure acquired in the experiments can be compared to the numerically predicted wall pressure. As stated in Chapter 3, the pressure taps are installed with an offset of 10 mm to prevent any impact on the center-plane flow.

Altogether, the flow field obtained by the two-dimensional simulation does not significantly differ from the center-plane flow field of the three-dimensional simulation. Thus, the simplified numerical setup with symmetry boundary conditions on the front and the back of the domain can be applied for later comparison with the experiments.

4.1.3 Selected Base Flow Case

For further study, the wedge angle is fixed to $\alpha = 9.5^\circ$ in the three-dimensional simulations and experiments, and to $\alpha = 10.5^\circ$ for the simulations of the center segment. Thus, the presence of the Mach stem is ensured, and the first expansion waves generated by the rear edge of the shock generator are ensured to reflect at the wall downstream of the later installed bleed. Figure 4.5 illustrates the flow field inside the wind tunnel. The wall shear stress is visualized on the back and the bottom wall. An isocontour of the density gradient, colored by the spanwise position, highlights the shock topology. The incident shock provoked by the shock generator is non-regularly reflected on the wall. A lambda shock foot is apparent, enclosing the separation bubble. The yellow isocontour highlights the volumes of reversed flow in the streamwise direction. Center and corner separation can be easily distinguished.

Figure 4.6 shows the center-plane flow field. The incident oblique shock provoked by the shock generator, the reflected shock, and the Mach stem are apparent, as well as the Lambda shock foot. The streamlines highlight the boundary-layer growth induced by the adverse pressure gradient.

A closer look at the flow field in the vicinity of the wall (see zoom-in view in Figure 4.6) reveals the presence of a separation bubble. This separation bubble is limited in size because

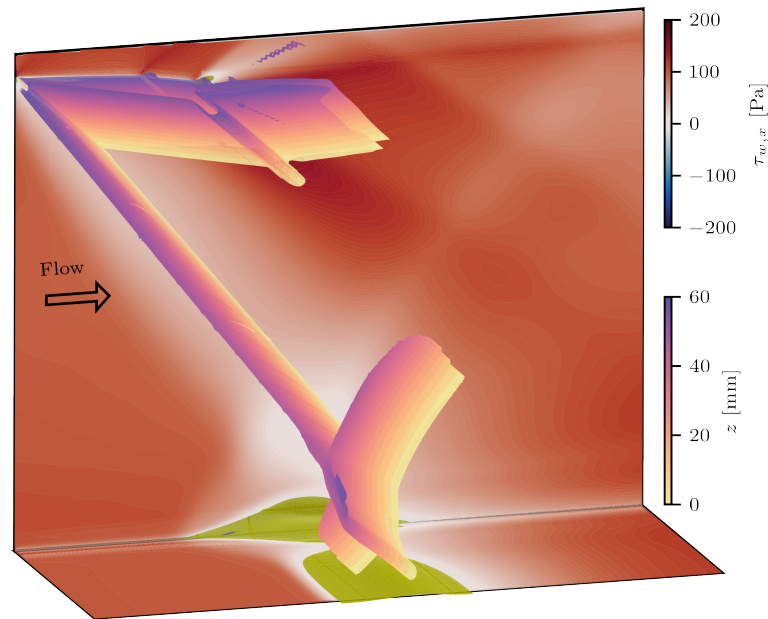


Figure 4.5: Uncontrolled base flow in the wind tunnel for a wedge angle of $\alpha = 9.5^\circ$; contours on bottom and back wall showing wall shear stress; isocontour $u = 0$ m/s highlighted in yellow; shock pattern illustrated by isocontour of the density gradient and colored by the spanwise position.

of an expansion fan generated by the rear edge of the shock generator, which accelerates the flow and leads to its reattachment. The aim of the porous bleed system is the mitigation of the separation bubble.

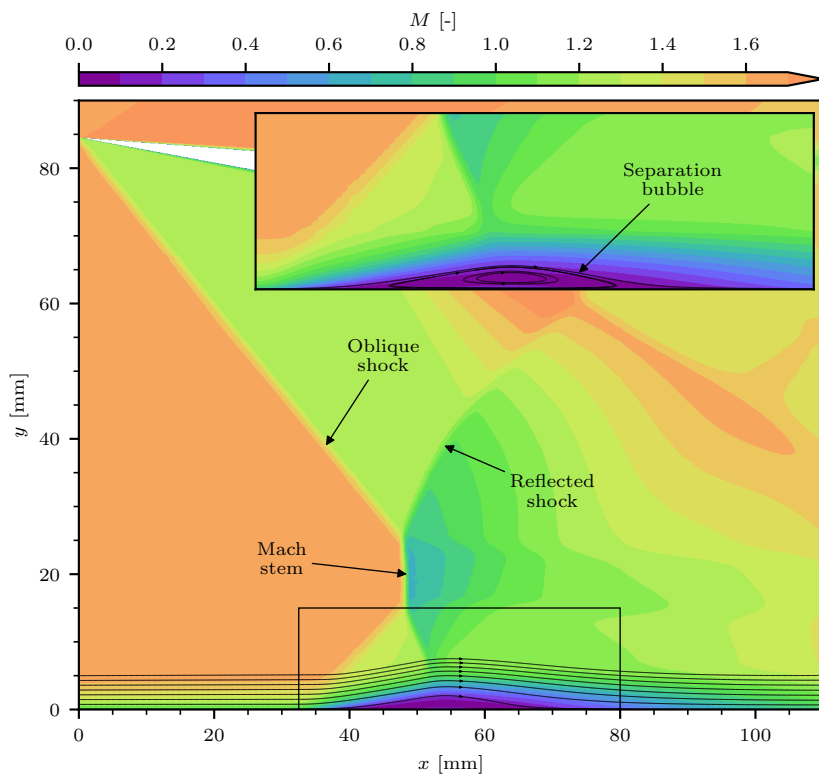


Figure 4.6: Mach number contours for the uncontrolled case with SBLI.

4.2 Control of the Shock-Wave/Boundary-Layer Interaction

The flow field for a controlled case is presented in Figure 4.7 for a bleed configuration with a plate length of $L_w = 40$ mm, a hole diameter of $D = 2$ mm, a thickness-to-diameter ratio of $T/D = 1$, a porosity level of $\phi = 22.67\%$, and a stagger angle of $\beta = 60^\circ$. Figure 4.7a shows the flow on the hole-cutting plane. A relatively large hole diameter ($D/\delta_{1,c} = 2.25$) is selected in this chapter to visualize better compressible effects caused by the bleed holes. The wedge angle is fixed to $\alpha = 10.5^\circ$ like in the base flow case since the sidewall is not included in the numerical domain.

A slight thinning of the supersonic boundary layer can be observed by following the streamlines upstream of the shock. After passing the shock, the streamlines are bent towards the wall, which indicates a high mass removal downstream of the shock where the flow is subsonic close to the wall. No shock-induced flow separation is notable as the low-momentum flow is removed by the bleed.

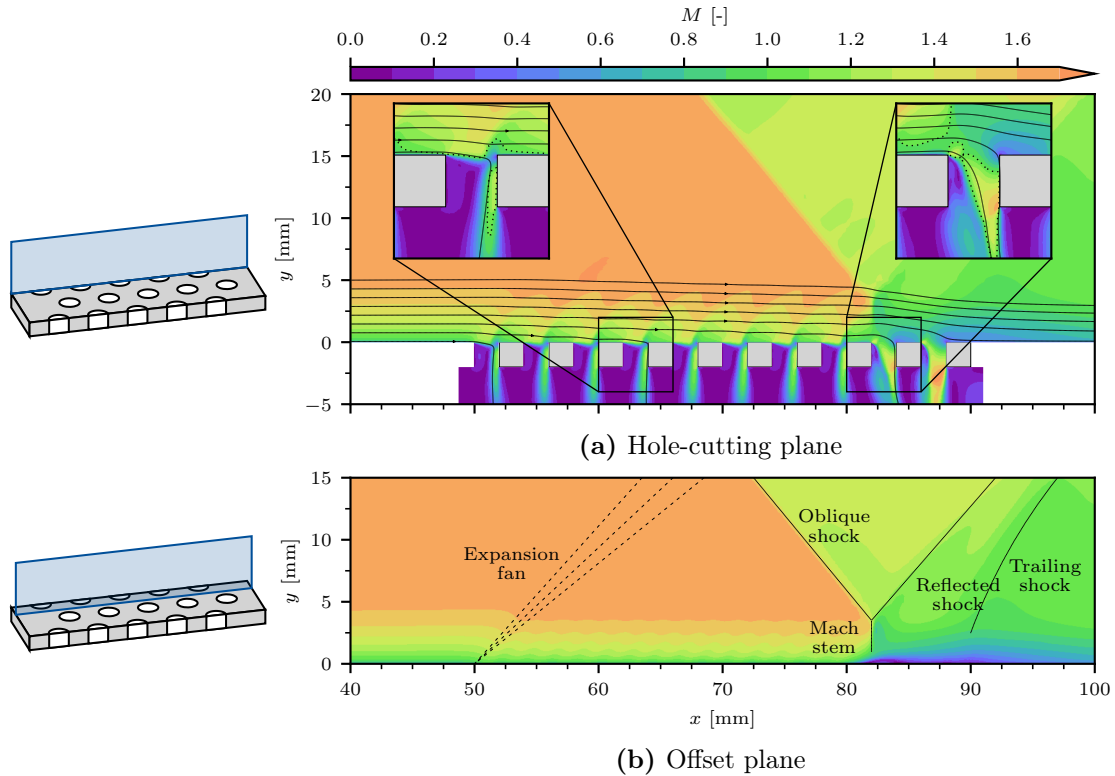


Figure 4.7: Mach number field for an SBLI control; gray patches illustrate the out-of-plane holes ($TR = 0.7$).

The zoom-in view on the left-hand side shows the flow field inside a bleed hole upstream of the shock where the external flow is supersonic. The suction rate in this region is relatively low, the holes are unchoked, and the flow inside the hole becomes only supersonic in a small area, as illustrated by the sonic line (dotted). Moreover, a sizeable separated region is observed.

A completely different flow field is apparent on the zoom-in view on the right, presenting the flow inside the hole in the subsonic region downstream of the shock. Here, the external flow is subsonic. Thus, no barrier shock is evident, and the expansion fan is limited to a small area close to the leading edge, where the flow is accelerated to supersonic conditions again. The flow inside the hole is choked, as visualized by the sonic line. The separated region inside the

holes in the subsonic region is significantly lower. Moreover, the streamlines directed toward the plate indicate a substantial thinning of the boundary layer and an increase in the flow momentum in the wall vicinity.

The flow on the hole-cutting plane between the holes is detailed in Figure 4.7b, where the pattern of the shock reflection, as well as the expansion fan and the trailing shock induced by the porous bleed, are illustrated. In the supersonic region upstream of the shock, small out-of-plane effects caused by the hole located outside the plane are evident in the form of irregularities in the Mach number inside the boundary layer. Downstream of the shock, where the external flow is subsonic, no out-of-plane effects are apparent. Close to the shock, the Mach number in the vicinity of the wall is low, which indicates the presence of a small local flow separation.

The different flow topologies inside the holes upstream and downstream of the shock, as well as the interaction of the incident shock, highlight the complexity of this flow case. Thus, the finding of comprehensive conclusions is challenging, since the operation of the bleed is linked to both supersonic and subsonic regions as the bleed uses the same cavity plenum, and the bleed interacts with the SBLI. As a consequence, the complex problem is simplified by investigating supersonic and subsonic boundary-layer bleed separately to deepen the knowledge about the flow physics in the regions upstream and downstream of the shock before applying a porous bleed for SBLI control.

4.3 Boundary-Layer Control

In the following, control of a turbulent boundary layer by porous bleed is presented for supersonic and subsonic external flows. The characteristics of the perforated plate are equal to the previously described flow case of the SBLI control ($L_w = 40$ mm, $D = 2$ mm, $T/D = 1$, $\phi = 22.67\%$). The flow field inside the holes is characterized in more detail to describe the flow behavior upstream and downstream of a shock.

4.3.1 Supersonic External Flow

An example of the flow field inside the bleed holes, the cavity plenum, and externally of the bleed is presented in Figure 4.8 for supersonic flows with a Mach number of $M = 1.6$ and an inlet boundary-layer profile with a compressible displacement thickness of $\delta_{1,c} = 0.89$ mm, similar to the inflow characteristics in the ONERA S8Ch wind tunnel.

The flow field on the plane that cuts the holes is shown in Figure 4.8a. The gray patches show the out-of-plane holes that are located at another streamwise position as a result of the hole staggering with the hole columns. A strong impact of the bleed holes on the flow inside the boundary layer is apparent, where the mass removal induces expansion fans, which, in turn, cause a bending of the flow towards the wall. The holes capture the flow close to the wall, which is sucked into the cavity plenum. Moreover, the lower streamlines reveal a rapid thinning of the boundary layer above the bleed holes as was already found by Oorebeek et al. [77].

The zoom-in in Figure 4.8a illustrates the typical flow structure inside a bleed hole for a supersonic (upstream) bleed, which is similar to those observed by Hamed et al. [60] (see Figure 1.42). An expansion fan is provoked at the front of the hole, turning the flow into the hole. Further downstream, a barrier shock is formed since the flow must be redirected either in the wall-parallel direction or into the hole. This bow shock can be divided into two segments as reported by Shih [94]. The first segment of the shock is located inside the hole, decelerating the flow to subsonic conditions and bending the flow into the hole. The upper part of the shock redirects the flow in the wall-parallel direction and weakens with further distance to the wall

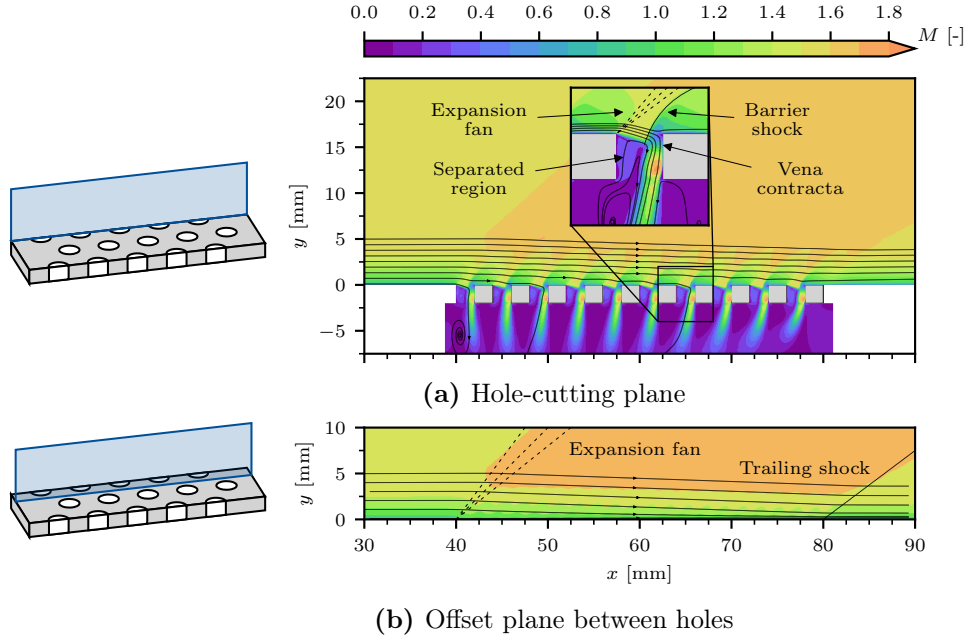


Figure 4.8: Mach number field for a supersonic turbulent boundary bleed; gray patches illustrate the out-of-plane holes.

and turns into an oblique shock wave. Faintly visible is a small portion of the flow that leaves the hole at the rear edge, as the stagnation point is located inside the hole, which agrees with the findings of Oorebeek et al. [77].

A large separated flow region inside the bleed hole is apparent. A result of its presence is the deformation of the stream tube in the shape of a convergent-divergent nozzle, as described by Ghosh et al. [43] and also seen in Figure 1.42. If the pressure ratio drops below the critical pressure ratio ($p_{pl}/p_w \leq 0.528$), which results in choking conditions, the flow is accelerated to supersonic conditions and emits as an under-expanded jet into the plenum. The mass flow rate passing the bleed hole is limited by the minimum size of the stream tube, the so-called vena contracta area. Its position is roughly at the imaginary intersection of the barrier shock with the (lower) outer streamline of the captured flow. Even though a choking of the bleed hole is apparent, the bleed rate does not necessarily reach its maximum. A decrease in the plenum pressure may influence the flow in the separated region, which is subsonic and linked to the cavity plenum. Thus, the lower pressure propagates in this region and causes a stronger expansion fan. Hence, the size of the separated region decreases, which in turn increases the size of the vena contracta area, enabling the passing of higher mass flow rates.

Figure 4.8b shows the flow field on the plane between two columns of holes where the wall is fully solid. Still, the effect of the expansion fans and barrier shocks provoked by the holes is evident. The first hole generates a particularly distinctive expansion fan associated with a strong flow deflection. Downstream, the out-of-plane effects of the holes are apparent, similar to the studies of Oorebeek et al. [77] and Schwartz et al. [93] even though the inter-hole distance in the spanwise direction is relatively larger in the current study. The flow passes several expansion and compression waves induced by the flow into the holes located out of the plane. Moreover, a trailing shock at the end of the plate is prominent, which is the barrier shock of the last holes, redirecting the flow into the wall-parallel direction. The slope of the streamlines demonstrates the thinning of the boundary layer.

4.3.2 Subsonic External Flow

The flow topology for subsonic conditions is described for an inflow Mach number of $M = 0.6$, representing the application downstream of a normal shock wave. The flow field around and inside the bleed holes is visualized in Figure 4.9 for the same plate as shown in Figure 4.8.

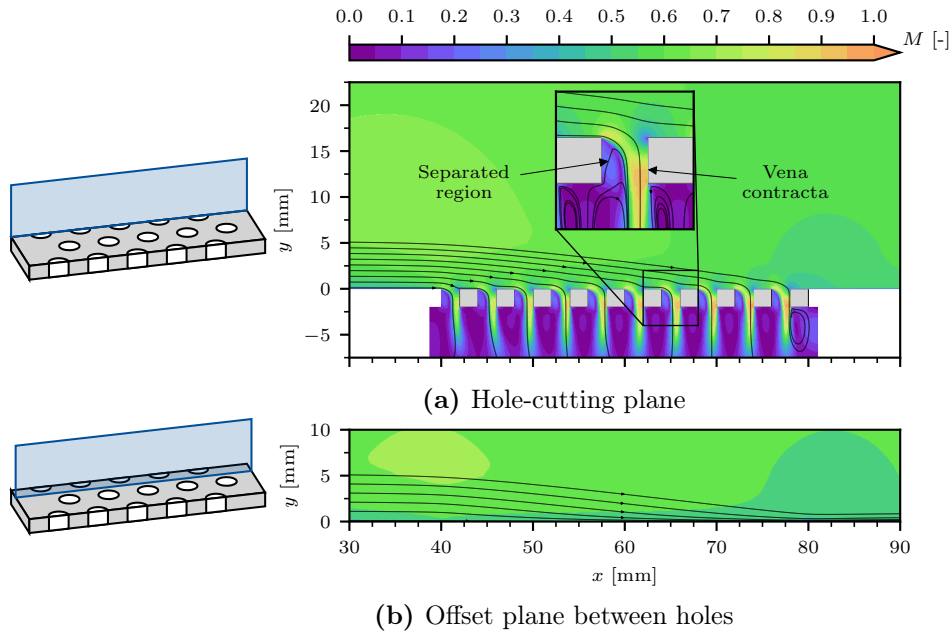


Figure 4.9: Mach number field for a subsonic turbulent boundary bleed; gray patches illustrate the out-of-plane holes.

Again, the flow field on the hole-cutting plane is presented in Figure 4.9a. The zoom-in view illustrates the flow topology inside a bleed hole. No expansion fans and barrier shocks are apparent since the flow at the hole inlet is fully subsonic. The separated region is smaller compared to supersonic conditions, leading to a larger vena contracta area, and thus, higher bleed rates. Moreover, the stream tube inside the holes is shaped like a convergent nozzle, resulting in an acceleration of the flow inside the holes to supersonic conditions.

The flow field on the offset plane (see Figure 4.9b) shows the deflection of the flow toward the wall at the beginning of the bleed region similar to supersonic flows. However, no expansion fan is apparent because of the subsonic conditions. Moreover, a deflection of the streamlines upstream of the bleed reveals an upstream influence. Also, no trailing shock is apparent as the flow is not accelerated to supersonic conditions. Interestingly, the Mach number downstream of the bleed region is slightly decreased compared to the upstream flow in the region close to the wall.

Chapter Summary

In this chapter, we introduced the investigated flow cases. First, preliminary studies of the wedge angle on the flow field of the SBLI were discussed, as well as the impact of the corner flow on the center-plane flow. Based on the results, the base flow case to control was selected. Afterward, the controlled SBLI case was presented before this complex case was simplified by showing the boundary-layer control for supersonic and subsonic flow.

The wedge angle was found to significantly influence the SBLI. A Mach stem was apparent from a wedge angle of $\alpha = 8^\circ$, while a separation bubble at the wind tunnel center and corner separation were already observed for $\alpha = 6^\circ$. With increasing wedge angle, the interaction length increased. Moreover, a comparison with two-dimensional simulations revealed an impact of the corner flow on the center-plane flow. Thus, the wedge angle needed to be increased in the two-dimensional setup by approximately 1° to obtain a flow field similar to the three-dimensional simulation with sidewalls. Finally, the wedge angle was fixed to 9.5° in the three-dimensional setup to obtain the desired flow field with a Mach stem to investigate the bleed for subsonic flow downstream of the shock.

The control with porous bleed significantly changed the flow field. The separation bubble was effectively mitigated, and the size of the Mach stem was reduced. Upstream of the shock, where the flow is supersonic, a different flow field was found inside the bleed holes compared to downstream of the shock, where the flow is subsonic close to the wall. Following this, the flow fields for the supersonic and subsonic boundary-layer bleed were separately presented. For supersonic flows, each bleed hole created an expansion fan and a bow shock, the so-called barrier shock. Inside the hole, a large separated region was observed. At the front of the bleed region, an expansion fan was generated, and the so-called trailing shock appeared at the end of the bleed region. In contrast, no shock waves were present for the subsonic boundary-layer bleed, as the removed air had a lower momentum. Also, the separated region inside the holes was smaller compared to supersonic external flows.

Key Points:**Characterization of the uncontrolled flow**

- ❑ Influence of **wedge angle**
 - **Mach reflection** from $\alpha = 8^\circ$
 - **Separation bubble** already apparent at $\alpha = 6^\circ$
 - Increase of **separation length** and **corner separation** with increasing wedge angle \rightarrow higher shock intensity
- ❑ Impact of the **three-dimensionality** on the center-plane flow
 - **Corner flow** increases **interaction length**
 - Increase in the **wedge angle** enables mirroring of the center-plane flow field in a two-dimensional setup
 - **Wall pressure distribution** with an offset of 10 mm identical to the center distribution
 - **Adjustment** of the **wedge angle required** for comparison of simulations of the wind tunnel center segment with experiments in Chapter 5
- ❑ **Base flow case** with wedge angle of $\alpha = 9.5^\circ$

Control of the shock-wave/boundary-layer interaction

- ❑ **Separation bubble** successfully mitigated
- ❑ **Different flow topology** inside the bleed holes upstream and downstream of the shock
- ❑ **Expansion fan** and **trailing shock** induced by the suction through the perforated plate

Boundary-layer control

- ❑ **Supersonic** external flow
 - **Expansion fan** at the front of the bleed hole
 - **Barrier shock** decelerates flow to subsonic conditions for redirection into the bleed hole
 - Large **flow separation** inside the bleed holes
- ❑ **Subsonic** external flow
 - Absence of **shock waves**
 - Smaller **flow separation** inside the bleed holes

Comparison of Experiments and Simulations

No amount of experimentation can ever prove me right; a single experiment can prove me wrong.

ALBERT EINSTEIN

Chapter Introduction

In the following, the experimental and numerical findings are compared. First, the supersonic experiments of Willis et al. [117] and Eichorn et al. [40] are numerically reproduced to validate the computed sonic flow coefficient, and thus the bleed efficiency, for different plate geometries and Mach numbers.

After validating the numerical setup with existing data, new supersonic and subsonic experiments on boundary-layer bleed are performed to validate the numerical findings regarding the flow field. Boundary-layer profiles for two different plate geometries are experimentally and numerically acquired for several bleed rates under supersonic and subsonic conditions. Moreover, three-dimensional effects (e.g., spanwise variation in the boundary-layer profiles) are evaluated for supersonic flows. Previous experiments have focused on these effects to a limited extent, even though they are essential for SBLI control in supersonic air intakes.

Afterward, experiments are conducted to investigate the control effect on the incident shock wave, and the flow field is compared to the numerical simulations by using wall pressure measurements and LDV measurements along the bleed region. Thereafter, the three-dimensionality of the flow is numerically investigated and compared to the BOS visualizations.

5.1 Existing Experimental Data	91
5.1.1 Experiments of Eichorn et al.	91
5.1.2 Experiments of Willis et al.	92
5.2 New ONERA Experiments	93
5.2.1 Supersonic Boundary-Layer Bleed	93
5.2.1.1 Flow Field Analysis	93
5.2.1.2 Boundary-Layer Profiles at the Wind Tunnel Center	98
5.2.1.3 Three-Dimensionality of the Flow	100
5.2.2 Subsonic Boundary-Layer Bleed	104
5.2.3 Shock-Wave/Boundary-Layer Interaction Control	106
5.2.3.1 General Flow Field	106
5.2.3.2 Three-Dimensionality of the Flow Field	109

5.1 Existing Experimental Data

The validation of the numerical setup concerning the bleed rate is conducted based on two experimental datasets from supersonic experiments. In the first step, a single-hole approach is used to compare the simulation with the data obtained by Eichorn et al. [40], where three different plate geometries are simulated. Moreover, the experimental data of the investigation of Willis et al. [117] for the C1 plate are used to validate the multi-hole setup.

The inlet profiles are reproduced for both setups by performing flat plate simulations with identical total conditions. The inlet profiles are extracted at the position where the boundary-layer thickness δ_{99} is equal to the experimental data. Furthermore, the external wall pressure is in this section computed using the isentropic relations for the inflow Mach number, and not locally extracted as described in Section 2.4.

5.1.1 Experiments of Eichorn et al.

Eichorn et al. [40] measured the mass flow rate for 21 plates with different inclination angles, thickness-to-diameter ratios, and hole diameters for Mach numbers $M = 1.33, 1.62, 1.97, 2.46,$ and 2.96 . In this study, we only focus on the 90° -holes and the measurements for a Mach number of $M = 1.62$. Thus, three plates with varying hole diameters and thickness-to-diameter ratios are selected for validation; their geometrical parameters are shown in Table 5.1. Even though the experiments were single-hole studies, a single-row setup with 15 holes in the spanwise direction was used for plate 1501 with the smallest holes to obtain an almost constant bleed rate for all plates. No interaction between the holes was expected since the hole spacing was more than four hole diameters.

Plate	D	T/D	N_z
101	6.350 mm	2.000	1
102	6.350 mm	1.125	1
1501	0.794 mm	2.000	15

Table 5.1: Simulated plates from Eichorn et al. [40].

The results of the computation with *elsA* are compared to the data of Eichorn et al. [40] and the regression of Slater [98] in Figure 5.1. The numerical simulations have a good fit with the experiments, especially for plates 101 and 102, where the simulations mirror almost perfectly the trend of the experiments.

For plate 1501, two different numerical setups are used: a single-hole approach and a single-row approach, where three holes in the spanwise direction are simulated with symmetry boundary conditions at the front and the back of the domain (see sketch in Figure 5.1). The spanwise hole spacing is four diameters in the single-row approach to mirror the experimental setup of Eichorn et al. [40]. Interestingly, the simulation of multiple holes leads to a notable degradation of the bleed performance, contrary to the statements of Eichorn et al. [40]. While the single-hole approach overpredicts the sonic flow coefficient, the single-row approach better fits the experimental data. Thus, an even more pronounced difference between the single-hole and multi-hole approach is assumed for larger porosity levels or reduced hole spacing.

Moreover, two parameter effects are apparent in experimental and numerical data with the single-hole approach. First, the thickness-to-diameter ratio significantly affects the sonic flow coefficient. The lower the ratio, the higher the coefficient. For $T/D = 2.0$, the data fits the regression of Slater [98], while the data for lower ratios lies below this regression. The second

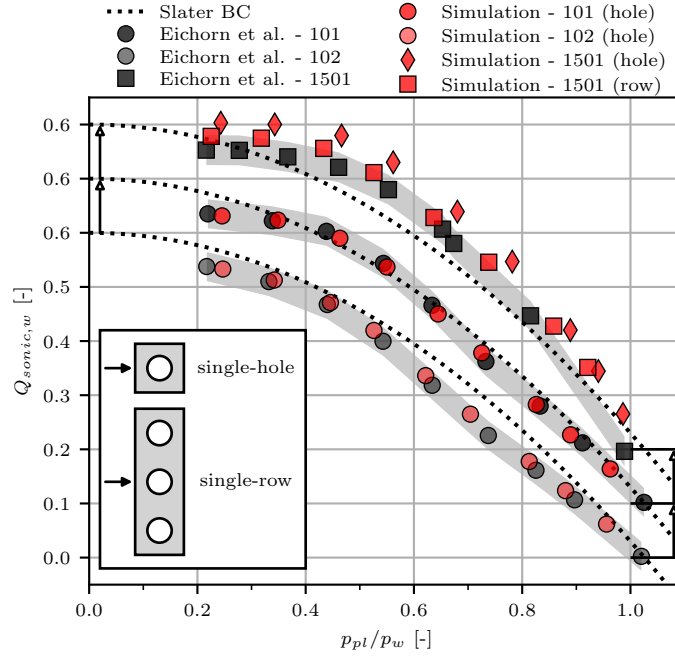


Figure 5.1: Experimentally and numerically determined surface sonic flow coefficient for the plates of Eichorn et al. [40] compared to the regression of Slater [98]; plates 101 and 1501 are shifted upwards to increase the readability of the graph; gray area illustrates 5% range around the experimental data.

effect is the impact of the hole diameter. The upper two curves (plates 101 and 1501) represent holes with an equal thickness-to-diameter ratio. However, the sonic flow coefficient is higher for small hole diameters. Regarding the spanwise interaction of the holes, it is assumed that the effect would have been even more visible if the experiments were repeated with only one hole.

5.1.2 Experiments of Willis et al.

The C1 plate from the experiments of Willis et al. [117] has a hole diameter $D = 6.35$ mm, a thickness-to-diameter ratio $T/D = 1$, a stagger angle $\beta = 30^\circ$, and a porosity $\phi = 19.63\%$. The numerical setup consists of three columns and three rows of holes.

Again, the numerically obtained data fits very well with the experiments independently of the free-stream Mach number. The overall simulation trend is equal, as apparent in Figure 5.2. Here, the sonic flow coefficient based on the total quantities is computed. Please note that the simulations are conducted for $M = 1.3, 1.6, 2.0,$ and 2.5 . Consequently, a slightly lower sonic flow coefficient is expected. The highest deviation between experiments and simulations is found for higher pressure ratios p_{pl}/p_t and Mach numbers $M = 1.27$ and 1.58 . As stated before, an underpredicted sonic flow coefficient is expected because of the higher Mach number in the simulations, leading to a lower static pressure, and thus, to a lower pressure in the cavity plenum. However, the experimental data in this area might overpredict the sonic flow coefficient. The experiments were performed using two different diameter ASME nozzles to measure the bleed rate. The presented data represent the smaller nozzle, while measurements with the wider nozzle led to lower flow sonic flow coefficients. Moreover, a scaling of the data to p_{pl}/p_w shows an intersection with the abscissa at $p_{pl}/p_w \approx 1.05$ for $M = 1.58$.

Altogether, a good agreement between CFD simulations and experiments is found regarding the sonic flow coefficient independently of the inflow Mach number.

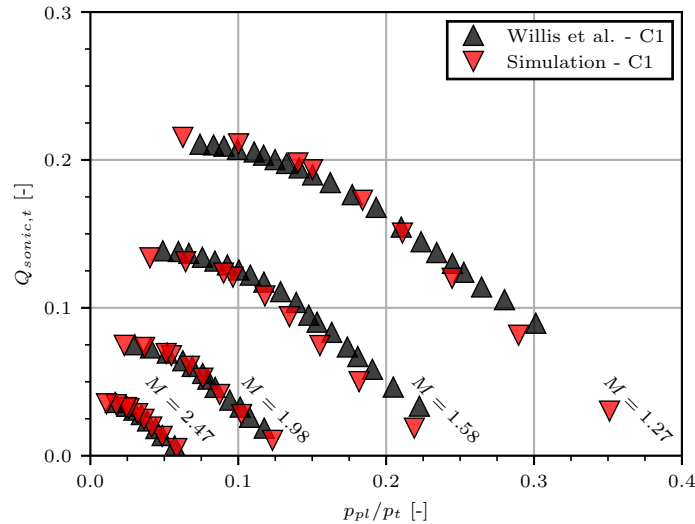


Figure 5.2: Experimentally and numerically determined sonic flow coefficient for the C1 plate of Willis et al. [117].

5.2 New ONERA Experiments

The experiments presented in the following are performed in the ONERA S8Ch wind tunnel, as introduced in Chapter 3, and the numerical domain corresponds to that presented in Section 2.1.1. All three flow cases consisting of supersonic boundary-layer bleed, subsonic boundary-layer bleed, and SBLI control are presented. In contrast to Chapter 4, we start with the boundary-layer bleed to understand first the flow physics upstream and downstream of the incident shock before applying this knowledge to the complex flow case of the SBLI control.

5.2.1 Supersonic Boundary-Layer Bleed

First, experiments without the shock generator are conducted to investigate the supersonic boundary-layer bleed for a free-stream Mach number of $M = 1.6$. In the first step, the general flow field is compared before evaluating boundary-layer profiles upstream and downstream of the bleed region. In the last step, three-dimensional effects are emphasized.

5.2.1.1 Flow Field Analysis

The flow topology in the vicinity and inside the holes is shown for the simulations of the center segment using symmetry boundary conditions on the front and the back with both perforated plates in Figure 5.3. The chosen working regime is characterized by choked holes, caused by a low pressure ratio from the external wall to the cavity plenum. Thus, the bleed operates close to the limiting conditions, i.e., the maximum bleed rate. In Figure 5.3a, the flow field for the low-porosity plate AR (see Table 3.2 for more details) with $D = 0.5$ mm is illustrated. Following the streamlines, a deflection of the flow towards the wall is noted at the beginning of the plate as part of the boundary layer is sucked. This leads to an increase in the Mach number as the flow is accelerated. The so-called trailing shock is located at the end of the plate, where the perforated plate ends, redirecting the flow in the wall-parallel direction.

Close to the wall, further expansion and shock waves are generated by the flow streaming into the holes, as seen in the zoom-in view in Figure 5.3. At each hole front, an expansion fan is located, bending the flow inside the hole. Further downstream, the barrier shock returns the

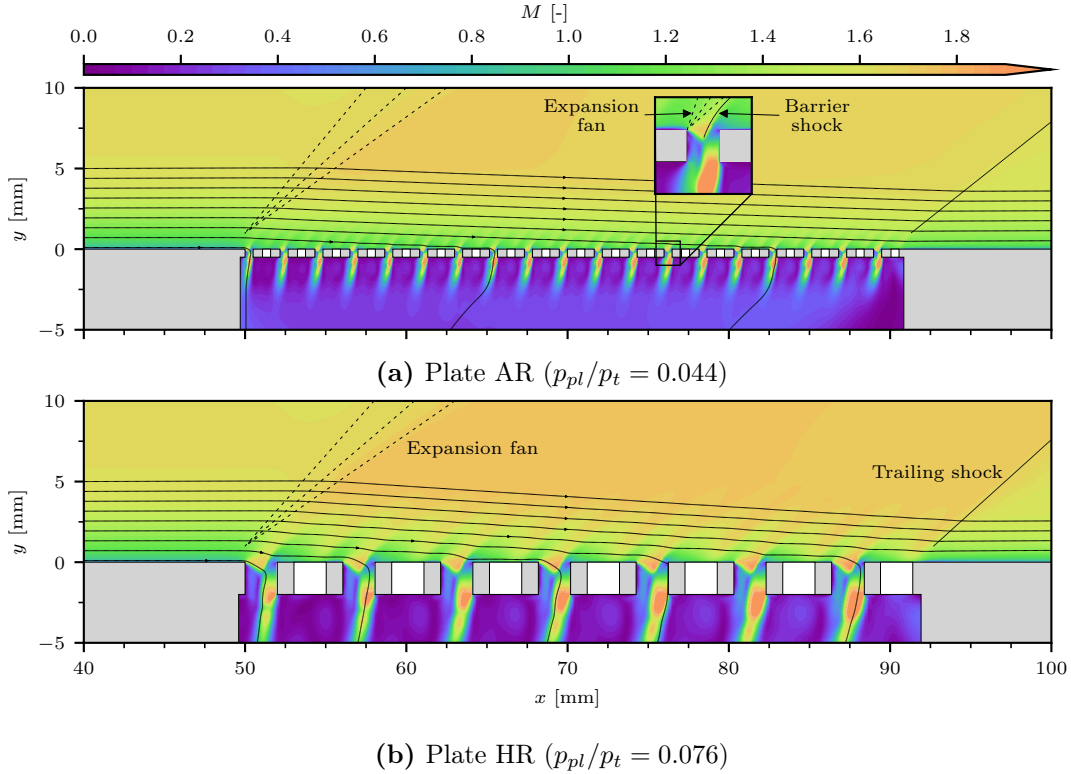


Figure 5.3: Mach contour fields; white areas illustrate holes of the second column.

flow parallel to the wall. Inside the hole, the flow is choked, leading to a supersonic under-expanded jet into the cavity plenum.

A similar flow field is apparent for the high-porosity plate HR, as shown in Figure 5.3b. In comparison to the first plate, the thinning of the boundary layer is more prominent as highlighted by the stronger bending of the streamlines. This is a consequence of the higher porosity level, which is approximately twice the one for the low-porosity plate AR, and in turn, the higher bleed rate as the open area is increased. Moreover, the local flow phenomena induced by the bleed holes have a more significant effect on the flow field and penetrate deeper inside the boundary layer. The higher momentum of the captured flow is the reason because the higher flow momentum results in stronger barrier shocks.

The flow fields observed for both perforated plates using the BOS method are illustrated in Figure 5.4. The pressure ratio from the cavity plenum to total pressure p_{pl}/p_t is similar to those from the simulations shown in Fig. 5.3. The Mach angle for $M = 1.62$ is pinpointed on the left side to identify Mach waves. Both the expansion fan at the beginning of the plate and the trailing shock at the end are visible. Moreover, as the displacement d , which is the deviation of the light rays in pixels, is the highest close to the wall where the density gradient is the maximum, the thinning of the boundary layer is perceptible. Downstream of the bleed region, the boundary layer is significantly fuller and smaller in both cases.

On the perforated plate, the effect of the hole flow is apparent. Especially for plate HR with $D = 2.0$ mm holes, the effect on the flow inside the boundary layer is observed as expansion and compression waves are evident. Since the perforated plate is mounted on the floor, an overlapping of the pocket and the plate closes the holes located at the first 10 mm of the plate. Thus, no suction is present in this region, but the hole contour creates roughness. Also, a Mach wave caused by the junction from the floor to the perforated plate is present. The holes downstream of the bleed region are closed with plaster, which induces further Mach waves that do not affect the flow so that the measurement of the boundary-layer profiles in this region is

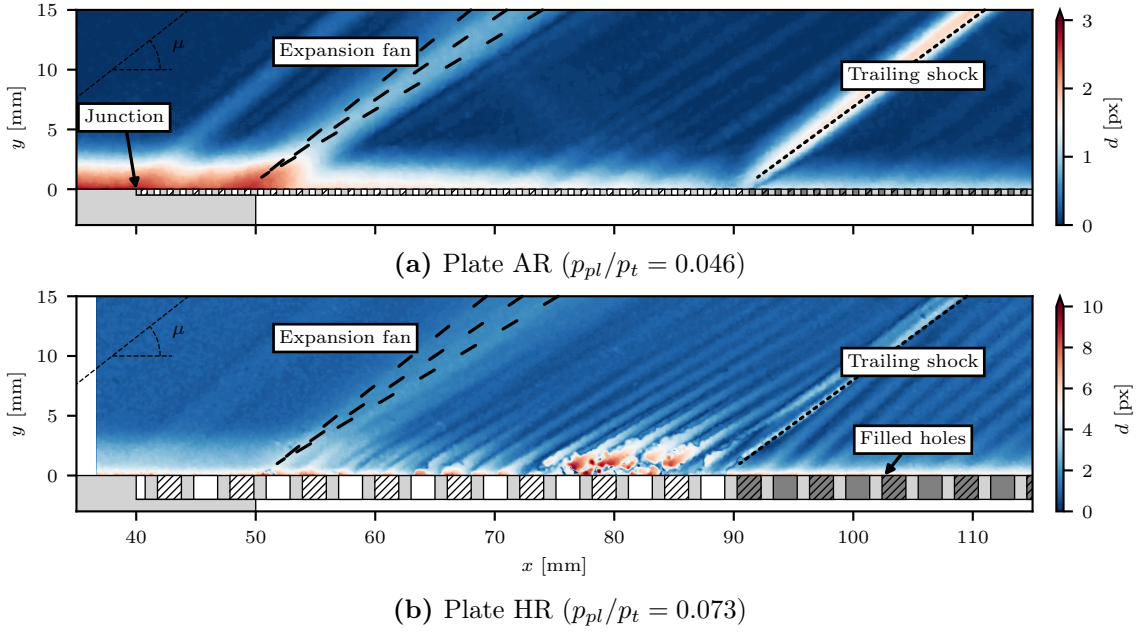


Figure 5.4: BOS visualization of the flow around the perforated plate.

feasible. The appearance of these Mach waves is more prominent for the larger holes as the filled area is increased.

Altogether, the same flow topology is found in both experiments (Figure 5.4) and simulations (Figure 5.3). However, expansion fans and shock waves are more smeared using the BOS visualization compared to the simulations. Contrary to a Schlieren visualization, no mirrors are used to obtain parallel light rays passing the wind tunnel. Thus, the view is only aligned with the spanwise coordinate in the center of the image. Consequently, the deflection is higher in the center at $x \approx 80$ mm, resulting in occasional bad correlations, as visible in Figure 5.4b.

For a more quantitative comparison, the whole flow field measured by means of LDV is shown against the numerical results in Figure 5.5 in streamwise (Figure 5.5a) and wall-normal direction (Figure 5.5b). Both velocity components are normalized by the free-stream velocity to eliminate temperature variations that occurred between the different runs in the experiments.

A look at Figure 5.5a illustrates a good fit of the streamwise component of the flow for both hole diameters. The effect of the bleed on the boundary layer is well modeled in the simulations for both plates. In the case of the small holes, the LDV measurements are not able to reliably resolve the local flow phenomena around the holes, which is caused by the size of the measurement volume in the spanwise direction of approximately one hole diameter. On the contrary, the flow field is in the simulations directly extracted on the symmetry plane. Moreover, a Mach wave induced by the junction of the plates at $x = 40$ mm is apparent in the experimental data, leading to a slight thickening of the boundary layer. In contrast, no Mach wave is found in the LDV data for the larger holes, where the inflow is more homogeneous compared to the measurements for the $D = 0.5$ mm plate. Moreover, the expansion fans and barrier shocks induced by the bleed holes are resolved since the hole diameter is in this case significantly larger than the measurement volume, and the phenomena are more pronounced.

Also, the wall-normal velocity component is well reproduced by the RANS simulations, as shown in Figure 5.5b. A relatively low deflection of the flow towards the wall is found for the small holes compared to the large holes, caused by the lower porosity level. Moreover, the flow field is more homogeneous for the small hole diameters. In contrast, penetration of the expansion fans and barrier shocks even on the flow outside the boundary layer is notable. This effect is visible in the experimental data for the $D = 2.0$ mm holes. In comparison, the flow

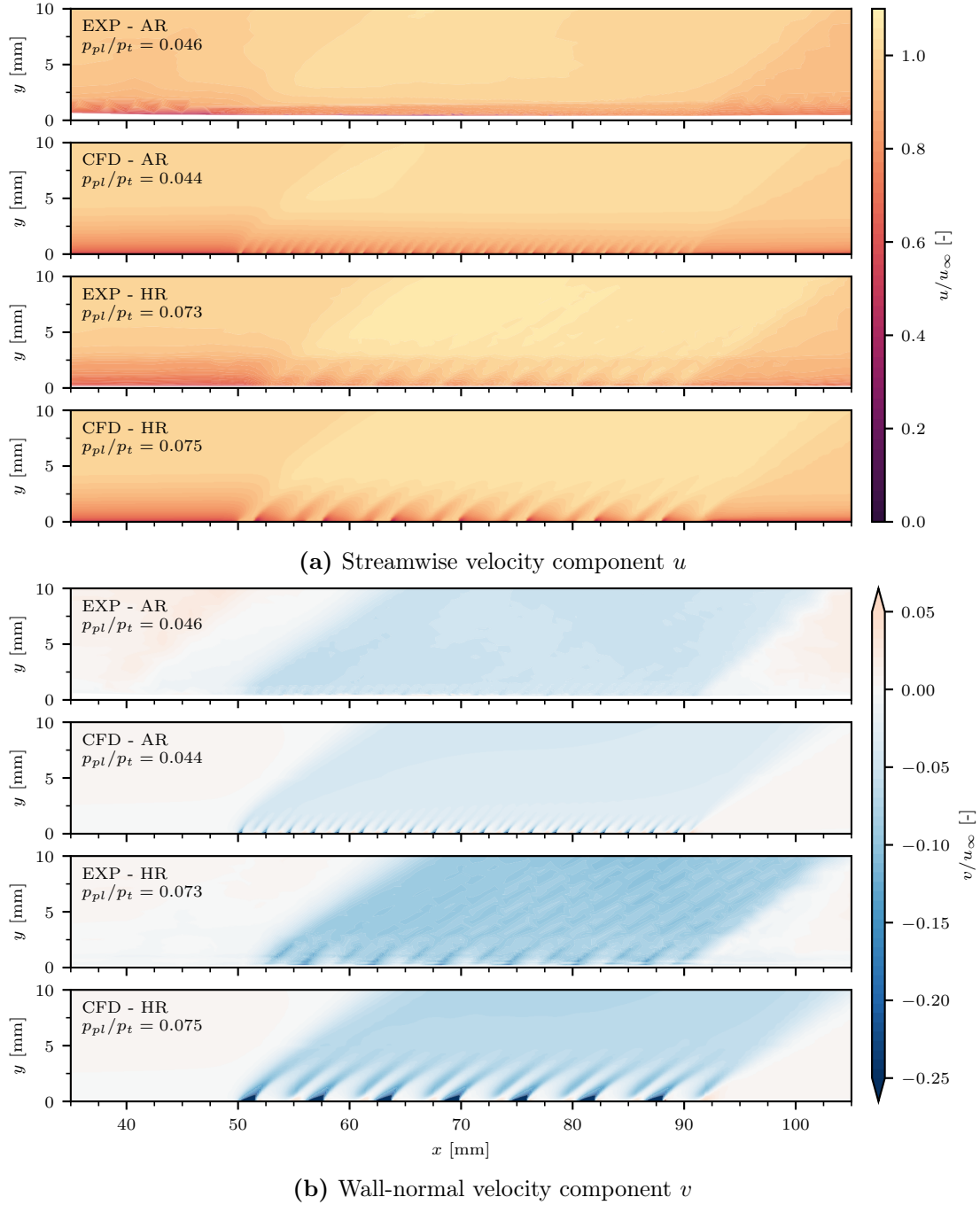


Figure 5.5: Comparison of flow field from LDV measurements and simulations.

field acquired from the simulations looks more homogeneous.

The wall pressure along the bleed region is presented in Figure 5.6. On the top, the numerically extracted pressure contour on the wall is illustrated for the first bleed holes with a diameter of $D = 0.5$ mm. The pressure field surrounding the hole looks similar to the fields acquired by Bodner et al. [12] (see Figure 1.28), even though the Mach number is here lower. The suction effect is evident: near the front of the holes, the pressure decreases because of the presence of an expansion fan. Further downstream, the so-called barrier shock inside the hole leads to an adverse pressure gradient resulting in a significantly higher wall pressure downstream of the hole. On the bottom, the high-porosity plate HR is shown, illustrating the same phenomena. However, the wall pressure below the holes is significantly lower, which is a result of the lower relative distance between the holes, and the consequently more effective flow control.

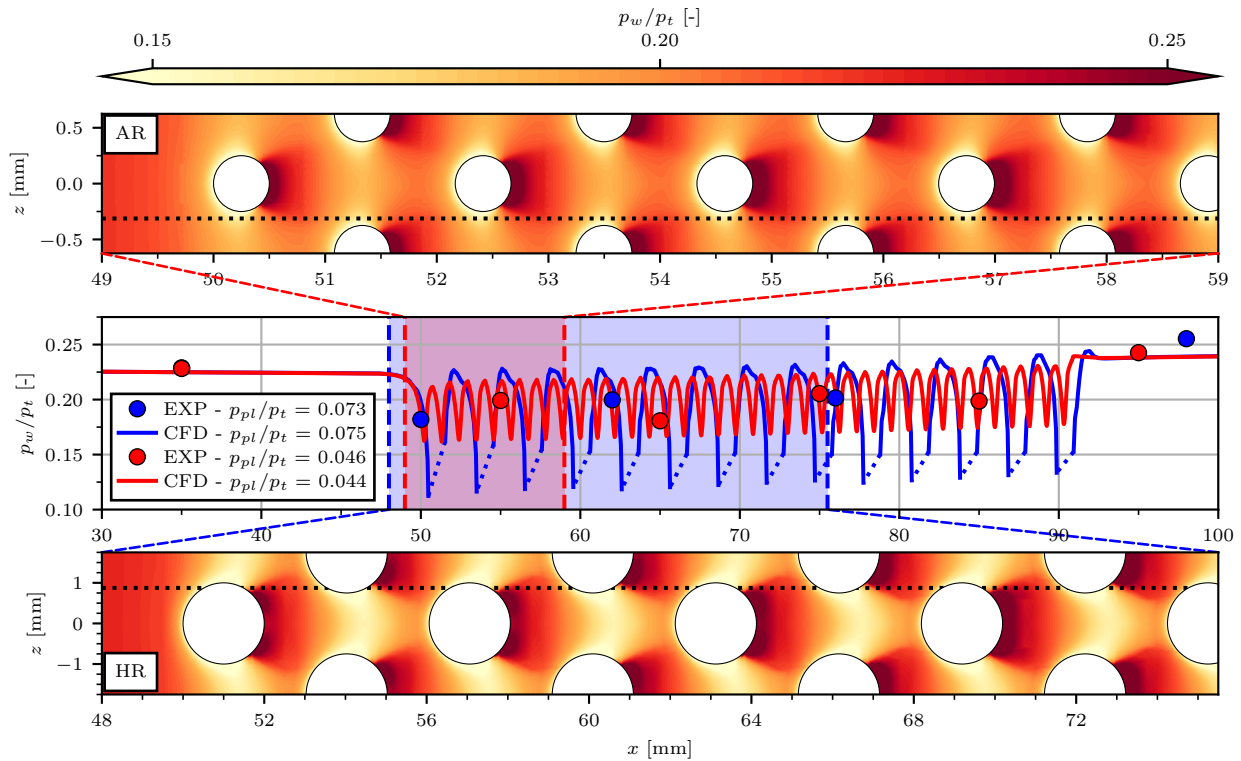


Figure 5.6: Wall pressure distributions along the bleed region for the two plates; contours at top and bottom from CFD.

For a comparison with the experiment, the wall pressure is extracted on a line between two hole columns (dotted line), where the wall is fully solid for the plate with $D = 0.5$ mm holes, and largely fully for the second plate. The plot in the center details the trend of the wall pressure along these lines. At the beginning of the plate, where an expansion fan is located, the wall pressure drops. Along the perforated plate, the pressure fluctuates caused by the flow phenomena induced by the bleed holes. These fluctuations are more prominent for the plate with the large holes. However, positive slopes along the plates are notable due to the compression along the perforated plates. Since the boundary-layer thinning is not linear but stronger at the beginning of the plate, the flow is continuously deflected towards the wall-normal direction. At the end of the bleed region, the pressure increases because of the trailing shock, resulting in a slightly increased wall pressure downstream of the plate compared to the upstream pressure.

In the experiments, the wall pressure is measured at discrete locations around and in the bleed region, as illustrated by the points. Upstream and downstream of the bleed region, the measured wall pressure is slightly higher, which may be caused by the three-dimensionality of the flow inside the wind tunnel. However, the deviation equals upstream and downstream, which proves the same behavior of the bleed system. Along the plate, the measured pressure is within the range of the pressure fluctuations. The non-steady trend of the experiments results from the diameter of the pressure taps and their positions with respect to the bleed holes. As the diameter is of the same order of magnitude as the smaller bleed hole diameter, the pressure is averaged above a relatively large area. Depending on the position, the acquired pressure is mainly affected by the expansion fan or barrier shock and thus lower or higher.

Overall, the numerically and experimentally observed flow fields are similar. The same flow topology is apparent, and the flow is not strongly affected by any geometrical differences.

5.2.1.2 Boundary-Layer Profiles at the Wind Tunnel Center

In the following, the boundary-layer profiles are compared. Figure 5.7 schematically visualizes the location of the observed profiles. The profiles are measured 15 mm upstream and downstream of the plate in both simulations and experiments. Upstream of the plate, this distance is chosen as the position is unaffected by the junction from the floor to the perforated plate and the non-suction holes. Moreover, the upstream influence of the porous bleed is numerically found to be below 5 mm, which results in similar boundary-layer profiles independent of the bleed rate.

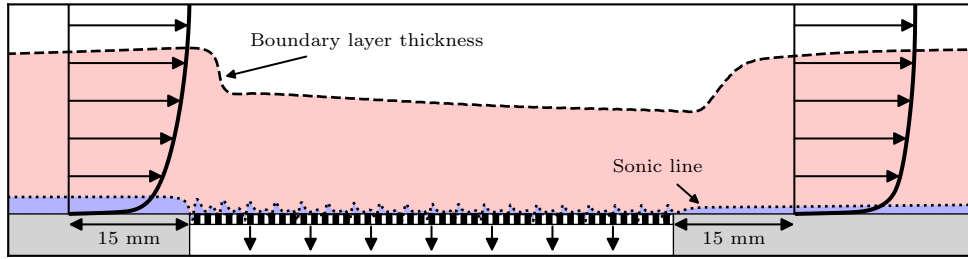
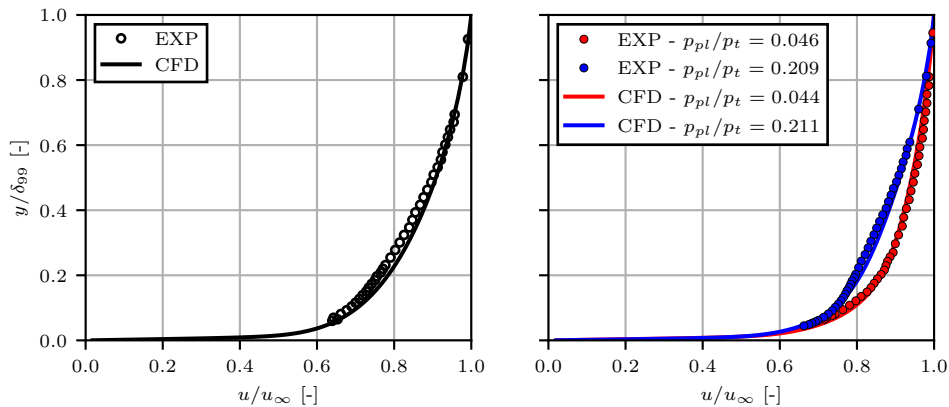


Figure 5.7: Illustration of the effect of the porous bleed system on the boundary layer based on numerical results.

As described in Section 5.2.1.1, a trailing shock is caused by a deflection of the flow at the end of the porous bleed. Consequently, the boundary layer downstream of the bleed region is disturbed by the shock. With the aim to achieve undisturbed profiles, a distance of 15 mm, equal to the upstream profiles, is selected to assess the effect of bleed on the downstream boundary-layer profile. A view in Figure 5.7 reveals that the boundary-layer thickness is almost identical downstream of the trailing shock compared to the inflow profile. However, the sonic line height is significantly lower, resulting in a fuller boundary layer.



(a) 15 mm upstream of the bleed region (b) 15 mm downstream of the bleed region

Figure 5.8: Comparison of boundary-layer profiles for low-porosity plate AR from experiments and simulations.

Figure 5.8 compares the velocity profiles extracted from the simulation and the measured profiles using LDV. The simulation fits very well with the experimental measurements. The boundary-layer thickness $\delta_{99} = 4.3 \text{ mm}$ is equal in both experiments and simulations, even though the stagnation flow conditions are slightly different (see Table 3.1).

The boundary-layer profile upstream of the bleed region (Figure 5.8a) extracted from the simulations is slightly fuller than the extracted profile from the experiments. This is probably

caused by the higher wall roughness in the experimental setup due to manufacturing imperfection compared to the perfectly smooth numerical simulations. However, the differences are negligibly minor.

With the aim of validating the simulations for different working conditions of the porous bleed, the boundary-layer profiles downstream of the bleed region are measured for several bleed rates. Comparison is made with the simulation for the same pressure in the cavity plenum. As the flow at the center plane is assumed to be two-dimensional, the ratio of plenum pressure to total pressure is more suitable than using the bleed rate, which may be affected by the three-dimensionality of the flow inside the wind tunnel close to the sidewalls. The pressure is expected to be more uniform than the bleed mass flux.

The comparison of the simulations and the experiments downstream of the bleed region is detailed in Figure 5.8b for the lowest and the highest bleed rates. For the lowest bleed rate, the plenum pressure is slightly lower than the wall pressure inside the test section ($p_w/p_t \approx 0.226$). Both experiments and simulations show the same trend again. However, the simulations predict a slightly fuller profile which is an artifact of the fuller inflow profile. Remarkably, the boundary-layer thickness $\delta_{99} = 4.8$ mm is thicker than upstream of the bleed region, which is caused by the trailing shock.

For the highest bleed rate, the holes are choked, as shown by the simulations in Figure 5.3. The boundary-layer profiles obtained from simulations and experiments show an almost perfect fit in this case. The boundary layer is significantly fuller than in the case of a low bleed rate. Also, the boundary layer is thinner than the upstream profile with $\delta_{99} = 3.7$ mm.

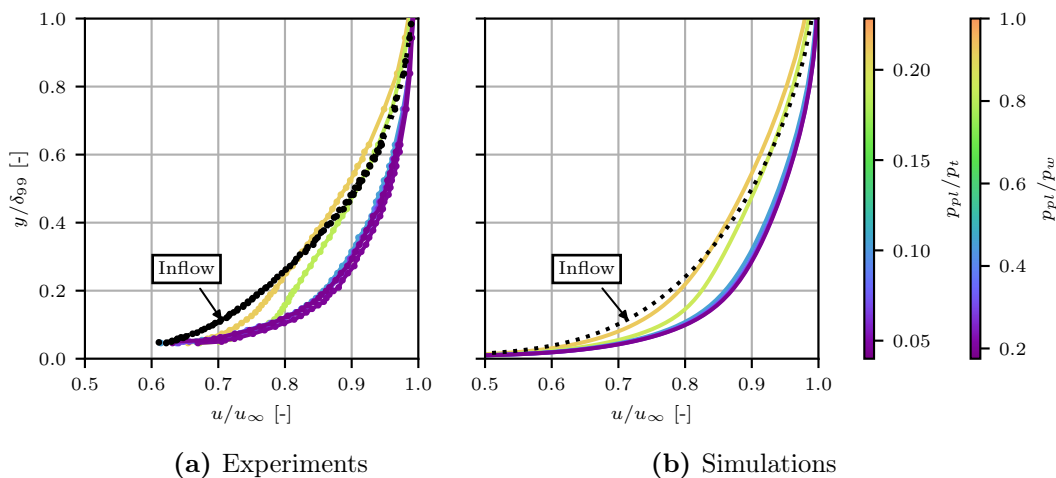


Figure 5.9: Boundary-layer profiles 15 mm downstream of the bleed region for low-porosity plate AR.

All experimentally acquired boundary-layer profiles are compared in Figure 5.9a for the $D = 0.5$ mm plate. Wall-normal coordinate and streamwise velocities are normalized with the inflow boundary-layer thickness and free-stream velocity. The significant influence of the cavity plenum pressure is apparent: The lower the plenum pressure, the higher the bleed rate and the fuller the boundary-layer profile. A significantly fuller boundary layer is already found for the lowest bleed rate. However, the suction mainly affects the lower part of the boundary layer, while the velocity is lower with further wall distance compared to the inflow.

A further increase in the bleed rate leads to an even fuller boundary-layer profile. Again, the major difference is found in the near-wall region, while the outer boundary layer is mainly unaffected. For more significant bleed rates, the whole boundary layer is fuller. From a pressure ratio $p_{pt}/p_t \approx 0.1$, the profiles converge, which means that the maximum effect is achieved, and a lower pressure inside the cavity plenum does not lead to fuller profiles. This results from choking the flow inside the holes, which limits the bleed rate.

The same trends are found in the numerical simulations, as shown in Figure 5.9b. Low bleed rates mainly affect the near-wall region, while the outer boundary layer is unaffected, and natural boundary-layer growth is found. Lower pressure ratios increase the control effectiveness of the porous bleed system until choking is achieved, which limits the bleed effect. Moreover, a certain amount of bleed is required to sustain the inflow conditions and to prevent natural boundary-layer growth, which is additionally increased by the induced roughness due to the perforated plate geometry.

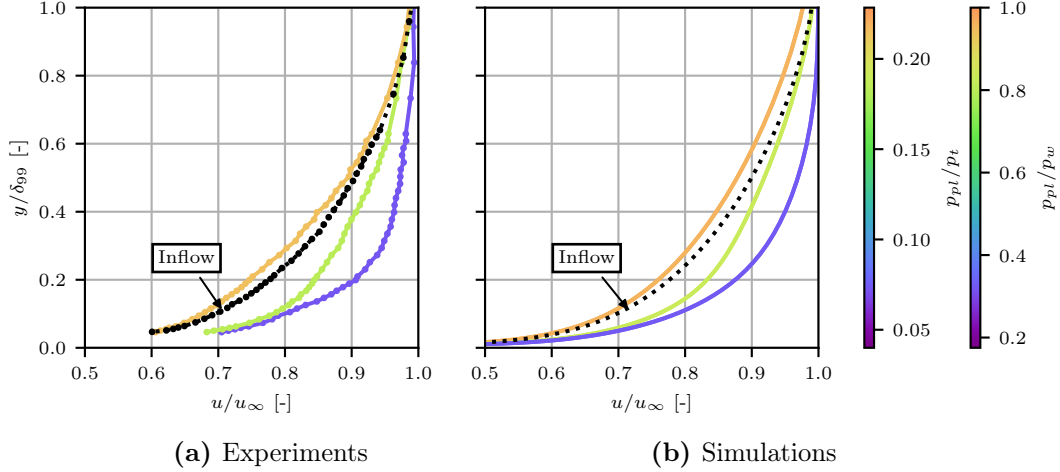


Figure 5.10: Boundary-layer profiles 15 mm downstream of the bleed region for high-porosity plate HR.

The same comparison is found for the plate with the $D = 2.0$ mm holes in Figure 5.10. On the left side (Figure 5.10a), the experimentally acquired profiles are shown for three different bleed rates. In the case of the lowest bleed rate, corresponding to the highest pressure ratio, a degradation of the boundary layer with respect to the inflow is found. Thus, the bleed rate is not enough to prevent boundary-layer growth. For higher mass removals, the boundary-layer profiles are significantly fuller. Again, the positive effect on the boundary layer first appears in the near-wall region and is found for higher mass flow rates also with further distance to the wall.

RANS simulations of the same plate validate the experimental findings, as shown in Figure 5.10b. In comparison to the first plate, we see a more significant reduction in the boundary-layer thickness, which is a result of the higher control effectiveness caused by the higher porosity level.

5.2.1.3 Three-Dimensionality of the Flow

The three-dimensionality of the flow field has already been described in previous numerical [60, 118] and experimental [77] studies. However, experiments showing the impact of the hole geometry on the boundary layer along the span are found to a limited extent. Particularly large hole diameters may lead to inhomogeneous flow fields since the inter-hole distance is large, and a high-momentum captured flow results in strong compressible effects. For the investigation of three-dimensional effects, we focus on plate HR with $D = 2.0$ mm holes as the flow field for small holes is too homogeneous and in the range of the measurement uncertainties. Moreover, the smaller amount of bleed holes in the case of large diameters makes simulations of the wind tunnel half-span feasible in terms of the required mesh size.

Figure 5.11 illustrates the flow inside the wind tunnel off the center plane. Effects of the corner flow, but also variations of the flow field along the span downstream of the bleed region

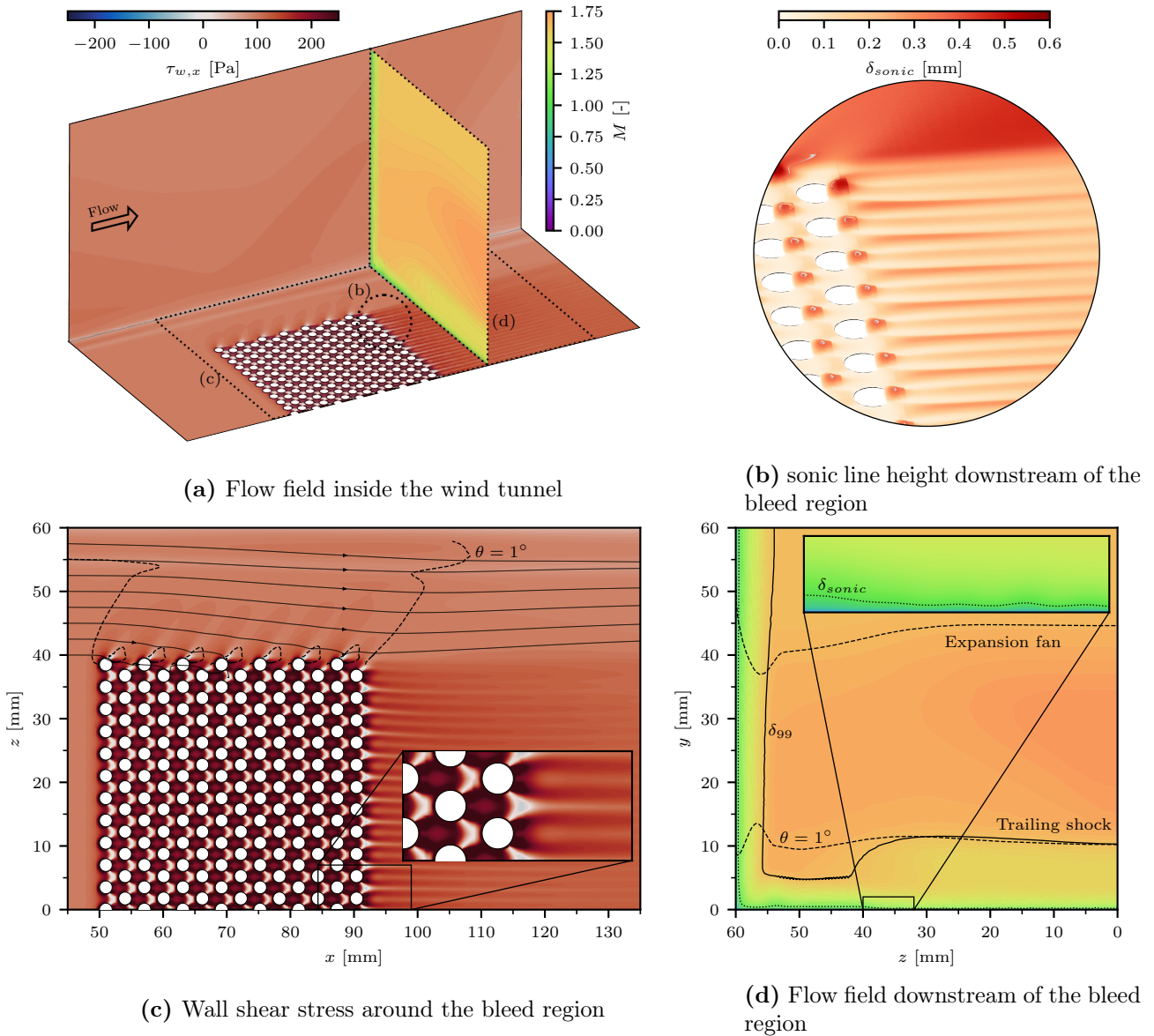


Figure 5.11: Flow topology inside the wind tunnel for supersonic boundary-layer bleed from simulation ($p_{pl}/p_t = 0.073$).

are significant. A general overview of the flow field is given in Figure 5.11a, visualizing the wall shear stress on the bottom and sidewall of the wind tunnel, as well as a slice showing the flow field at a cross-section downstream of the bleed region, corresponding to the distance where the velocity profiles are extracted. Since the porous bleed covers only two-thirds of the span, the seemingly low impact on the corner flow is visible. Moreover, downstream of the bleed region, streaks of higher and lower wall shear stress are present.

A closer look at the last row of holes and the region downstream can be seen in Figure 5.11b. Around the holes, the sonic line height is extracted as a characteristic measure of the boundary-layer health. With regard to (strong) SBLIs, the sonic line height can be directly linked to the interaction length and is therefore of major importance [4]. As seen in the figure, the sonic line height varies significantly along the span. Downstream of the holes, a drastic increase is noted as the barrier shock induces a strong adverse pressure gradient. Also, a second streak of large sonic line heights between the holes is found. Moreover, a low spanwise influence of the porous bleed on the corner flow is apparent. The flow close to the sidewalls seems to be unaffected as

the sonic line height is not reduced.

A better view of the control effect on the corner flow is shown in Figure 5.11c. As already stated before, the boundary-layer suction generates an expansion as the flow is redirected towards the wall. However, also flow from the side is captured, leading to the propagation of expansion waves in the spanwise direction. As a consequence, the flow is redirected from the sidewalls to the bleed, as highlighted by the streamlines. The isocontours of a deflection angle of $\theta = 1^\circ$ illustrate the location of the first expansion waves, but also the propagation of the trailing shock further downstream at the plate end. Consequently, the application of the porous bleed on only two-thirds of the wind tunnel span leads to an increase in the size of the corner flow, which may result in a need for further flow control in these regions [113]. Since the flow momentum decreases inside the corner, the flow is more vulnerable to separate if adverse pressure gradients are present.

Moreover, the footprints of the varying boundary-layer profiles along the span are found in the wall shear stress. The same streaks as for the sonic line height are found. Directly downstream of the holes, as well as between the holes, the wall shear stress is significantly lower. The pattern of the footprint of the wall shear stress fits also very well the pattern found in the oil-flow visualization of Oorebeek and Babinsky [75] for a similar plate geometry but for a higher Mach number of $M = 2.5$ (see Figure 1.29).

The flow in the cross-section of the wind tunnel is shown in Figure 5.11d. Here again, the propagation of the expansion fan in the spanwise direction is notable, leading to an increase in the Mach number, as well as the propagation of the trailing shock. Moreover, the sonic line as well as the boundary-layer thickness, based on the 99% of the free-stream velocity at the inflow, are plotted as characteristic measures to evaluate the boundary-layer health. The trend of the boundary-layer thickness reveals apparently a thickening of the boundary layer. However, this is caused by a decrease in the Mach number as a result of the losses due to several barrier shocks and the trailing shock. Consequently, the flow momentum outside of the boundary layer is smaller. In contrast, the sonic line height is reduced compared to the flow at the sidewalls, as visible in the zoom-in view. As a result, the porous bleed achieved the aim of increasing the flow momentum inside the boundary layer.

For the validation of the numerical findings, LDV measurements are performed at a horizontal plane with a distance of $y/D = 0.25$, similar to those of Oorebeek et al. [77] (see Figure 1.27). At the same height, the velocity components in streamwise and wall-normal directions are extracted. Figure 5.12 shows both the numerical and experimental results. Since the measurements are acquired aside from the center plane ($z = 10$ mm), the velocity components are compared to the full simulation including the sidewalls. Again, a bending of the streamlines towards the wind tunnel center is found in Figure 5.12a and 5.12b, even downstream of the bleed region.

For the comparison with the experiments, we focus on the area between three columns of holes while the center column is staggered. The observed plane is acquired off the center plane. Figure 5.12c shows the comparison of simulations and experiments for the streamwise velocity components, which reveal the same flow characteristics. The holes induce expansion waves, leading to an increase in the flow velocity before passing the barrier shocks. Downstream of the last holes, the streaks are noted, as well as their bending towards the wind tunnel center. In contrast to the simulations, the measured velocity differences are smaller, which is a consequence of the lower resolution of the measurements caused by the size of the measurement volume and the smaller amount of points. Consequently, the results are more smeared because of larger averaging areas. Please note, that the length of the perforated plate differs slightly between experiments and simulations as the staggered column has one hole less in the experiments.

Also, the measurements in the wall-normal direction fit well with the simulations (see Fig-

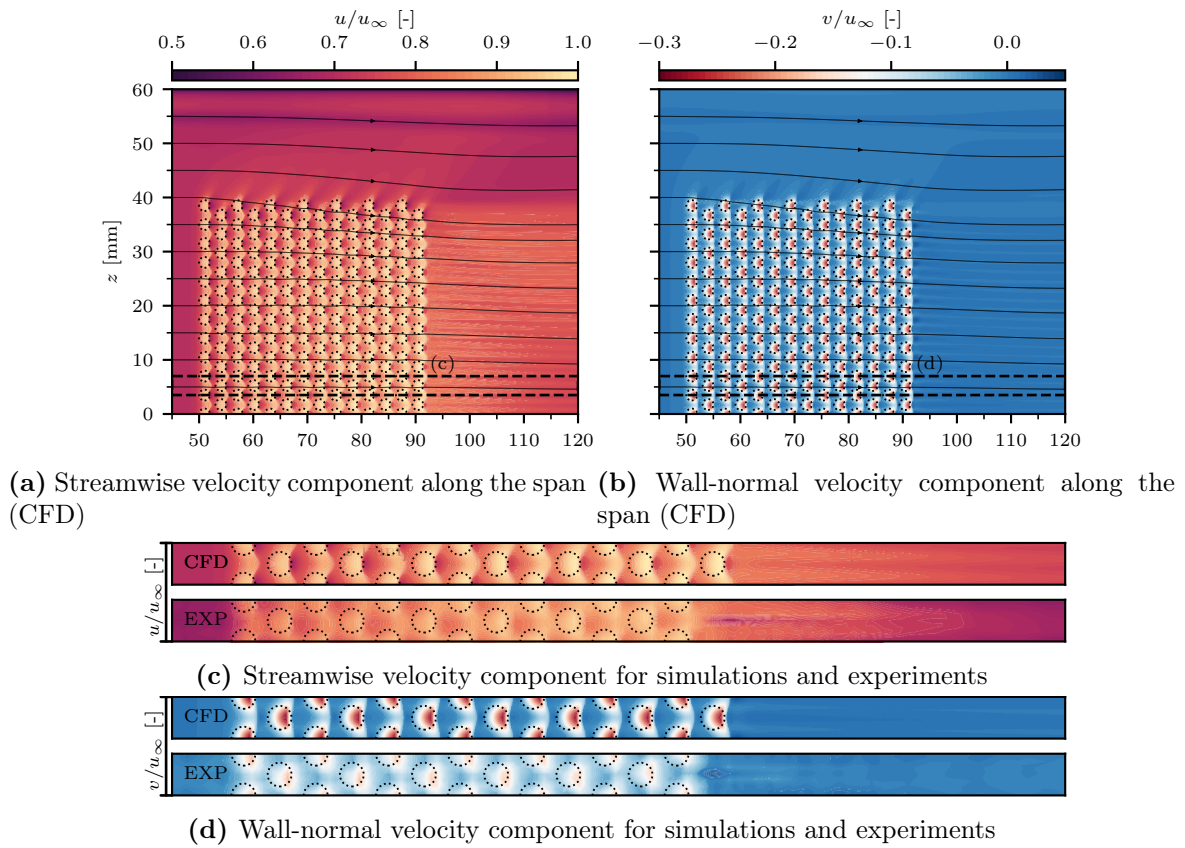


Figure 5.12: Velocity contours at a wall-normal distance of $y/D = 0.25$ ($y/\delta_{99} \approx 0.12$) for experiments ($p_{pl}/p_t = 0.072$) and simulations ($p_{pl}/p_t = 0.073$); plots in (c) and (d) show zoom-view to area highlights by dashed lines.

ure 5.12d). As stated before, the streaks are less characteristic than for the streamwise velocity components. Again, the experimentally measured variations are smaller than in the simulations because of the lower resolution.

For a more detailed validation, multiple boundary-layer profiles at different spanwise positions are acquired numerically and experimentally, and shown in Figure 5.13. Figure 5.13b visualizes the envelopes of profiles dependent on the pressure ratio. A significant difference

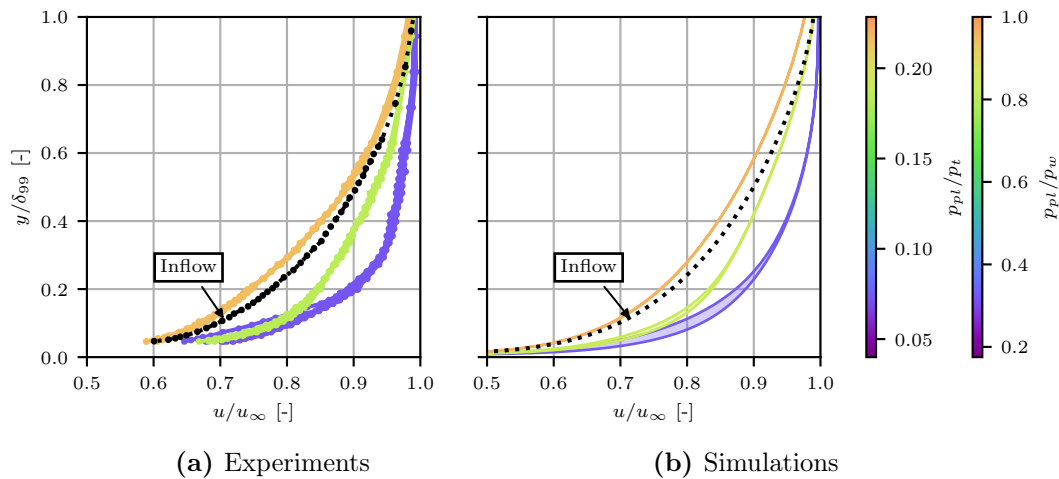


Figure 5.13: Variations in the boundary-layer profiles 15 mm downstream of the bleed region along the span.

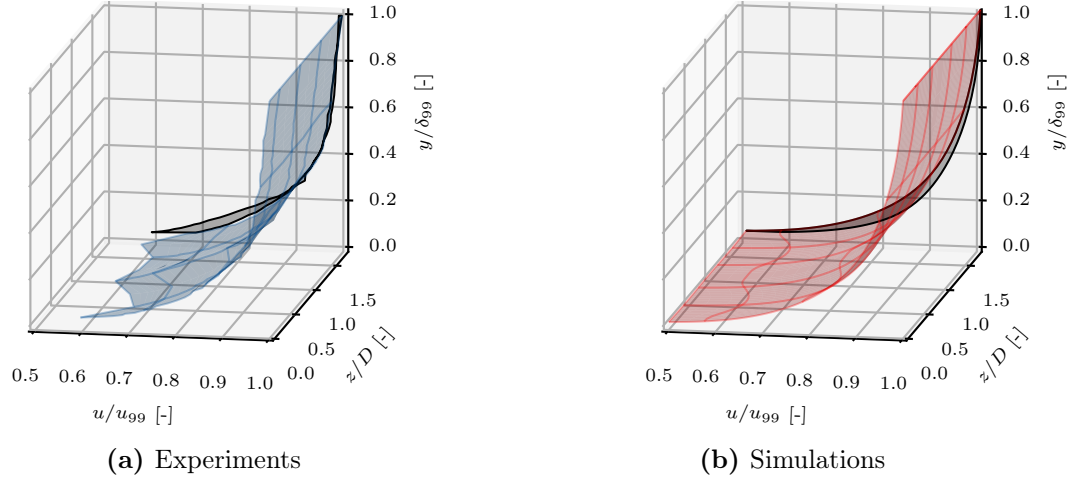


Figure 5.14: Illustration of the velocity profiles along the span for experiments ($p_{pl}/p_t = 0.072$) and simulations ($p_{pl}/p_t = 0.073$).

between high and low pressure ratios is apparent. For high pressure ratios, which correspond to low bleed rates, the profiles are found to be homogeneous in the simulations. The hole geometry does not cause any three-dimensional disturbances. With lower plenum pressures, the bleed rate increases, as well as the variability in the boundary-layer profiles along the span, which is mainly found in the lower 20% of the boundary layer. Further increase of the bleed rate by lowering the plenum pressure enhances the variability as the strength of the barrier shocks and expansion fans induced by the holes increase.

The experiments mirror the same trend, as visible in Figure 5.13a. For the highest pressure ratio, the measurements at three different spanwise positions vary only marginally. For a lower pressure ratio, the variation is found to be larger between the three positions. For the lowest pressure ratio, the measurements are conducted at eight different positions, showing the largest variability. All these measurements are shown in comparison to the simulations in Figure 5.14, showing a periodic variation in the boundary-layer profiles caused by the periodic pattern of the holes.

5.2.2 Subsonic Boundary-Layer Bleed

After investigating supersonic boundary-layer bleed, we focus on subsonic flows since we found them downstream of normal SBLIs. Therefore, experiments are conducted in the same test section using the convergent-divergent nozzle in an entirely subsonic regime, resulting in a free-stream Mach number of $M = 0.5$. The subsonic experiments are limited to the $D = 0.5$ mm as simulations have shown no significant variations of the boundary-layer profiles along the span. Moreover, the lower porosity level results in a lower bleed rate, which facilitates keeping the inflow conditions constant. Since the subsonic bleed influences the flow in the upstream direction, high bleed rates may result in fuller inflow profiles or an increase in the external Mach number.

The flow topology around a subsonic bleed is illustrated in Figure 5.15. Like a supersonic bleed, the flow is redirected towards the wall, creating a diverging stream tube. Contrary to supersonic flows, the result is not an acceleration but a deceleration of the outer flow, as highlighted by the contour lines for the Mach number $M = 0.45$ and $M = 0.5$. Since the observed case is an internal flow, the diffuser effect is even more pronounced as the stream tube is limited in size. However, simulations without a top wall limiting the domain have shown similar results. Also, a strong upstream influence is noted contrary to the supersonic

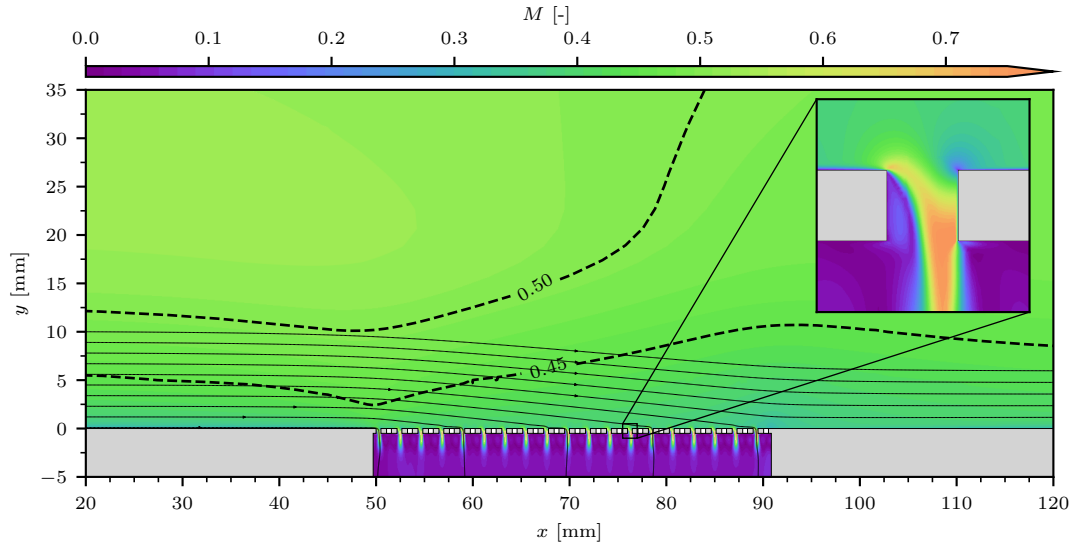


Figure 5.15: Mach contour field for plate HR ($p_{pl}/p_t = 0.651$); white areas illustrate holes of the second column.

bleed, resulting in an acceleration of the flow upstream of the bleed. The zoom-in view gives an impression of the flow topology inside the holes. In this case, the flow is fully subsonic. In comparison to Figure 5.3a, the separated area in the front of the hole is smaller. Since no barrier shock exists, the losses are smaller compared to the supersonic case, and the control effectiveness of the bleed in increasing the flow momentum in the wall vicinity is assumed to be higher.

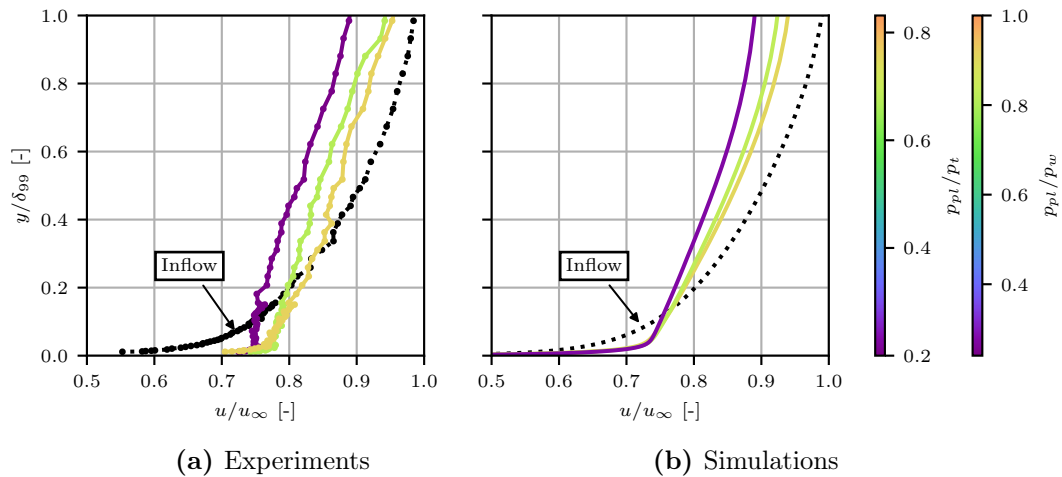


Figure 5.16: Boundary-layer profiles 15 mm downstream of the bleed region for subsonic conditions.

In the next step, we focus on the effect of the porous bleed on the boundary-layer profiles. Figure 5.16 shows the state of the boundary layer upstream and downstream of the porous bleed acquired from the experiments and the simulations. Again, the profiles are normalized by the inflow boundary-layer thickness and the free-stream velocity. The simulations (see Figure 5.16b) demonstrate the effect of the bleed. Even low bleed rates lead to an increase in the momentum in the lower 20% of the boundary layer. Lowering the pressure ratio, and in turn, the bleed rate, results in a saturation of the effect. Below a pressure ratio of $p_{pl}/p_t \approx 0.7$, the maximum achievable improvement is achieved. On the contrary, there is still a change in the effect on the outer boundary layer notable. A further decrease in the pressure ratio increases the bleed rate and consequently reduces the external flow velocity as more mass is removed, and the bleed

generates a larger divergent stream tube.

The experimentally measured boundary-layer profiles are illustrated in Figure 5.16a. The findings are similar to the simulations, even though the velocity in the vicinity of the wall is found to be smaller for low pressure ratios. This deviation is assumed to be a consequence of the experimental methodology. As the bleed has an upstream influence, high bleed rates lead to higher inflow mass flow rates. Moreover, the inflow profile becomes asymmetric, meaning the free-stream velocity is higher in the lower part of the wind tunnel where the suction occurs compared to the upper, uncontrolled flow. The missing momentum in the upper part increases the diffuser effect, and thus, even the velocity in the boundary layer is found to be smaller. However, the inflow profiles measured upstream of the bleed region are equal independently of the bleed rate. In contrast, the numerical inlet is defined to be constant outside the boundary layer. Thus, the overall mass flowing through the test section might be higher as the momentum in the upper part is larger.

5.2.3 Shock-Wave/Boundary-Layer Interaction Control

In the next step, the control of an SBLI is experimentally and numerically investigated. A shock generator is mounted with a wedge angle of $\alpha = 9.5^\circ$ in the test section, as visible in Figure 3.1.

5.2.3.1 General Flow Field

Simulations are conducted on the center segment with symmetry planes on the front and back of the domain, as well as three-dimensionally by simulating the wind tunnel half-span with the high-porosity plate HR, as introduced in Section 2.1.1. In the numerical domain with symmetry boundary conditions, the wedge angle has to be increased by approximately 1° to obtain the same location of the incident shock as the three-dimensionality of the flow induced by the corner flow leads to a more intense shock.

The flow field around the incident shock is illustrated in Figure 5.17 for the simulations of the center segment. In the top (Figure 5.17a), the uncontrolled case is shown. The deflection angle of the incident shock is too high for a regular reflection of the shock, leading to a so-called Mach reflection. Thus, a normal shock (Mach stem) is found in the vicinity of the wall. The adverse pressure gradient of the shock is sufficiently high to make the flow separate, resulting in a separation bubble with its length being approximately two-thirds of the bleed length ($\sim 6\delta$).

The successfully controlled interaction is shown in Figure 5.17b, demonstrating the effect of the porous bleed. The flow separation is significantly mitigated, resulting in the elimination of the lambda shock foot and a downstream movement of the shock foot. Since the porous bleed induces a bending of the flow towards the wall, the deflection angle along the shock, and hence the shock intensity decreases. Especially downstream of the incident shock, a strong aspiration flow is generated, resulting in a seemingly regular shock reflection. However, a small Mach-stem is found and decelerates the flow to subsonic conditions in the wall vicinity.

The zoom-in views visualize the flow topology inside the holes upstream and downstream of the shock. On the right side, the flow topology is identical to the bleed in the purely supersonic case. The expansion fan at the hole front and the barrier shock are notable. In this area, the momentum in the boundary layer is increased to decrease the upstream influence of the adverse pressure gradient. In contrast, the flow inside the holes downstream of the shock is identical to a subsonic porous bleed. The flow around the hole is purely subsonic and accelerated to supersonic conditions at the hole inlet because of the low pressure ratio. The separated region in the front of the hole is found to be significantly smaller than upstream of the shock, resulting in higher bleed rates. The presence of different flow topologies upstream and downstream of

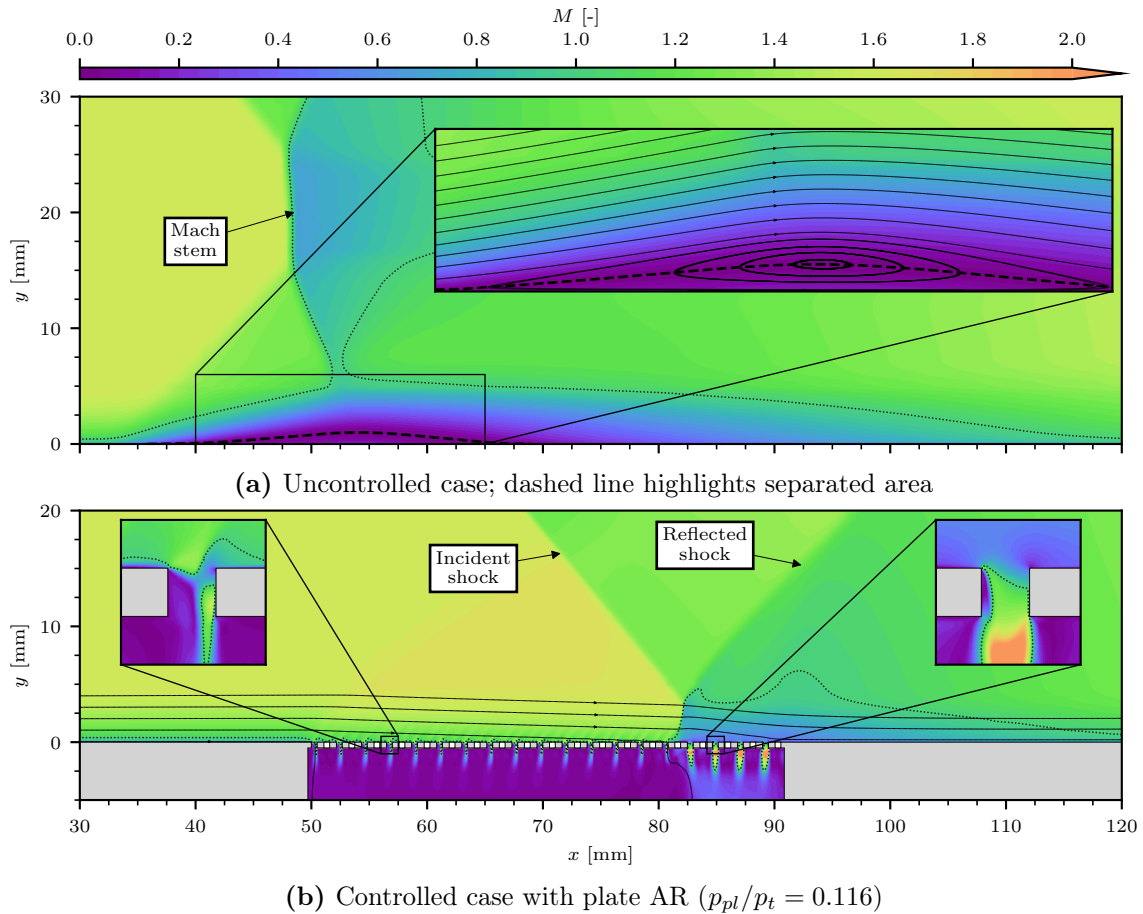


Figure 5.17: CFD Mach contours for SBLI in controlled and uncontrolled case; dotted lines highlight sonic line.

the incident shock is essential for the derivation of an adequate porous bleed model since both super- and subsonic regimes need to be considered to predict the effect of the porous bleed on the SBLI.

The trend of the wall pressure is shown for both plates in Figure 5.18. Again, the numerical pressure contour fields are visualized at the top and the bottom while the curves are compared to the acquired data from the pressure taps. For both plates, the pressure fields focus on the region around the shock foot to illustrate the pressure rise. A different location of the shock foot is apparent, which is caused by the different porosity levels, resulting in a higher bleed rate in the case of the high-porosity plate HR. In addition, the wall pressure distribution of the high-porosity plate HR is shown for the simulation of the wind tunnel half-span, which is discussed later. At the center, the curves along the bleed region are shown. Here again, the shock foot is found to be located further upstream for the low-porosity plate AR (red), as seen by the pressure rise around $x = 82$ mm. Further downstream, the pressure continues to increase steadily until the end of the bleed region, terminated by the trailing shock. The same trend is apparent for the high-porosity plate HR, with the difference of a further downstream located pressure rise. Moreover, the experimentally acquired pressure values fit very well with the simulations.

For the comparison of experiments and simulations, velocity profiles are acquired along the bleed region. As described in Section 5.2.1.3, the large size of the holes of the high-porosity plate HR results in strong variations of the boundary-layer profiles along the span. For this reason, LDV measurements have been only performed on the low-porosity plate AR to keep

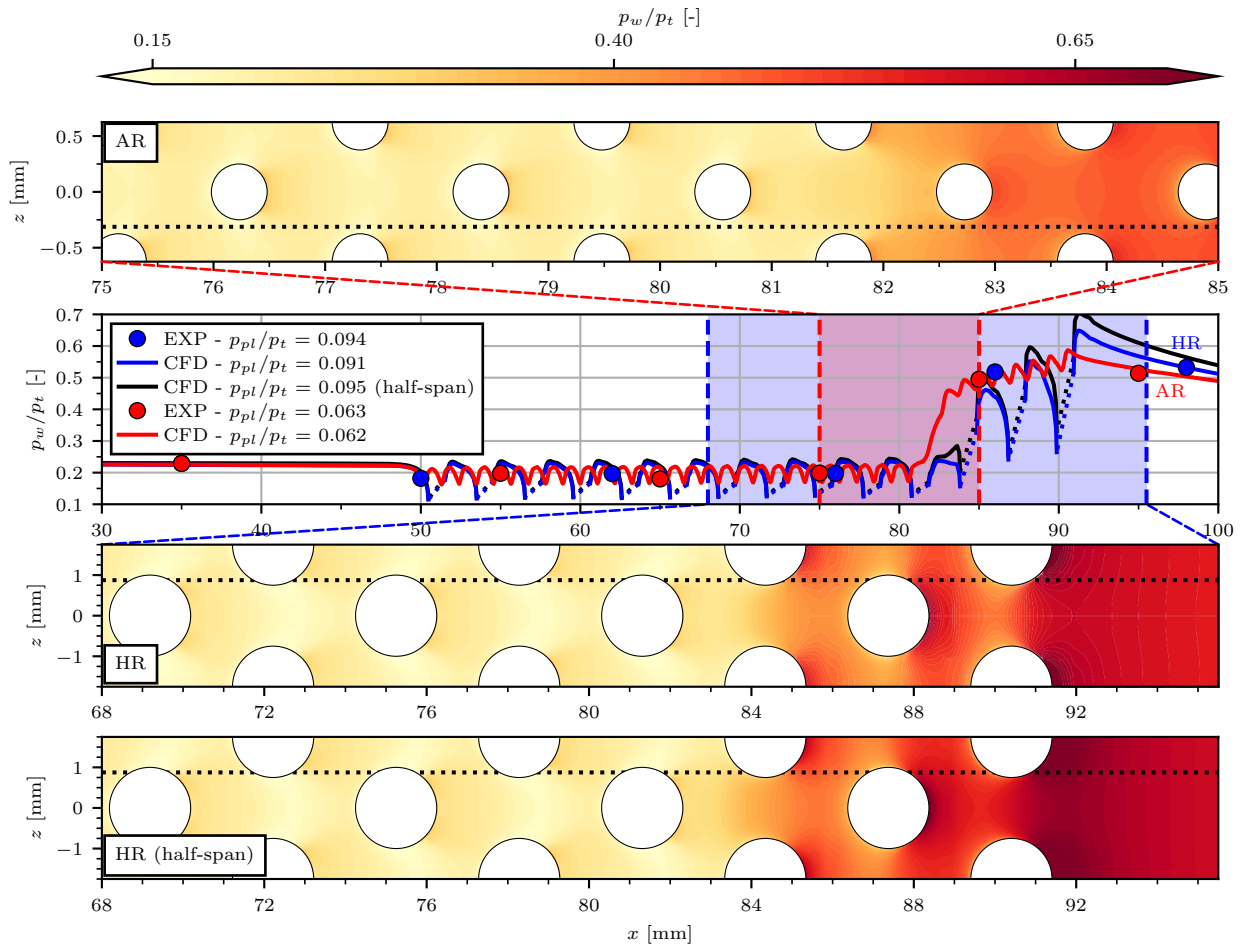


Figure 5.18: Wall pressure distributions along the bleed region for the two plates; contours at top and bottom from CFD; last row shows pressure contours from wind tunnel half-span simulations.

the number of required measurements low. All the measurements, as well as the numerically extracted profiles, are shown in Figure 5.19. At the top, the unscaled velocity profiles are illustrated to evaluate the conformity of the overall flow field for the simulations of the center segment and the experiments. In both cases, the incident shock has the same shock angle, as seen by the knee in the profiles in Figure 5.19a independent of the bleed rate. In contrast, the shock reflection is found to be affected by the porous bleed. The lower the pressure ratio and the higher the bleed rate, the further the downstream movement of the shock. Hence, the reflected shock is located closer to the wall for the further downstream positions. The zoom-in view demonstrates the effect of the bleed rate on the velocity profiles. The agreement between experiments and simulations is very good.

For the observation of the near-wall region inside the boundary layer, the profiles are scaled by the incoming boundary-layer thickness (see Figure 5.19b). The profiles upstream of the incident shock, which is located between $x = 80$ mm and 85 mm, show the increase of the momentum inside the boundary layer dependent on the bleed rate. The higher the bleed rate, the fuller the boundary-layer profile, as visible in the zoom-in view on the left. Please note that the knees in the numerical profiles are caused by the relative position to the bleed holes and the resulting passing of shocks and expansion waves. In the experiments, these effects are more smeared because of the size of the measurement volume.

Downstream of the shock, artifacts of the supersonic control are notable. The higher the momentum in the boundary layer upstream of the shock the higher the momentum downstream of the shock. However, a higher momentum downstream of the shock is expected to result in

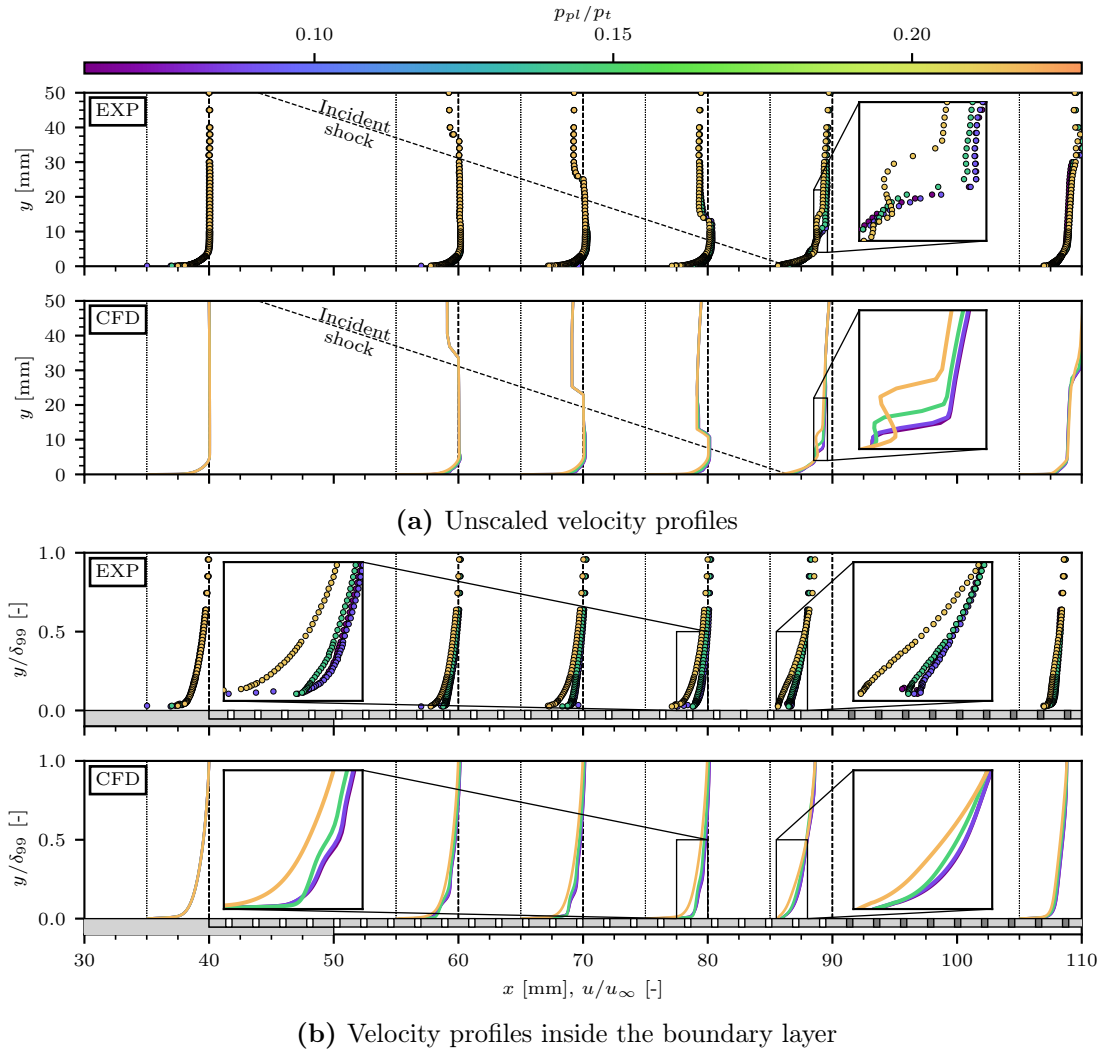


Figure 5.19: Velocity profiles along the bleed region for low-porosity plate AR.

a lower bleed efficiency as the flow separation inside the holes increases, and hence, the vena contracta area decreases. Since the adverse pressure gradient along the plate below the shock foot leads to lower pressure ratios p_{pl}/p_w , the relative difference between the cases becomes smaller, and the bleed works close to, or under choked conditions ($p_{pl}/p_w \leq 0.528$). Thus, a lower bleed efficiency results in lower bleed rates, and a lower increase of flow momentum near the wall. Consequently, the differences between the cases are found to be smaller than upstream of the shock, as illustrated in the zoom-in view on the right. Downstream of the bleed region, the variations in the boundary-layer profiles are even smaller compared to the differences upstream of the shock.

5.2.3.2 Three-Dimensionality of the Flow Field

In the last step, the wind tunnel half-span simulations are compared to the flow visualization for the high-porosity plate HR. Simulations with the low-porosity plate AR are not applicable since the mesh size is too large. On the contrary, LDV measurements of the boundary-layer profiles are too time-consuming for this case because of the spanwise variations.

Figure 5.20 gives an overview of the flow topology inside the wind tunnel. In Figure 5.20a, the wall shear stress as well as the flow field downstream of the bleed region are shown. Moreover, an isocontour of the density gradient is added to visualize the incident as well as the

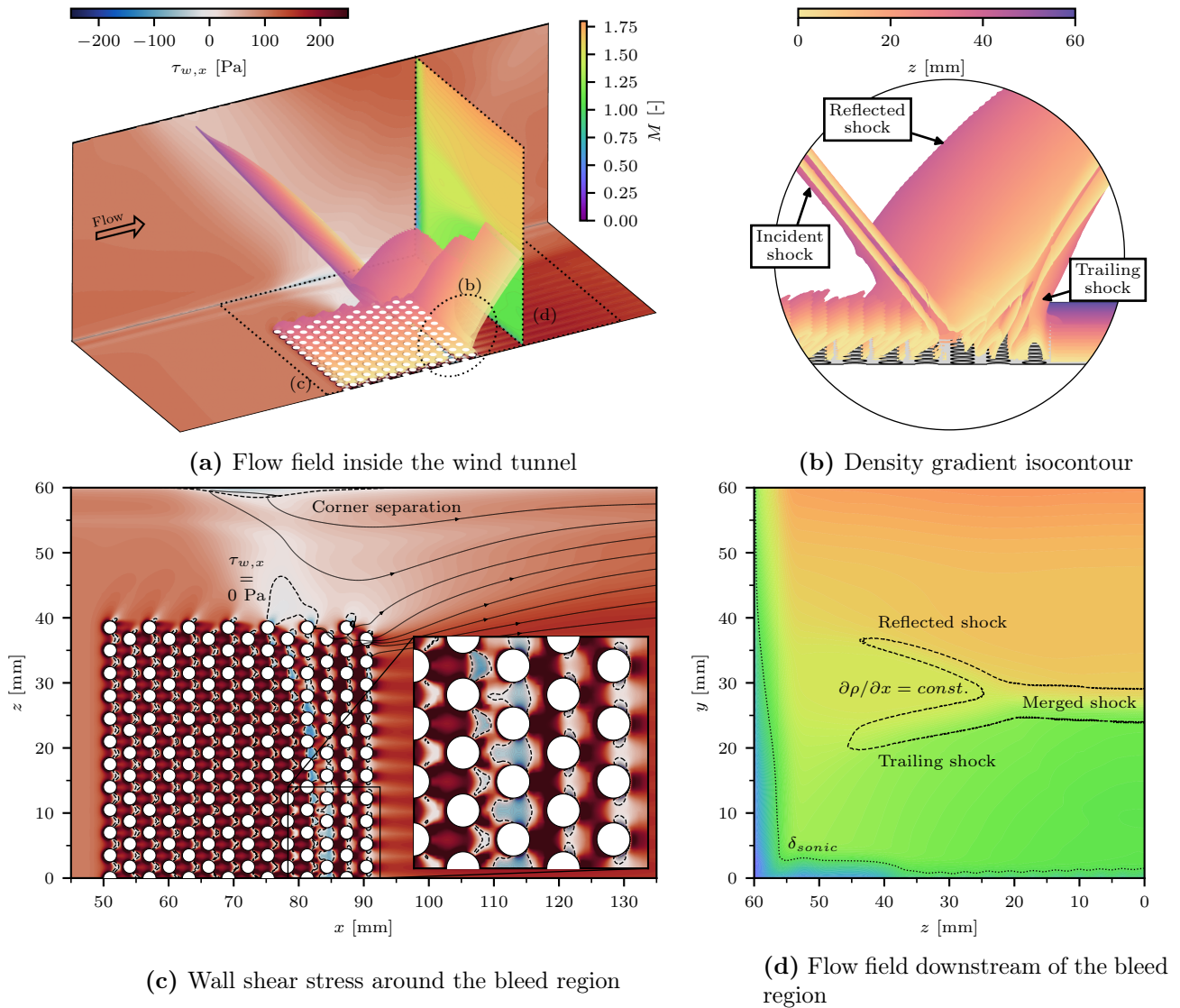


Figure 5.20: Flow topology with SBLI inside the wind tunnel from simulation ($p_{pl}/p_t = 0.095$).

reflected shock. Directly at first glance, a significant three-dimensionality of the flow is observable. The curvature of the shock is used as a measure to evaluate the variation of the flow along the span. Therefore, the isocontour of the density gradient is closer observed in Figure 5.20b. The darker the color of the isocontour, the closer the location with regard to the wind tunnel sidewall. The incident shock has only a small variation along the span and is only slightly curved in the upstream direction towards the sidewall. On the contrary, the reflected shock is strongly curved. The low flow momentum of the corner flow increases the upstream influence of the incident shock, moving the shock foot and the reflected shock upstream. Interestingly, the reflected shock merges with the trailing shock at the center of the test section.

The footprint of the shock is visible in Figure 5.20c which shows the wall shear stress. The positive pressure gradient induces a local flow separation, visualized by the blue color range and surrounded by the dashed line. The size of the separation is limited to the area between the holes, as the suction leads to a fast reattachment of the flow. At the center of the test section, the shock can be located at $x \approx 83$ mm since the flow starts to separate even between the holes at this station. Along the span, the incident flow separation moves upstream. Alongside the bleed region, a small area of separated flow is apparent, as well as a separation of the corner flow. However, the flow separation does not cover the entire span of the wind tunnel as the

bleed energizes the flow at the center. The streamlines demonstrate how the suction confines the width of the stream tube. Similar effects were found in earlier investigations with vortex generators controlling the center-plane flow [112, 113].

The flow field on a slice downstream of the bleed region is shown in Figure 5.20d. In the upper part, the Mach number is found to be higher as the reflected shock has not passed the flow at this location, while the Mach number is significantly reduced in the lower part of the test section. The isoline of the density gradient pinpoints the approximate position of the reflected shock. Here again, the merging of trailing and reflected shock is observed in the center of the test section. With further distance from the center, the two shocks divide. Near the sidewalls, the intensity of the shocks decreases as they merge with the expansion waves caused by the bleed and the rear edge of the shock generator. Particularly the expansion fan caused by the shock generator results in a smearing of the density gradient and leads to a re-acceleration of the flow.

Furthermore, the sonic line height is extracted and highlighted by the dotted line. Its high amount at the sidewalls near the corner illustrates the thickening of the boundary layer caused by the adverse pressure gradient of the shock. Thus, the sonic line height is larger at the top before passing the shock and increases against the corner. In the area downstream of the bleed, the sonic line height is smaller as the suction increases the momentum inside the boundary layer. The lowest sonic line height is found around $x = 30$ mm with its value slightly increasing towards the center of the test section. As the shock position is further upstream towards the sidewall, the area with a subsonic working regime of the bleed is larger. Hence, the effect of the flow control is increased in this area and the momentum is higher in the wall vicinity. However,

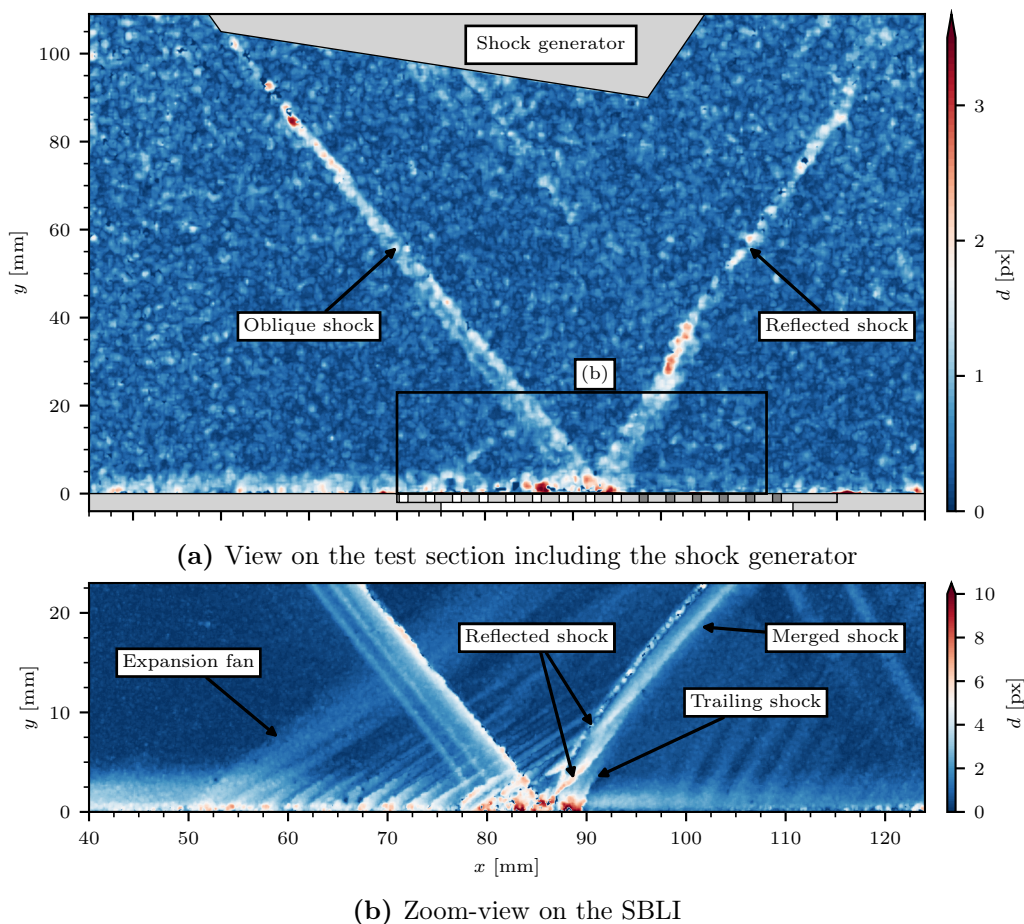


Figure 5.21: BOS visualization of the SBLI control for $p_{pl}/p_t = 0.094$.

no significant effect of the bleed on the corner flow is apparent. The presence of an expansion fan caused by the rear edge of the shock generator leads to a reattachment of the flow and counteracts the negative effect of the porous bleed.

As stated earlier, the wall pressure distribution of the simulation of the center segment and the wind tunnel half-span are compared in Figure 5.18. A good agreement is observed. Upstream of the shock, no differences in the curves are apparent. However, around the shock foot, a small deviation appears. The wall pressure increases stronger for the half-span simulations, even though the plenum pressure is slightly higher. However, the plenum pressure is averaged over the entire cavity plenum and local differences might be apparent. Altogether, the wall pressure distributions show the same trends and the deviations are small.

BOS visualizations of the experiments with the high-porosity plate HR are shown in Figure 5.21. At the top, the flow field is illustrated from a distance, showing almost the entire test section including the shock generator. The generated oblique shock is seemingly regularly reflected at the bottom wall. Faintly visible is the expansion fan created by the bleed region, as well as the expansion fan generated by the rear edge of the shock generator. A closer look at the interaction is shown in Figure 5.21b, where the camera is positioned closer to the test section focusing on the impingement point of the shock, revealing more information about the shock structure. A distinct incident shock is visible with its impingement point located at $x \approx 85$ mm. The reflected shock is divided into two distinct parts and smeared between them. One part of the shock has a significantly lower shock angle and is located further downstream, where it merges with the trailing shock. The second distinct part is located further upstream and forms a shock wave located with an offset to the merged shock. Since the BOS visualization is an integration of the density gradient along the visual axis of the camera, it is expected that the first part of the reflected shock is located close to the center of the wind tunnel, while the second part is found near the sidewalls. Thus, the structure of the shock system is expected to be the same as in the numerical simulations.

Chapter Summary

In this chapter, we investigated experimentally and numerically the flow control by porous bleed systems. First, the numerical setup was validated against existing experimental data. Afterward, the effect of the porous bleed on a shock-wave/boundary-layer interaction was presented after simplifying the complex problem into two separate problems: super- and subsonic boundary-layer control by porous bleed. The findings supported the idea of separately characterizing the working principle of porous bleed systems for both flow regimes, as the flow topology inside the bleed holes significantly differed, resulting in different effects on the boundary layer and interaction with an incident shock.

The comparison with the experimental datasets of Eichorn et al. [40] and Willis et al. [117] showed a good agreement. The parameterized setup was validated for three different plate geometries and a Mach number of $M = 1.6$ using the data of Eichorn et al. [40]. Moreover, a spanwise interaction of the bleed holes was observed using a single-row approach compared to a single-hole approach. Also, a good agreement with the data of Willis et al. [117] was demonstrated for supersonic Mach numbers from $M = 1.3$ to $M = 2.5$ for a perforated plate with several holes in the spanwise and streamwise direction. Altogether, the deviation between experiments and simulations in determining the sonic flow coefficient was less than 5% for all samples.

In the supersonic flow case, we found a good agreement between experimental and numerical results. The effect of the porous bleed on the boundary layer was well resolved by the numerical simulations, as proven by the LDV-obtained velocity fields, boundary-layer profiles, and static wall pressure measurements. The deviations between experiments and simulations in acquiring the profiles for several bleed rates and two plate geometries were in a negligible range, which proved the numerical ability to predict the control effectiveness. Moreover, three-dimensional effects resulting in variations of the boundary-layer profiles along the span for the use of large bleed holes were proven for the first time in experiments. Furthermore, the effect of the bleed on the corner flow and the impact of the corner flow on the three-dimensionality of the center-plane flow was illustrated.

In addition, the effect of the porous bleed on a subsonic flow was determined using the same experimental and numerical setup. For the first time, one study described the working principle of a porous bleed in both supersonic and subsonic conditions by means of experiments and RANS simulations. The deviations between experiments and simulations in this flow case were larger than for supersonic flows. Experiments and simulations on subsonic boundary-layer bleed were more challenging to perform as the mass removal significantly affected the upstream boundary layer. The ONERA S8Ch wind tunnel was not designed for subsonic conditions, and the uncertainty of controlling the inflow Mach number was estimated to be up to 5% (see Chapter 3). Also, the high bleed rate strongly influenced the upstream conditions in the simulations, requiring multiple simulations to obtain equal inflow conditions.

Finally, the shock-wave/boundary-layer interaction control was studied. Even for this complex flow topology, a very good agreement between simulations and experiments was achieved. The effect on the boundary layer along the bleed region was well replicated by the experiments. Also, three-dimensional simulations of the wind tunnel half-span were performed to study the impact of the corner flow on the interaction of shock, boundary layer, and porous bleed. Like in previous studies, a reinforcement of the corner flow was observed. In both experiments and simulations, the same structure of the shock topology was found.

The findings of this study legitimate the use of RANS simulations to investigate the effect of porous bleed systems in subsonic and supersonic flows with and without shock-wave/boundary-layer interactions. Numerical simulations enable the observation of the flow inside the bleed

holes, which facilitates the understanding of the flow physics. However, turbulence modeling and discretization of the domain might lead to inaccuracies and errors. Therefore, experimental data is required to validate the setup before interpreting the results. As experiments are time- and cost-intensive to examine comprehensive parametric studies, numerical simulations can help to deepen the knowledge about the working principle of bleed systems to improve bleed models. Therefore, the following chapters purely focus on numerical results as they allow a detailed view of the flow fields inside and surrounding the bleed holes and a wide variation of inflow conditions and plate characteristics.

Key Points:**Experimental data for the bleed rate**

- ❑ Data of Eichorn et al. [40]
 - Very good agreement for **different plate geometries** for $M = 1.6$
 - **Spanwise interaction** of bleed holes observed
 - **Hole diameter** and **Thickness-to-diameter effects** proven
- ❑ Data of Willis et al. [117]
 - **Good fit** of data for **supersonic conditions** from $M = 1.3$ to $M = 2.5$
- **Validation** of the prediction of the **bleed rate** using RANS simulations

Supersonic boundary-layer bleed

- ❑ **Good agreement** of the **flow field** between experiments and simulations
- ❑ **Effect of bleed rate** on the **boundary-layer profiles** well predicted by simulations for two **different plate geometries**
- ❑ **Spanwise variation** of the **boundary-layer profiles** observed in experiments and simulations → increase with bleed rate
- **Validation** of the control effect on the **supersonic boundary layer**

Subsonic boundary-layer bleed

- ❑ **Effect of bleed rate** on the **boundary-layer profiles** well predicted by simulations
- ❑ **Diffuser effect** observed in both experiments and simulations → **deceleration** of external flow for high bleed rates
- ❑ Quick saturation of the momentum increase in the near-wall region
- **Validation** of the control effect on the **subsonic boundary layer**

Shock-Wave/Boundary-Layer Interaction Control

- ❑ **Effect of bleed rate** on the **boundary-layer profiles** along the bleed region is well predicted by simulations
- ❑ **Good agreement** of the **flow field** between experiments and simulations
- ❑ **Confinement effects** of the center bleed predicted by means of CFD
- ❑ **Merging** of the **trailing shock** and the **reflected shock** anticipated from BOS visualization and simulations
- **Validation** of the control effect on the **SBLI**

Numerical Study of the Parameter Influences

*Have you ever thought that it could be a blessing to not know
the details of something? That one might perhaps need the
space created by uncertainty?*

MARC-UWE KLING

Chapter Introduction

After the numerical setup is validated, it can be used for a parametric study, which forms the heart of this thesis. This chapter is dedicated to the influence of inflow and geometrical parameters on the performance of a porous bleed. Previous research (see Chapter 1) has shown the influences of both flow conditions and geometry. For the evaluation of all these influences, a comprehensive numerical study is performed consisting of hundreds of simulations.

First, the inflow conditions are examined to identify the typical flow topology in the holes for both supersonic and subsonic conditions. Afterward, the five geometrical parameters plate length, hole diameter, porosity level, thickness-to-diameter ratio, and stagger angle are separately varied to identify their effect on both bleed efficiency and control effectiveness for a wide range of pressure ratios. These investigations are conducted for supersonic and subsonic conditions using the numerical domain introduced in Section 2.1.2, but also for the SBLI control with the numerical domain from Section 2.1.1.

We remind the reader of the definitions of bleed efficiency and control effectiveness. The bleed efficiency describes the capability of removing the highest possible bleed rate for a given pressure drop from the external wall to the bleed plenum. For the quantification of the bleed efficiency, the surface sonic flow coefficient $Q_{sonic,w}$ is computed as a function of the pressure ratio p_{pl}/p_w . The throat ratio TR (see equation 2.1) is fixed to obtain similar pressure ratios independently of the plate geometry, which is challenging since both external wall pressure p_w and cavity plenum pressure p_{pl} vary with the surface sonic flow coefficient.

On the contrary, the control effectiveness describes the ability to achieve the maximum effect on the boundary layer, i.e., the increase of the momentum in the near-wall region, for a

given bleed rate. Therefore, the bleed rate \dot{m}_{bl} with respect to the mass deficit of the inflow $\dot{m}_{\delta_{1,c}}$ is fixed by iteratively varying the throat ratio during the computation. Thus, the rise in the wall shear stress ϵ_τ along the bleed region is computed to evaluate the control effectiveness.

Please refer to Section 2.4 for more information regarding the evaluation of bleed efficiency and control effectiveness. Additionally, caution must be exercised when interpreting the pressure ratio. A low plenum pressure p_{pl} results in a low pressure ratio p_{pl}/p_w , which may be counterintuitive for the reader. In other words, a low pressure ratio corresponds to a high pressure difference from the external wall to the cavity plenum, and hence, high bleed rates.

6.1	Influence of the Inflow Conditions	120
6.1.1	Mach Number	120
6.1.2	Displacement-Thickness-to-Diameter Ratio	123
6.2	Geometry Influence on Supersonic Boundary-Layer Bleed	126
6.2.1	Plate Length	126
6.2.2	Hole Diameter	131
6.2.3	Porosity Level	136
6.2.4	Thickness-to-Diameter Ratio	139
6.2.5	Stagger Angle	142
6.2.6	Comparison of all Geometrical Parameters	144
6.3	Geometry Influence on Subsonic Boundary-Layer Bleed	146
6.3.1	Plate Length	146
6.3.2	Hole Diameter	148
6.3.3	Porosity Level	150
6.3.4	Thickness-to-Diameter Ratio	152
6.3.5	Stagger Angle	152
6.3.6	Comparison of all Geometrical Parameters	153
6.4	Geometry Influence on Shock-Wave/Boundary-Layer Interaction Control	155
6.4.1	Hole Diameter	155
6.4.2	Porosity Level	160
6.4.3	Thickness-to-Diameter Ratio	161
6.4.4	Stagger Angle	162
6.4.5	Comparison of all Geometrical Parameters	164

6.1 Influence of the Inflow Conditions

We start by investigating the impact on the inflow conditions before heading toward the geometrical parameter influences. As illustrated in Chapter 4, the flow topology inside and around the bleed holes significantly differs between supersonic and subsonic conditions. Moreover, the experiments highlighted differences in the control effect. In this section, the impact of the Mach number but also the boundary-layer profile on the bleed efficiency and control effectiveness are investigated. The selected domain is an open domain with a far-field boundary condition at the top to avoid influences of the domain size, especially for subsonic flows (see 2.1.2).

6.1.1 Mach Number

In the first step, the inflow Mach number is varied from $M = 0.0$ to 2.0 . The investigated perforated plate is defined with a length $L_w = 40$ mm, a hole diameter $D = 0.5$ mm, a porosity $\phi = 22.67\%$, a thickness-to-diameter ratio $T/D = 1$, and a stagger angle $\beta = 60^\circ$. Thus, the geometry is equal to the perforated plate in Chapter 4 except for the smaller hole diameter, which is closer to the classical ratio $D/\delta_{1,c} = 1$. For this investigation, the throat ratio is fixed instead of the mass flow ratio $\dot{m}_{bl}/\dot{m}_{\delta_{1,c}}$ as the higher bleed rates of a subsonic boundary-layer bleed significantly complicates fixing this value, and simulations are also performed for zero tangential flow, where no inflow boundary-layer can be defined. However, all inflow profiles, except for the $M = 0$ case, have an equal displacement thickness of $\delta_{1,c} = 0.89$ mm.

The flow topology inside the bleed holes is analyzed first. Figure 6.1 visualizes the wall-normal flow component at three different locations along the perforated plate. The first row shows the first hole, and the second and third rows show the holes at 20% and 80% of the plate length, respectively. From the left to the right, the inflow Mach number is increased from $M = 0.1$ to 2.0 . The dashed lines highlight the contours of zero velocity, which illustrates the border of the stream tube, and thus, the size of the separated region inside the bleed holes. The magenta dotted lines show the contours of the supersonic regions, i.e., the sonic lines.

The observation of the first holes reveals significant differences in the flow field close to the wall depending on the free-stream Mach number. The lower the Mach number, the higher the flow deflection towards the wall as visualized by the streamlines. Inside the holes, we find a larger vena contracta area for low Mach numbers, which confirms the findings of Harloff and Smith [61]. However, between $M = 0.8$ and $M = 1.6$, the differences are faintly visible and no significant decrease in the size is notable. For $M = 2.0$, the vertical position of the vena contracta moves towards the hole exit. Moreover, a region of upward-directed flow is apparent downstream of the aft edge of the holes, which is a consequence of outflow from the holes. [77] This phenomenon is found from a Mach number of $M = 0.4$ and increases with an increasing Mach number. From a Mach number of $M = 1.0$, an expansion fan at the front of the hole is induced by the flow deflection. Further downstream, the barrier shock decelerates the flow to subsonic conditions. For lower pressure ratios, the supersonic regions are found for lower free-stream Mach numbers because of a higher acceleration of the flow around the front edge of the hole.

A look at 20% of the plate length reveals interesting differences between supersonic and subsonic free-stream conditions. Again, a decrease in the vena contracta area is found for increasing Mach numbers. However, for subsonic conditions, the vena contracta area is larger compared to the first hole. Moreover, the flow deflection towards the wall is stronger, and the region of upward-directed flow downstream of the holes decreases in size. In the case of supersonic conditions, the effects are the contrary. The vena contracta area slightly decreases

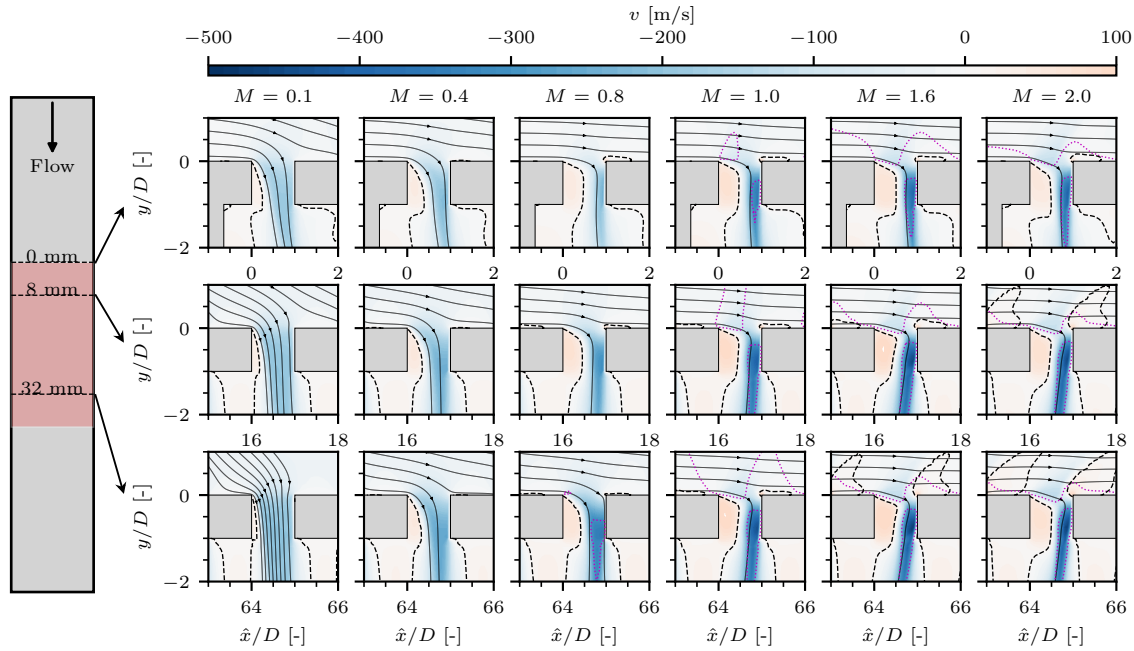


Figure 6.1: Contours of the wall-normal velocity component in the bleed holes for different Mach numbers at $\hat{x} = 0$ mm, 8 mm, and 32 mm (top to bottom) for $TR = 0.7$; dashed lines highlight zero wall-normal velocity contour; dotted magenta lines illustrate sonic lines.

in size, the region of upward-directed flow increases, and the flow deflection becomes smaller. Moreover, the barrier shock moves towards the aft edge of the hole.

In the last row of Figure 6.1, the same trends are apparent. For the lowest Mach number of $M = 0.1$, the wall-normal flow becomes more and more the main velocity component. The separated region inside the hole almost disappears. For a high subsonic Mach number of $M = 0.8$, a tiny supersonic region is apparent at the front edge of the hole since the bending of the streamlines significantly increased. Moreover, the flow inside the hole is choked. For supersonic conditions, the vena contracta area remains constant in size. However, the barrier shock moves further downstream, which leads to a stronger outflow at the aft edge of the holes.

The explanation of the different effects of supersonic and subsonic conditions is the diffuser effect of the bleed. Figure 6.2 illustrates the stream tube captured by the porous bleed dependent on the free-stream Mach number. As stated before, the (compressible) displacement thickness of the inflow boundary-layer profiles is equal independently of the Mach number, i.e., the mass deficit of the boundary layers is the same. Thus, for the same throat ratio, a significantly higher part of the inflow is removed by the bleed for low Mach numbers compared to high Mach numbers.

The removal of mass from the external flow has the same effect on the main flow as a divergent nozzle. In the case of supersonic flow, the main flow is accelerated, which results in a higher momentum flow captured by the successive hole. On the contrary, the divergent flow channel leads to a decrease in the external flow velocity for subsonic conditions. Consequently, the momentum of the captured flow decreases for each successive hole even though the captured stream tube includes flow from the outer region of the boundary layer.

As shown in Figure 6.2, the diffuser effect is the highest for small free-stream Mach numbers. Consequently, the deceleration of the flow is the strongest, which explains the significant differences found between the first hole and the holes further downstream in Figure 6.1. For high Mach numbers, the stream tube of the captured flow is smaller. However, in the case of lower plenum pressures and, in turn, higher bleed rates, the effect strengthens. For internal

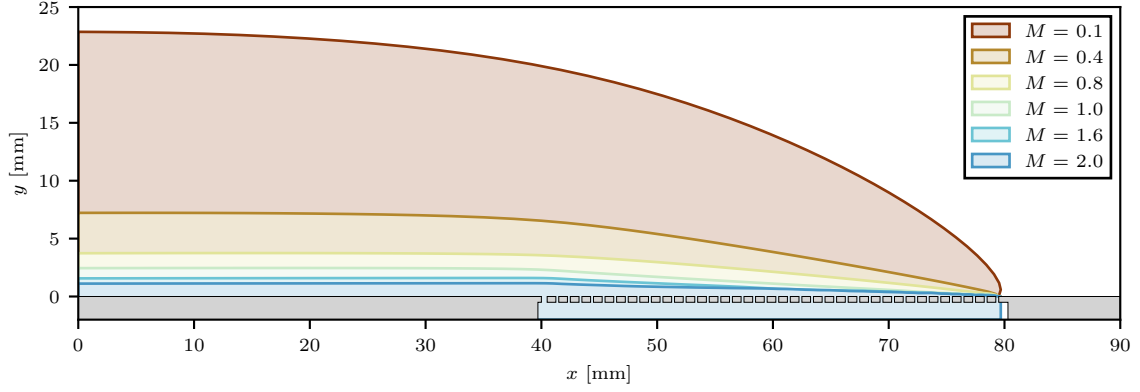


Figure 6.2: Stream tube captured by porous bleed for different Mach numbers.

flows, this effect can be significant as small changes in the area of the main stream tube result in great changes in the Mach number.

Another important effect visualized in Figure 6.2 is the upstream influence of the porous bleed on the external flow. For supersonic flows, there is no change in the size of the stream tube upstream of the first bleed hole apparent since the subsonic part of the incoming boundary layer is too small. However, for subsonic conditions, the porous bleed has a significant impact on the flow upstream of the holes as seen by the curvature of the upper boundary of the stream tube. In the case of an SBLI, this may have an essential impact as it decreases the shock intensity as the deflection angle along the shock decreases. Consequently, the application of porous bleed below the shock foot is expected to be advantageous compared to the sole control of the supersonic flow upstream of the shock.

The effect of the Mach number on the bleed efficiency is evaluated by computing the sonic flow coefficient based on the wall properties. Therefore, more simulations are conducted for different throat ratios TR . Figure 6.3 shows the computed sonic flow coefficient as a function of the pressure ratio from the plenum to the external wall p_{pl}/p_w along the bleed region. One solid line represents one simulation with one throat ratio. The right triangle (\blacktriangleright) illustrates the mass flow rate associated with the first hole, while the left triangle (\blacktriangleleft) stands for the last hole and the circle (\bullet) for the averaged value, i.e., the global plate working regime. Furthermore, two models are illustrated for comparison. One bleed model is the regression of Slater [98], which is validated for supersonic flows only. The second model is the model of Grzelak et al. [54], which does not consider any external flow ($M = 0.0$).

At first glance, the strong impact of the Mach number on the sonic flow coefficient is apparent. The higher the Mach number, the lower the sonic flow coefficient. In other words, the lower the Mach number, the higher the bleed rate, as the sonic flow coefficient is the normalized bleed rate over the sonic mass flow rate. The reason is the smaller separated region inside the holes. Moreover, the pressure drop from the external wall to the plenum is smaller for low free-stream Mach numbers. On the one hand, the smaller separated region leads to a smaller form drag, and on the other hand, wave drag appears as soon as the flow becomes locally supersonic.

By following one line, we can observe the change in the sonic flow coefficient and the pressure ratio along the perforated plate. As discussed before, the momentum of the captured flow decreases in subsonic conditions and increases in supersonic conditions. As a consequence, the sonic flow coefficient increases along the plate under subsonic conditions as the separated region decreases in size. Moreover, the deceleration of the flow increases the wall pressure, which leads to a rise in the pressure drop, and thus, to an additional rise in the sonic flow

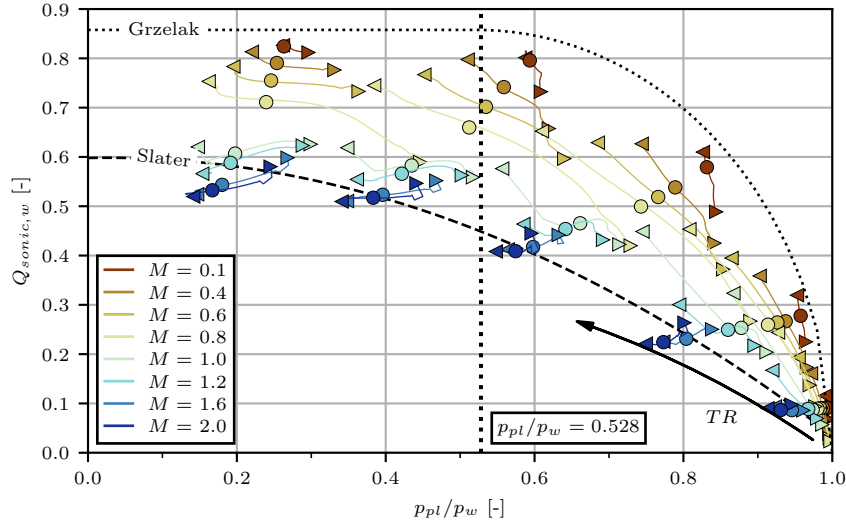


Figure 6.3: Surface sonic flow coefficient for different Mach numbers; right triangle (►) symbolizes the first hole, left triangle (◄) the last hole, and circle (●) the mean value.

coefficient. Under supersonic conditions, we see the opposite effect. As the increase of the Mach number of the captured flow also strengthens the shock intensity, the pressure losses are higher. This effect is not considered by Harloff and Smith [61] (see Figure 1.44), resulting in an overestimated sonic flow coefficient for high supersonic flows.

The comparison to the models of Slater [98] and Grzelak et al. [54] demonstrates the necessity of including the flow conditions in the modeling. While the model of Grzelak et al. [54] overestimates the sonic flow coefficient even for the lowest Mach number, the model of Slater [98] gives a good indication of the sonic flow coefficient under supersonic conditions but underestimates the bleed rate in the case of subsonic flow. The comparison of the bleed models with the data also reveals a shift in choking conditions. As considered by Grzelak et al. [54], the flow in the holes is expected to be choked for pressure ratios below the critical pressure ratio $p_{pl}/p_w = 0.528$. External flows diminish the importance of this ratio. The reason is the interaction of external flow momentum, pressure ratio, and size of the separated region. Smaller pressure ratios lead to a stronger bending of the flow into the hole. Consequently, the separated region decreases in size, leading to an increase in the vena contracta area and the sonic flow coefficient. Even though the flow inside the hole is supersonic (and theoretically choked), the bleed rate still increases. This effect is more important for high Mach numbers, while the effect is less prominent for subsonic flows as the size of the separated region is smaller.

6.1.2 Displacement-Thickness-to-Diameter Ratio

The ratio of compressible boundary-layer displacement thickness to hole diameter is a commonly used similarity parameter in the literature [3, 40, 61, 108]. However, this ratio has never been proven to show a similarity. Therefore, simulations of two different plates with hole diameters of $D = 2$ mm and 2.0 mm, and displacement thicknesses of $\delta_{1,c} = 0.89$ mm and 3.56 mm are conducted to maintain the same ratio $\delta_{1,c}/D$. Please note that maintaining a desired boundary-layer profile upstream of the bleed is challenging for subsonic conditions because of the significant upstream influence of the bleed. Therefore, the displacement thickness is defined with the velocity profile provided as the inlet boundary condition.

The surface sonic flow coefficient for both plates is shown in Figure 6.4. The graphic demonstrates differences between the two plates, which are mainly caused by the change in

the boundary-layer shape along the bleed region with each successive hole. Independent of the Mach number and the throat ratio, the surface sonic flow coefficient is found to be higher in the case of a larger hole diameter and a thicker boundary layer. Using boundary-layer properties to scale geometrical hole parameters is therefore seen as not practical.

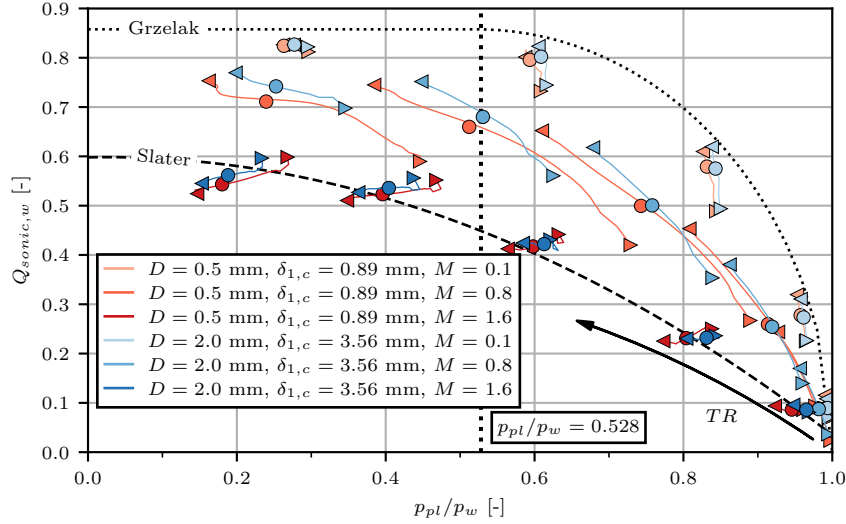


Figure 6.4: Surface sonic flow coefficient for both plates with equal $\delta_{1,c}/D$ and different Mach numbers; right triangle (\blacktriangleright) symbolizes the first hole, left triangle (\blacktriangleleft) the last hole, and circle (\bullet) the mean value.

Nevertheless, the sonic flow coefficient may be expected to be equal for the first hole as the ratio of displacement thickness to hole diameter is similar, or even equal for supersonic flows. As explained in the previous section, the bleed rate is highly affected by the flow momentum of the captured air. However, the extent of this stream tube is a function of the pressure ratio, the hole size, and the boundary-layer shape, which is more complex and consists of more quantities than only the displacement thickness. Moreover, all holes are linked to the same cavity plenum,

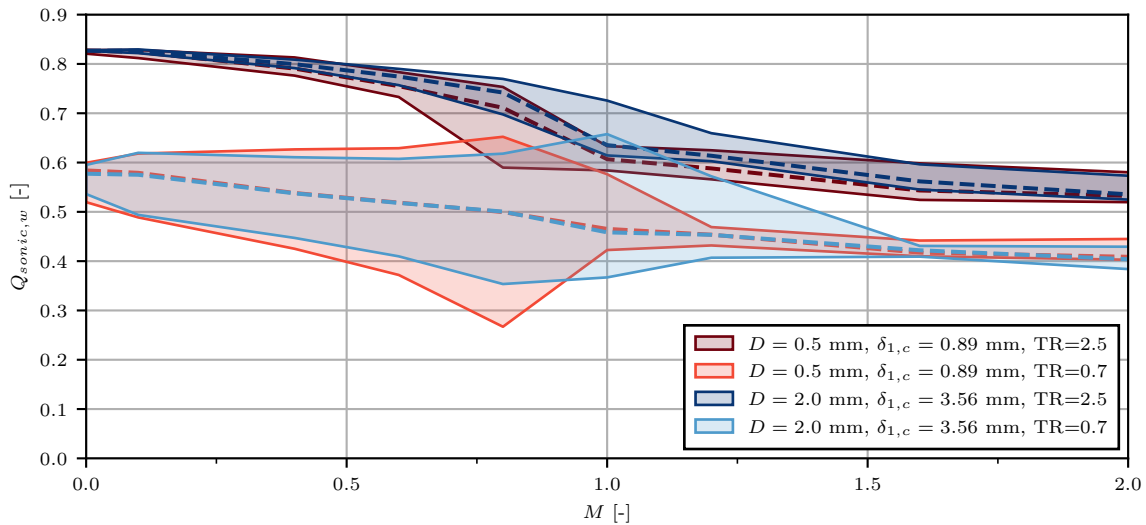


Figure 6.5: Surface sonic flow coefficient as a function of the Mach number for two plates with different hole diameters and $\delta_{1,c}/D = const.$ ($TR = 0.7$ and 2.5); patches illustrate the envelope of local values and dashed lines illustrate the global trend.

resulting in an interaction between the holes. Therefore, also the pressure inside the holes is affected by the change of the boundary-layer profile along the perforated plate, which in turn changes the bleed rate. In addition, a plate of larger holes also results in a lower amount of bleed holes for the same plate length. This results in a smaller number of barrier shocks passed by the flow. Thus, the pressure losses are expected to be smaller.

Figure 6.5 illustrates the surface sonic flow coefficients as a function of the Mach number for both plates and throat ratios $TR = 0.7$ and 2.5 . For $TR = 2.5$, all holes are choked, which allows us to show the mismatch between the two cases globally. First, the decrease of the sonic flow coefficient as a function of the Mach number is visible. Again, a higher surface sonic flow coefficient is observed for the thicker boundary layer with the larger holes. The largest differences are found around $M = 1$, where the whole curve seems to be shifted to higher Mach numbers for the thicker inflow boundary layer. In total, the trend is similar to that found by Harloff and Smith [61], which is shown in Figure 1.44.

For the lower throat ratio of $TR = 0.7$, the results are more interesting. While the global trends (dashed lines) show a good agreement, the local variation is found to be higher for smaller holes, which is a consequence of the larger amount of holes. This affects the boundary layer, and thus, the flow of the consecutive hole.

6.2 Geometry Influence on Supersonic Boundary-Layer Bleed

The following sections explain the influence of the different parameters on bleed efficiency and control effectiveness for supersonic conditions. At any time, only one parameter is altered to isolate its effect. The default plate has a length $L_w = 40$ mm, a hole diameter $D = 0.5$ mm, a porosity $\phi = 22.67\%$, a thickness-to-diameter ratio $T/D = 1$, and a stagger angle $\beta = 60^\circ$. Again, the selected domain is an open domain with a far-field boundary condition at the top to avoid influences of the domain size (see Section 2.1.2).

6.2.1 Plate Length

The influence of plate length (or size) on bleed efficiency and control effectiveness has never been investigated to the author's knowledge. Syberg and Koncsek [109] stated that the perforated plate should be optimally sized to operate near the choking conditions. A choked plate removes the highest possible mass flow rate by simultaneously having the smallest possible plate size, which reduces roughness losses. The term roughness is used in their study to describe the mixing of low- and high-momentum flow caused by the hole geometry leading to a higher pressure drag. As a result, the boundary-layer thickness increases, and the flow momentum in the wall vicinity decreases. Also, Shih [94] states that roughness-like effects can be caused by the barrier shocks inside the holes. However, no study compares two plates of different sizes with identical hole patterns.

In this study, several plate lengths are examined while the other parameters (hole diameter, porosity level, thickness-to-diameter ratio, and stagger angle) are kept constant. Figure 6.6 shows the flow field along three plates with $L_w = 2$ mm, 12 mm, and 40 mm. The throat ratio $TR = 0.7$ (see Equation 2.1) is kept constant for the simulation to illustrate similar working regimes with all the holes being close to choking conditions. Independently of the size, a thinning of the boundary layer is notable. However, the effect increases with longer plates as more mass is removed since the bleed area is larger than for short plates with fewer holes. The bending of the streamlines is illustrated by the dotted line, which serves as a reference indicating the upstream location of a streamline outside the boundary layer. Thus, the deflection is equal to those at the boundary-layer edge.

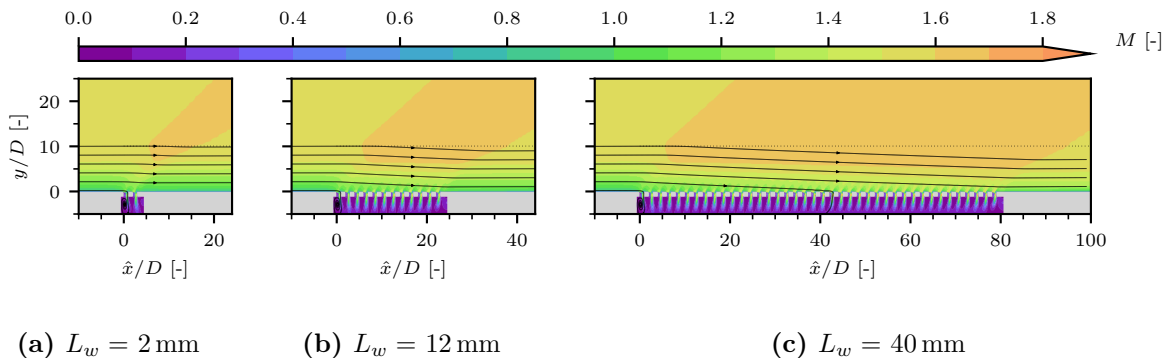


Figure 6.6: Mach number contours for different plate lengths ($TR = 0.7$); dotted line refers to the wall distance of a streamline outside the boundary layer at the beginning of the plate.

The trends of the static wall and plenum pressure along the perforated plates are detailed in Figure 6.7. Independently of the plate length, the trend for the wall pressure is the same. At the beginning of the plate, the pressure drops with an expansion fan because of a flow deflection toward the wall. Further along the plate, the pressure then increases because of

continuous compression caused by the barrier shocks and the steady deflection in the wall-parallel direction. However, the positive slope of the pressure decreases with further distance to the plate beginning. For the last hole, the wall pressure is higher because of the presence of the trailing shock and the extraction of the wall pressure around the hole (see Figure 2.8). Moreover, the isentropic pressure ratio for $M = 1.6$ is illustrated to pinpoint that the wall pressure on the bleed region is significantly lower than the wall pressure without control, leading to higher ratios p_{pl}/p_w . This might lead to bleed model deficiencies as stated by Choe et al. [21].

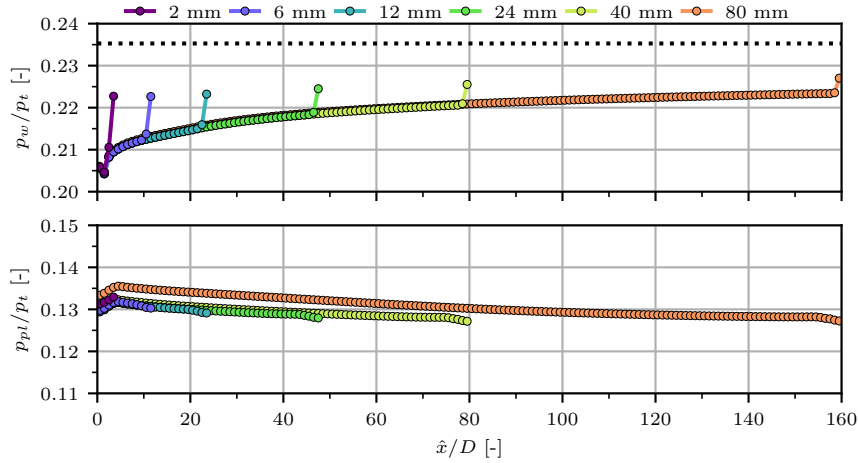


Figure 6.7: Static external wall and plenum pressure for different plate lengths ($TR = 0.7$); the dotted line highlights the isentropic pressure ratio for $M = 1.6$.

The trend for the plenum pressure is shown in the lower graph of Figure 6.7. Its value contrasts with the wall pressure since it decreases along the plate, caused by increasing pressure losses as the momentum of the sucked flow increases. Thus, the shock waves inside the holes become more intense. For longer plates, the plenum pressure is shifted to higher values at the beginning of the plate. In contrast, its average value stays approximately the same due to the choked throat. The higher the losses, the lower the plenum pressure, leading to a lower density and hence a lower mass flow rate for choking conditions. Consequently, the plenum pressure increases until an equilibrium between the sonic mass flow rate leaving the cavity plenum and the bleed rate is achieved, as described by Slater and Saunders [99].

More simulations are performed for different throat ratios. Figure 6.8 shows the local surface sonic flow coefficient as a function of the pressure ratio from the plenum to the external wall. Again, one solid line represents one simulation with one throat ratio. Furthermore, the regression of Slater [98], which does not include any sensitivity to geometrical parameters, is shown as a reference.

A closer look at Figure 6.8 reveals essential differences between the plates for pressure ratios $p_{pl}/p_w < 0.9$. For the first holes, the trend is similar to those of the regression of Slater [98], even though the surface sonic flow coefficient is higher. Along the plate, the pressure ratio is decreasing, which is a consequence of the increasing external wall pressure and higher total pressure losses induced by the shocks at the hole entry and inside the holes. The decrease in the pressure ratio along the plate is the strongest for long plates and high throat ratios. Simultaneously, the sonic flow coefficient decreases due to the higher momentum of the sucked flow and, thus, increased size of the separated region inside the holes. Consequently, the momentum of the flow in the vicinity of the wall increases, and hence, the intensity of the barrier shock.

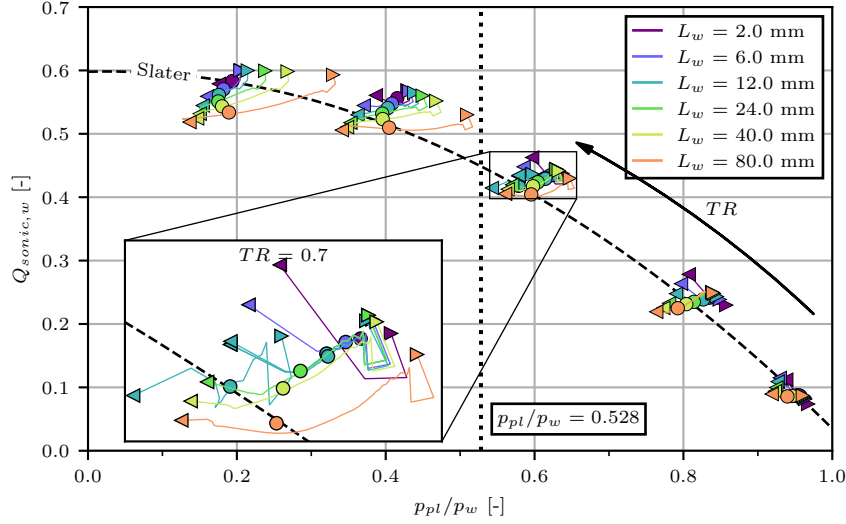


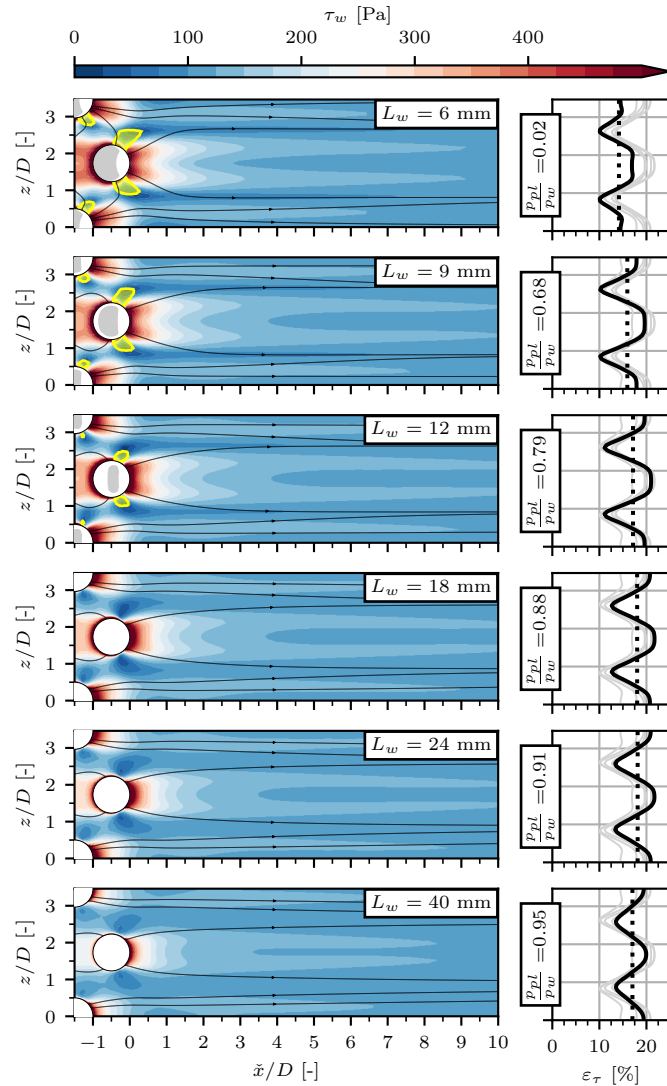
Figure 6.8: Surface sonic flow coefficient for different plate lengths; right triangle (▶) symbolizes the first hole, left triangle (◀) the last hole, and circle (●) the mean value.

Since longer plates consist of more bleed holes, the negative effects induced by the barrier shocks become stronger. Thus, the global sonic flow coefficient decreases with the plate length. Another trend in the plot is the increase of the sonic flow coefficient at the last hole for short plates and unchoked conditions. The adverse pressure gradient induced by the trailing shock, resulting in a higher pressure around the last hole, is the reason for the higher bleed rate. The effect is weaker for long plates, as the boundary-layer thinning is asymptotic, and the main flow direction bends successively back in the wall-parallel direction (see Figure 6.6). Thus, the pressure rise around the last hole is higher for short plates, as shown at the top of Figure 6.7.

If the holes are choked, the deviation between the plates is more significant. For low pressure ratios, the sonic flow coefficient is around 10% higher for a 2 mm plate compared to an 80 mm plate. However, the total bleed rate is significantly lower. On the contrary, no significant differences are apparent for high pressure ratios $p_{pl}/p_w > 0.9$ as the holes are far from choking conditions.

In the second step, simulations with constant bleed rates are performed to evaluate the control effectiveness of the plates. The removed mass flow rate corresponds to 25% of the inflow mass deficit. In Figure 6.9, the wall shear stresses downstream of the bleed region are compared for plate lengths from 6 mm to 40 mm for an equal total bleed rate which varies between minimum and maximum by less than 2%. From top to bottom, the plate length and the pressure ratio p_{pl}/p_w increase. While the holes for the smallest plate are choked ($p_{pl}/p_w \leq 0.528$), choking conditions are not achieved for the other plates.

Significant differences in the flow field around and downstream of the last holes are apparent in Figure 6.9a. The shorter the plates, the more significant the rise in the wall shear stress at the rear edge of the holes, caused by the higher suction rate through the hole. Moreover, in the case of short plates, the flow at the hole entry is partially supersonic (gray patches), resulting in a barrier shock inside the holes. Besides, the high suction rates lead to local flow reversal, visualized by the yellow patches. These areas grow with the suction rate and are only apparent for plates shorter than $L_w = 18$ mm. As a result of the reversed flow, counter-rotating vortices are generated, as reported by Hamed et al. [60], causing an area of low wall shear stress further downstream. The friction lines follow the vortex traces, where the vortices are fed and the flow momentum is low. The smaller the plate and the pressure ratio, the more significant this effect. For the longest plate, the friction lines are significantly less bent. The deflection of the friction



(a) Nominal wall shear stress (b) Rise in wall shear stress

Figure 6.9: Comparison of the wall shear stress downstream of the bleed region for different plate lengths; yellow areas in (a) visualize regions with negative streamwise component and gray areas indicate supersonic hole entry flow; (b) wall shear stress 10 mm ($20D$) downstream of the last hole compared to its value 10 mm upstream of the first hole; dotted line illustrates averaged value along the spanwise direction and gray curves illustrate trends for other values.

lines in the spanwise direction also helps to visualize the out-of-plane effects. Oorebeek et al. [77] reported this effect inside the boundary layer. The current figure shows that the effect is even stronger in the wall vicinity.

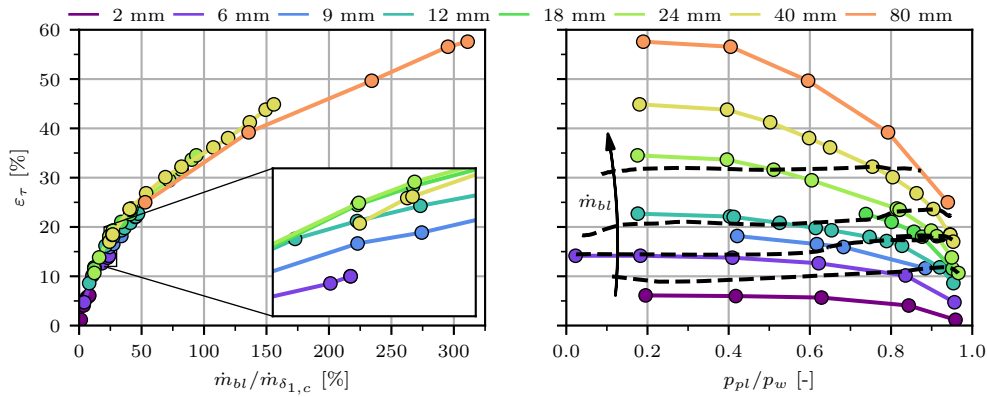
Figure 6.9b presents the relative rise in the wall shear stress 10 mm downstream of the plate compared to the value 10 mm upstream of the first hole, as defined in Equation 2.11. Independently of the pressure ratio, a spanwise variation of the wall shear stress is notable, with its highest values located in the slipstream of the holes and the lowest values at the spanwise position where no holes are located. The dotted line highlights the average value, while the gray lines present the curve for the other plate lengths.

Again, the effect of the reversed flow areas is apparent. For the three smallest plates, the rise in the wall shear stress between the holes is significantly lower and has a local value of approximately 10% compared to the 15% for the long plates. Hence, short plates with high

suction rates negatively influence the effect of the porous bleed.

Another negative effect is visible for the three shortest plates, where the wall shear stress downstream of the holes drops. The reason is the stronger adverse pressure gradient induced by the barrier shock caused by the partially supersonic flow in the hole entry. The more extended the supersonic area, the higher the Mach number upstream of the shock and, thus, the shock intensity. Moreover, the barrier shock moves closer to the rear edge, and some outflow is present [77]. Especially for the shortest plate with a 6 mm length, the increase in the wall shear stress is significantly lower.

However, a plate that is too long also results in a lower rise in wall shear stress, as seen in Figure 6.9b. A lower increase downstream of the holes is notable for the longest plate with $L_w = 40$ mm. Apparently, the roughness effect plays for low suction rates a more significant role. Altogether, the best increase of the wall shear stress is found for plates around 20 mm, corresponding to a pressure ratio of $p_{pl}/p_w \approx 0.9$.



(a) Rise in wall shear stress as a function of the bleed rate

(b) Rise in wall shear stress as a function of the pressure ratio

Figure 6.10: Rise in the wall shear stress as a function of the bleed rate \dot{m}_{bl} and the pressure ratio p_{pl}/p_w for varying plate lengths; dashed lines in (b) pinpoint lines of constant bleed rate.

All simulations performed for the standard plate for various relative bleed rates are evaluated regarding the control effectiveness and shown in Figure 6.10. First, the rise in the wall shear stress is plotted as a function of the relative bleed rate (see Figure 6.10a). As expected, the higher the sucked mass, the more effective the porous bleed. However, large plates are required for large mass flow rates since choking limits the maximum removable mass flow rate of short plates. Moreover, the slope of the general trend decreases with the plate length and bleed rate.

In order to assess the overall performance of the porous bleed, we plot the rise in the wall shear stress as a function of the pressure ratio. As shown in Figure 6.10b, an optimum can be located for each bleed rate (dashed lines) around $p_{pl}/p_w \approx 0.9$. Contrary to Syberg and Koncsek [109], choking conditions decrease the effect of the porous bleed and are more critical than the bleed roughness induced by the hole contours. With the choking of the holes, the wall shear stress downstream of the bleed region decreases again. Nevertheless, it must be stated that too high pressure ratios may lead to undesired behavior (e.g., blowing) if the inflow conditions change and the external wall pressure drops below the plenum pressure.

For the application of a bleed system, the following statements can be made. Choking conditions are not the optimum conditions to operate a porous bleed. On the contrary, longer plates accompanied by higher pressure ratios above the critical ratio, result in a higher flow momentum in the wall vicinity even though the bleed rate is fixed, because the losses caused by shock waves are smaller. However, the margin to undesired operation regimes, i.e., blowing,

is small. On the contrary, smaller plates generally have a higher bleed efficiency, as the smaller size results in lower losses caused by the flow entering the bleed holes. However, choking the holes leads to a rapid rise in pressure losses.

6.2.2 Hole Diameter

The second investigated parameter is the hole diameter. Multiple studies [3, 33, 40] have shown a hole diameter influence. However, these effects are not considered in state-of-the-art bleed models. In this study, the hole diameter is varied by more than one order of magnitude from $D = 0.25$ mm to 4.00 mm, while keeping the inflow boundary layer constant.

In the first step, the flow fields inside the holes are compared without altering the boundary-layer thickness at different positions along the perforated plate for a fixed throat ratio $TR = 0.7$ and a length of 40 mm, as shown in Figure 6.11. Both streamwise and wall-normal coordinates are normalized by the hole diameter to check the similarity in the flow topology. From left to right, the hole diameter increases, and going from top to bottom corresponds to a shift in the streamwise direction. The different positions are illustrated in the schematic on the left and correspond to 0 %, 20 %, and 80 % of the plate length.

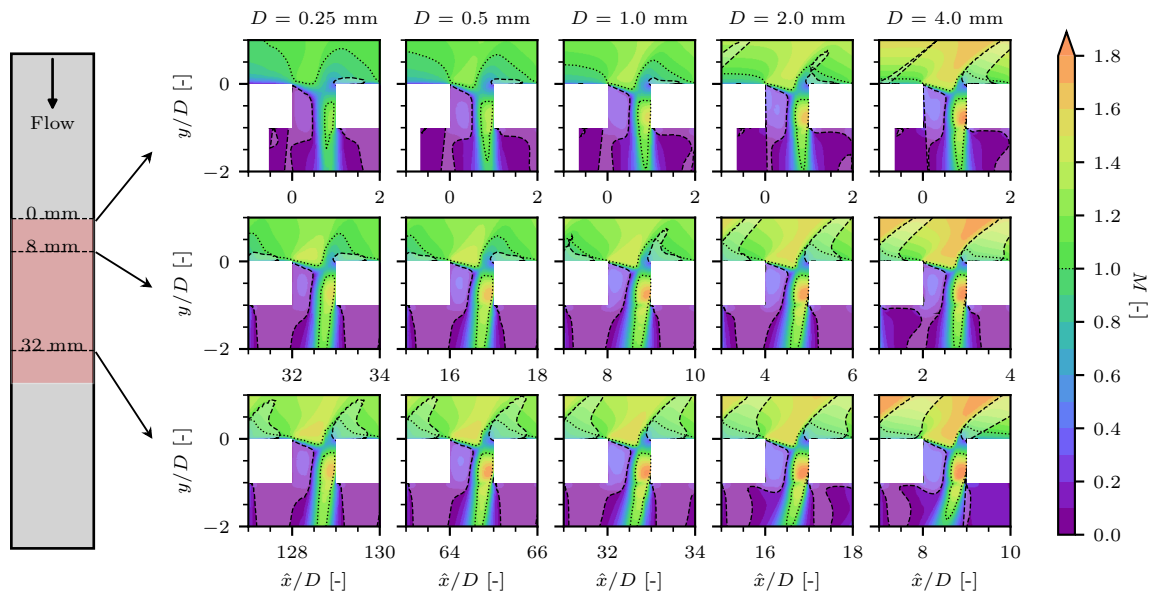


Figure 6.11: Mach number contours of the flow in the bleed holes for different hole diameters at $\hat{x} = 0$ mm, 8 mm, and 32 mm (top to bottom) for $TR = 0.7$; dotted line illustrates sonic line; brightened areas outlined by dashed lines illustrate regions with positive wall-normal flow momentum.

The sonic line is added as a dotted line to the plots as a characteristic indicator of the boundary-layer fullness or quantity of momentum close to the wall. Observing the sonic line in the first row of the figure reveals significant differences in the flow field for different hole diameters. The smaller the hole diameter, the lower the captured momentum since the maximum mass flow rate passing the hole is fixed by the hole area. Thus, small holes enable the sole removal of flow in the very near-wall region with low flow momentum. For the maximum diameter of $D = 4$ mm, the sonic line is relatively close to the wall, illustrating the high momentum in the vicinity of the wall. A strong expansion fan is observed, and the maximum Mach number inside the hole is higher than for smaller diameters. As a consequence, the barrier shock increases in intensity and moves downstream. Thus, higher pressure losses are expected and consequently a lower bleed efficiency.

As a second tool to compare the flow fields, the areas with a positive wall-normal momentum are brightened and outlined by dashed lines. Two significant differences are apparent between the different diameters in the first holes. First, a flow in the upward direction downstream of the rear edge of the holes is visible. This is caused by the stagnation point inside the hole, causing a local blowing into the boundary layer in the rear part of the hole. As a result, the boundary layer thickens locally, which is an undesired effect. The higher the momentum of the flow and the shock intensity of the barrier shock, the larger the upward flow area. Thus, the larger holes have a negative effect on the boundary-layer thinning and lead to a lower-momentum flow in the wall vicinity.

Moreover, the upward flow inside the holes indicates the size of the flow separation in the front, which limits the vena contracta area, and hence, the bleed efficiency. For all hole diameters, the separated region inside the first hole is of similar size. However, the vena contracta area is slightly more constricted for large diameters. Furthermore, the reversed flow has a higher Mach number indicating a higher momentum and more losses.

The second row of Figure 6.11 shows the holes at 20% of the perforated plate length. The flow fields are more similar in all cases, as seen by the position of the sonic line upstream of the hole. The main difference is the shock intensity since the upstream Mach number is again a function of the hole size. Also, the Mach number in the core of the supersonic jet streaming into the plenum is enlarged for increasing diameters. Thus, the losses inside the cavity plenum caused by the under-expanded jet are higher and decrease the bleed efficiency. Moreover, the higher shock intensity leads to a higher wall-normal flow momentum downstream of the hole, independently of the hole size. Thus, all negative effects are enhanced, which goes in line with the findings from Section 6.2.1.

In the last row of Figure 6.11, the flow fields look self-similar for all diameters. The shape of the sonic line is equal, and only the external Mach number is higher for large diameters, which is a result of the higher momentum of the removed flow. However, the areas with a positive wall-normal flow momentum are significantly smaller for small holes, and also the momentum of the backflow inside the holes.

Comparing the changes in the flow field along the plate, a stronger thinning effect is observed for small holes. While the distance of the sonic line to the wall remains constant for large diameters, it moves closer to the wall for small hole diameters. As a consequence, higher control effectiveness is expected for small holes. Additionally, the close-up view of the flowfield inside the holes enables the comparison to the findings of Oorebeek et al. [77]. In their paper, the expansion fan inside the hole is found to become weaker along the bleed region because of an increase in the captured flow momentum. Our results do not confirm this observation. On the contrary, the deflection angle seems to increase along the bleed region faintly, and also with increasing hole diameter. However, the shock angle of the upper part of the barrier shock decreases as the Mach number increases. This effect is mainly apparent for small hole diameters, as the Mach number remains almost constant for larger holes.

The influence of the hole diameter on the bleed efficiency is illustrated in Figure 6.12, where the sonic flow coefficient as a function of the pressure ratio p_{pl}/p_w is shown. As stated in the last section, the wall pressure increases along the plate, which leads to a variation in the pressure ratio and a change in the sonic flow coefficient. The smaller the holes, the more important the variation of the pressure ratio since the number of holes increases along with the thinning effect, leading to a more marked expansion fan at the beginning of the plate.

Observing the first holes, significant differences are apparent. As shown in Figure 6.11, the flow into the holes differs as the sucked flow has a lower momentum for small holes. The vena contracta area is more extensive, which increases the removed mass flow rate and, as a result, the sonic flow coefficient. Moreover, the pressure ratio is higher as the main flow deflection

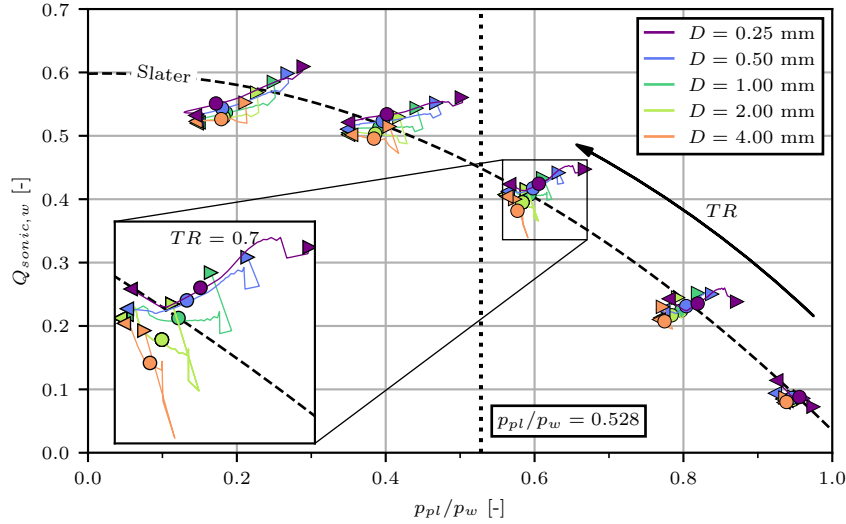


Figure 6.12: Surface sonic flow coefficient for different hole diameters; right triangle (▶) symbolizes the first hole, left triangle (◀) the last hole, and circle (●) the mean value.

caused by the boundary-layer thinning is more distinct. As for the plate length, the higher the throat ratio, the more pronounced the deviation between the different curves.

Interestingly, the differences for the last holes are minor, which can be linked to the self-similarity found in Figure 6.11. As the sucked flow momentum increases along the plate, the sonic flow coefficient decreases as the vena contracta area become smaller. Moreover, the positive slope of the pressure along the plate is higher for small hole diameters resulting in similar conditions for the last holes. However, significant differences in the global flow coefficient for the plates are visible: the smaller the holes, the higher the sonic flow coefficient and the pressure ratio. This effect increases with choking conditions. Our results are in line with the previous results of Eichorn et al. [40] and confirm the influence of the hole diameter on the sonic flow coefficient even for plates with more than one hole.

Next, the boundary-layer profiles downstream of the bleed region are discussed in order to evaluate the control effectiveness. Davis et al. [33] measured significantly fuller boundary-layer profiles using microporous plates compared to the C1 plate used by Willis et al. [117]. Thus, an increase in the control effectiveness is expected for decreasing hole diameters. Figure 6.13 shows the boundary-layer profiles along the span 10 mm downstream of the last hole for three different hole diameters. For all investigated hole diameters, the bleed rate is set to be 107% of the inflow mass deficit. All profiles are normalized by the free-stream streamwise velocity. Moreover, the boundary-layer thickness δ_{99} extracted 10 mm upstream of the holes is used to normalize the wall-normal direction. The boundary-layer thickness is not locally extracted, as the trailing shock induced by the porous bleed may lead to an overestimation.

The gray patch in the back corresponds to the envelope of the boundary-layer profiles along the spanwise direction. The larger the diameter of the holes, the less homogeneous the flow field along the span resulting in locally fuller profiles. The variation of the boundary-layer shape factor is given in Table 6.1. For all diameters, the shape factor is lower compared to the inflow ($H = 1.36$) as intended. However, the profiles downstream of the plate with $D = 0.25$ mm are significantly fuller while using larger holes leads to local spots where no fuller profile is obtained.

Additionally, the variation of the (compressible) displacement thickness is shown in Figure 6.13. The dashed line indicates the inflow displacement thickness ($\delta_{1,c} = 0.87$ mm), and the red area is the one extracted downstream of the bleed region. The area between is colored in green and pinpoints the improvement compared to the inflow. Again, the minimum and

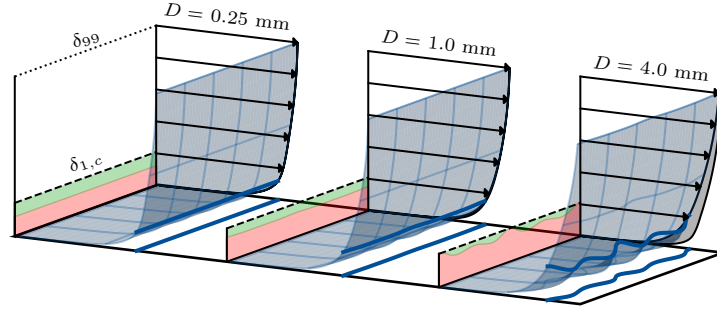


Figure 6.13: Boundary layer 10 mm downstream of the bleed region for $D = 0.25$ mm, 1.00 mm, and 4.00 mm (left to right); gray patch illustrates the envelope of the boundary-layer profiles along the spanwise direction; red area details the compressible displacement thickness and green area the difference to the inflow.

maximum are listed in Table 6.1. We see a similar trend for the displacement thickness as for the shape factor with larger values and variations for big holes. For the $D = 4$ mm holes, even a local reduction of the flow momentum inside the boundary layer is apparent at certain spanwise locations.

D	H_{min}	H_{mean}	H_{max}	$\delta_{1,cmin}$	$\delta_{1,cmean}$	$\delta_{1,cmax}$	$\varepsilon_{\tau min}$	$\varepsilon_{\tau mean}$	$\varepsilon_{\tau max}$
0.25 mm		– 1.25 –			– 0.49 mm –		37.4 %	40.9 %	43.7 %
1.00 mm	1.27	1.28	1.30	0.59 mm	0.60 mm	0.61 mm	18.7 %	28.7 %	34.4 %
4.00 mm	1.25	1.30	1.35	0.64 mm	0.72 mm	0.88 mm	–9.7 %	17.6 %	37.1 %

Table 6.1: Incompressible boundary-layer shape factor, compressible displacement thickness, and rise in the wall shear stress for the boundary-layer profiles shown in Figure 6.13.

The difference in the wall shear stress between the different hole diameters is visualized in Figure 6.14. Again, the bleed rate is kept constant and corresponds to 107 % of the inflow mass deficit. Similar trends as for the boundary-layer profiles are found: the smaller the hole, the higher the increase in the wall shear stress. Even though some local reversed flow is present close to the holes, the smallest holes lead to a significantly more homogeneous wall shear stress distribution downstream of the plate. This is a result of the lower shock intensity of the barrier shock caused by a lower Mach number at the hole entry. The rise in the wall shear stress is, on average, two times greater for $D = 0.25$ mm compared to $D = 4.00$ mm.

Moreover, the wall shear stress varies substantially along the spanwise direction for the largest holes. Downstream of the hole center on the hole-cutting plane, the wall shear stress is negatively affected at some spanwise positions as the higher intensity of the barrier shock leads to a local boundary-layer regrowth. Also, between the holes, the increase of the wall shear stress is significantly lower. On the other hand, local peaks are visible, which is in line with the trend for the boundary-layer displacement thickness. Altogether, the rise in the wall shear stress is of the same order of magnitude as the decrease in the displacement thickness (see Table 6.1), which underpins the use of this value to quantify the control effectiveness.

In the last step, the rise in the wall shear stress is shown as a function of the bleed rate and the plenum pressure in Figure 6.15. Similar to Figure 6.10, higher wall shear stresses are found with an increase in air removal. However, the slope strongly depends on the hole diameter. The smaller the holes, the higher the slope. Thus, the control effectiveness is notably affected by the hole diameter. The same trend is visible in Figure 6.15b, where the rise in the wall shear stress is plotted as a function of the pressure ratio.

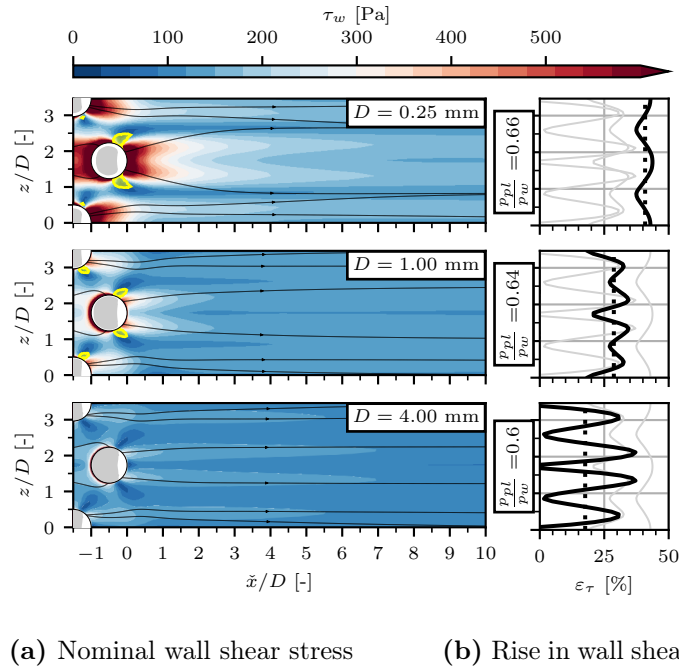
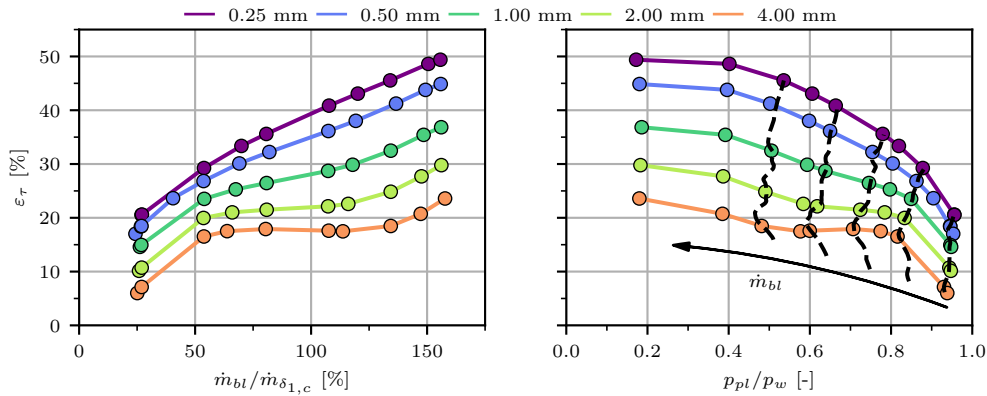


Figure 6.14: Comparison of the wall shear stress downstream of the bleed region for different hole diameters; yellow areas in (a) visualize regions with negative streamwise component and gray areas indicate supersonic hole entry flow; (b) wall shear stress 10 mm downstream of the last hole compared to its value 10 mm upstream of the first hole; dotted line illustrates averaged value along the spanwise direction and gray curves illustrate trends for other values.

We can conclude that there is a clear advantage of using the smallest possible holes for the application of a porous bleed system as small holes increase both bleed efficiency and control effectiveness of the control system. Moreover, the flow downstream of the perforated plate is more homogeneous. On the contrary, too large holes may lead to a decrease in the flow momentum in the wall vicinity.



(a) Rise in wall shear stress as a function of the bleed rate (b) Rise in wall shear stress as a function of the pressure ratio

Figure 6.15: Rise in the wall shear stress as a function of the bleed rate \dot{m}_{bl} and the pressure ratio p_{pl}/p_w for varying hole diameters; dashed lines in (b) pinpoint lines of constant bleed rate.

6.2.3 Porosity Level

The porosity level, which describes the area fraction of holes in the solid wall, is of major importance in removing a required mass flow rate. Low porosity levels result in a lower removable amount of air as the total suction area is small with respect to the plate area. A porosity of 100 % corresponds to a bleed slot, which may have a lower length, but, consequently, also a more localized impact on the flow. In this study, the porosity varies from $\phi = 5.67\%$ to 40.31 % by altering the spacial distance between the holes while keeping the stagger angle and the hole diameter constant (see Figure 2.3). The other parameters (plate length and thickness-to-diameter ratio) are kept constant as well.

The flow field inside the holes is shown in Figure 6.16 for all investigated porosity levels and a throat ratio of $TR = 0.7$. Independently of the porosity, the hole diameter remains constant ($D = 0.5$ mm), which leads to the assumption of equal flow fields in the first holes as the inflow is supersonic, and hence, the upstream influence is small. However, by looking at the first row of Figure 6.16, differences in the flow fields are apparent. The higher the porosity, the more prominent the interaction between the holes. This is visible by following the sonic line, which reveals the position of the barrier shock. As a reference, the sonic line for the lowest porosity is illustrated by the red dash-dotted line. Even though the pressure ratio is similar, the position of the barrier shock is further downstream for high porosities. This is a result of the suction of the subsequent hole, which reduces the back pressure leading to a movement of the shock. A consequence of the further downstream lying barrier shock is a higher shock intensity and a higher Mach number of the flow inside the holes, leading to higher losses.

A second effect of the hole interaction seen in the first row is the smaller longitudinal size of the region of an upward-directed momentum between the holes. The size of the area is limited by the expansion fan of the next hole, which is closer in case of high porosities. Thus, the boundary-layer regrowth is expected to be less pronounced. Also, the trend of the sonic line confirms this assumption as it is located significantly closer to the wall downstream of the holes

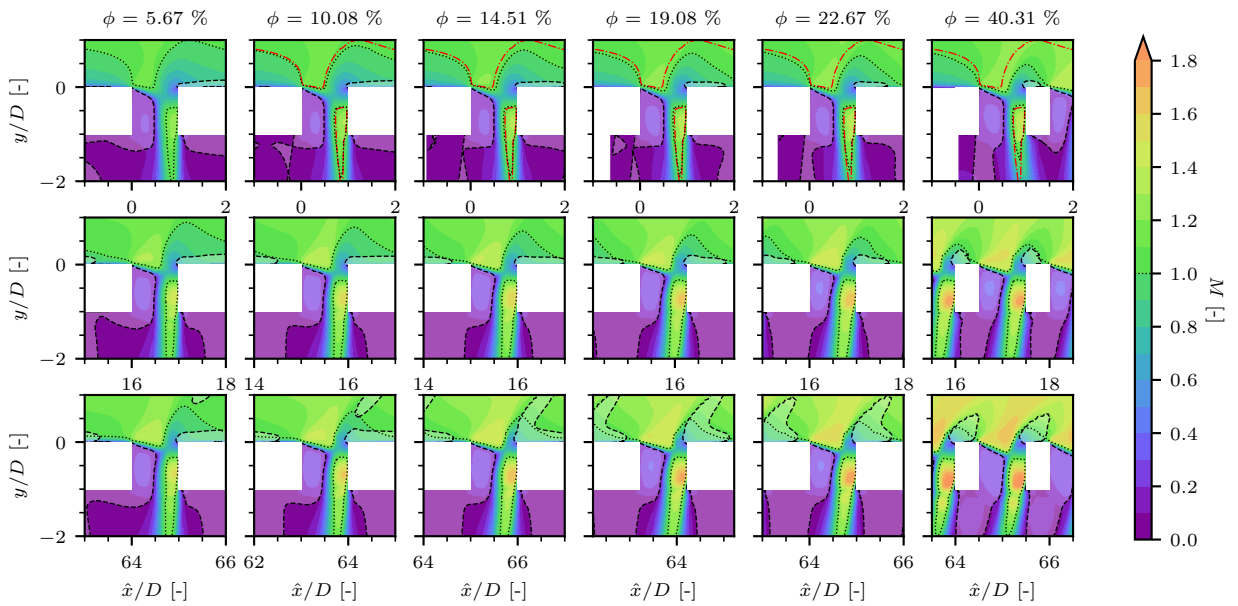


Figure 6.16: Mach number contours of the flow in the bleed holes for different porosity levels at $\hat{x} \approx 0$ mm, 8 mm, and 32 mm (top to bottom) for $TR = 0.7$; dotted line illustrates sonic line; brightened areas outlined by dashed lines illustrate regions with positive wall-normal flow momentum; red dash-dotted line in the first row highlights the sonic line for $\phi = 5.67\%$.

for high porosities.

Further downstream on the plate, the same effects are present, as shown in the second row. The sonic line moves closer to the wall for high porosities. Moreover, the Mach number is higher, and thus the shock intensity is stronger. In the last row, all effects are strengthened. The deflection of the flow inside the holes is the strongest for the highest porosity, which results in a significantly higher Mach number at the entry of the hole. The barrier shock is consequently stronger and located further downstream, with the losses expected to be more significant. Moreover, the sonic line is located closer to the wall, and the area of upward-directed momentum is smaller in size. Hence, higher control effectiveness of large porosities is expected by having a lower bleed efficiency simultaneously.

The locally extracted surface sonic flow coefficient is shown compared to the model of Slater [98] in Figure 6.17. A variation of the pressure ratio along the perforated plate is apparent. The higher the porosity level, the higher the difference in the pressure drop between the first and last holes. This might be explained by the higher pressure losses induced by stronger barrier shocks and the larger number of holes. Moreover, the effect is enhanced for large throat ratios where the drop in the total pressure along the bleed region increases because of enhanced shock intensities with lower pressure ratios.

A second trend is the decrease of the sonic flow coefficient with the position along the plate. This behavior is a function of the porosity and increases for low porosity levels. The explanation can be found in Figure 6.16, where a constriction of the vena contracta area is faintly visible for the downstream lying holes. Interestingly, the sonic flow coefficient slightly increases with the position along the high-porosity plates. It seems that the vena contracta area increases along the plate.

Remarkably, all the points for the first holes lie on one curve. This demonstrates that the first hole is mainly influenced by the diameter, even though an upstream influence of the following holes is observable. In contrast to Figure 6.12 for the hole diameter influence, the points for the last holes do not converge because the bleed mass flux, and hence the thinning of the boundary layer along the plate, are not similar.

The influence of the porosity level on the wall shear stress for a constant bleed rate is detailed in Figure 6.18. Similar to the plate length, porosity has an essential impact on the removable mass flow rate. The lower the porosity, the lower the number of holes. Therefore,

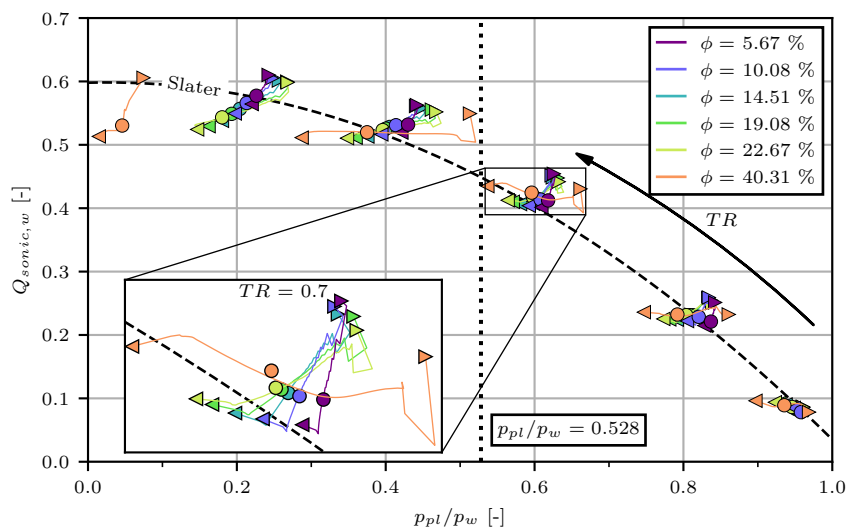


Figure 6.17: Surface sonic flow coefficient for different porosity levels; right triangle (▶) symbolizes the first hole, left triangle (◀) the last hole, and circle (●) the mean value.

lower pressure ratios are required to obtain the same relative bleed rate as in the case of high porosity levels. Figure 6.18 shows the behavior for removing 53% of the mass flow rate computed on the displacement thickness.

The general trend for the effect of the porosity is the following: the higher the porosity, the higher the control effectiveness. The smaller hole spacing is the key parameter, as the area of boundary-layer regrowth decreases. Additionally, an impact of the spanwise distance is apparent, resulting in less homogeneous flow downstream of the perforated plate because of the lower increase of the wall shear stress between the holes. Consequently, the average rise in the wall shear stress is lower. The wall shear stress downstream on the hole-cutting plane is unaffected and similar for different porosity levels. Only for very low porosity is a lower shear stress rise observed as the intensity of the barrier shock is significantly higher.

As stated in the previous section, a smaller increase in the wall shear stress corresponds to boundary layers with a greater shape factor. A more homogeneous boundary layer along the span is present in the case of high porosities. On the contrary, lower porosities result in higher

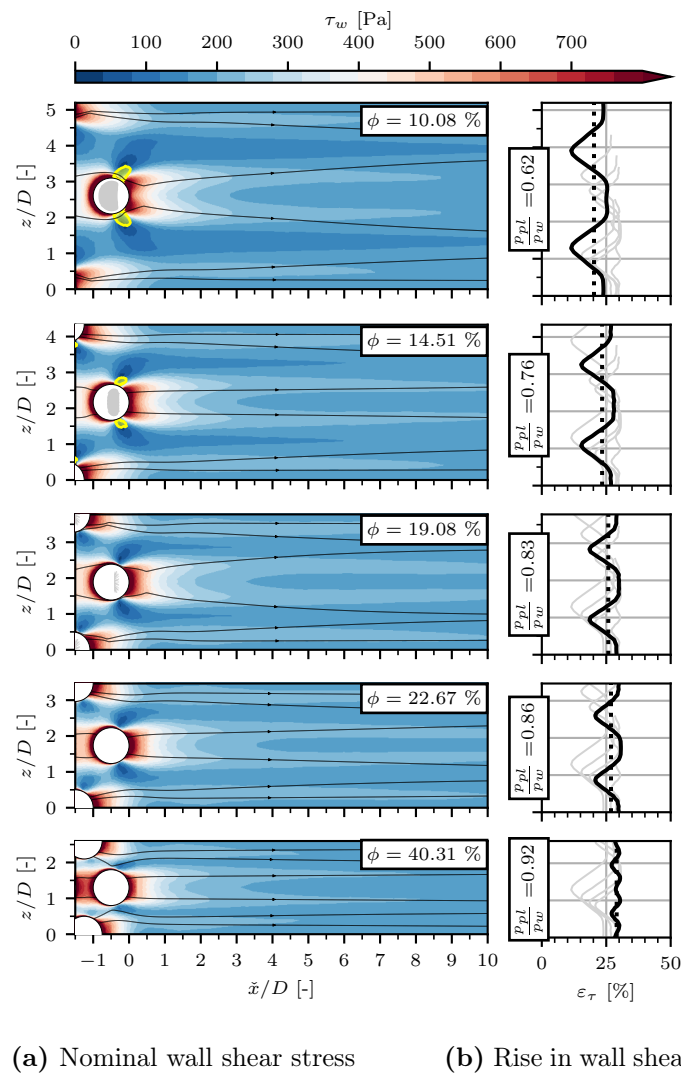
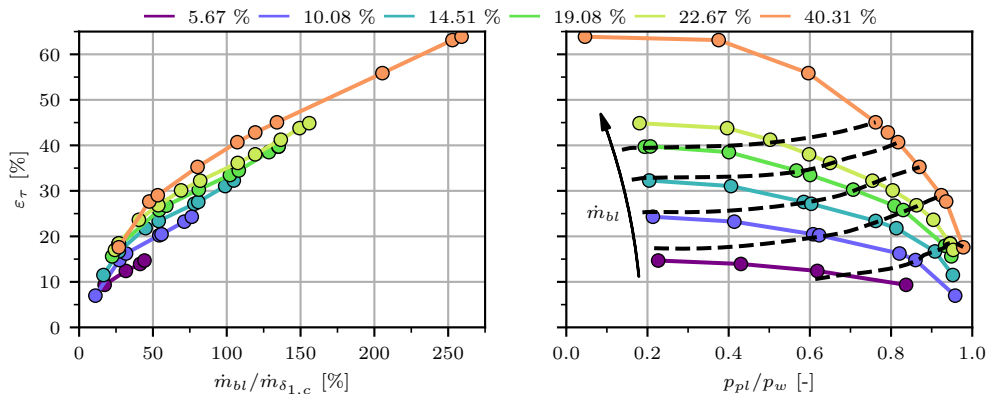


Figure 6.18: Comparison of the wall shear stress downstream of the bleed region for different porosities; yellow areas in (a) visualize regions with negative streamwise component and gray areas indicate supersonic hole entry flow; (b) wall shear stress 10 mm ($20D$) downstream of the last hole compared to its value 10 mm upstream of the first hole; dotted line illustrates averaged value along the spanwise direction and gray curves illustrate trends for other values.

variations in the spanwise directions as we find higher variations in the rise in the wall shear stress. Thus, fuller profiles are found downstream of the bleed holes, while the suction less affects the flow between the holes.

The evaluation for different bleed rates is visualized in Figure 6.19. As already stated, a large porosity increases the maximal bleed rate for a given pressure ratio since the open area increases. Figure 6.19a demonstrates this effect. A higher control effectiveness for large porosities is revealed in Figure 6.19b, where the dashed line illustrates constant bleed rates. Similar to the graph for the plate length, the best effect is achieved for pressure ratios $p_{pl}/p_w \approx 0.9$. For choking conditions, the thinning of the boundary layer is lower.



(a) Rise in wall shear stress as a function of the bleed rate (b) Rise in wall shear stress as a function of the pressure ratio

Figure 6.19: Rise in the wall shear stress as a function of the bleed rate \dot{m}_{bl} and the pressure ratio p_{pl}/p_w for varying porosities; dashed lines in (b) pinpoint lines of constant bleed rate.

For the application in supersonic air intakes, similar conclusions as for the plate length can be drawn. Generally, high porosity levels have a higher control effectiveness even though the bleed efficiency is lower as the pressure losses are increased. Again, high pressure ratios (unchoked conditions) are found to be preferable. To sum up, both porosity and plate length are parameters with a significant influence on the mass flow rate that can be removed. If high mass flow rates are required to be reduced on a small area, small plates with high porosities are recommended, whereas small porosities are preferable for large plates in combination with low mass flow rates as pressure fluctuations in the external flow might lead to blowing.

6.2.4 Thickness-to-Diameter Ratio

The influence of the thickness-to-diameter ratio is considered in several existing bleed models [54, 61]. However, the flow topology that causes the change in the bleed efficiency has not been sufficiently regarded. Therefore, the thickness-to-diameter ratio is varied from 0.5 to 8 in this study. In contrast to the previous sections, the hole diameter is increased to 1.0 mm to reduce the mesh size and computational costs.

The influence of the thickness-to-diameter ratio on the sonic flow coefficient is detailed in Figure 6.20. Significant differences are apparent depending on the pressure ratio. For high pressure ratios, higher sonic flow coefficients and pressure ratios are found for high thickness-to-diameter ratios. The maximum pressure ratio and sonic flow coefficient are found to be around $T/D = 6$. A very low T/D leads to a major degradation of bleed efficiency.

Interestingly, the trend is inverted for choking conditions, where higher sonic flow coefficients are obtained for small T/D . For $p_{pl}/p_w \approx 0.2$, the sonic flow coefficient for the thinnest plate

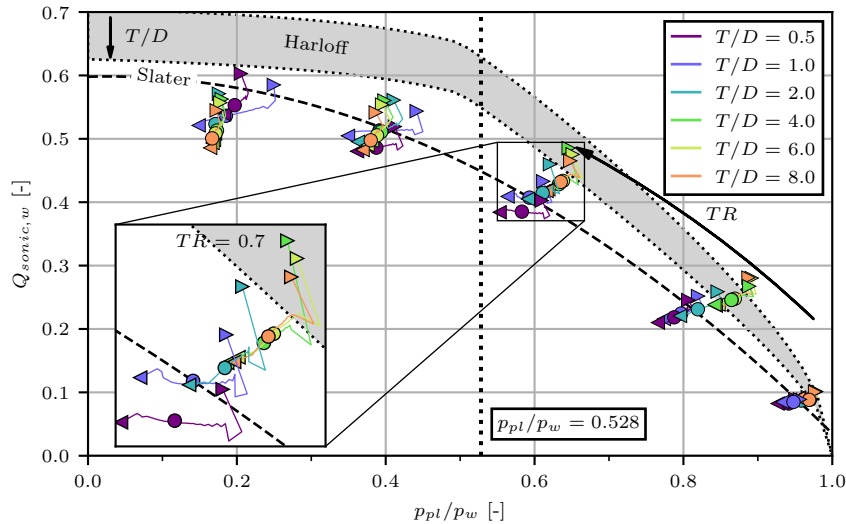


Figure 6.20: Surface sonic flow coefficient for different thickness-to-diameter ratios; right triangle (\blacktriangleright) symbolizes the first hole, left triangle (\blacktriangleleft) the last hole, and circle (\bullet) the mean value.

is approximately 10 % higher than for the thickest plate. On the contrary, for $p_{pl}/p_w \approx 0.6$, the sonic flow coefficient for the thinnest plate is more than 10 % lower compared to the thickest plates.

Moreover, significant differences in the pressure ratios are apparent for unchoked conditions (low TR). This results from higher pressure losses caused by the flow inside the holes. In order to explain it, the wall shear stress and the friction lines inside the holes are visualized in Figure 6.21 for $T/D = 1, 2, \text{ and } 4$ (top to bottom) and $TR = 0.3, 0.7, \text{ and } 1.3$ (left to right). The holes are shown from the bottom-up view, and the external flow goes from the left to the right. The gray patches represent the external wall with the friction lines around the holes illustrated. Inside the holes, the wall shear stress contours in the vertical direction (the main direction of the transpiration flow) are presented on the wall. The dashed lines present the $\tau_{w,y} = 0$ isolines to highlight the areas of reversed flow, the solid lines the friction lines on the anterior face. Moreover, the separated areas on the hole-cutting plane are illustrated by the blue patches.

The first column of Figure 6.21 shows the flow inside the holes for large pressure ratios where high throat-to-diameter ratios are beneficial. Inside the holes, a large separated area is observed independently of the plate thickness. However, its size on the hole-cutting plane decreases with further distance to the hole entry. For a ratio $T/D = 4$, the separated region is almost closed; thus, only a small amount of flow streams from the cavity plenum inside the hole. In contrast, a significant fraction of the outlet cross section for thin plates is covered by reversed flow streaming into the hole. It is assumed that higher pressure losses are a consequence and lead to lower pressure ratios compared to higher thickness-to-diameter ratios, as shown in Figure 6.20. Moreover, all mass sucked from the cavity plenum into the hole must also exit the hole again. As a result, the bleed rate is assumed to be lower, as indicated by the sonic flow coefficient.

In the second column, similar effects are apparent even though the pressure ratio is lower as the throat ratio increases. The shape of the separated region on the hole-cutting plane is equal for all plate thicknesses. However, a strong bending of the friction lines close to the hole entry towards the front of the hole is notable. Consequently, the wall areas with negative shear stress decrease in size compared to those with larger pressure ratios. Thus, less air streams from the cavity plenum into the hole independently of the thickness, which explains the lower

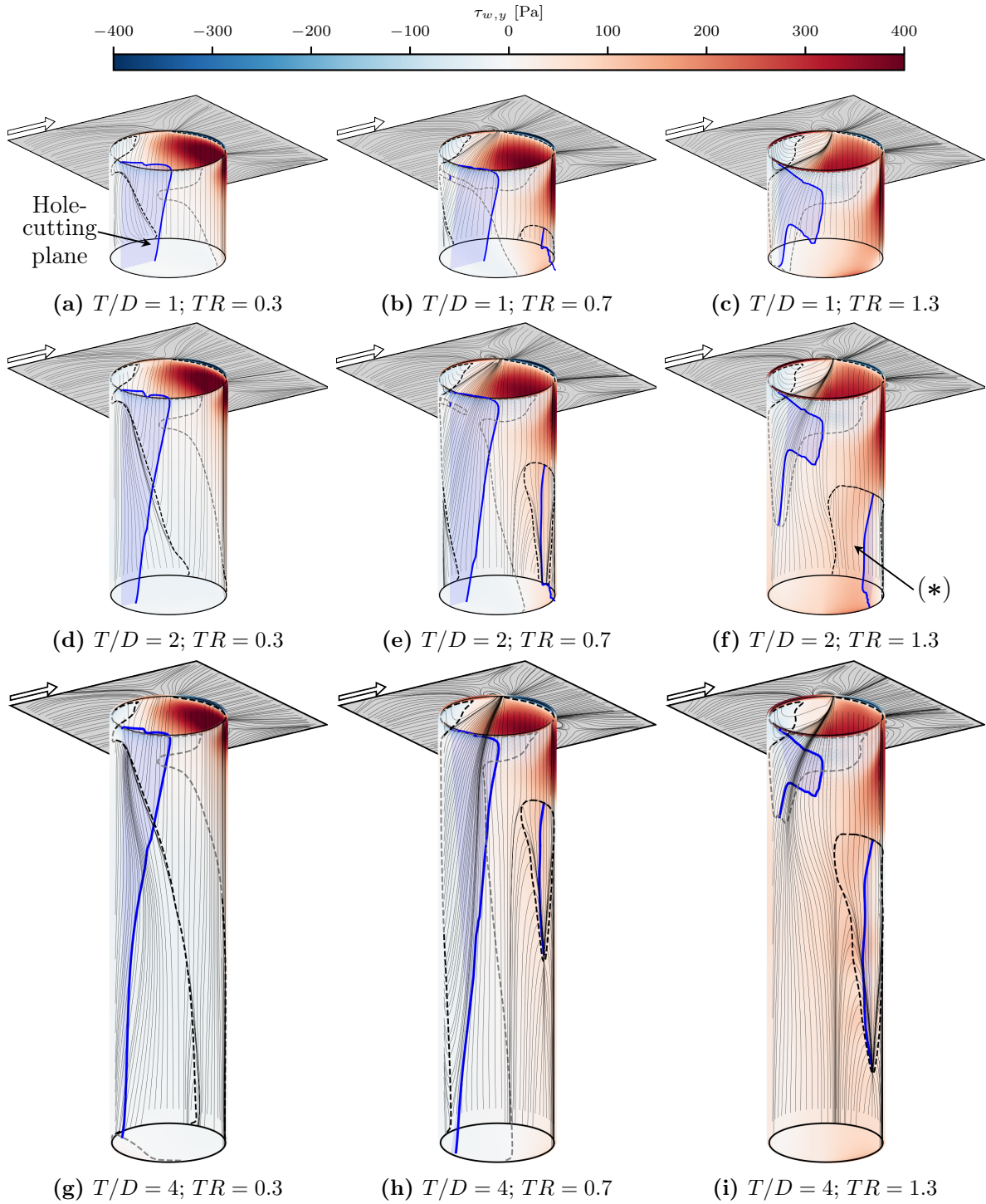


Figure 6.21: Wall shear stress inside the holes at $\hat{x} = 8 \text{ mm}$ ($16D$); dashed lines illustrate $\tau_{w,y} = 0 \text{ Pa}$ isolines; blue patches visualize areas with upward-directed momentum on the hole-cutting plane.

differences between the thickness-to-diameter ratios, as shown in Figure 6.20.

The last column illustrates the throat ratio $TR = 1.3$, corresponding to $p_{pl}/p_w \approx 0.4$. According to Figure 6.20, a ratio of $T/D = 1$ results in the highest sonic flow coefficient. Contrary to higher pressure ratios, the separated region in the front of the holes is closed, even for the thinnest plate. Thus, there is only a recirculation of flow inside the hole but no suction from the cavity plenum. As a result, the sonic flow coefficient is higher. For $T/D = 2$, the sonic flow coefficient is the lowest.

In contrast to the thinnest plate, a second separated area at the rear of the hole is present (*), which causes a flow from the cavity plenum into the hole. Also, a second separated area is apparent for the thickest plate. However, it is closed, and the flow is fully attached at the hole outlet leading to an increase in the sonic flow coefficient. Nevertheless, the pressure ratio is slightly lower than for $T/D = 1$, resulting from friction drag losses inside the hole because of the longer length of the attached flow.

Our findings do not support the assumption of Harloff and Smith [61] that ratios $T/D > 3$ lead to a degradation of the sonic flow coefficient, as shown in Figure 6.20. In contrast, higher thickness-to-diameter ratios improve the performance of the porous bleed for unchoked conditions. Interestingly, the thickness-to-diameter ratio has no significant effect on the external flow. As apparent in Figure 6.21, the friction lines on the external wall are almost identical, independent of the plate thickness. Also, only marginal differences in the wall shear stress are notable downstream of the porous bleed region, leading to the conclusion of no significant influence of the thickness-to-diameter ratio on the control effectiveness of the porous bleed.

For the design of a porous bleed system, the thickness-to-diameter ratio has to be selected according to the desired pressure ratio. For choked conditions, thin plates are preferable as the friction losses inside the holes may be high. On the contrary, if the bleed operates mainly in unchoked conditions, longer holes are advantageous because the pressure losses are significantly lower.

6.2.5 Stagger Angle

The last investigated parameter is the stagger angle which defines the hole pattern on the plate. In this study, the angle takes values of 30° , 45° , 60° , and 90° . The plates with $\beta = 30^\circ$ and $\beta = 60^\circ$ are equal with the holes arranged in the shape of an equilateral triangle but rotated by 90° . For the plates with $\beta = 45^\circ$ and $\beta = 90^\circ$, the holes are arranged in a square shape. Thus, every second column of holes is located at the same streamwise position.

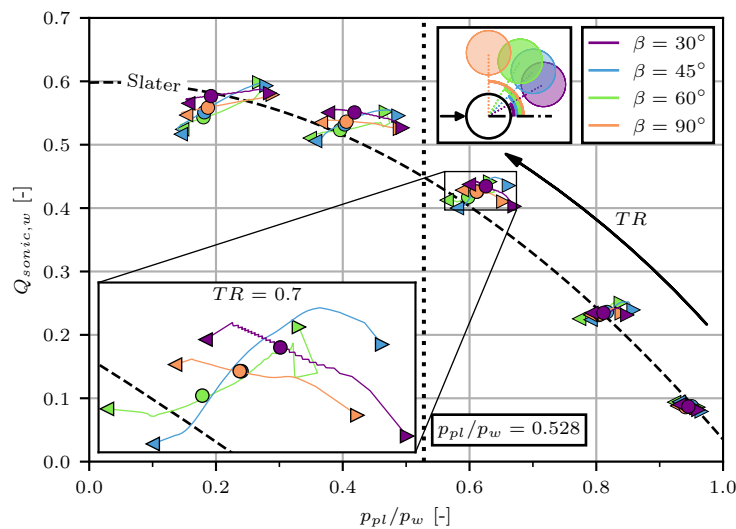
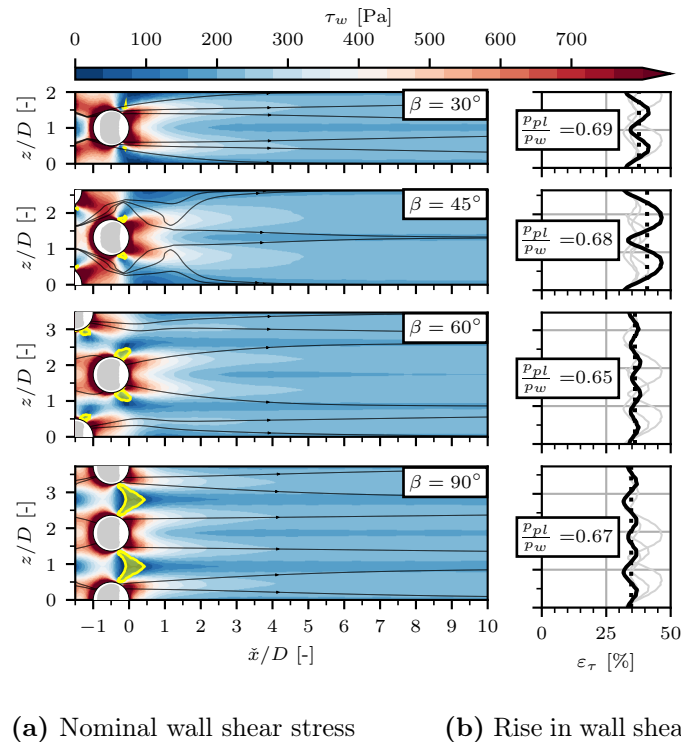


Figure 6.22: Surface sonic flow coefficient for different stagger angles; right triangle (▶) symbolizes the first hole, left triangle (◀) the last hole, and circle (●) the mean value.

The surface sonic flow coefficient for the different stagger angles is shown in Figure 6.22. Independently of the pressure ratio, the mean sonic flow coefficient is highest for $\beta = 30^\circ$ and lowest for 60° even though the plates are identical but only rotated. This results from the longer streamwise distance between the holes that induces a lower momentum upstream of the

hole as the wall area where the boundary layer regrows is longer. However, the opposite trend is found for the first holes. There, the spanwise distance is assumed to be more relevant, which is in line with the findings from Section 5.1.1, where the degradation of the sonic flow coefficient is stated for multi-column plates.

The wall shear stress downstream of the perforated plate for the different stagger angles is visualized in Figure 6.23. The removed bleed rate corresponds to 107% of the inflow mass deficit. Similar to the sonic flow coefficient, the variation of the span- and streamwise distances between the holes lead to a variation in the control effectiveness. The smaller the spanwise distance, the lower the size of the area with the reversed flow. This leads to a more significant rise in wall shear stress.



(a) Nominal wall shear stress (b) Rise in wall shear stress

Figure 6.23: Comparison of the wall shear stress downstream of the bleed region for different stagger angles; yellow areas in (a) visualize regions with negative streamwise component; (b) wall shear stress 10 mm ($20D$) downstream of the last hole compared to its value 10 mm upstream of the first hole; dotted line illustrates averaged value along the spanwise direction and gray curves illustrate trends for other values.

However, with lower spanwise distances between the holes, also the intensity of the barrier shock increases, which leads, in turn to a decrease in the wall shear stress on the hole-cutting plane downstream of the holes. Consequently, the flow field downstream of the plate is less homogeneous. For $\beta = 45^\circ$, the highest rise in the wall shear stress is found but with the most extensive variations along the spanwise direction. The plates with a stagger angle of 60° and 90° affect the flow more homogeneously but less drastically.

Altogether, a stagger angle of $\beta = 60^\circ$ is unfavorable for the application of porous bleed as both bleed efficiency and control effectiveness are low compared to other patterns. Smaller angles lead to a more effective but less homogeneous control. A stagger angle of $\beta = 45^\circ$ is the most effective and a stagger angle of $\beta = 30^\circ$ is the most efficient one.

6.2.6 Comparison of all Geometrical Parameters

The influence of all the investigated parameters on the sonic flow coefficient is gathered in Figure 6.24. The colored lines show the global trend of the plates for a variation of one parameter, and the gray circles represent the spreading of all locally extracted sonic flow coefficients. The arrows show the direction in which the parameter grows. It must be noted that the thickness-to-diameter ratio and the stagger angle show no steady trend but have an optimum with the result of the highest value not being equal to the maximum or minimum. The global trends are generally similar: an increase in the plate length or hole diameter leads to lower sonic flow coefficients and pressure ratios. Thus, lower values are more efficient. Also, the pressure ratio decreases for higher porosities. However, the sonic flow coefficient is less affected and slightly increases for high pressure ratios. As stated in the previous section, the best stagger angle regarding the bleed efficiency is $\beta = 30^\circ$, resulting in lower flow coefficients and plenum pressures for other values. High thickness-to-diameter ratios are preferable for high pressure ratios, while thin plates are more efficient for choked conditions.

While the global data is close to the regression of Slater [98], the local values can drastically differ from this trend. For a throat ratio of $TR = 0.7$, the model of Slater [98], as well as other state-of-the-art bleed models, are not able to take the spreading of the sonic flow coefficient, corresponding to more than 35 % of the estimated value, into account. For other parameter combinations, the deviation might be even higher.

The differences between the investigated perforated plates are more significant if the control effectiveness is regarded, as visualized in Figure 6.25. Colored lines represent a parameter variation for a fixed bleed rate. A steep slope of a line highlights a strong parameter impact on the control effectiveness. For example, large hole diameters result in a significantly lower thinning of the boundary layer and hence in a weaker rise in the wall shear stress. On the contrary, the thickness-to-diameter ratio does not affect the thinning of the boundary layer. However, the required plenum pressure to obtain the desired effect differs depending on the bleed efficiency.

Altogether, the parameter can be ranked regarding control effectiveness: the hole diameter has the most decisive impact, followed by porosity, stagger angle, plate length, and the thickness-to-diameter ratio having the lowest influence.

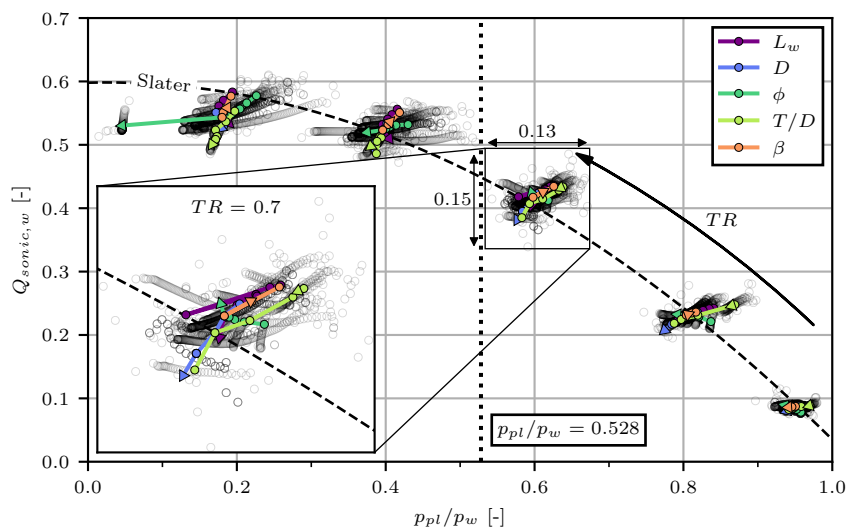


Figure 6.24: Surface sonic flow coefficient for all parameters for supersonic conditions; right triangle (▶) symbolizes the first hole, left triangle (◀) the last hole, and circle (●) the mean value.

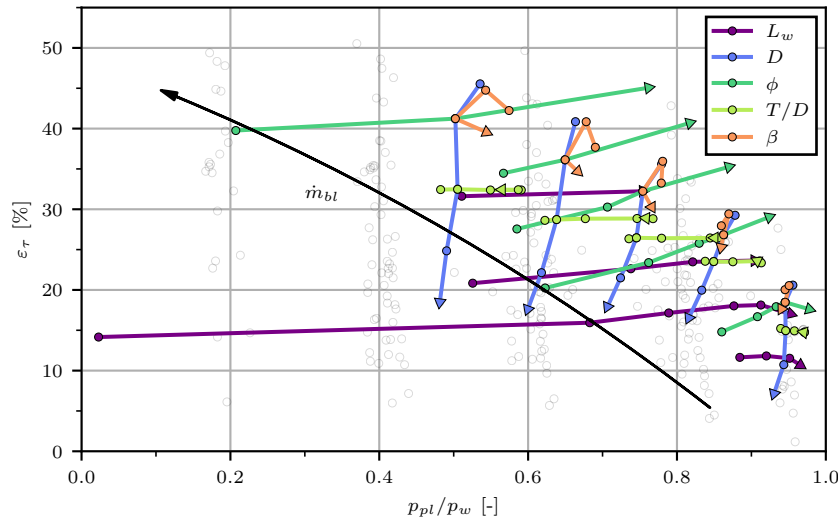


Figure 6.25: Rise in the wall shear stress for all parameters for supersonic conditions.

Table 6.2 highlights the impact of all parameters on bleed efficiency and control effectiveness. Moreover, the recommendations for the application of porous bleed systems, as mentioned in the previous sections, are stated. As discussed earlier, the stagger angle has no general trend for increasing values. Therefore, the optimums in terms of bleed efficiency and control effectiveness are indicated, even though the flow field becomes less homogeneous for the most efficient and effective control.

Parameter	Bleed efficiency	Control effectiveness	Application recommendation
$L_w \nearrow$	\searrow	\nearrow	$p_{pl}/p_w \sim 0.9$
$D \nearrow$	\searrow	\searrow	Small D
$\phi \nearrow$	\searrow	\nearrow	$p_{pl}/p_w \sim 0.9$
$T/D \nearrow$	\nearrow (unchoked)	—	$T/D \sim 4$ (unchoked)
	\searrow (choked)		$T/D \sim 1$ (choked)
β	$\beta = 30^\circ$	$\beta = 45^\circ$	$\beta = [30^\circ, 45^\circ] \rightarrow$ less homogeneous flow

Table 6.2: Trends on bleed efficiency and control effectiveness and recommendations for all investigated parameters for supersonic conditions.

6.3 Geometry Influence on Subsonic Boundary-Layer Bleed

Parameter influences on bleed efficiency and control effectiveness for subsonic conditions are explained in the following. The inflow Mach number is fixed to $M = 0.6$. Again, only one parameter is varied to isolate its effect. The default plate has a shorter length of $L_w = 12$ mm, a hole diameter $D = 0.5$ mm, a porosity $\phi = 22.67\%$, a thickness-to-diameter ratio $T/D = 1$, and a stagger angle $\beta = 60^\circ$. As illustrated in Figure 6.2, the captured stream tube is significantly larger than for supersonic flows, which is the reason for the smaller size of the perforated plate.

6.3.1 Plate Length

The first observed parameter is the plate length, which is varied from 2 mm to 40 mm. All other geometrical parameters are kept constant and the bleed rate is fixed using a constant throat ratio. The (static) external wall pressure and the plenum pressure are shown in Figure 6.26. An external pressure rise along the perforated plate is induced by the diffuser effect, resulting in a deceleration of the flow. The longer the plate, the higher the pressure rise, which is caused by the higher removed mass, and in turn, the increased diffuser effect. Moreover, a lower wall pressure is found at the beginning of the plate for longer plates. Because of the upstream influence in subsonic conditions, the flow is already accelerated before the plate. The higher the bleed rate, the more significant the upstream acceleration of the flow. Thus, the wall pressure around the first holes decreases with the plate length.

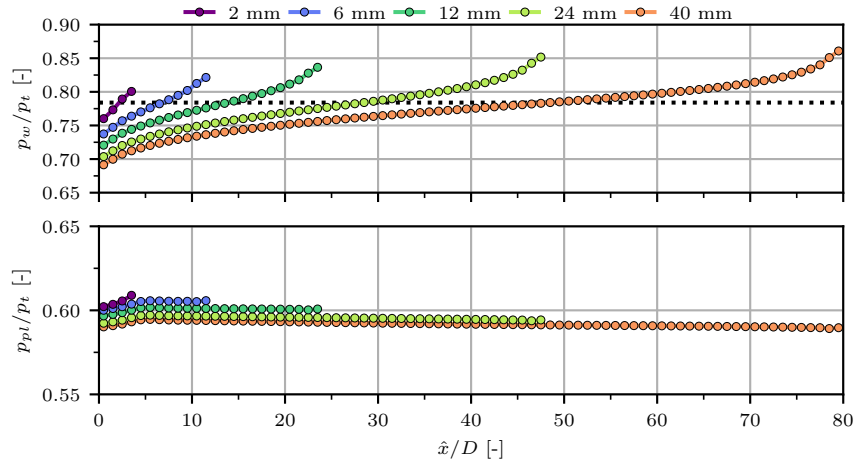


Figure 6.26: Static external wall and plenum pressure for different plate lengths ($TR = 0.7$); the dotted line highlights the isentropic pressure ratio for $M = 0.6$.

Moreover, the plenum pressure is illustrated in the lower part of Figure 6.26. A negligible variation of the plenum pressure inside the cavity plenum is observed compared to the wall pressure. Thus, the plenum pressure can be assumed as constant. Furthermore, a higher plenum pressure is found for smaller plates, which is probably caused by the stronger acceleration of the flow upstream of the bleed, resulting in a larger separated region inside the holes. Thus, the pressure losses are increased, and the plenum pressure decreases.

A low impact of the plate length on the surface sonic flow coefficient is found, as shown in Figure 6.27. The longer the plate, the higher the variation of the pressure ratio p_{pl}/p_w and the sonic flow coefficient along the bleed region. The global sonic flow coefficient is found to be lower for long plates, which is a result of the stronger flow acceleration upstream of the bleed, resulting in an enlarged flow separation in the first holes. The computed surface sonic flow

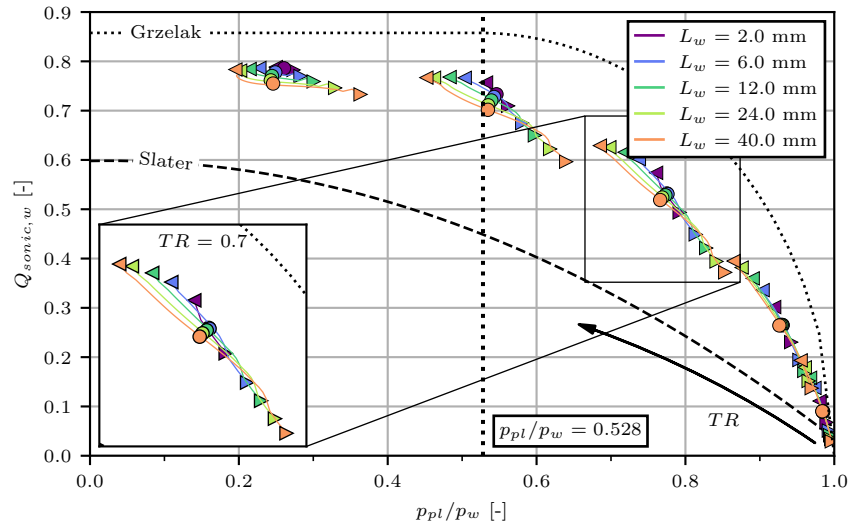
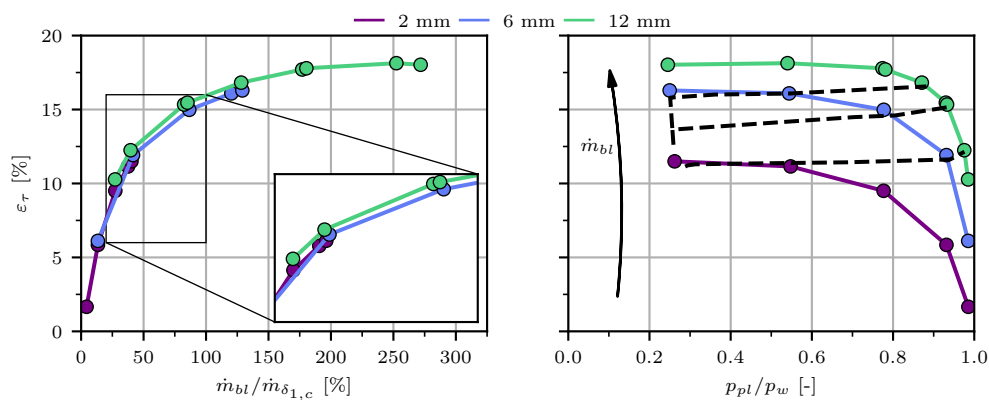


Figure 6.27: Surface sonic flow coefficient for different plate lengths; right triangle (\blacktriangleright) symbolizes the first hole, left triangle (\blacktriangleleft) the last hole, and circle (\bullet) the mean value.

coefficients are significantly higher than the estimated flow coefficient by using the model of Slater [98], but lower than for the model of Grzelak et al. [54]. This is expected as the models are validated for supersonic flow and no external flow, respectively.

Finally, the impact of the plate length on the control effectiveness is evaluated. Again, the rise in the wall shear stress from upstream to downstream is computed and shown in Figure 6.28. Please note, that this evaluation is challenging for subsonic conditions as the bleed creates an acceleration of the flow even upstream of the bleed. The higher the bleed rate, the stronger the acceleration. Hence, the rise in the wall shear stress might be underestimated. Moreover, strong bleed rates result in a significant deceleration of the flow, and thus, a lower wall shear stress downstream of the bleed. For this reason, only short plates up to 12 mm are considered for the comparison.

The plate length has no significant influence on the rise in the wall shear stress, as visible in Figure 6.28a. All curves are overlapping, highlighting that the rise is only a function of the



(a) Rise in wall shear stress as a function of the bleed rate

(b) Rise in wall shear stress as a function of the pressure ratio

Figure 6.28: Rise in the wall shear stress as a function of the bleed rate \dot{m}_{bl} and the pressure ratio p_{pl}/p_w for varying plate lengths; dashed lines in (b) pinpoint lines of constant bleed rate.

bleed rate and not the plate length. Moreover, the maximum rise in the wall shear stress seems to be limited. On the right side (Figure 6.28b), the rise in the wall shear stress is visualized as a function of the pressure ratio p_{pl}/p_w . The higher the plate length, the higher the maximum bleed rate as the open surface increases. However, the maximal rise is already achieved for high pressure ratios $p_{pl}/p_w \approx 0.7$.

For the application, it can be stated that short plate lengths are preferable as the sonic flow coefficient is slightly increased, and high control effectiveness is achieved even for small sizes.

6.3.2 Hole Diameter

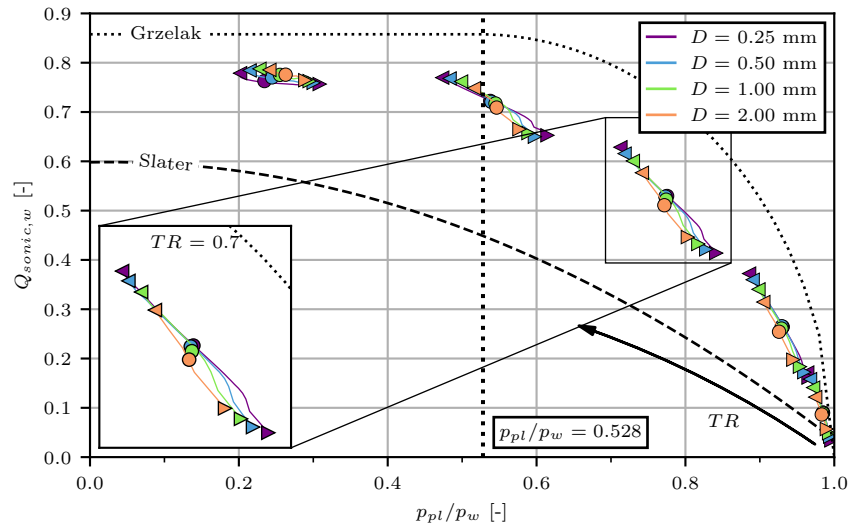


Figure 6.29: Surface sonic flow coefficient for different hole diameters; right triangle (\blacktriangleright) symbolizes the first hole, left triangle (\blacktriangleleft) the last hole, and circle (\bullet) the mean value.

The hole diameter is the second observed geometrical parameter. Its influence on the bleed efficiency can be seen in the surface sonic flow coefficient in Figure 6.29. Similar to the plate length, the impact of the hole diameter is small. For unchoked conditions, small holes are slightly more efficient, while larger holes are preferable for choked conditions. However, the differences are negligible.

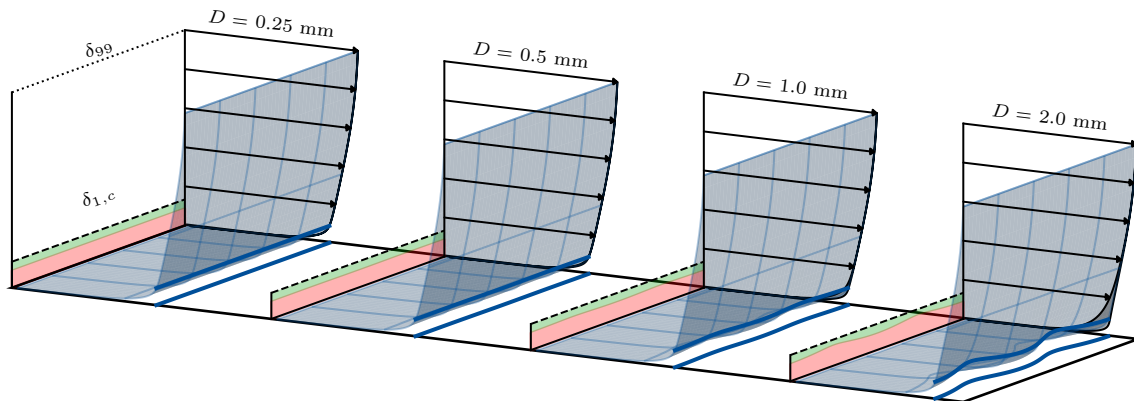


Figure 6.30: Boundary layer 10 mm downstream of the bleed region for $D = 0.25$ mm, 0.50 mm, 1.00 mm, and 2.00 mm (left to right); gray patch illustrates the envelope of the boundary-layer profiles along the spanwise direction; red area represents the compressible displacement thickness and green area the difference to the inflow.

D	H_{min}	H_{mean}	H_{max}	$\delta_{1,cmin}$	$\delta_{1,cmean}$	$\delta_{1,cmax}$	$\varepsilon_{\tau_{min}}$	$\varepsilon_{\tau_{mean}}$	$\varepsilon_{\tau_{max}}$
0.25 mm		- 1.21	-		- 0.48 mm	-	15.7 %	16.4 %	17.2 %
0.50 mm	1.20	1.21	1.21		- 0.48 mm	-	14.6 %	16.3 %	17.9 %
1.00 mm	1.20	1.21	1.23	0.48 mm	0.49 mm	0.50 mm	10.0 %	16.5 %	21.6 %
2.00 mm	1.18	1.22	1.27	0.46 mm	0.51 mm	0.57 mm	-1.7 %	16.5 %	31.5 %

Table 6.3: Incompressible boundary-layer shape factor, compressible displacement thickness, and rise in the wall shear stress for the boundary-layer profiles shown in Figure 6.30.

On the contrary, the hole diameter has, like in supersonic conditions, a large influence on the boundary-layer profiles downstream of the bleed region, and hence, on the control effectiveness. Figure 6.30 illustrates the profiles along the span downstream of the plate. Again, the displacement thickness is compared to that upstream of the bleed region. The bleed rate is kept constant independently of the hole diameter for a rigorous comparison ($\dot{m}_{bl}/\dot{m}_{\delta_{1,c}} \approx 176\%$). The gray patch at the back illustrates the envelope of the boundary-layer profiles.

For all hole diameters, the displacement thickness seems to be reduced by approximately the same amount. However, large holes are found to produce a less homogeneous flow along the span, as it is already found for supersonic flow conditions. The larger the hole diameter, the stronger the variations in the boundary-layer profiles along the span.

Table 6.3 lists the boundary-layer properties for the profiles shown in Figure 6.30. Inter-

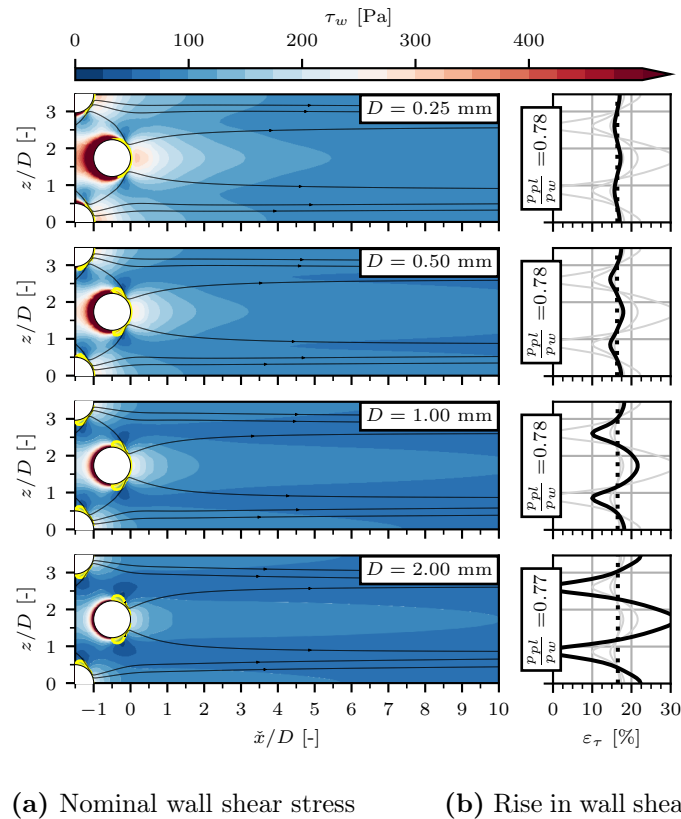
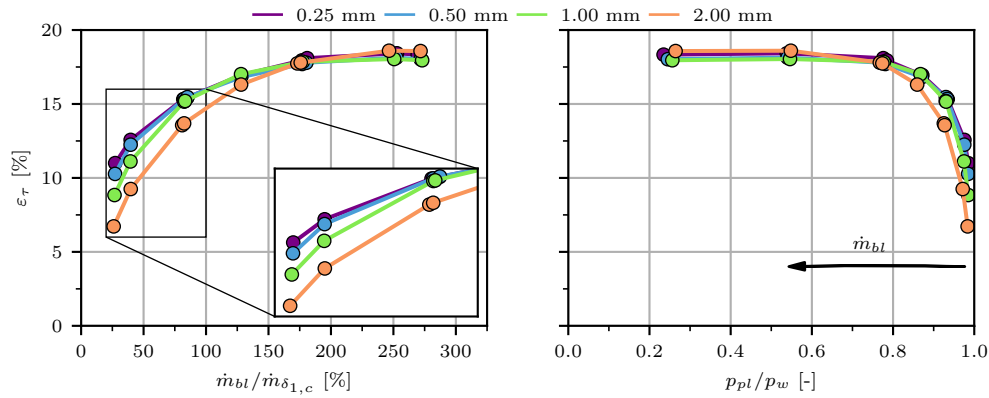


Figure 6.31: Comparison of the wall shear stress downstream of the bleed region for different hole diameters; yellow areas in (a) visualize regions with negative streamwise component and gray areas indicate supersonic hole entry flow; (b) wall shear stress 10 mm downstream of the last hole compared to its value 10 mm upstream of the first hole; dotted line illustrates averaged value along the spanwise direction and gray curves illustrate trends for other values.



(a) Rise in wall shear stress as a function of the bleed rate

(b) Rise in wall shear stress as a function of the pressure ratio

Figure 6.32: Rise in the wall shear stress as a function of the bleed rate \dot{m}_{bl} and the pressure ratio p_{pl}/p_w for varying hole diameter; dashed lines in (b) pinpoint lines of constant bleed rate.

estingly, even though strong variations along the span are observed for larger bleed holes, the averaged shape factor of the downstream boundary-layer profiles is approximately the same. Also, the displacement thickness does not significantly vary along the spanwise direction. Thus, the effect of the hole diameter on the boundary layer is weaker than for supersonic flows.

More significant is the diameter effect on the wall shear stress as seen in Figure 6.31 for a fixed bleed rate. Downstream of the bleed region, the wall shear stress is found to be homogeneous for small holes, as shown in Figure 6.31a. This is also apparent in the rise in the wall shear stress (Figure 6.31b).

With increasing hole size, a growing area of reversed flow is found at the side of the holes, as highlighted by the yellow patches. While the area of reversed flow leads to an increase in the wall shear stress and a more homogeneous flow for supersonic conditions (see Figure 6.14), it induces areas of low flow momentum between the holes for subsonic conditions. Consequently, the rise in the wall shear stress is smaller in this area. The larger the holes, the more pronounced this effect, resulting in significant variation along the span. Compared to the supersonic boundary-layer bleed (see Section 6.2.2), this effect is more significant even though the mean value is not affected, as seen in Table 6.3.

The overall trend for the increase in the wall shear stress is shown in Figure 6.32. A diameter influence is found for high pressure ratios ($p_{pl}/p_w > 0.8$), where small hole diameters lead to a higher increase in the wall shear stress along the bleed region for the same bleed rate. However, for lower pressure ratios the hole diameter does not influence the control effectiveness. However, the boundary layer downstream of the bleed is observed to be less homogeneous.

Small hole diameters may have advantages if the bleed system is applied to subsonic flows and high pressure ratios. For the control of SBLIs, where the pressure ratio is downstream of the incident shock generally low, no trend is found, and the hole diameter influence is negligible.

6.3.3 Porosity Level

The influence of the porosity level on the surface sonic flow coefficient is low, as seen in Figure 6.33. The observations of Grzelak et al. [54], finding a significant positive influence of the porosity ratio, can not be confirmed. However, their model is based on data without external flow, which may be the reason for different trends.

The higher the porosity level, the larger the open area, resulting in higher bleed rates.

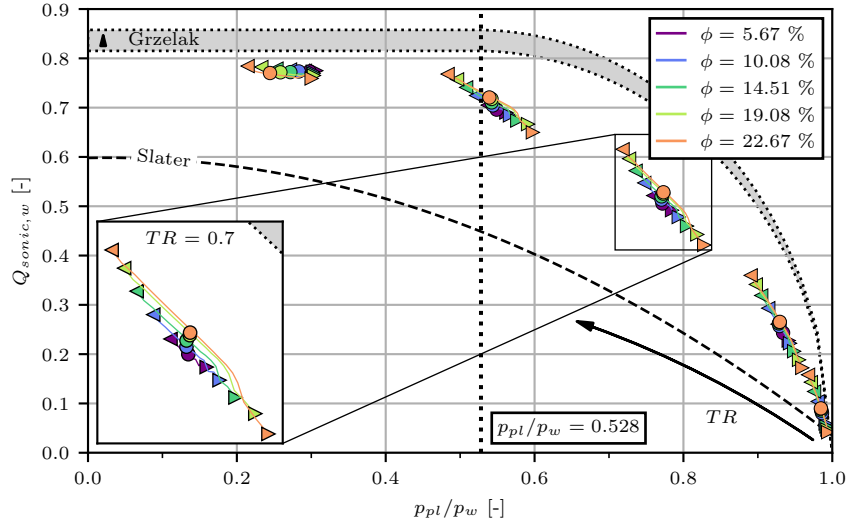
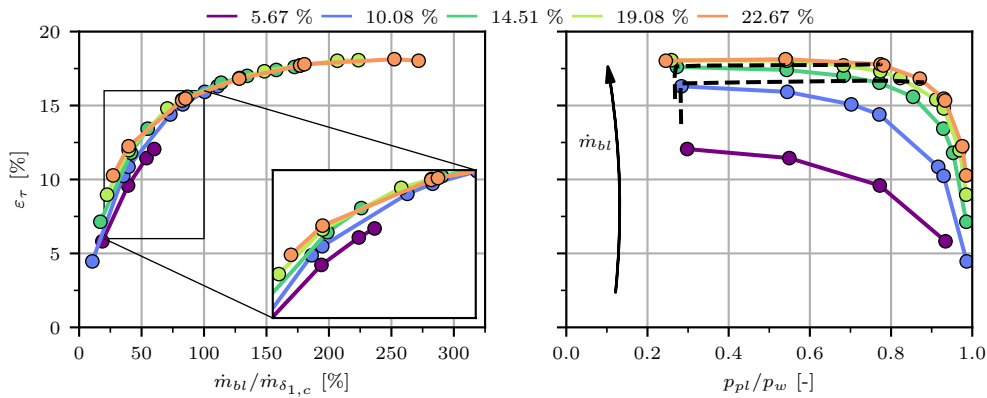


Figure 6.33: Surface sonic flow coefficient for different porosity ratios; right triangle (\blacktriangleright) symbolizes the first hole, left triangle (\blacktriangleleft) the last hole, and circle (\bullet) the mean value.

As a consequence, the pressure variation along the bleed region is increased, as seen for the plate length in Figure 6.26. Moreover, the sonic flow coefficient is slightly increased for high porosity levels. The explanation for this effect is the higher bleed mass flux, resulting in a stronger deflection of the flow towards the wall. Thus, the flow deflection angle in the hole inlet decreases, accompanied by a slightly smaller size of the separated region into the holes.

Lower porosity levels are associated with larger inter-hole distances, which result in a less homogeneous increase in the wall shear stress as illustrated for supersonic conditions in Figure 6.18. The same effect leads in subsonic flows to a slightly lower wall shear stress rise, as seen in Figure 6.34. However, with increasing porosity levels, saturation is reached, where the growing porosity levels do not further lead to an increase in the wall shear stress.

Nevertheless, high porosity levels increase the bleed rate as the open area is larger. Figure 6.34b shows the higher bleed rate, which is associated with a higher rise in the wall shear stress, independently of the pressure ratio from the plenum to the external wall.



(a) Rise in wall shear stress as a function of the bleed rate

(b) Rise in wall shear stress as a function of the pressure ratio

Figure 6.34: Rise in the wall shear stress as a function of the bleed rate \dot{m}_{bl} and the pressure ratio p_{pl}/p_w for varying porosity levels; dashed lines in (b) pinpoint lines of constant bleed rate.

As for supersonic flow conditions, the porosity level has to be chosen concerning the desired bleed rate and size of the bleed region. High porosity levels are slightly more efficient and effective, but also decrease the system size or increase the bleed rate. Therefore, low porosity levels are preferred if flow control is required for large areas.

6.3.4 Thickness-to-Diameter Ratio

The ratio of plate thickness to hole diameter has the most significant influence on the surface sonic flow coefficient for subsonic conditions. Figure 6.35 demonstrates strong variations in the bleed efficiency for unchoked conditions. As for supersonic conditions, the optimal ratio is found around $T/D = 4$ in this working regime. With decreasing plenum pressure, the effect inverts, and low plate thicknesses lead to a higher sonic flow coefficient. Again, the pressure losses inside the holes are large for high pressure ratios and small guidance inside the holes, i.e., thin plates. The lower the pressure ratio, the higher the friction losses inside the hole. In the case of choked holes, our findings agree with those of Grzelak et al. [54]. However, for unchoked conditions, the opposite trend is observed.

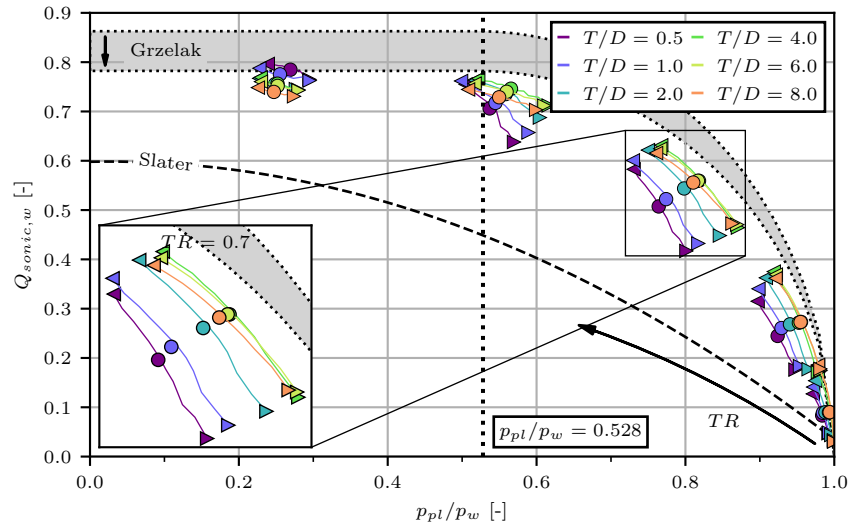


Figure 6.35: Surface sonic flow coefficient for different thickness-to-diameter ratios; right triangle (\blacktriangleright) symbolizes the first hole, left triangle (\blacktriangleleft) the last hole, and circle (\bullet) the mean value.

Again, no effect of the thickness-to-diameter ratio on the boundary-layer control is noted. Consequently, the thickness-to-diameter ratio should be chosen concerning the desired pressure ratio. A $T/D = 4$ is advantageous, as the bleed efficiency is the highest for unchoked conditions and the degradation for choked conditions is low compared to that for thinner plates in the unchoked working regime.

6.3.5 Stagger Angle

Remarkably, no effect of the stagger angle on both the bleed efficiency and control effectiveness of the bleed system is found. Figure 6.36 illustrates the negligible influence of this parameter on the sonic flow coefficient. For the subsonic application, the stagger angle can be ignored in the design process.

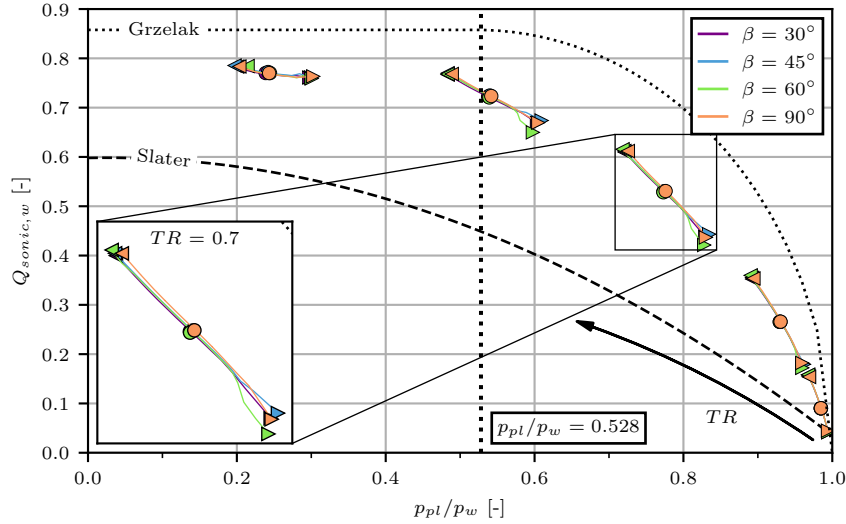


Figure 6.36: Surface sonic flow coefficient for different stagger angles; right triangle (\blacktriangleright) symbolizes the first hole, left triangle (\blacktriangleleft) the last hole, and circle (\bullet) the mean value.

6.3.6 Comparison of all Geometrical Parameters

The influence of the geometrical parameters on the bleed efficiency is illustrated in Figure 6.37 showing the surface sonic flow coefficient. Compared to supersonic conditions, the spreading of the data is lower. Starting with unchoked conditions ($p_{pl}/p_w > 0.528$), a strong influence of the thickness-to-diameter ratio is observed. High ratios are beneficial in this working regime. The other quantities have only a negligible influence on the sonic flow coefficient.

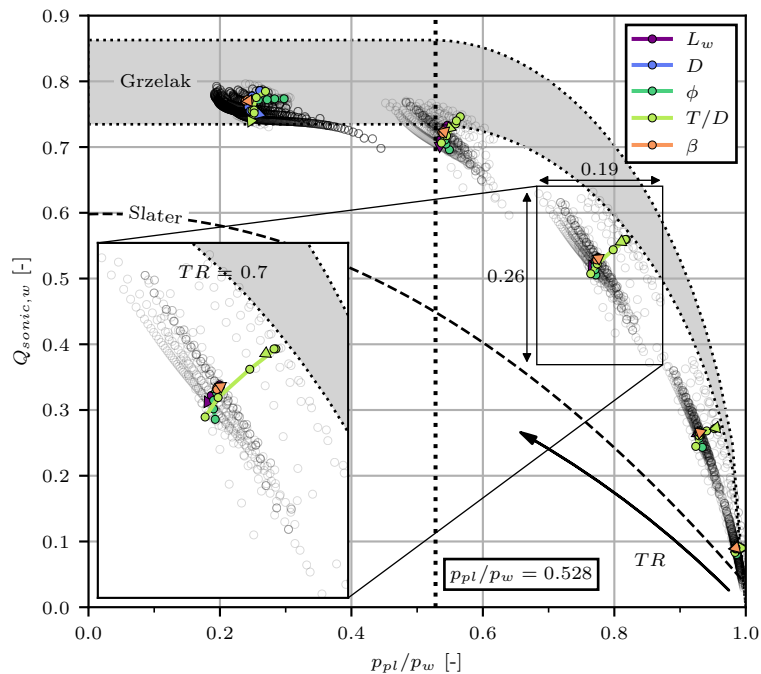


Figure 6.37: Surface sonic flow coefficient for all parameters for subsonic conditions.

Moreover, a strong variation of the sonic flow coefficient along the plate is observed, as shown by the gray points. As discussed in Section 6.1.1, the Mach number decreases along the plate, leading to higher bleed rates and lower pressure ratios p_{pl}/p_w .

Parameter	Bleed efficiency	Control effectiveness	Application recommendation
$L_w \nearrow$	\searrow	–	small L_w
$D \nearrow$	\searrow	\searrow	Small D
$\phi \nearrow$	\nearrow	\nearrow	High ϕ
$T/D \nearrow$	\nearrow (unchoked) \searrow (choked)	–	$T/D \sim 4$ (unchoked) $T/D \sim 1$ (choked)
β	–	–	–

Table 6.4: Trends on bleed efficiency and control effectiveness and recommendations for all investigated parameters for subsonic conditions.

In contrast, more data spreading is observed for choked conditions. In this area, also the hole diameter influences the sonic flow coefficient. Smaller holes become advantageous compared to large holes. Moreover, the effect of the thickness-to-diameter ratio is reversed, meaning that thin plates are more efficient. Also, small effects of the porosity level and the plate length are observed.

The parameter influences on the bleed control effectiveness are not shown, as their impact is significantly smaller than for supersonic conditions. All influences on bleed efficiency and control effectiveness are presented in Table 6.4. As discussed, low plate length and hole diameter are advantageous concerning the bleed efficiency. In contrast, the porosity level should be high. The thickness-to-diameter ratio has been selected depending on the working regime of the bleed. In terms of control effectiveness, small hole diameter and high porosity levels are beneficial.

6.4 Geometry Influence on Shock-Wave/Boundary-Layer Interaction Control

Simulations have been performed for different hole diameters, porosity levels, thickness-to-diameter ratios, and stagger angles over a range of throat ratios. Here, the effect of the geometrical parameters on the control of the SBLI is investigated. The wedge angle is fixed to $\alpha = 10.5^\circ$ in the parametric study.

6.4.1 Hole Diameter

The flow fields for the different hole diameters are shown in Figure 6.38 for a throat ratio of $TR = 0.7$. On the left, the contours are extracted on the hole-cutting plane so that the flow inside the holes is visible. The flow on the offset plane between the two rows is shown on the right side. From top to bottom, the hole diameter is increased. The gray patches illustrate the position of the second row of bleed holes.

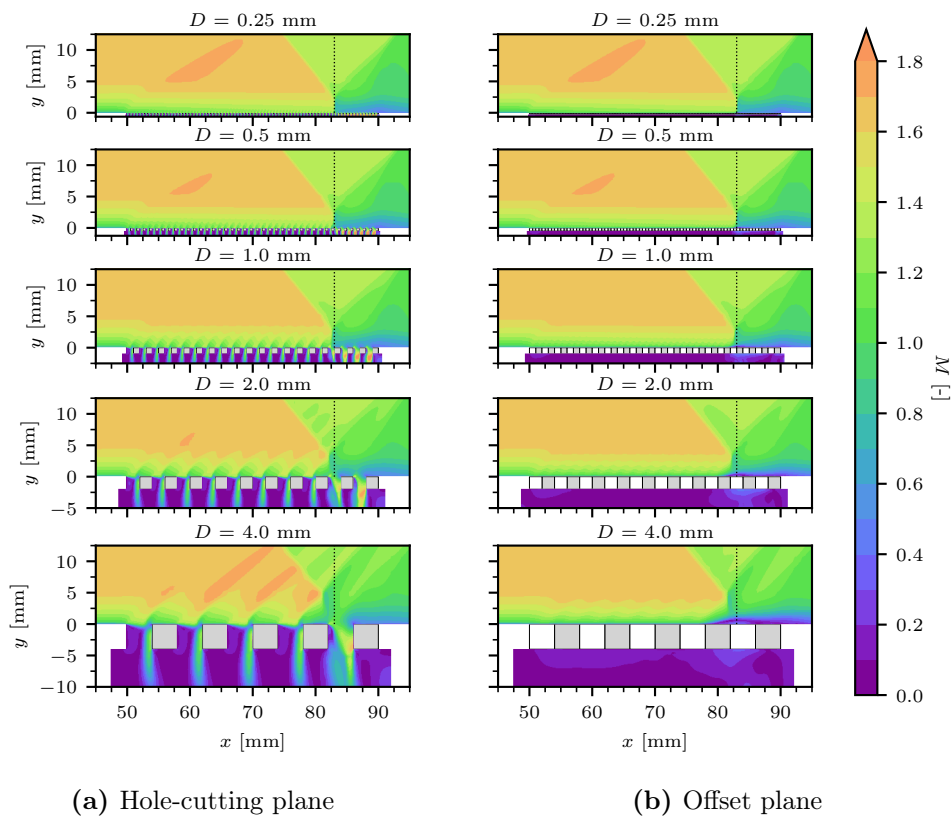


Figure 6.38: Mach number contours for different hole diameters; gray patches illustrate the second row hole positions; dotted line highlights shock location for $D = 0.25$ mm.

A view of Figure 6.38a reveals significant differences between the flow fields. For the smallest diameter $D = 0.25$ mm, the flow field upstream of the shock is very homogeneous. There is no apparent penetration of the barrier shocks in the boundary layer. The shock is located at $x = 83$ mm (dotted vertical lines), and no lambda foot is found. This is a consequence of the strong thinning of the upstream boundary layer. Thus, the interaction of the shock with the boundary layer is effectively mitigated with no apparent flow separation. Downstream of the shock, a strong transpiration flow is evident with the high-velocity jets in the plenum. As a result, no flow separation is apparent. At the end of the plate, the trailing shock, which leads to a weak thickening of the boundary layer, is visible.

With larger hole diameters, a slight upstream displacement of the shock foot is apparent. Moreover, for hole diameters $D \geq 1$ mm, the flow field is less homogeneous, and penetration of the barrier shocks through the boundary layer is found. This also affects the shape of the shock wave, which is strongly bent in the vicinity of the holes. For the largest diameter of $D = 4$ mm, a strong interaction of the holes with the boundary layer can be observed. Every hole creates an expansion fan and a barrier shock that penetrates the boundary layer and the incoming oblique shock wave. The shock wave is curved, and the shock foot is approximately 3 mm further upstream than for the smallest holes. Also, downstream of the shock, differences can be noted: The boundary layer is thicker, and the trailing shock is less prominent. These findings indicate a lower bleed efficiency.

On the offset plane in Figure 6.38b, the effect of the hole diameter is more significant. For small hole diameters $D \leq 1$ mm, the flow field looks identical to the left-hand side. This means that the flow field is very homogeneous in the spanwise direction. For larger holes $D \geq 2$ mm, the impact of the barrier shock and the expansion waves is evident. Moreover, the Mach number in the vicinity of the wall below the shock foot is very low. Here, a lambda shock foot is observable, which indicates the presence of local flow separation.

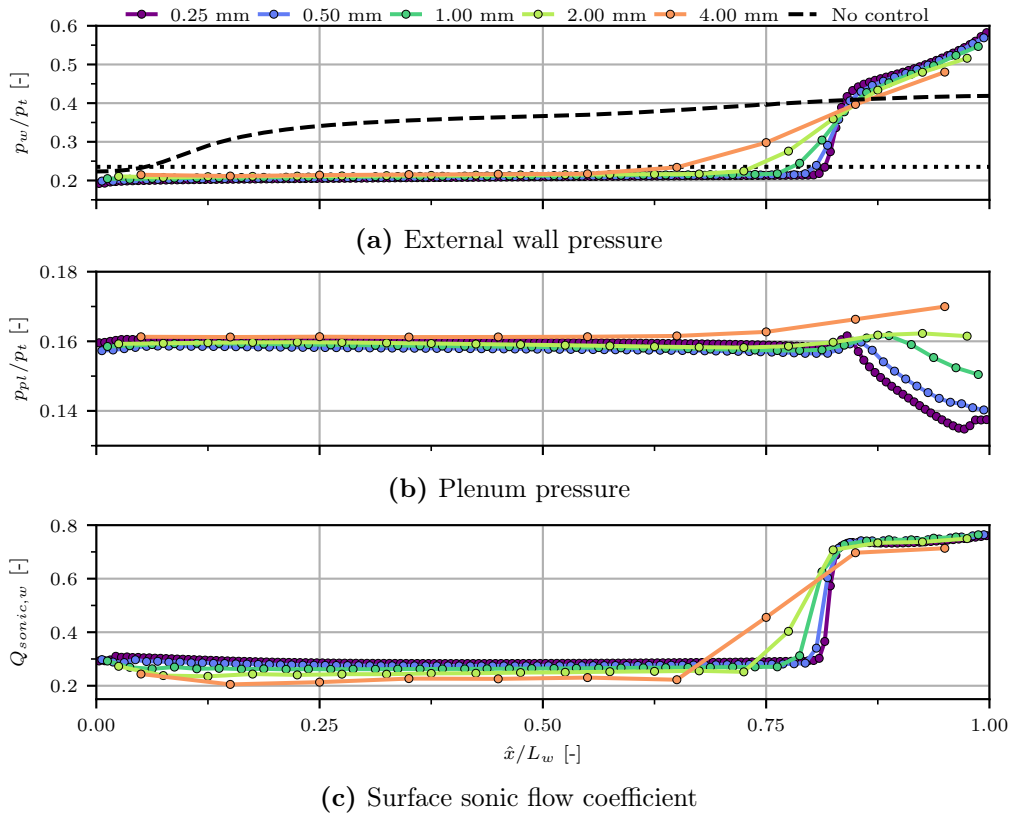


Figure 6.39: Comparison of the flow quantities for different hole diameters along the bleed region.

Figure 6.39 shows the curves of the external wall pressure and the plenum pressure, which are scaled by the stagnation pressure p_t , and the surface sonic flow coefficient along the bleed region. Moreover, the pressure distribution for the uncontrolled case is shown as a comparison. The shock position is located between $\hat{x}/L_w = 75\%$ and 80% , as seen by the pressure rise in Figure 6.39a, and thus significantly further downstream than for the uncontrolled case. Upstream of the shock, the same behavior as shown in Section 6.2.2 is observed: The larger the hole, the higher the wall pressure. Moreover, the shock is more smeared for larger hole diameters. Downstream of the shock, the differences are smaller. Only at the end of the plate, a larger pressure rise for tiny holes is found, leading to the assumption of a stronger trailing

shock as the pressure information can spread upstream inside the boundary layer. Independent of the hole size, a higher wall pressure is observed downstream of the incident shock.

The surface sonic flow coefficient (Figure 6.39c) behaves similarly to the wall pressure. Upstream of the shock, the flow coefficient is the highest for the smallest holes. Passing the shock foot, the sonic flow coefficient sharply increases as the pressure difference from the external wall to the plenum increases. Downstream of the shock, a lower bleed efficiency is found for the largest diameter of $D = 4$ mm. The differences between the other hole diameters are small.

Also, the pressure inside the cavity plenum slightly varies downstream of the incident shock, as shown in Figure 6.39b. Since the bleed rate is higher in this area, the transpiration flow is stronger, leading to secondary flows inside the cavity plenum. Also, losses induced by the under-expanded jet are increased. However, the pressure difference inside the plenum is low compared to the change in the external wall pressure. Thus, the assumption of constant pressure inside the cavity plenum, as used in the bleed modeling, is valid.

The surface sonic flow coefficient as a function of the pressure ratio is visualized in Figure 6.40. Additionally, the bleed models of Slater [98] and Grzelak et al. [54] are shown. In comparison to the previous curves for the sonic flow coefficient for supersonic and subsonic conditions, the trend for the SBLI is more challenging to grasp on one view since an extensive range of working regimes is covered by one throat ratio. The zoom-in view qualitatively shows the variation of the surface sonic flow coefficient and the pressure ratio along the bleed region for a throat ratio of $TR = 0.7$. For low throat ratios, the plenum pressure can exceed the external wall pressure upstream of the shock. Thus, the air is not removed but added to the boundary layer (blowing). Consequently, the momentum inside the boundary layer decreases instead of increases as desired.

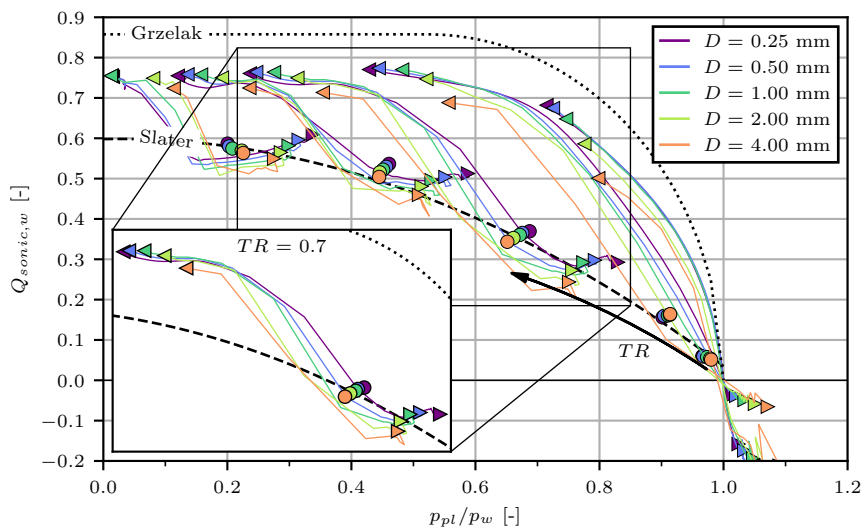


Figure 6.40: Variation of the surface sonic flow coefficient for different hole diameters for the SBLI; right triangle (▶) symbolizes the first hole, left triangle (◀) the last hole, and circle (●) the mean value.

Downstream of the shock, the pressure ratio is higher regardless of the throat ratio. Thus, the sonic flow coefficient sharply increases. Since the flow momentum in the vicinity of the wall is low, the size of the separated region decreases, resulting in a larger vena contracta area and hence a higher flow coefficient than for the supersonic bleed. The bleed operates here in subsonic flow conditions, as described in Section 6.3.2.

A diameter dependence on the flow coefficient is apparent, similar to supersonic and subsonic flows. The higher the hole diameter, the lower the sonic flow coefficient. However, this trend is smaller for the holes downstream of the shock, where the hole flow is choked, and the external

flow is subsonic. The findings support the distinction between supersonic and subsonic flows as considered in this thesis.

A more detailed view of the control of the shock-induced flow separation is shown in Figure 6.41, which displays the streamwise wall shear stress below the shock foot. The absolute values for the coordinates are given to grasp the size of the separated region. For the comparison, the length of the flow separation bubble in the base flow case is approximately 25 mm (see Section 4.1.3). For the largest holes of $D = 4$ mm, a large region of reversed flow is apparent between the rows starting from $x = 78$ mm. This region is induced by the adverse pressure gradient of the incident shock and ends with the end of the plate ($x = 90$ mm), where the flow reattaches due to the strong bleed rate, but also because of the expansion fan caused by the rear edge of the shock generator.

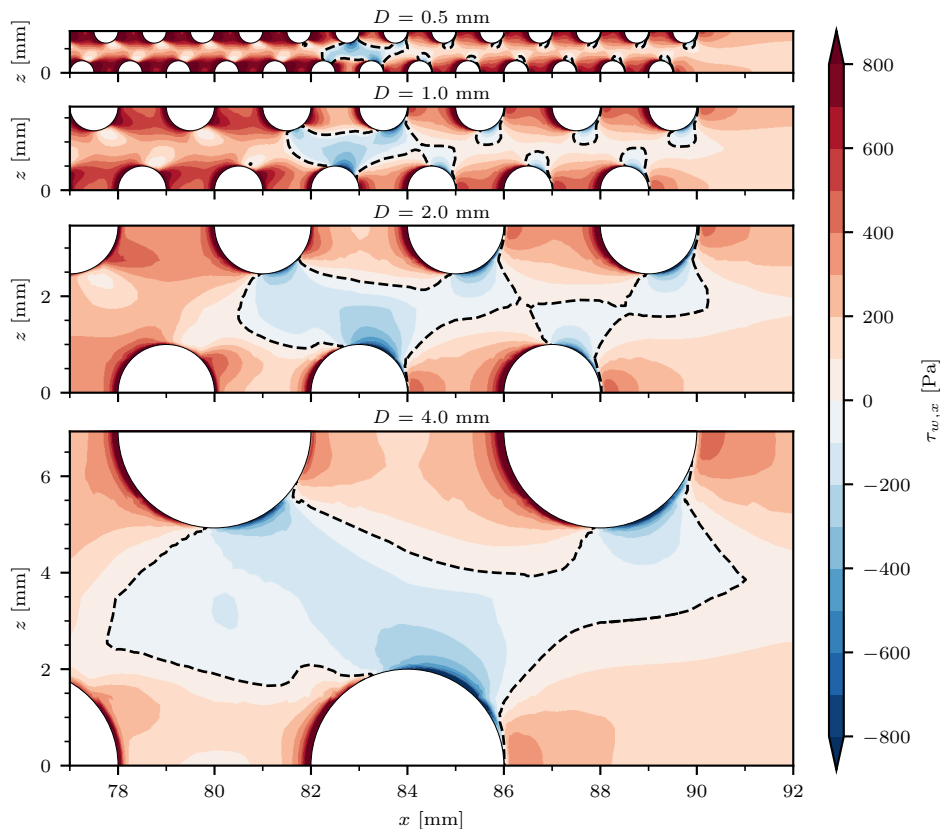


Figure 6.41: Streamwise wall shear stress below the shock foot for different hole diameters; dashed lines mark $\tau_{w,x} = 0$ contour line.

For smaller holes, the upstream influence of the incident shock inside the boundary layer is smaller, as indicated by the smaller extent of the region of reversed flow. With regard to Figure 6.38b, it can be stated that the smaller hole sizes lead to a higher flow momentum inside the boundary layer, resulting in a shorter interaction length. The size of the lambda shock foot is smaller, and the separation bubble below decreases in size. Directly downstream of the bleed holes, there is no flow separation apparent, as the momentum in the wall vicinity is too high to separate. Thus, the flow separation is limited to the spanwise area between the holes, which is a function of the porosity level and the hole diameter. Hence, smaller diameters have a better control effect as the solid area between two holes is reduced.

The boundary-layer profiles downstream of the bleed region are illustrated in Figure 6.42. The observed effects are similar to the investigations for the boundary-layer bleed but even stronger. The use of tiny holes guarantees a higher momentum of the flow in the wall vicinity downstream of the impinging shock.

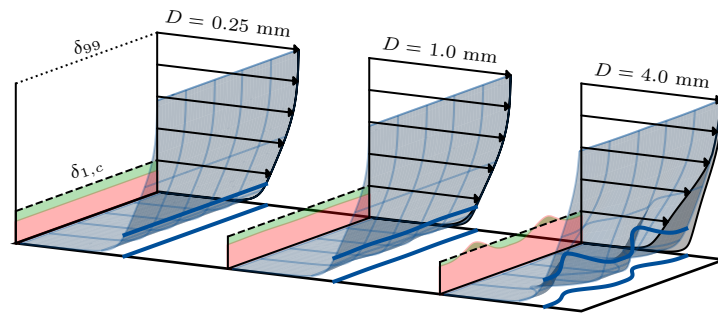


Figure 6.42: Boundary layer 10 mm downstream of the bleed region for $D = 0.25$ mm, 1.00 mm, and 4.00 mm (left to right); gray patch illustrates the envelope of the boundary-layer profiles along the spanwise direction; red area details the compressible displacement thickness and green area the difference to the inflow.

The application of large holes to control SBLIs results in strong variations of the boundary-layer profiles along the span. As observed in Sections 6.2.2 and 6.3.2, large hole diameters lead to a less homogeneous flow for both supersonic and subsonic conditions. The appearance of the adverse pressure gradient caused by the shock wave enforces this effect. Fluctuations in the sonic height result in variations of the interaction length along the span. Thus, the flow momentum between the holes is further decreased and negative effects sum up. Consequently, the variations along the span increase.

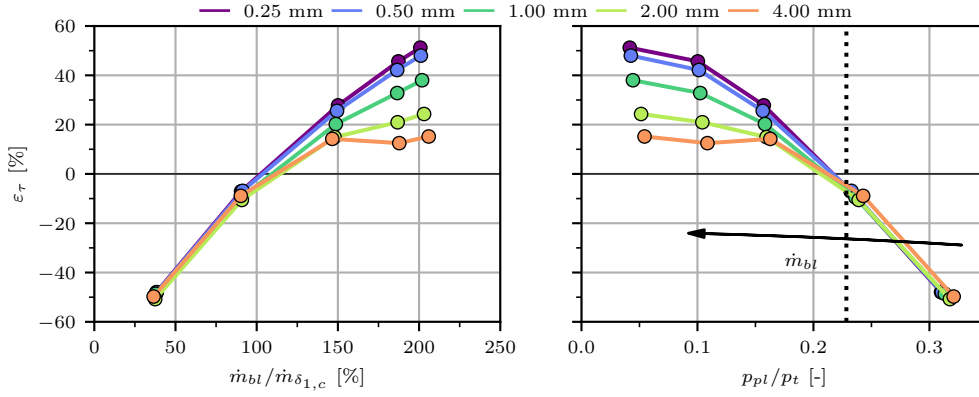
More information about the boundary-layer quantities is presented in Table 6.5. The smaller the hole diameter, the fuller the boundary-layer profiles downstream of the bleed region. Also, the displacement thickness downstream of the bleed region is significantly lower for smaller holes. Interestingly, the variations in the shape factor and the displacement thickness for $D = 4$ mm are even stronger than for supersonic flows (see Table 6.1), which underlines the additional impact of the incident shock and the resulting adverse pressure gradient.

D	H_{min}	H_{mean}	H_{max}	$\delta_{1,cmin}$	$\delta_{1,cmean}$	$\delta_{1,cmax}$	$\varepsilon_{\tau min}$	$\varepsilon_{\tau mean}$	$\varepsilon_{\tau max}$
0.25 mm		– 1.30 –			– 0.59 mm –		27.6 %	27.8 %	28.1 %
1.00 mm	1.31	1.32	1.34	0.65 mm	0.66 mm	0.67 mm	14.1 %	20.2 %	25.3 %
4.00 mm	1.26	1.37	1.57	0.65 mm	0.83 mm	1.08 mm	–28.2 %	14.2 %	41.8 %

Table 6.5: Incompressible boundary-layer shape factor, compressible displacement thickness, and rise in the wall shear stress for the boundary-layer profiles shown in Figure 6.42.

The rise of the wall shear stress along the bleed region as a function of the bleed rate and pressure ratio p_{pl}/p_t is shown in Figure 6.43. The stagnation pressure p_t is used to scale the plenum pressure since the wall pressure p_w varies along the bleed because of the incident shock. A view at Figure 6.43a reveals significant differences in the boundary-layer bleed: for low bleed rates, a degradation of the wall shear stress is apparent. This is a result of a lower Mach number downstream of the impinging shock, but also of the presence of blowing for lower bleed rates as highlighted in Figure 6.40. As long as blowing occurs, no differences between the different hole diameters are found. With reaching a plenum pressure below the external wall pressure, the bleed operates in full-suction mode, resulting in differences in the control effectiveness between the different hole diameters.

Figure 6.43b confirms that a pressure lower than the isentropic static pressure upstream of the shock is necessary to obtain a higher wall shear stress. If the plenum pressure is higher, the blowing occurs upstream of the shock, which eliminates diameter influences. The lower the



(a) Rise in wall shear stress as a function of the bleed rate (b) Rise in wall shear stress as a function of the pressure ratio

Figure 6.43: Rise in the wall shear stress as a function of the bleed rate \dot{m}_{bl} and the pressure ratio p_{pl}/p_t for varying hole diameters; dotted line in (b) highlights isentropic pressure ratio for $M = 1.62$.

plenum pressure, the higher the control effectiveness in increasing the wall shear stress along the bleed region. However, tiny holes are advantageous, which are linked to the lower extent of the reversed flow region below the shock foot.

6.4.2 Porosity Level

The influence of the porosity level on the SBLI is shown in Figure 6.44 for various throat ratios. Again, the sonic flow coefficients and the models of Slater [98] and Grzelak et al. [54] are illustrated. Generally, it must be noted that comparing different porosity levels is challenging as the global bleed mass flux strongly differs. The higher the bleed mass flux, the better the control of the SBLI because of the higher momentum close to the wall. Figure 6.44 still allows the comparison of the bleed efficiency of different porosity levels.

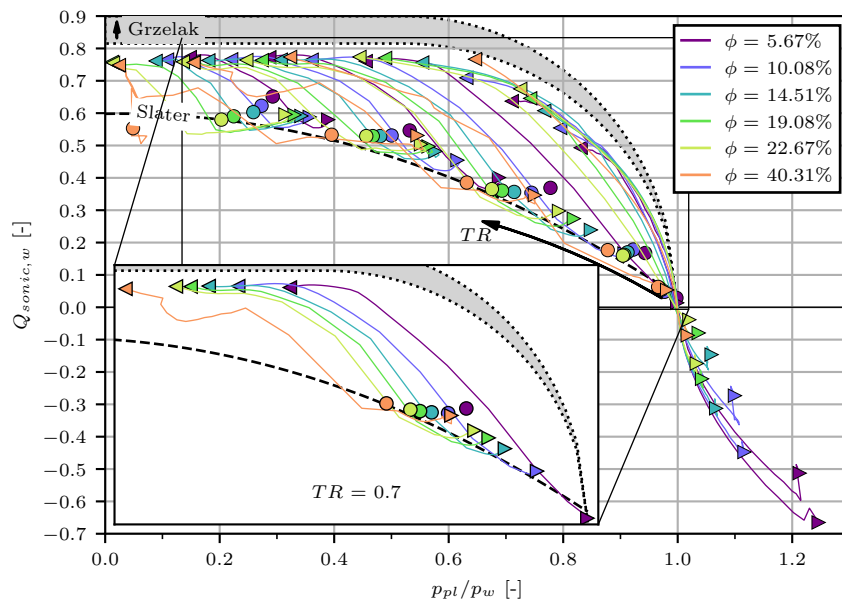
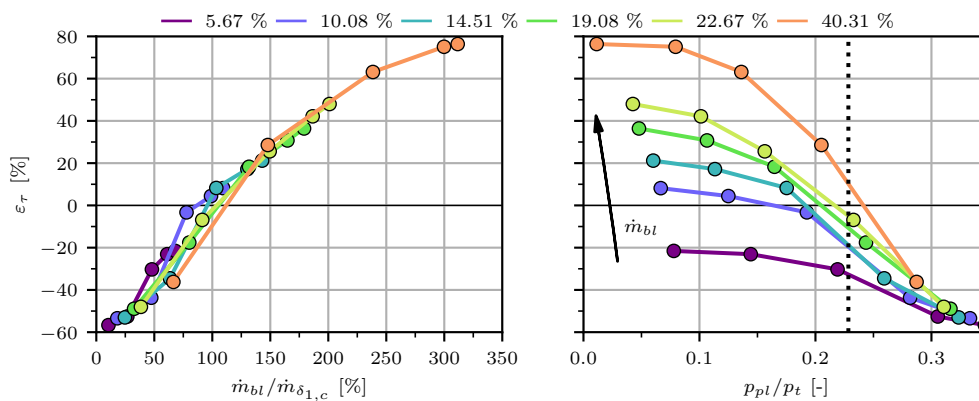


Figure 6.44: Variation of the surface sonic flow coefficient for different porosity levels for the SBLI; right triangle (\blacktriangleright) symbolizes the first hole, left triangle (\blacktriangleleft) the last hole, and circle (\bullet) the mean value.

For low throat ratios, blowing takes place upstream of the shock for all porosity levels with higher intensity for low-porosity plates. The reason is the weaker control of the shock. As a result, the location of the shock foot moves upstream, and the plenum pressure and the blowing rate increase.

Downstream of the shock, the differences between the different porosity levels are minor. All points of the last holes show a similar trend. For unchoked conditions, high porosity levels seem to be slightly more efficient, whereas the contrary is the case for choked holes. Also, the findings of Grzelak et al. [54] cannot be confirmed as they found a higher bleed efficiency for larger porosity levels. However, their study was limited to small porosity levels and no tangential flow.

Since the porosity level is strongly linked to the achievable bleed rate, this parameter has an essential impact on the control effectiveness of the bleed. The higher the bleed rate, the higher the effect. Figure 6.45 demonstrates the higher rise in the wall shear stress for higher porosity levels. As already shown for the hole diameter, a certain amount of bleed rate is required to obtain an equal wall shear stress downstream of the bleed compared to upstream. However, the maximum bleed rate for the lowest porosity level of $\phi = 5.67\%$ is not high enough to reach this point.



(a) Rise in wall shear stress as a function of the bleed rate (b) Rise in wall shear stress as a function of the pressure ratio

Figure 6.45: Rise in the wall shear stress as a function of the bleed rate \dot{m}_{bl} and the pressure ratio p_{pl}/p_t for varying hole diameters; dotted line in (b) highlights isentropic pressure ratio for $M = 1.62$.

Nevertheless, a difference between the porosity levels in terms of control effectiveness is observed in Figure 6.45a: the lower the porosity level, the lower the required bleed rate to obtain the same wall shear stress downstream of the SBLI compared to upstream.

6.4.3 Thickness-to-Diameter Ratio

As already stated in Sections 6.2.3 and 6.3.3, the thickness-to-diameter ratio of the perforated plate has no significant effect on the boundary layer. Therefore, only the sonic flow coefficient is regarded in Figure 6.46. Like for the other parameters, blowing occurs for small throat ratios, which is unaffected by the thickness-to-diameter ratio. With increasing throat diameter, effects on the sonic flow coefficient become apparent. Upstream of the shock, where the flow is supersonic, large ratios are advantageous if the holes are unchoked. This is in line with the results from Section 6.2.3. For low pressure ratios, this effect inverts, and lower thicknesses are found to be more efficient.

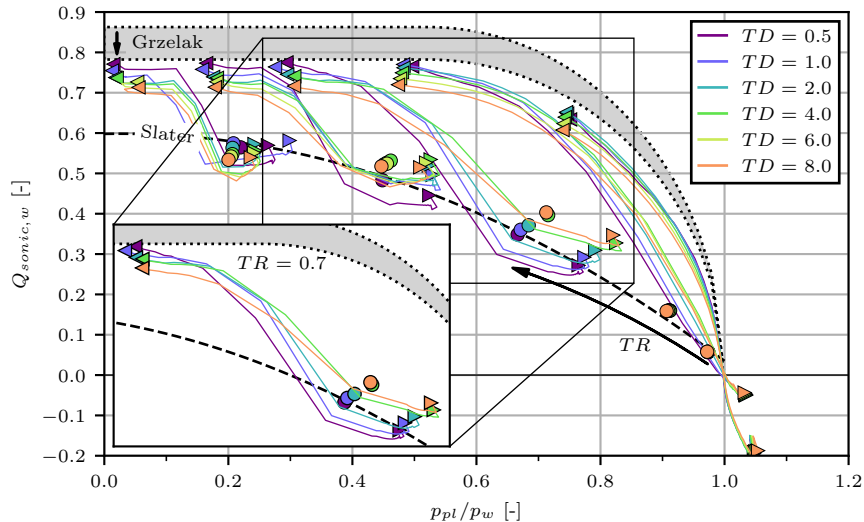


Figure 6.46: Variation of the surface sonic flow coefficient for different thickness-to-diameter ratios for the SBLI; right triangle (▶) symbolizes the first hole, left triangle (◀) the last hole, and circle (●) the mean value.

In contrast, downstream of the shock, where the pressure ratio is always lower because of the jump in the external wall pressure, high thickness-to-diameter ratios are observed to negatively affect the sonic flow coefficient. In this area, the tangential flow momentum is very low, resulting in a small size of the separated region inside the holes. Thus, the flow is fully attached inside the holes, and friction increases with further hole length, i.e., plate thickness. Grzelak et al. [54] also found a degradation of the bleed performance for $T/D \geq 1.5$. However, no separated region was induced by external flow in their study, and the observed hole diameters and porosity levels were smaller.

The difference between subsonic and supersonic conditions complicates the definition of an optimal geometry for the control of SBLIs. However, thickness-to-diameter ratios $T/D > 4$ result in high friction losses and should be avoided. Since the highest mass fluxes are achieved downstream of the shock, a higher sonic flow coefficient in this area is advantageous. Thus, the thickness-to-diameter ratio should not be higher than $T/D = 2$.

6.4.4 Stagger Angle

The last investigated geometrical parameter is the stagger angle, which is unconsidered in all bleed models. Its effect on the sonic flow coefficient is shown in Figure 6.47. The findings are similar to those from Section 6.2.5 and 6.3.5: for subsonic conditions, no difference in the sonic flow coefficient is apparent. For supersonic conditions, the stagger angles $\beta = 30^\circ$ and 45° are preferable to use since the pressure losses are lower. Overall, the effects are in a negligible range.

More interesting is the effect on the SBLI control. Therefore, the streamwise wall shear stress is extracted and illustrated in Figure 6.48 below the shock foot. Thus, the size of the separation bubble between the holes can be estimated. From top to bottom, the stagger angle is increased, leading to higher spanwise but lower streamwise distances between the holes.

For the stagger angles $\beta = 30^\circ$ and 45° , the region of reversed flow is very small. The high density of holes in the spanwise direction prevents the occurrence of one large separated area, as the flow reattaches directly downstream of the bleed holes because of the high transpiration flow, leading to an energizing of the boundary layer in this region. On the contrary, a large

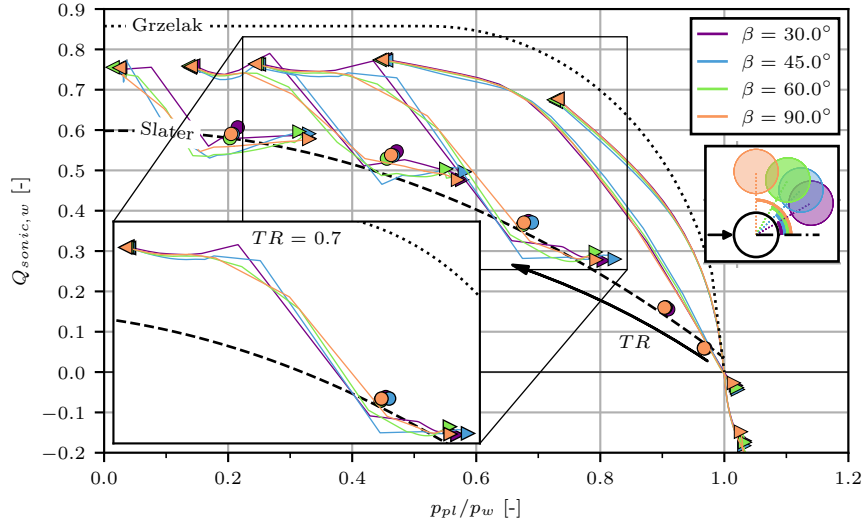


Figure 6.47: Variation of the surface sonic flow coefficient for different stagger angles for the SBLI; right triangle (▶) symbolizes the first hole, left triangle (◀) the last hole, and circle (●) the mean value.

area of reversed flow is found for large stagger angles, as the spanwise distance between the bleed holes is larger, and the near-wall momentum is low. Thus, the control effectiveness of the bleed is expected to be smaller.

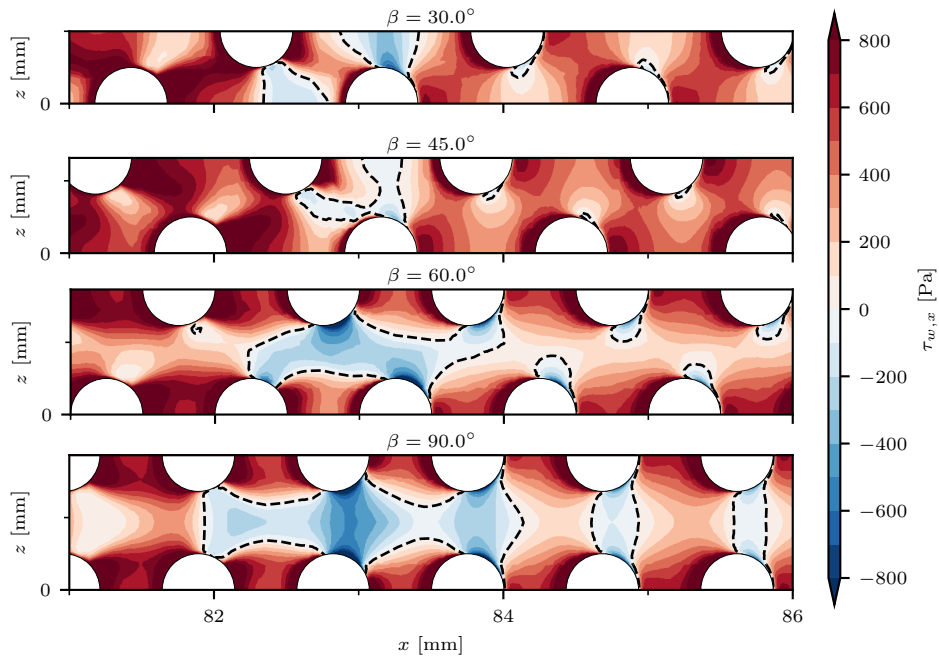
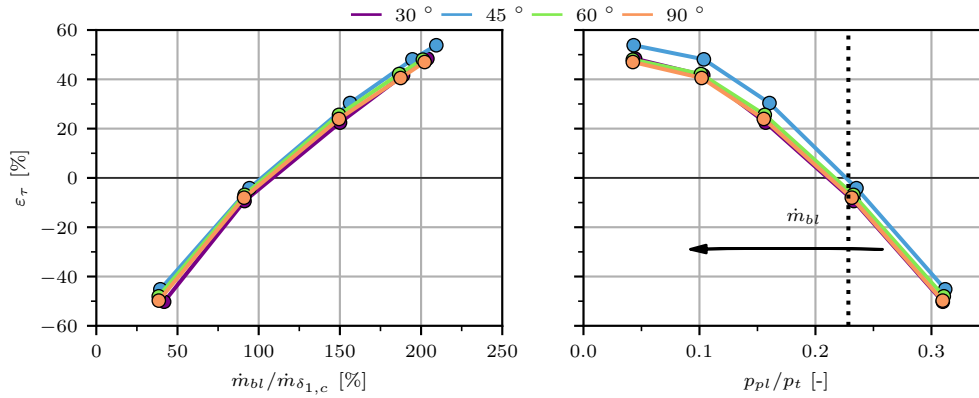


Figure 6.48: Streamwise wall shear stress below the shock foot for different stagger angles; dashed lines mark $\tau_{w,x} = 0$ contour line.

The rise in the wall shear stress is illustrated in Figure 6.49. Surprisingly, no significant differences are observed if the rise in the wall shear stress is shown as a function of the bleed rate, as seen in Figure 6.49a. However, a higher control effectiveness is achieved for $\beta = 45^\circ$ if the pressure ratio p_{pl}/p_t is kept constant. Thus, it can be stated that a 45° staggering has the biggest control effect on an SBLI.



(a) Rise in wall shear stress as a function of the bleed rate
 (b) Rise in wall shear stress as a function of the pressure ratio

Figure 6.49: Rise in the wall shear stress as a function of the bleed rate \dot{m}_{bl} and the pressure ratio p_{pl}/p_t for varying stagger angles; dotted line in (b) highlights isentropic pressure ratio for $M = 1.62$.

6.4.5 Comparison of all Geometrical Parameters

Generally, the influence of the geometrical parameters on the SBLI control is similar to those for the boundary-layer bleed. Upstream of the shock, the same effects as for the supersonic boundary-layer bleed are observed, and downstream of the shock, the bleed performs as a subsonic boundary-layer bleed. The higher bleed rates in the subsonic region result in a dominance of the effects caused by the subsonic bleed. Nevertheless, some phenomena are forced or strengthened by the adverse pressure gradient due to the incident shock. Table 6.6 summarizes all parameter effects on bleed efficiency and control effectiveness and gives application recommendations.

The strongest parameter influence is induced by the hole diameter. As observed for supersonic flows, the hole diameter affects the sonic flow coefficient and thus the bleed efficiency. For subsonic flows, the effect is smaller. A small effect of the hole diameter on the bleed efficiency is also found for the SBLI control. More interesting is the diameter effect on the control effectiveness. For both supersonic and subsonic flows, larger variations of the boundary-layer profiles along the span are observed for large holes. This effect is even strengthened because of the adverse pressure gradient, which strongly affects the sections of the boundary layer with larger subsonic regions.

The porosity level has different influences on bleed efficiency and control effectiveness. The bleed efficiency, i.e., the surface sonic flow coefficient, increases with decreasing porosity levels.

Parameter	Bleed efficiency	Control effectiveness	Application recommendation
$D \nearrow$	\searrow	\searrow	Small D
$\phi \nearrow$	\searrow	\nearrow	High ϕ
$T/D \nearrow$	\nearrow (unchoked) \searrow (choked)	–	$T/D \sim 4$
β	–	$\beta = 45^\circ$	$\beta = 45^\circ$

Table 6.6: Trends on bleed efficiency and control effectiveness and recommendations for all investigated parameters for the SBLI control.

However, high porosity levels enable better control as more air can be removed because of the increased open area. However, a larger bleed rate is required for high porosities to obtain an equal rise in the wall shear stress along the bleed region compared to a low-porosity plate which allows an equal bleed rate.

The thickness-to-diameter ratio of the perforated plate affects only the bleed efficiency as already observed for supersonic and subsonic external flows. Again, the optimal ratio is different for low and high bleed rates. With regard to the different bleed rates upstream and downstream of the shock, there is no optimal ratio. However, a ratio of $T/D = 4$ seems to be the best compromise to obtain high sonic flow coefficients in both areas. In contrast, the stagger angle only influences the control effectiveness with an optimum stagger angle of $\beta = 45^\circ$.

Chapter Summary

In this chapter, we evaluated the influence of the inflow characteristics and plate parameters on the bleed performance. Different flow topologies around the bleed region were found for supersonic and subsonic external flows, and significantly higher bleed rates were achieved with subsonic boundary-layer bleed compared to supersonic boundary-layer bleed for a given pressure ratio. Scaling the hole diameter with the compressible displacement thickness, which is commonly used in literature, could not be confirmed to be applicable as the boundary-layer state significantly varied along the bleed region.

The geometrical parameter influences were separately evaluated for supersonic and subsonic boundary-layer bleed before investigating their impacts on the SBLI control. The hole diameter was observed to have the highest impact on the control effectiveness, while the thickness-to-diameter ratio had the strongest influence on the bleed efficiency. Plate length and porosity level mainly influenced the bleed rate because they led to variation in the open area. Since higher bleed rates typically affected the control effect positively, larger plate lengths and higher porosity levels increased the control effectiveness. More information regarding all geometrical parameter influences is summarized in Sections 6.2.6, 6.3.6, and 6.4.5.

The major conclusion drawn from this chapter is the impact of the flow momentum of the removed air on the bleed efficiency and the control effectiveness. Higher flow momentum increased the size of flow separation inside the bleed holes, reducing the bleed rate. Moreover, in the case of supersonic external flow, the flow momentum increased the intensity of the barrier shock. Thus, a stronger boundary-layer growth downstream of the barrier shock was observed, reducing the control effect. These observations are important for bleed modeling.

Altogether, a comprehensive database was numerically generated showcasing the influences of geometrical parameters and tangential flow on the bleed performance. Some of the results are used for benchmarking state-of-the-art bleed models in Chapter 7 and a new, later introduced, bleed model in Chapter 8. This model is derived from the presented database.

Key Points:

Influence of the inflow conditions

- ❑ Significant influence of **Mach number**
 - **Higher bleed efficiency** for **subsonic** conditions
 - **Strong decrease** of the sonic flow coefficient for **subsonic** conditions from $M = 0.0$ to 1.0
 - **Small influence** of **supersonic** Mach number on sonic flow coefficient
 - **Diffuser effect** → larger for low Mach numbers
 - **Distinction** between **supersonic** and **subsonic** conditions required in modeling approach → Chapter 8
- ❑ **Displacement thickness** with influence on bleed efficiency
 - **Variation** along the bleed region → challenging to extract and use locally
 - **Scaling** with hole diameter helps to predict diameter effect globally, **but** more parameters influence the behavior of the bleed
 - **Higher bleed efficiency** for thicker boundary layers
 - Useful for estimation, but not for modeling

Geometrical influences for supersonic conditions

- ❑ **Plate length**
 - **Higher bleed efficiency** for short plates
 - **Highest control effectiveness** for $p_{pl}/p_w \sim 0.9$ → long plates
- ❑ **Hole diameter**
 - **Higher bleed efficiency** for small hole diameters
 - **Higher control effectiveness** for small hole diameters
 - **More homogeneous** flow downstream of bleed with small holes
- ❑ **Porosity level**
 - **Higher bleed efficiency** for low porosities
 - **Highest control effectiveness** for $p_{pl}/p_w \sim 0.9$ → high porosities
- ❑ **Thickness-to-diameter ratio**
 - **Significant influence** on **bleed efficiency** → distinction between choked and unchoked holes
 - **No influence** on **control effectiveness**
- ❑ **Stagger angle**
 - **Influence** on both **bleed efficiency** and **control effectiveness**
 - **Homogeneity** of downstream flow field depending on stagger angle

Geometrical influences for subsonic conditions

❑ Plate length

- Higher bleed efficiency for short plates
- No influence on control effectiveness

❑ Hole diameter

- Higher bleed efficiency for small hole diameters
- Higher control effectiveness for small hole diameters
- More homogeneous flow downstream of bleed with small holes

❑ Porosity level

- Higher bleed efficiency for high porosities
- Higher control effectiveness for high porosities

❑ Thickness-to-diameter ratio

- Significant influence on bleed efficiency → distinction between choked and unchoked holes
- No influence on control effectiveness

❑ Stagger angle

- No influence on both bleed efficiency and control effectiveness

Geometrical influences on the controlled case

❑ Hole diameter

- Shorter interaction length for small hole diameters
- Higher control effectiveness for small hole diameters
- More homogeneous flow downstream of bleed with small holes

❑ Porosity level

- Highest control effectiveness for high porosities because of higher achievable bleed rates
- Higher bleed efficiency for low porosities

❑ Thickness-to-diameter ratio

- Significant influence on bleed efficiency → distinction between choked and unchoked holes
- No influence on control effectiveness

❑ Stagger angle

- No influence on bleed efficiency
- Higher control effectiveness for $\beta = 45^\circ$

Generated database

- ❑ **Comprehensive database** including influences of **geometrical parameters** and impact of **tangential flow** velocity
- Used for **benchmarking** of state-of-the-art models → Chapter 7
- Basis for **novel bleed model** → Chapter 8

Benchmark of State-of-the-Art Bleed Models

Even if a scientific model, like a car, has only a few years to run before it is discarded, it serves its purpose for getting from one place to another.

DAVID L. WINGATE

Chapter Introduction

In this chapter, the prediction accuracy of state-of-the-art porous bleed models, which are implemented in the in-house RANS-solver *elsA*, are evaluated. The flow cases presented in Chapter 4 are used as a baseline to highlight deviations. Moreover, a second perforated plate with smaller holes is used as a reference to showcase model inaccuracies caused by unconsidered geometry parameters. Numerical data is chosen as the reference for this comparison to highlight only accuracy losses induced by the bleed modeling. Turbulence modeling and solver settings are equal for the reference simulations and the simulations using bleed models as a boundary condition.

The comparison consists of two steps: First, the bleed models are applied a posteriori on the extracted data from the reference simulations. In the second step, all models are applied by using them as a boundary condition. All models are tested for both supersonic and subsonic inflow conditions, before applying the model to the complex case of the control of an SBLI. Until now, no study comparing state-of-the-art bleed models to this extent has been performed.

7.1	Supersonic Boundary-Layer Bleed	173
7.1.1	A Posteriori Comparison	173
7.1.2	Implementation as a Boundary Condition	174
7.2	Subsonic Boundary-Layer Bleed	178
7.2.1	A Posteriori Comparison	178
7.2.2	Implementation as a Boundary Condition	179
7.3	Shock-Wave/Boundary-Layer Interaction Control	182
7.3.1	A Posteriori Comparison	182
7.3.2	Implementation as a Boundary Condition	183

7.1 Supersonic Boundary-Layer Bleed

In the following, the eight selected state-of-the-art models from Section 1.2.4.3 are evaluated based on two reference simulations from Chapters 4 and 6. The two investigated perforated plates have a length of $L_w = 40$ mm, a porosity level of $\phi = 22.67\%$, a thickness-to-diameter ratio of $T/D = 1$, and a stagger angle of $\beta = 60^\circ$. The first plate has a hole diameter of $D = 0.5$ mm and the second has a $D = 2.0$ mm diameter. The variation of the hole diameter is chosen since this parameter significantly influences bleed efficiency and control effectiveness, as shown in Chapter 6. The throat ratio is fixed to $TR = 0.7$ for all simulations.

7.1.1 A Posteriori Comparison

The extracted physical values from the reference simulations are used for the a posteriori comparison. First, the surface sonic flow coefficient, as introduced by Slater [98], is computed for all selected bleed models for pressure ratios p_{pl}/p_w from 0 to 1, as shown in Figure 7.1. A sonic flow coefficient of one corresponds to a wholly choked hole cross-section and, thus, to a Mach number of $M_{bl} = 1$ inside the holes. A surface sonic flow coefficient higher than one is therefore regarded as unphysical as the bleed rate cannot be higher than the sonic rate.

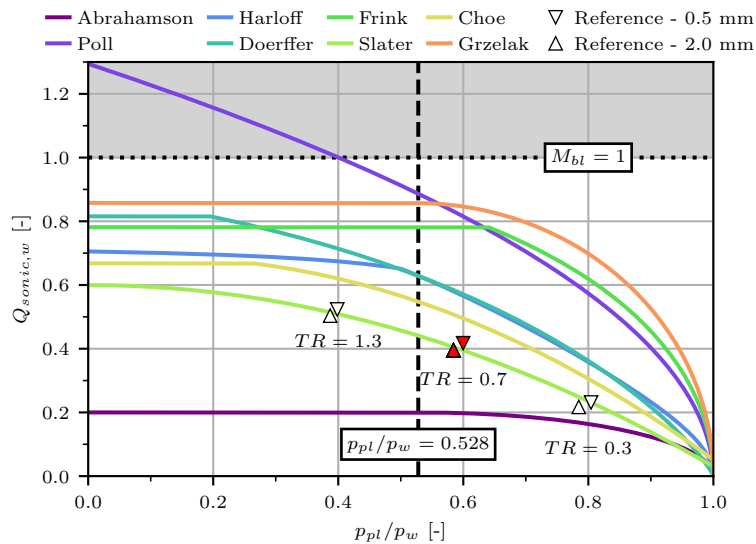


Figure 7.1: Predicted surface sonic flow coefficient $Q_{sonic,w}$ of the selected bleed models as a function of the pressure ratio p_{pl}/p_w a posteriori compared to the reference simulations.

Additionally, the critical pressure ratio $p_{pl}/p_w = 0.528$ is highlighted, which depicts the required pressure ratio to obtain choked conditions. Hence, the sonic flow coefficient is assumed to be constant or at least converging for pressure ratios below the critical one. As shown in Figure 7.1, the bleed model of Poll et al. [85] does not follow this assumption and increases even for lower pressure ratios. Moreover, the computed sonic flow coefficient using this model becomes greater than one for ratios $p_{pl}/p_w < 0.40$, which is unphysical. Besides, a significant difference between the models validated with and without external flow is apparent. The models of Poll et al. [85], Frink et al. [41], and Grzelak et al. [54] predict significantly higher sonic flow coefficients, especially for large pressure ratios.

Interestingly, the models of Harloff and Smith [61] and Doerffer and Bohning [38] show almost the same trend for pressure ratios higher than the critical pressure ratio, even though their approaches are entirely different. Below the critical ratio, the models diverge as different

approaches to forecast choked flow are used. The model of Abrahamson and Brower [1], one of the first introduced bleed models, estimates a notably lower bleed flow, which is a consequence of the empirically derived constant $c_b = 0.2$.

Moreover, the sonic flow coefficients obtained from the reference simulations are plotted in Figure 7.1 for the throat ratios $TR = 0.3, 0.7$, and 1.3 . The values obtained for $TR = 0.7$ are marked in red. It can be shown that the bleed model of Slater [98] fits best with the reference data.

All bleed models are a posteriori applied to the reference data from the previous Subsection and illustrated in Figure 7.2 to evaluate their accuracy. As expected, the models validated without external flow overestimate the bleed mass flux along the entire bleed region. The best fitting is the model of Slater [98], which is not surprising as it is based on experimental data on supersonic turbulent boundary bleed. Interestingly, the model of Doerffer and Bohning [38] underestimates the bleed mass flux for small holes and overestimates it for large holes. This difference is attributed to the wall shear stress, which is used as input in this model and is twice as high for the small hole diameter as for the larger hole. Thus, relying on the wall shear stress seems to be unsuitable in a bleed model.

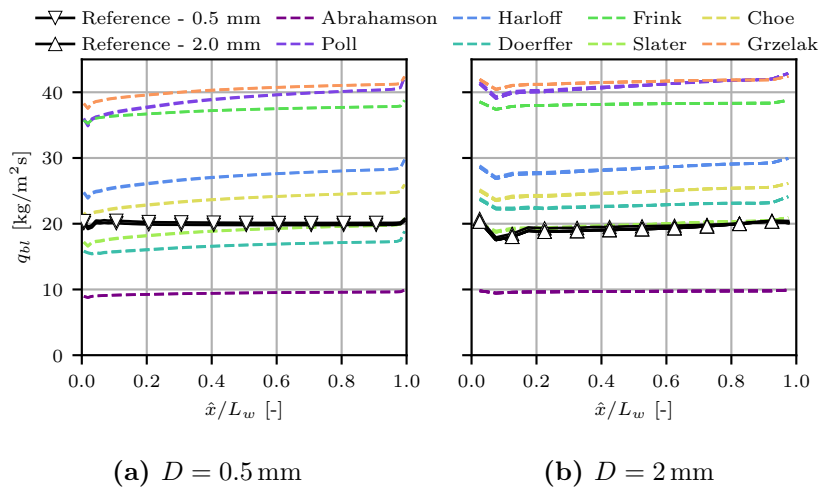


Figure 7.2: Prediction of the bleed mass fluxes based on physical quantities for various bleed models ($TR = 0.7$).

Please note that the model of Harloff and Smith [61] is not shown in Figure 7.2 as it requires the Mach number at the boundary-layer edge. The automatic extraction of this value is challenging, if not impossible, because of the complexity of the flow field around the holes in the reference simulations. Thus, the Mach number on the boundary-layer edge of the inflow profile is used.

7.1.2 Implementation as a Boundary Condition

In the next step, the bleed models were implemented and applied as a boundary condition in the RANS-solver. Figure 7.3 shows the Mach number contours for the models of Slater [98] and Grzelak et al. [54] compared to the reference simulations. Since both models do not consider the hole diameter, the outcome is independent of the hole diameter. Thus, any hole diameter effects, as a difference in the control effectiveness regarding the thinning of the boundary layer, can not be predicted by the models.

The observation of Figures 7.3c and 7.3d reveals an impact of the model on the control effectiveness. By applying the model of Grzelak et al. [54], the thinning of the boundary layer

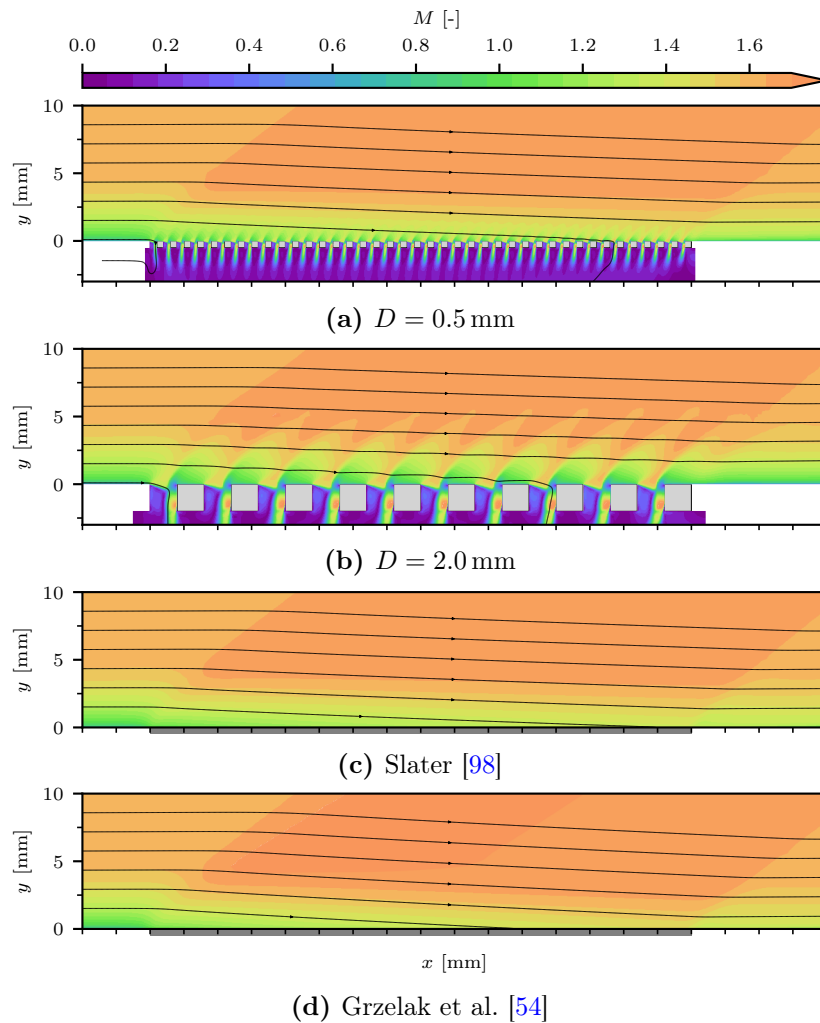


Figure 7.3: Mach number contour fields for the applied bleed boundary condition compared to the reference simulation.

is more marked. This can be seen by the stronger expansion fan at the beginning of the plate leading to higher Mach numbers outside the boundary layer and higher momentum in the vicinity of the wall at the end of the plate.

A significant difference between the boundary condition and the reference simulations becomes apparent. Since the suction occurs over all the cells and not only through locally distributed holes (see Figure 2.10), local flow phenomena such as the expansion fans and barrier shocks generated by the holes are not reflected. Only the expansion fan at the beginning and the trailing shock at the end of the plate are present.

More details of the flow along the bleed region are plotted in Figure 7.4. Figure 7.4a shows that the wall pressure is underestimated for all models, except the model of Abrahamson and Brower [1], which should lead to an underestimation of the bleed rate since the pressure ratio p_{pl}/p_w is increased. By looking at the bleed mass flux (Figure 7.4b), similar results to Figure 7.2 are found. The models of Slater [98] and Choe et al. [21] show the best agreement with the reference data. Moreover, the model of Harloff and Smith [61] is close to the reference simulations. The models of Poll et al. [85], Frink et al. [41], and Grzelak et al. [54] overestimate the mass flux as expected. However, the values are lower than in the a posteriori comparison as the external wall pressure is underestimated (see Figure 7.4a). In contrast, applying the model of Abrahamson and Brower [1] leads to the same results as in the a posteriori calculation, as the external wall pressure is almost identical.

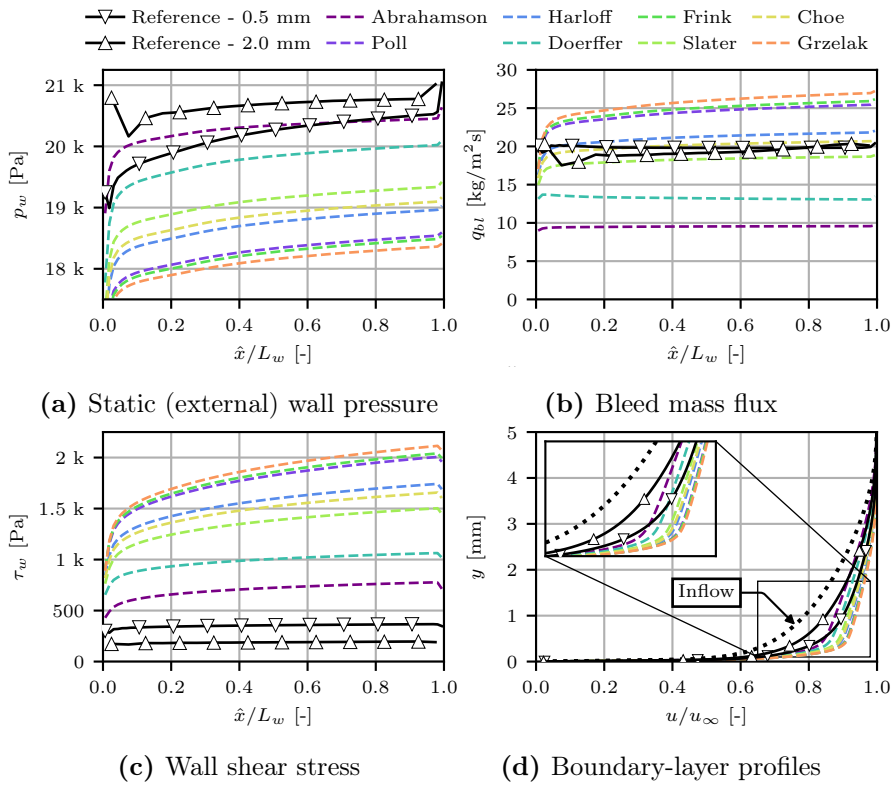


Figure 7.4: Applied boundary condition compared to the reference simulations.

In Figure 7.4c, the wall shear stresses predicted by the bleed models are compared to those of the reference cases. The wall shear stress is interesting as it allows the assessment of the flow momentum in the wall vicinity. Moreover, it is used by the model of Doerffer and Bohning [38]. Applying the bleed boundary condition induces high wall shear stresses independently of the model compared to those extracted from the reference simulations. The higher the predicted bleed mass flux of the model, the higher the wall shear stress.

Special attention must be drawn to the fact that the overestimation of the wall shear stress

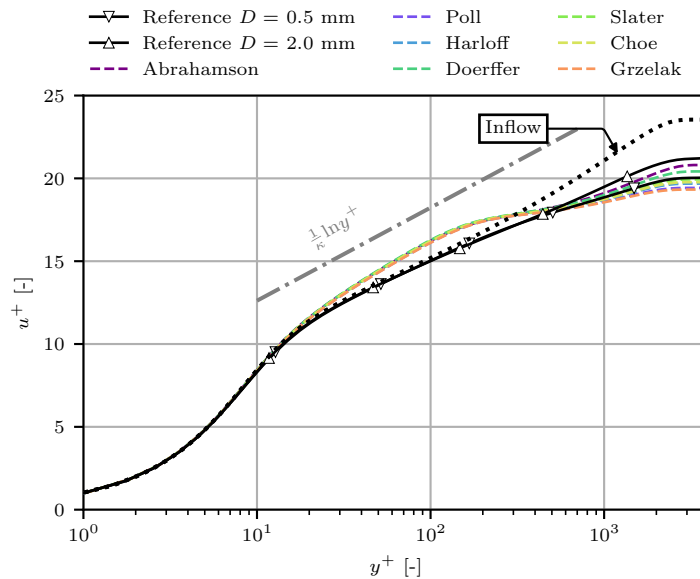


Figure 7.5: Comparison of the boundary layers downstream of the plate in dimensionless numbers.

does not necessarily mean an overestimation of the modeled drag force along the bleed region. Pressure drag forces caused by the bleed holes are not considered in the bleed modeling. More information about the drag can be found in our previous paper [46]. The high friction drag can be associated with fuller boundary-layer profiles downstream of the bleed region, as shown in Figure 7.4d.

Figure 7.5 shows boundary-layer profiles 10 mm downstream of the bleed region and the inflow profile in dimensionless units for velocity and wall distance. Again, a difference between the boundary condition and reference simulations is apparent. If the bleed models are implemented in the boundary condition, the slope of the dimensionless velocity is greater than $\frac{1}{\kappa} \ln y^+$ in the overlap layer, corresponding to an overestimation of the velocity. In contrast, the boundary layers extracted from the reference simulation fit with the inflow profile in this region, meaning the slope is not increased.

We now discuss the influence of the way the bleed working regime is set. As stated in Section 2.5, three options to apply the boundary condition have been implemented. Figure 7.6 compares these three models applied for the methods of Slater [98], which shows a good fit with the reference simulations regarding the bleed mass flux, and Grzelak et al. [54], which overestimates the mass flux. The plenum pressure p_{pl} and the bleed rate \dot{m}_{bl} are extracted from the reference simulation with $D = 2$ mm and applied to the models. While the bleed rate is measured directly at the plenum outlet, the plenum pressure is acquired by averaging the static pressure on a slice inside the cavity plenum with a distance of three hole diameters from the hole exits.

As all bleed models rely on the plenum pressure p_{pl} to compute the bleed mass flux, applying this option is assumed to be the closest to the a posteriori comparison (see Section 7.1.1). A view in Figure 7.6b proves this assumption since the mass flux predicted by the model of Grzelak et al. [54] is closer to that of the a posteriori comparison. However, its value is slightly lower

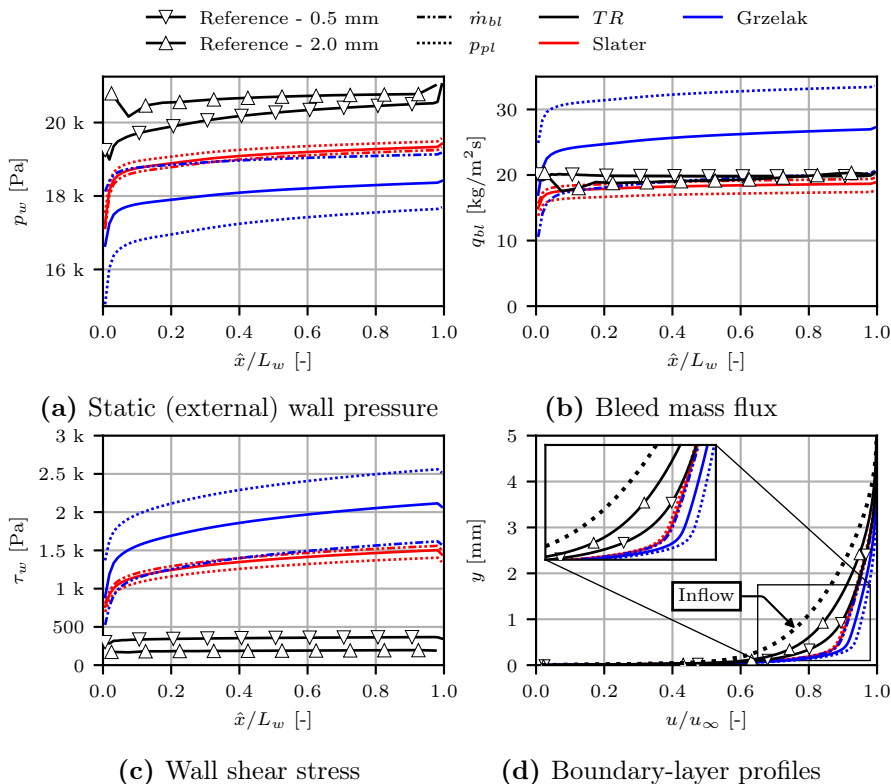


Figure 7.6: Comparison of the different bleed options for the models of Slater [98] and Grzelak et al. [54].

due to the underestimated external wall pressure (see Figure 7.6a). The same effect also leads to an underestimation of the bleed mass flux using the model of Slater [98].

Consequently, it must be stated that the higher control effectiveness predicted by the boundary condition leads to an underestimated wall mass flux for all models. Since the thinning of the boundary layer is enhanced, the expansion fan at the beginning of the plate is strengthened. Thus, the static wall pressure is lower. In other words, a bleed model, which fits the reality perfectly in a posteriori comparison, will predict a lower bleed mass flux when implemented as a boundary condition and produce a fuller profile.

In contrast, fixing the bleed rate correctly estimates the bleed mass flux. Nevertheless, slight deviations between the models and the reference simulations, and also between the models, are notable. While the application of the model of Slater [98] prognosticates an almost constant mass flux along the plate, the model of Grzelak et al. [54] predicts a positive slope. Fixing the bleed rate also results in similar trends of the external wall pressure, the wall shear stress, and the boundary-layer profile downstream of the plate for both models.

The default option of a fixed throat ratio TR always gives an outcome between the other options since both bleed rate and plenum pressure are related to the throat area of the exit nozzle. Larger ratios result in a larger bleed volume flow rate and, thus, in a lower plenum pressure. However, with the decreasing plenum pressure, the density and, as a result, the rate decrease.

Moreover, a high deviation in the outcome of the different options highlights the inaccuracy of a model. For the model of Slater [98], all three options lead to the same results. In contrast, the options significantly impact the performance of the model of Grzelak et al. [54]. Fixing the mass flow rate results in an overestimated plenum pressure, whereas fixing the plenum pressure leads to an overestimated bleed rate.

7.2 Subsonic Boundary-Layer Bleed

In the next step, the application of the bleed models is evaluated for subsonic conditions. The same configurations as for supersonic conditions are chosen. The inflow Mach number is $M = 0.6$ in this case.

7.2.1 A Posteriori Comparison

For the first impression of the model outcomes, the surface sonic flow coefficient is computed as a function of the pressure ratio p_{pl}/p_w for all models and is shown in Figure 7.7. While some models are unaffected by the inflow conditions, we can see a different outcome of the models of Harloff and Smith [61] and Doerffer and Bohning [38] compared to Figure 7.1. The model of Harloff and Smith [61] estimates a significantly higher sonic flow coefficient, reaching almost one for a pressure ratio of $p_{pl}/p_w = 0$. Also, the outcome of the model of Doerffer and Bohning [38] is higher compared to supersonic conditions, which is caused by the lower wall shear stress for subsonic conditions.

Next, the bleed models are a posteriori compared to the reference simulations as shown in Figure 7.8 to illustrate the theoretical deviation from the reference data. Starting with the $D = 0.5$ mm plate (see Figure 7.8a), we see that all models differ significantly from the reference simulations in terms of the predicted bleed mass flux. The models of Poll et al. [85], Frink et al. [41], and Grzelak et al. [54] still overestimate the mass flux. In contrast, all supersonic models forecast significantly lower mass fluxes. The lowest error is found for the model of Poll et al. [85].

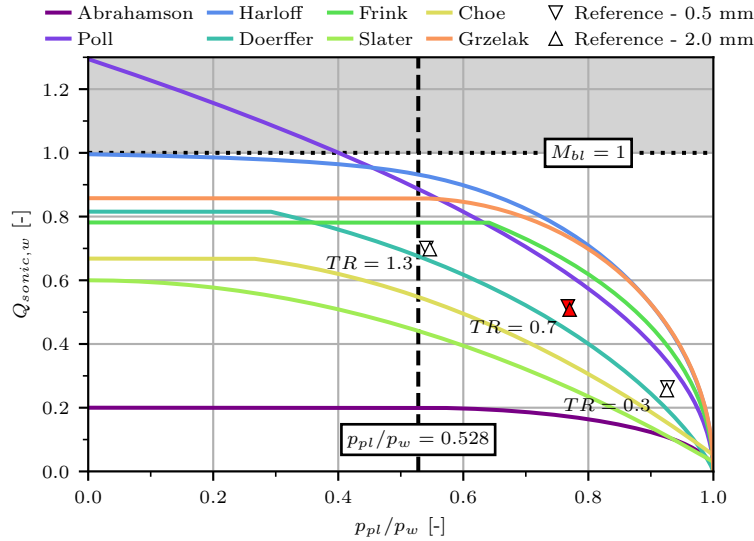


Figure 7.7: Predicted surface sonic flow coefficient $Q_{sonic,w}$ of the selected bleed models as a function of the pressure ratio p_{pl}/p_w a posteriori compared to the reference simulations.

For the case with the $D = 2.0$ mm holes, similar trends are observed, as illustrated in Figure 7.8b. However, the model of Doerffer and Bohning [38] performs very well and has a negligible deviation from the reference ($D = 2.0$ mm). The application of the wall shear stress to calculate the bleed mass flux is the key point for the significant difference in the prediction between the two cases. Again, the wall shear stress is lower for larger holes, as we are not in a choked case. Thus, the model outcome is higher than for smaller holes, where the wall shear stress is higher.

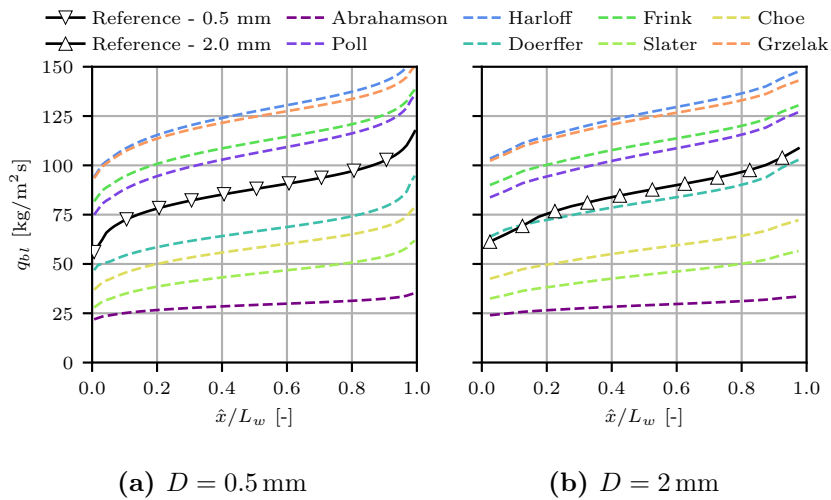


Figure 7.8: Prediction of the bleed mass fluxes based on physical quantities for various bleed models ($TR = 0.7$).

7.2.2 Implementation as a Boundary Condition

Finally, the bleed models are compared to the reference simulations with the models implemented into the solver. Therefore, the option of the fixed throat ratio is selected with $TR = 0.7$.

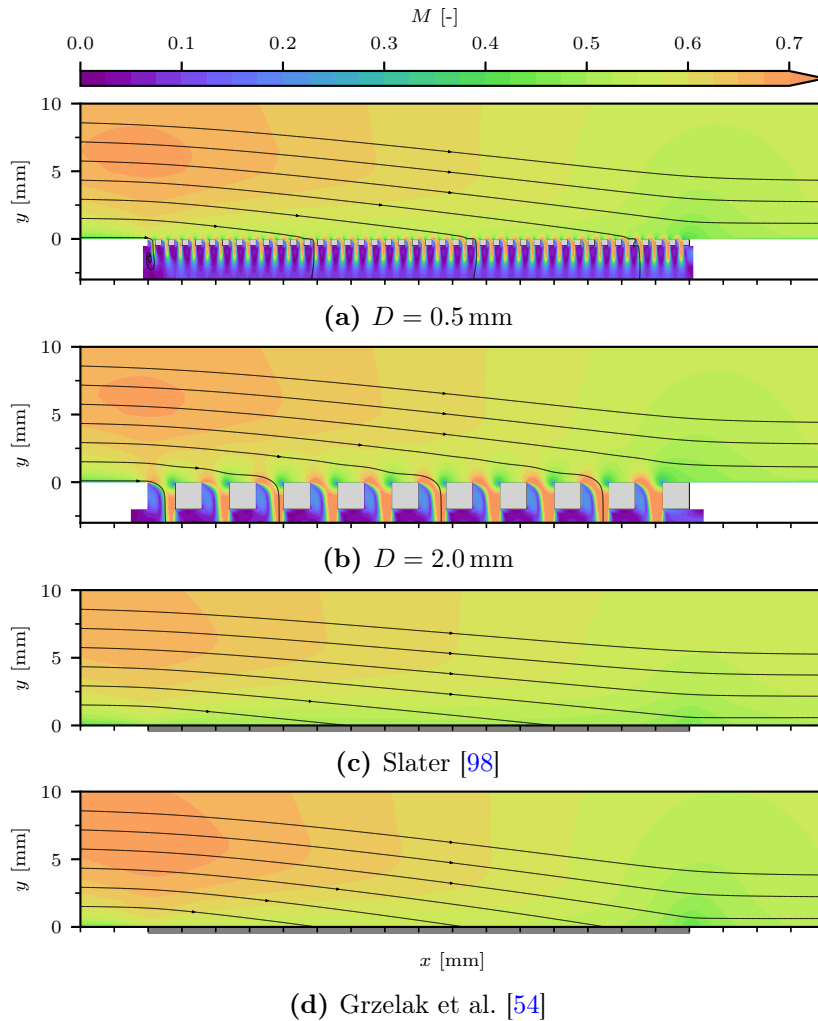


Figure 7.9: Mach number contour fields for the applied bleed boundary condition compared to the reference simulation.

Figure 7.9 shows two applied models (Slater [98] and Grzelak et al. [54]) in addition to the reference simulations. Basically, the same flow field is found for all four cases. However, a slightly increased bleed rate for the small holes leads to a stronger acceleration of the flow upstream of the bleed region. The models mirror the flow field well. However, the streamlines reveal a higher bleed rate by using the model of Grzelak et al. [54] (see Figure 7.9d). Thus, the upstream influence is enhanced and the Mach number is in this area higher. The model of Slater [98] (see Figure 7.9c) underestimates the mass flux, resulting in a lower Mach number upstream of the bleed region, and a smaller deflection of the streamlines towards the wall. Hence, the Mach number downstream of the bleed region is expected to be slightly higher as the diffuser effect is less pronounced.

A more detailed comparison between all the models and the reference simulations is shown in Figure 7.10. The pressure distribution along the bleed region is illustrated in Figure 7.10a. The agreement between reference simulations and bleed models is good. Along the perforated plate, the pressure increases as the Mach number decreases because of the diffuser effect. Only the model of Abrahamson and Brower [1] has a significantly lower deviation from the reference simulations, which was expected since the bleed rate is even for supersonic flow underestimated.

Surprisingly, the computed bleed rate of the models in the applied state shows a better agreement with the reference simulations, as illustrated in Figure 7.10b. The models of Poll et al. [85] and Frink et al. [41] perform the best with an overestimation of the mass flux

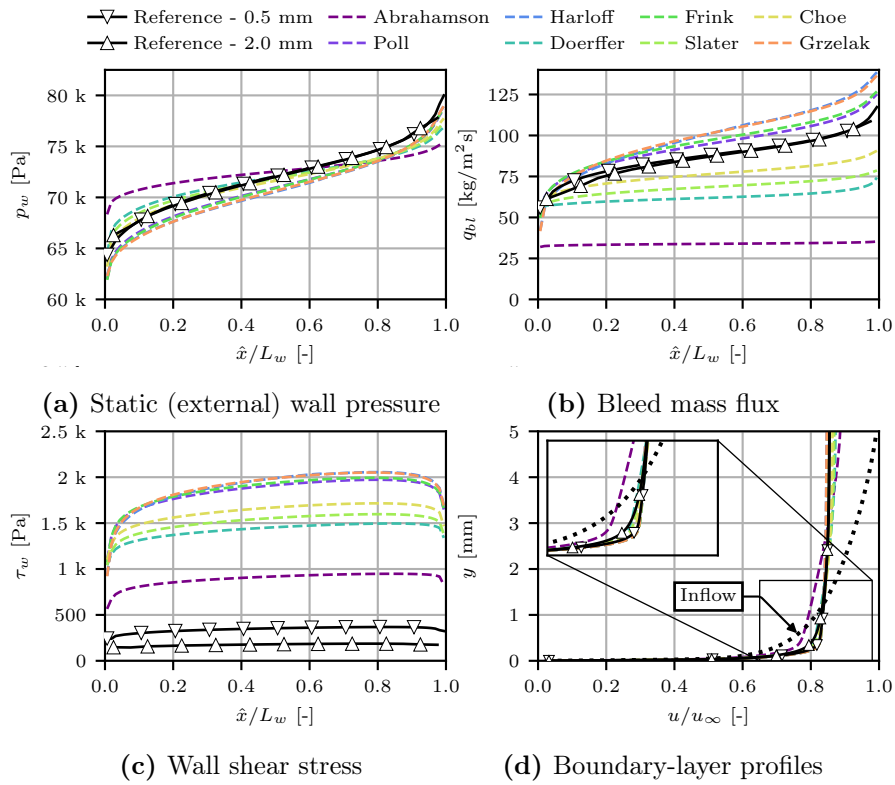


Figure 7.10: Applied boundary condition compared to the reference simulations.

by approximately 10% to 15%. As expected, the use of the supersonic models results in an underestimation of the bleed mass flux. The model of Doerffer and Bohning [38] underestimates the mass flux like in the supersonic case, because of the inaccurate prediction of the wall shear stress.

The evolution of the wall shear stress is shown in Figure 7.10c. As for supersonic conditions, the wall shear stress by the models is overestimated. The overall drag is here not shown as its value is significantly higher compared to the predicted wall shear stress of the models. The wall shear stress is found to be higher for the plate with the smaller holes. The overestimation

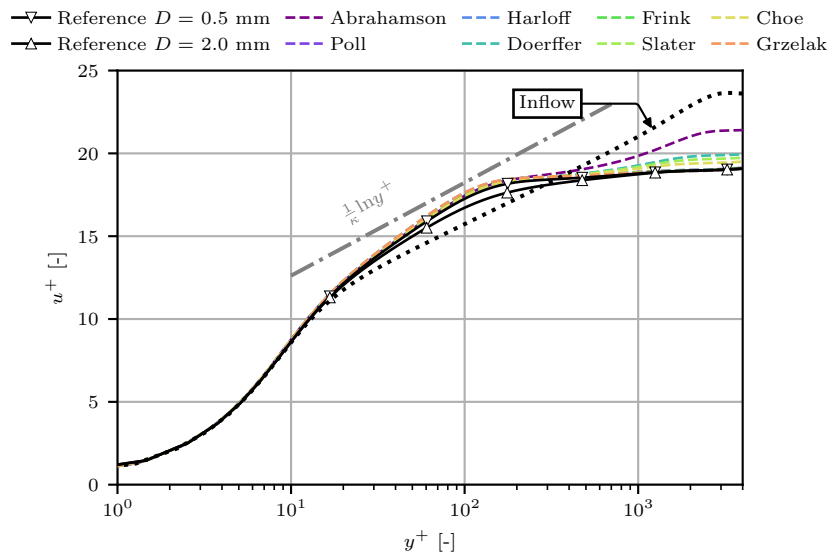


Figure 7.11: Comparison of the boundary layers downstream of the plate in dimensionless numbers.

of the wall shear stress is of high importance for the model of Doerffer and Bohning [38], which uses its values and predicts a lower bleed mass flux as in the a posteriori comparison.

In the last step, we have a look at the boundary-layer profiles (see Figure 7.10d). Interestingly, the profiles from the models downstream of the bleed region show a very good agreement with the reference simulations, even though the wall shear stress is significantly overestimated. The absence of barrier shocks for subsonic flows seems to be the reason for the good fit, as it simplifies the modeling. Moreover, in the outer boundary layer, an overestimation of the flow velocity is observed for the models that underestimate the bleed mass flux. This is a result of the reduced diffuser effect and therefore lower deceleration of the flow.

A closer look at the boundary-layer profiles in dimensionless units confirms a good agreement between bleed models and reference simulations, as shown in Figure 7.11. The characteristics of the boundary-layer profiles using the boundary condition are the same as for the supersonic application with a slope greater than $\frac{1}{\kappa} \ln y^+$. As discussed before, the velocity is overestimated in the outer layer for the models that underestimate the bleed mass flux. Moreover, the hole diameter effect, resulting in a less energetic flow inside the boundary layer for large holes, is not considered in the models and leads to a deviation from the reference simulations.

Altogether, the application of the bleed models as a boundary condition in the RANS solver shows a good agreement for subsonic conditions. The absence of barrier shocks seems to simplify the problem, leading to a higher prediction quality of the control effectiveness.

7.3 Shock-Wave/Boundary-Layer Interaction Control

In the final step, the application of the bleed models is evaluated for control of an SBLI. The same plate geometries as for boundary-layer bleed are chosen. The wedge angle is fixed to $\alpha = 10.5\%$ since a two-dimensional environment is used.

7.3.1 A Posteriori Comparison

Based on the extracted physical quantities from Chapters 4 and 6, the bleed mass fluxes using the bleed models are computed and shown in Figure 7.12. A clear distinction between the models validated with and without external flow can be made. The models of Poll et al. [85],

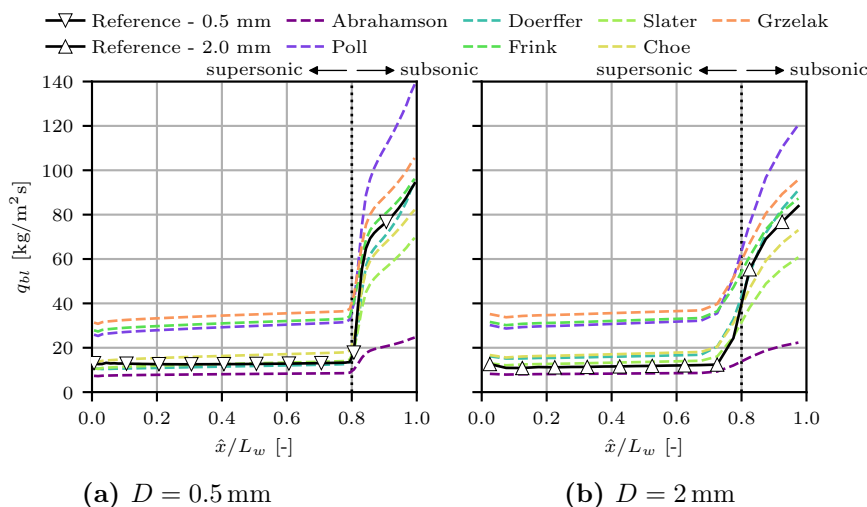


Figure 7.12: Prediction of the bleed mass fluxes based on physical quantities for various bleed models ($TR = 0.7$).

Frink et al. [41], and Grzelak et al. [54], which are not validated with the external flow, overestimate the mass flux. The relative deviation to the reference simulations is more significant in the supersonic region upstream of the incident shock than in subsonic conditions.

In contrast, the purely supersonic validated bleed models, such as the model of Slater [98], underestimate the bleed mass flux for subsonic conditions. All models except the model of Abrahamson and Brower [1] overestimate the bleed mass flux upstream of the shock, where the pressure difference from the external wall to the cavity plenum, and consequently the mass flux, is low. Altogether, the models of Doerffer and Bohning [38] and Choe et al. [21] fit best. However, the model of Doerffer and Bohning [38] fits better for the hole diameter of $D = 2.0$ mm because the wall shear stress is lower than for small holes. For the same reason as in the previous section, the model of Harloff and Smith [61] is not considered in this comparison.

7.3.2 Implementation as a Boundary Condition

Figure 7.13 illustrates the flow field around the bleed region for the models of Slater [98] and Grzelak et al. [54] compared to the reference simulations. Here, the model of Slater [98] shows a good agreement with the reference simulations even though the bleed mass flux is generally underestimated in the subsonic region. In contrast, applying the model of Grzelak et al. [54] overestimates the bleed mass flux and, hence, the removal of the low-momentum flow.

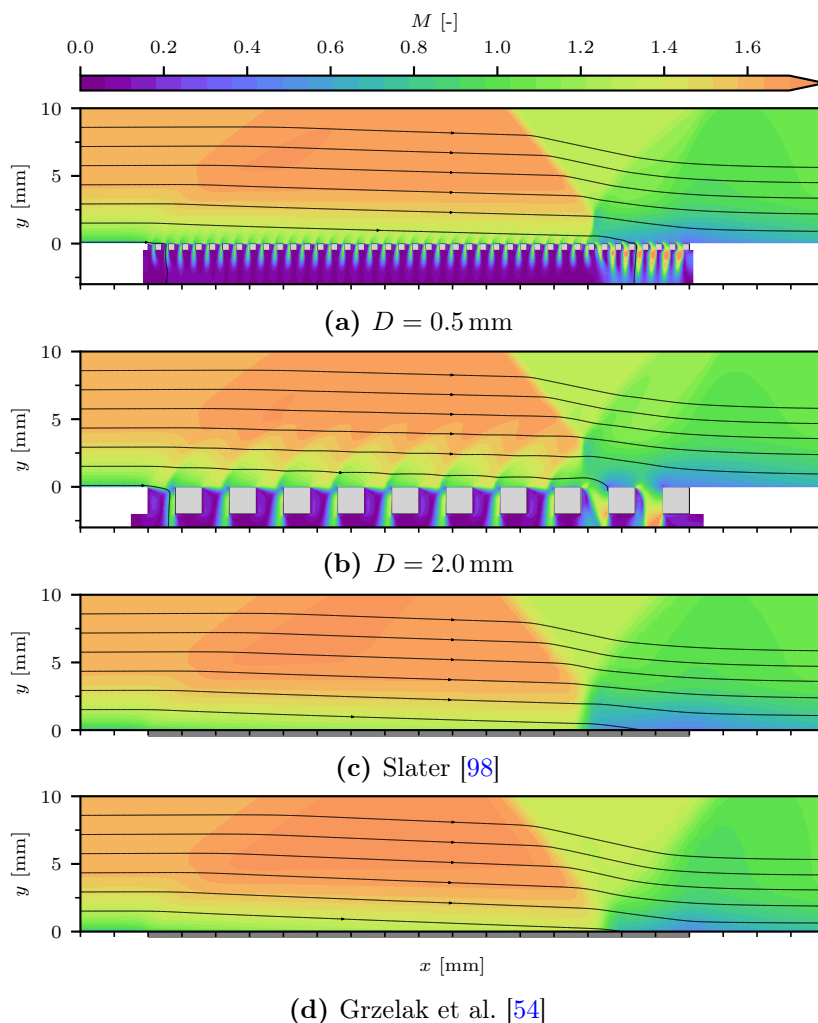


Figure 7.13: Mach number contour fields for the applied bleed boundary condition compared to the reference simulation.

Downstream of the shock, the Mach number in the vicinity of the wall is significantly higher, which results in a stronger trailing shock at the end of the plate.

Another observation from applying the bleed boundary condition is the low upstream influence of the shock wave since the subsonic fraction of the boundary layer is quasi-non-existent. The shock reflection looks inviscid without any flow separation, which is more notable for the model of Grzelak et al. [54].

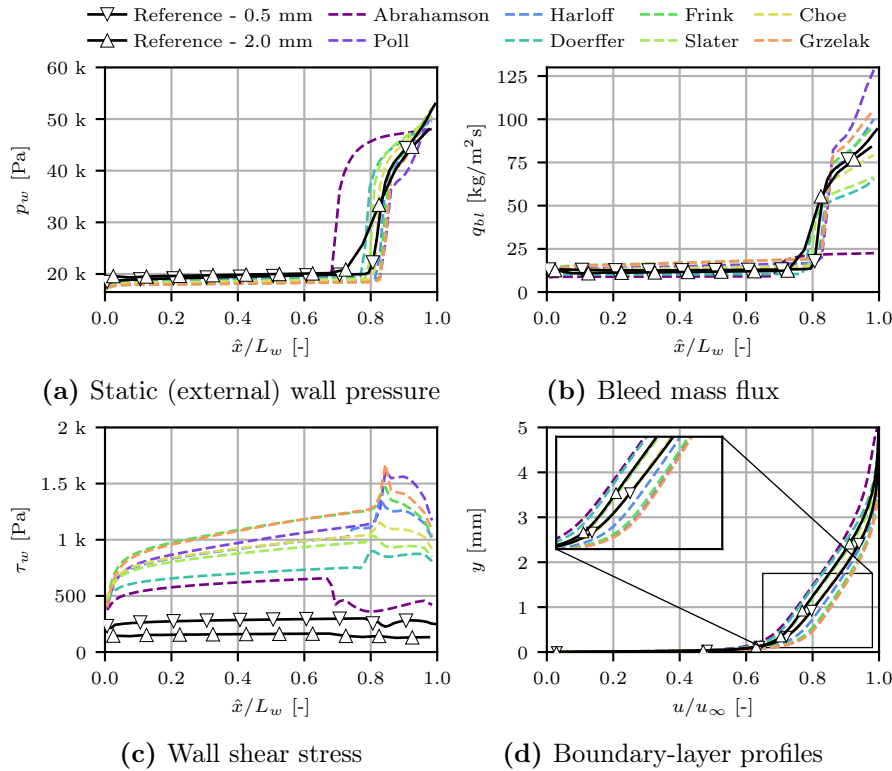


Figure 7.14: Applied boundary condition compared to the reference simulations with SBLI.

A deeper comparison of the bleed models with the reference simulations is shown in Figure 7.14, where the wall pressure, the bleed mass flux, the wall shear stress, and the boundary-layer profiles are compared. A view at Figure 7.14a reveals substantial differences between the models. The location of the shock, which is the position of the steepest pressure gradient, significantly differs between the models. The shock is located at 68% of the plate length if the model of Abrahamson and Brower [1] is applied and at 84% for the model of Grzelak et al. [54]. The reason for such a discrepancy is the higher estimated mass removal (see Figure 7.14b). Moreover, the pressure rise induced by the shock is increased if the mass flux is underestimated because the flow deflection along the shock simultaneously decreases. For large mass fluxes, the flow is bent towards the wall, inducing a higher deflection angle, and the shock intensity is consequently weaker. However, this effect results in a stronger trailing shock at the end of the plate, which is visible with the higher external wall pressure near the end of the perforated plate.

In the next step, we compare the predicted wall shear stress with those of the reference simulations (see Figure 7.14c) to assess the boundary-layer state along the bleed region and as input for the model of Doerffer and Bohning [38]. The higher the predicted mass flux, the higher the wall shear stress downstream of the shock. Contrary to the reference simulations, the wall shear stress rises below the shock foot for all models except those of Abrahamson and Brower [1] and Doerffer and Bohning [38]. Altogether, the models of Harloff and Smith [61], Frink et al. [41], and Choe et al. [21] show the best prediction quality.

Contrary to the first case, the overestimation of the wall shear stress is not associated with significantly fuller boundary-layer profiles downstream of the perforated plate (see Figure 7.14d). As revealed in the previous sections, the prediction quality is higher for subsonic conditions. Downstream of the incident shock, the controlled flow is subsonic, resulting in an improvement of the model's predictions. We assume this to be the reason for the better prediction of the boundary-layer profiles downstream of the bleed region. Moreover, the expansion fan generated by the rear edge of the shock generator results in a homogenization of the boundary layer.

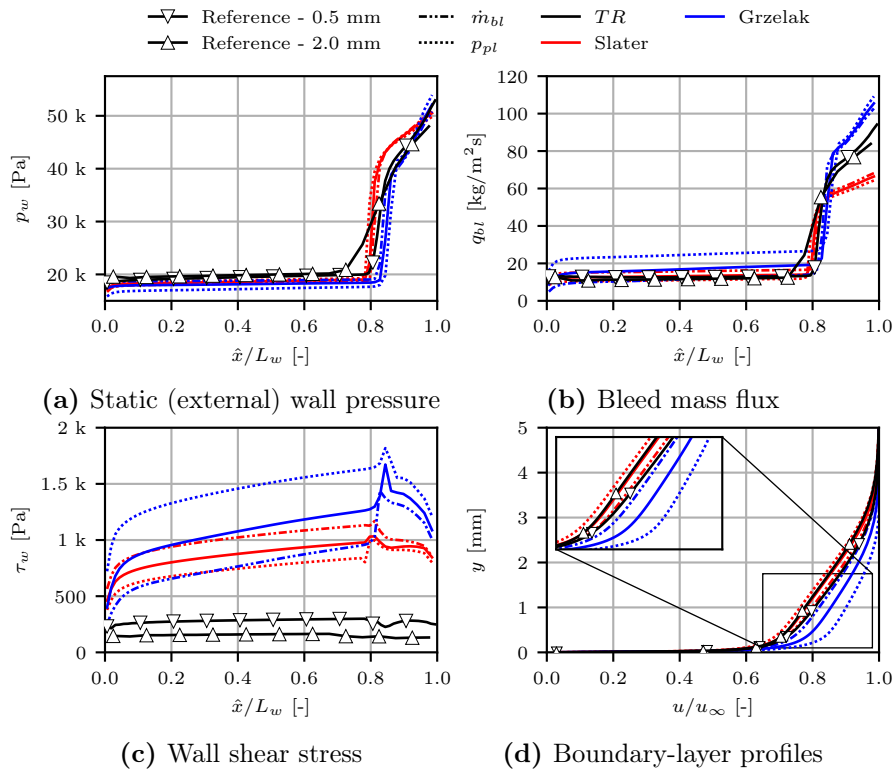


Figure 7.15: Comparison of the different bleed options for the models of Slater [98] and Grzelak et al. [54].

The influence of using the different options on the outcome of the models is shown in Figure 7.15. Again, the models of Slater [98] and Grzelak et al. [54] are chosen. In general, the same conclusion as in Section 7.1 for supersonic turbulent boundary-layer bleed can be made. The most interesting is the application of the fixed bleed rate \dot{m}_{bl} . If the mass flow rate is equal for both models, the shock position is the same, as visible in the static pressure curves (Figure 7.15a), as well as the boundary-layer profiles downstream of the bleed region (Figure 7.15d). However, the model of Grzelak et al. [54] underestimates the bleed mass flux in the supersonic and overestimates that in the subsonic region. The opposite trend is seen in the model of Slater [98].

Chapter Summary

In this chapter, we evaluated the prediction accuracy of state-of-the-art porous bleed models, which have been implemented as a boundary condition in the RANS-solver *elsA*. Three reference cases were simulated to assess the accuracy of the applied bleed models and to show the model deficiencies on two plate geometries. The models partially showed significant differences in predicting the bleed mass flux along the plate.

The reference simulations on supersonic boundary-layer bleed demonstrated an influence of the hole diameter on the flow. None of the models consider this effect in the computation of the bleed mass flux. However, the model of Slater Slater [98] fits well with the reference simulation in an a posteriori comparison. Remarkably, the model of Doerffer and Bohning [38] underestimates the bleed mass flux for small hole diameters and overestimates it for large diameters because of the wall shear stress used in the model.

Implementing the bleed models as a blowing/suction boundary condition revealed more significant deviations from the reference simulations. The boundary condition, applied on all patch cells, led to a more substantial boundary layer thinning in the case of supersonic external flows, which resulted in high wall shear stresses and significantly fuller boundary layer profiles downstream of the bleed region compared to the reference simulations. As a consequence of the overpredicted thinning effect, the expansion fan at the beginning of the porous plate is more intense, which lowers the static wall pressure. Thus, the driving pressure difference from the external wall to the cavity plenum, and hence, the bleed mass flux, are reduced compared to the a posteriori comparison. The non-prediction of the local flow phenomena induced by the bleed holes is assumed to be the main reason for the deviation between the boundary condition and reference simulations.

In the case of subsonic external flows, a fairly good fit was observed when applying the bleed models as a boundary condition, even though large deviations of all models were apparent in the a posteriori comparison. The subsonic bleed models provided the best estimations of the bleed mass flux, and the boundary-layer profiles downstream of the bleed region showed a good agreement with the reference data despite the overestimation of the wall shear stress along the bleed region.

Interesting observations were made for the complex flow case of controlling an SBLI. The implementation of the bleed models as a boundary condition resulted in a seemingly inviscid interaction. No flow separation was apparent, and the wall shear stress below the shock foot increased contrary to the reference simulations. However, the fit of the extracted boundary layer profiles downstream of the bleed region was satisfactory but improbable. One reason is the expansion fan generated by the rear edge of the shock generator, which accelerates the flow downstream of the bleed region. Moreover, Chapter 6 revealed a dominance of effects caused by the subsonic bleed downstream of the shock that may diminish inaccuracies from the supersonic region. Altogether, no model is suitable for the SBLI control.

Most models are not valid for both subsonic and supersonic flow. Moreover, essential parameters, such as the bleed hole diameter, are not considered and lead to substantial deviations. Besides, applying suction on all patch cells results in an overpredicted control effect by the boundary condition, making the appearance of a flow separation almost impossible. Thus, a new bleed model is required to consider the flow and geometrical characteristics and needs to be implemented in a way to model the effect of the bleed on the flow.

Key Points:

Supersonic conditions

- ❑ **A posteriori** comparison with reference simulation data
 - **Best agreement** found for the model of Slater [98]
 - **Overestimation of bleed rate** for models that are validated **without tangential flow**
- ❑ Comparison of **implemented models** with reference simulations
 - **Absence** of compressible phenomena (barrier shock and expansion fan) → **stronger boundary-layer thinning**
 - **Fuller boundary-layer profiles** downstream of the bleed region, because of missing bleed roughness → **overrated control effectiveness**
 - **Non-consideration** of hole diameter effect
 - **Best prediction** of bleed rate by models of Harloff and Smith [61], Slater [98], and Choe et al. [21]
- Modeling of **barrier shocks** required for the new model to predict the effect on the boundary layer → Chapter 8

Subsonic conditions

- ❑ **A posteriori** comparison with reference simulation data
 - **Best agreement** found for the model of Doerffer and Bohning [38] for $D = 2.0$ mm holes, **but** underestimation for small holes
 - **Overestimation of bleed rate** for models that are validated **without tangential flow**
 - **Underestimation of bleed rate** for models that are validated for **supersonic flow**
- ❑ Comparison of **implemented models** with reference simulations
 - **Good agreement** of predicted flow field
 - **Fuller boundary-layer profiles** downstream of the bleed region well-predicted
 - **Non-consideration** of hole diameter effect
 - **Higher accuracy** of the implemented models compared to the a posteriori comparison
 - **Best prediction** of bleed rate by models of Poll et al. [85] and Frink et al. [41]
- Subsonic flow **less sensitive** to bleed roughness effects
- **Tangential flow** must be considered in the new model for accurate prediction of the bleed rate → Chapter 8

SBLI control

- ❑ **A posteriori** comparison with reference simulation data
 - **Best agreement** found for the model of **Doerffer and Bohning [38]**
 - **Overestimation of bleed rate upstream of the shock** for models that are validated **without tangential flow**
 - **Underestimation of bleed rate downstream of the shock** for models that are validated for **supersonic flow**

- ❑ Comparison of **implemented models** with reference simulations
 - **Absence** of compressible phenomena (barrier shock and expansion fan) → **"inviscid" interaction** without lambda shock foot
 - **Rise in wall shear stress** below the shock foot
 - Application of **homogeneous suction** results in **mitigation of flow separation**
 - **Non-consideration** of hole diameter effect
 - **Best prediction** of bleed rate by models of Harloff and Smith [61], Frink et al. [41], and Choe et al. [21]

Derivation of a Novel Bleed Model

A theory has only the alternative of being right or wrong. A model has a third possibility: it may be right, but irrelevant.

MANFRED EIGEN

Chapter Introduction

In this chapter, a novel model is introduced. As described in Section 2.6, all values will be locally extracted and the suction boundary condition applied on a simplified hole contour to model the hole pattern. First, observations and numerical deficiencies observed from the implementation of the state-of-the-art bleed models are presented, and requirements for the new model are defined. Thereafter, the mathematical definition of the model is introduced, which is derived from the numerical database from Chapter 6. The model error of the introduced model is shown to be significantly lower than for the state-of-the-art bleed models.

The last step is the validation of the new model. The same reference data as in Chapter 7 is used to validate the model for supersonic and subsonic boundary-layer bleed, but also for the control of an SBLI. Moreover, the new model is compared to the respectively best state-of-the-art bleed model for each flow case to showcase its superiority.

8.1	Numerical Aims and Requirements for a Novel Model . . .	191
8.2	Computation of the Bleed Rate	191
8.3	Validation of the New Model	196
8.3.1	Supersonic Boundary-Layer Bleed	196
8.3.2	Subsonic Boundary-Layer Bleed	200
8.3.3	Shock-Wave/Boundary-Layer Interaction Control	202

8.1 Numerical Aims and Requirements for a Novel Model

The implementation of the state-of-the-art bleed models in Chapter 7 revealed several deficiencies in the implementation, performance, or applicability, which will be considered for a new modeling approach. In the following, these deficiencies and the conclusions for the novel model are presented.

The extraction of physical quantities inside the flow field is a method to obtain deeper knowledge about the flow characteristics, which simplifies the finding of a suitable model. Harloff and Smith [61] use the external Mach number to evaluate the degradation of the sonic flow coefficient. Thus, the model is applicable to both supersonic and subsonic flows. However, the definition of the boundary-layer edge for the extraction of the Mach number is challenging, especially in the case of shock-wave/boundary-layer interactions, separated flow, or the presence of shock waves and expansion fans. Several methods [53] have been implemented without finding a robust approach. Additionally, all of these methods lead to an increase of the computational costs. Wang et al. [114] extracted the Mach number at a wall distance of $0.06D$ above the opening face of the bleed hole. This approach is relatively simple to implement, but the value is arbitrarily selected to fit the simulations for a single-hole geometry.

Models such as the ones of Frink et al. [41] or Wang et al. [114] require iterative approaches to determine the bleed rate. These approaches might work quickly for a small amount of cells that are defined as the boundary condition. However, increasing mesh sizes lead to a significant increase in computational costs to compute the boundary condition. Thus, the advantage of using the boundary condition is reduced. In contrast, simple methods such as the model of Slater [98] or Grzelak et al. [54] have significantly lower computational costs, resulting in faster convergence of the simulations.

Moreover, a model shall be easily applicable without the requirement of significant mesh refinement. In the model of Wang et al. [114], the location of the barrier shock is modeled. Consequently, the mesh is required to be sufficiently fine to resolve its location. For decreasing hole sizes, this approach leads to a significant increase in required patch cells, and thus, computational costs. In addition, Benson et al. [11] have demonstrated that the exact position of the barrier shock is not required to predict the effect on the boundary layer.

The main aim of the new model is the improvement in the prediction quality of the implemented model in terms of bleed efficiency and control effectiveness. Nevertheless, the new model needs to be advantageous in comparison with resolved simulations, enabling a simple implementation and significantly reducing computational costs. Therefore, the following three requirements are defined based on the observed deficiencies of the existing models:

- ① Use of wall quantities only
- ② No iterative approach
- ③ Applicability without excessive mesh refinement.

Wall quantities are simple to extract without the need for complex extraction strategies. Iteration loops within the model increase the computational costs with every iteration, which is not beneficial. Any mesh refinement has the same consequence.

8.2 Computation of the Bleed Rate

The mathematical functions to compute the bleed rate are the heart of the model. One of the main issues with the existing bleed models tested in the previous chapter is the non-consideration of the inflow conditions. Hence, supersonic models underestimate the bleed mass

flux for subsonic conditions, and models defined for subsonic, or no external flow, overestimate the bleed mass flux in most cases. As observed in Chapter 6, but also by Harloff and Smith [61], the momentum of the captured flow has a significant influence on the size of the separated region inside the holes. In our novel model, we want to estimate it through wall quantities only (see Section 8.1). Therefore, the notation of Slater [98] is used, and the bleed rate

$$\dot{m}_{bl} = Q_{sonic,w} \dot{m}_{sonic,w} \quad (8.1)$$

is calculated with the $Q_{sonic,w}$, which is modeled, and the sonic mass flow rate based on the wall quantities:

$$\dot{m}_{sonic,w} = \frac{p_w A_{bl}}{\sqrt{T_w}} \sqrt{\frac{\gamma}{R_s}} \left(\frac{\gamma + 1}{2} \right)^{-\frac{\gamma+1}{2(\gamma-1)}} \quad (8.2)$$

The local distribution of the porosity, which was described in Section 2.6, enables the extraction of the flow velocity where the outflow boundary condition is applied (see Figure 8.1a). In the reference simulations, the velocity can be extracted in the hole opening (see Figure 8.1b). Thus, a comparison of the momentum for the boundary condition and reference simulations is possible. In this study, we focus on the tangential flow component, as the vertical flow component, i.e., the transpiration flow, is computed by the model. The tangential velocity component is used to calculate the tangential hole Mach number $M_{h,t}$ (see Figure 8.1). The tangential velocity component is used to calculate the tangential hole Mach number $M_{h,t}$ (see Figure 8.1). This quantity will be included in the novel model to estimate external flow momentum.

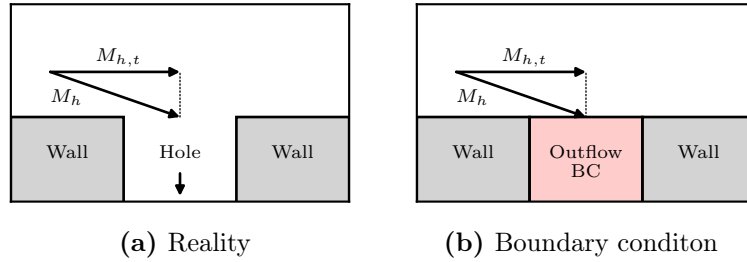


Figure 8.1: Schematic of the tangential hole Mach number.

The influence of the tangential hole Mach number on the surface sonic flow coefficient is demonstrated in Figure 8.2, illustrating the database from the parametric study in Chapter 6, which is the basis of the new model. Please note that all simulations independent of the plate geometry and the inflow conditions are considered. Figure 8.2a shows the surface sonic flow coefficient

$$Q_{sonic,w} = f \left(M_{h,t}, \frac{p_{pl}}{p_w} \right) \quad (8.3)$$

as a function of the tangential hole Mach number, which is averaged over the hole surface, and the pressure ratio from the plenum to the external wall. A degradation of the sonic flow coefficient with increasing Mach number and pressure ratio is observed. Higher Mach numbers lead to larger separated regions inside the hole (see insets in Figure 4.7a), limiting the vena contracta area. Moreover, with increasing Mach number, the intensity of the barrier shock increases for supersonic conditions in the hole entry. Thus, stagnation pressure losses, which have a further negative effect on the bleed rate, increase. With further distance to the origin of coordinates, the trend flattens, as the growth of the separation side inside the holes with the Mach number decreases.

In the next step, the plate averaged (global) values of the pressure ratio and tangential Mach number are shown in Figure 8.2b, distinguished between supersonic, sonic, and subsonic inflow

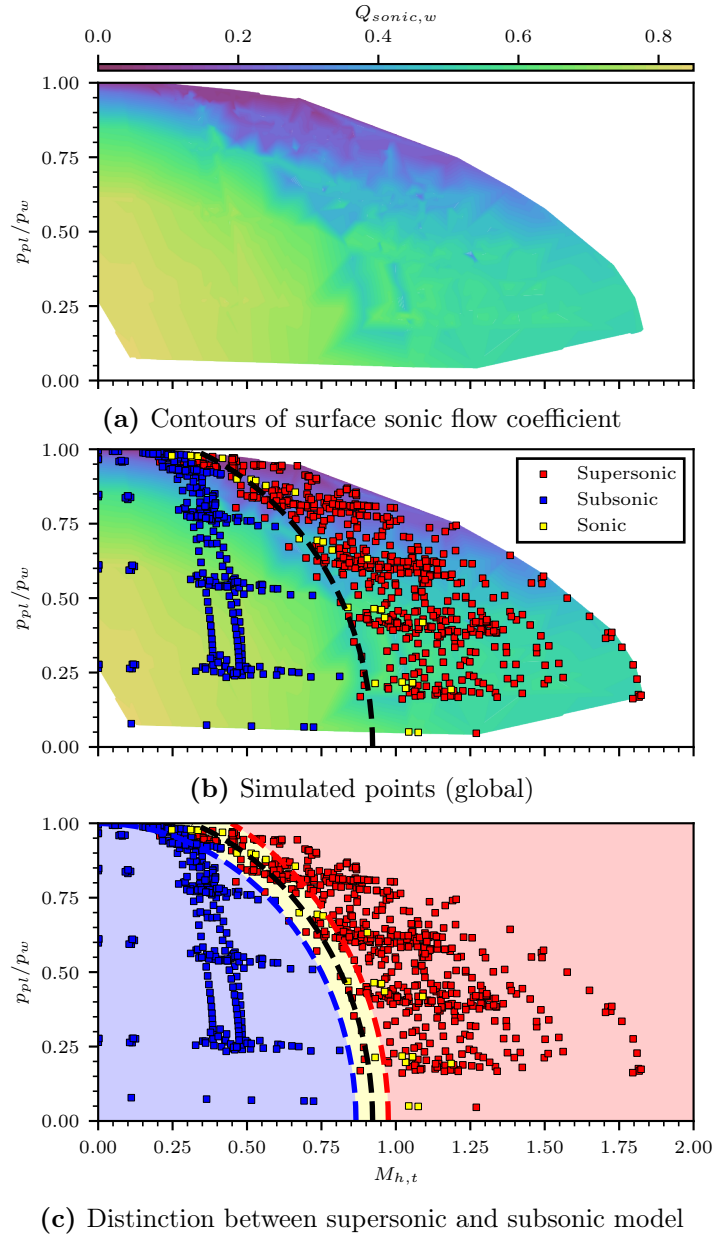


Figure 8.2: Surface sonic flow coefficient as a function of the pressure ratio p_{pl}/p_w and the tangential hole Mach number $M_{h,t}$.

conditions. A separation between supersonic and subsonic inflow conditions can be made, as highlighted by the black dashed line. A flatter trend for supersonic conditions is apparent, while the slope of the sonic flow coefficient with the distance from the origin of coordinates is high for subsonic conditions.

Since a distinction between supersonic and subsonic flow conditions is possible, and the trends significantly differ, two different regressions are used. The areas for the subsonic and supersonic models are highlighted in blue and red, respectively, in Figure 8.2c. Between, a transitional area is defined, where a blending function is applied. For the definition of the border between the regions, an ellipse

$$\sqrt{M_{h,t}^2 + 0.75 \left(\frac{p_{pl}}{p_w} \right)^2} = 0.85 \quad (8.4)$$

is defined from the origin of the coordinates.

First, the model for the subsonic region is defined. For the modeling, we divide the regression into three parts: one part is a function of the pressure ratio (ΔQ_p), one part is a function of the Mach number (ΔQ_M), and the last part is a function to model the interaction between both quantities (ΔQ_d):

$$\Delta Q_p = -0.006 \cdot 150 \frac{p_{pl}}{p_w} \quad (8.5)$$

$$\Delta Q_M = -7 \cdot 0.045^{M_{h,t}} M_{h,t}^{2.5} \quad (8.6)$$

$$\Delta Q_d = 0.18^d d^{2.6} \quad \text{with} \quad d = \sqrt{5.5 M_{h,t}^2 + \left(\frac{p_{pl}}{p_w}\right)^2} \quad (8.7)$$

$$Q_0 = 0.83 \quad (8.8)$$

$$Q_{subsonic} = Q_0 + \Delta Q_p + \Delta Q_d + \Delta Q_M \quad (8.9)$$

All three parts are added to the maximum achievable surface sonic flow coefficient Q_0 , which was computed in the simulations without external flow. Similar values are also found in the literature as incompressible discharge coefficients for holes, e.g., by Harloff and Smith [61] with $C_{D,i} = 0.82$ (see Section 1.2.4.3).

The same approach is used for the supersonic regression:

$$\Delta Q_p = -0.62 \left(\frac{p_{pl}}{p_w}\right)^3 \quad (8.10)$$

$$\Delta Q_d = -0.088 M_{h,t} \frac{p_{pl}}{p_w} \quad (8.11)$$

$$\Delta Q_M = -0.067 M_{h,t} \quad (8.12)$$

$$Q_0 = 0.67 \quad (8.13)$$

$$Q_{supersonic} = Q_0 + \Delta Q_p + \Delta Q_d + \Delta Q_M \quad (8.14)$$

Please note that the theoretical maximum sonic flow coefficient of $Q_0 = 0.67$ is not achievable as the model is not applied for Mach number $M_{h,t} < 0.4$. The maximum achieved surface sonic flow coefficient is with $Q_{supersonic} = 0.61$ comparable with the outcome of the model of Slater [98] (see Equation 1.42).

Finally, the surface sonic flow coefficient is computed using the subsonic flow coefficient $Q_{subsonic}$ for the blue area in Figure 8.2c, and $Q_{supersonic}$ for the red area:

$$d = \sqrt{M_{h,t}^2 + 0.75 \left(\frac{p_{pl}}{p_w}\right)^2} \quad (8.15)$$

$$Q_{sonic,w} = Q_{subsonic} \quad \text{if} \quad d < 0.75 \quad (8.16)$$

$$Q_{sonic,w} = Q_{supersonic} \quad \text{if} \quad d > 0.95 \quad (8.17)$$

$$Q_{sonic,w} = (1 - c_w) Q_{subsonic} + c_w Q_{supersonic} \quad \text{else} \quad (8.18)$$

$$\text{with} \quad c_w = 0.5 \times \left(\cos \left(\pi \frac{d - 0.75}{d_b} \right) + 1 \right) \quad (8.19)$$

In the yellow area between, both functions are merged using a cosine blending function with the blend distance $d_b = 0.2$. Thus, the new blended function regression is smooth and has the highest gradient at the defined border from Equation 8.4. Without any blending, the model may lead to unstable behavior caused by the discontinuity at the border.

The new bleed model is visualized in Figure 8.3 compared to the data from the database. A significant difference between the supersonic and the subsonic range is apparent. Close to

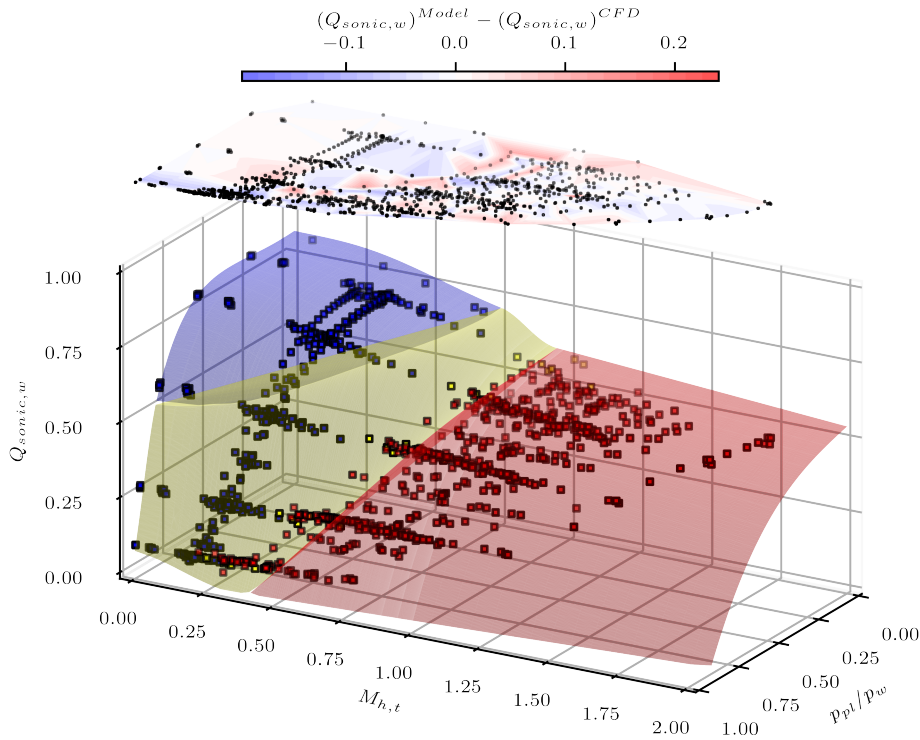


Figure 8.3: New model compared to the reference data.

the origin of the coordinates, a plateau is observed, which is caused by the choking for the holes below the critical pressure ratio of $p_{pl}/p_w = 0.528$, limiting the vena contracta area. As discussed in Chapter 6, the interaction of pressure ratio and Mach number with the vena contracta area results in the disappearance of the plateau.

Moreover, the deviation of the model from the database is highlighted by the contours at the top of Figure 8.3. Even though the overall agreement is well, there are some deviations for certain hole geometries. The largest deviations are found in the transitional area between supersonic and subsonic regression and for pressure ratios close to $p_{pl}/p_w = 1$, which is expected since the model slope is the steepest in these areas. The mean absolute error of the model over the entire database is $MAE = 0.033$, and the root-mean-square error $RMSE = 0.046$, which is significantly lower than for other state-of-the-art models evaluated in Chapter 7, as shown in Table 8.1.

Model	MAE	RMSE
New model	0.032	0.045
Doerffer and Bohning [38]	0.061	0.079
Slater [98]	0.099	0.143
Choe et al. [21]	0.101	0.119
Harloff and Smith [61]	0.152	0.161
Frink et al. [41]	0.220	0.255
Abrahamson and Brower [1]	0.254	0.305
Grzelak et al. [54]	0.284	0.315
Poll et al. [85]	0.308	0.355

Table 8.1: Error of the new model compared to state-of-the-art models.

8.3 Validation of the New Model

Finally, the new model is applied to the same reference data as in Chapter 7 to validate the model and to showcase its superiority to state-of-the-art bleed models. More details on the implementation approach are provided in Appendix A.

8.3.1 Supersonic Boundary-Layer Bleed

The new model with a resolution of 12×12 cells per hole is applied and evaluated in comparison to the reference simulation. Using this mesh resolution, the mesh size is decreased by a factor of 4 compared to the reference simulation and increased by a factor of 6 compared to state-of-the-art models. Furthermore, the model of Slater [98] is used as a reference for existing modeling approaches, as it has the highest prediction accuracy in the case of supersonic external flow (see Chapter 7). Figure 8.4 shows a comparison of the new model with the reference simulation and the model of Slater [98] for a plate with a hole diameter of $D = 2.0$ mm. At first glance, a significant improvement in terms of resolving local flow phenomena like barrier shocks is found. While the application of the model of Slater [98] leads to a homogeneous flow field, both reference simulations and the new model deliver insight into flow physics.

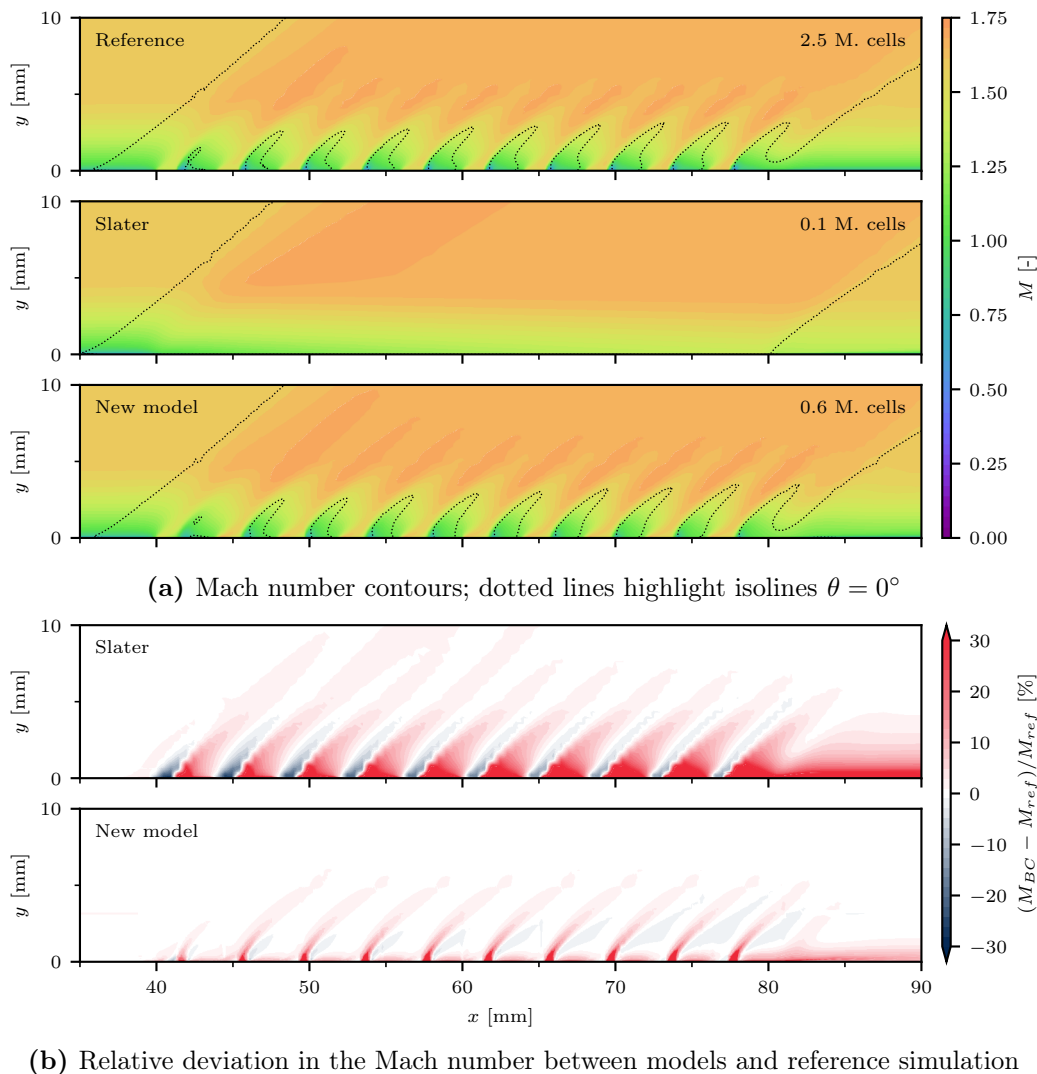


Figure 8.4: Flow field of the reference simulation with $D = 2.0$ mm compared to the model of Slater [98] and the new model.

In addition, the contour lines for the flow deflection angle $\theta = 0^\circ$ are visualized to highlight the position of the barrier shocks, the trailing shock, and the expansion fans caused by the bleed. By using the model of Slater [98], only the expansion fan at the front of the perforated plate and the trailing shock are modeled. In contrast, the flow pattern using the new model has a good agreement with that of the reference simulation.

For a deeper evaluation, the deviations of both models compared to the reference simulation are shown in Figure 8.4b. The non-consideration of local flow features results in a significant overestimation of the Mach number in the near-wall region for the application of Slater [98]. The new model shows a large improvement, as shown below. Only at the location of the barrier shocks, an overestimation of the Mach number is observed, which is a result of the non-modeling of the shock location (see Figure 8.4b). Therefore, the barrier shocks are located at the end of the holes. Downstream of the bleed region, a small overestimation of the Mach number in the near-wall region is still notable, but lower in magnitude than for the model of Slater [98].

A more detailed evaluation of the new bleed model is presented in Figure 8.5, where the models are applied and compared for two different perforated plates with $D = 0.5$ mm and 2.0 mm. Thus, the accuracy of the new model in predicting the hole diameter influence, which is the most important geometrical parameter, can be evaluated. For the comparison with the state-of-the-art models, the model of Slater [98] is added again, as it is one of the most suitable models for supersonic flows.

A more detailed evaluation of the new bleed model is presented in Figure 8.5, where the models are applied and compared for two different perforated plates with $D = 0.5$ mm and 2.0 mm. Thus, the ability of the new model to predict the hole diameter influence is evaluated. The hole diameter has the highest impact of all the geometrical parameters (see Chapter 6) and is not considered in state-of-the-art bleed models (see Chapter 7). For the comparison with the state-of-the-art models, the model of Slater [98] is added again, as it is one of the most suitable models for supersonic flows.

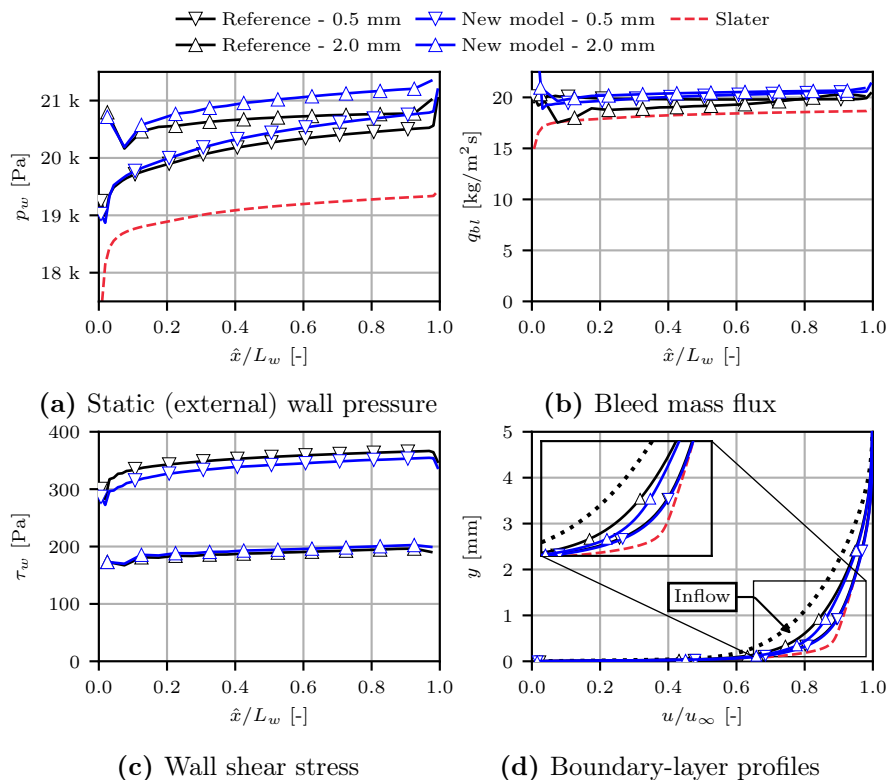


Figure 8.5: Applied boundary condition compared to the reference simulations.

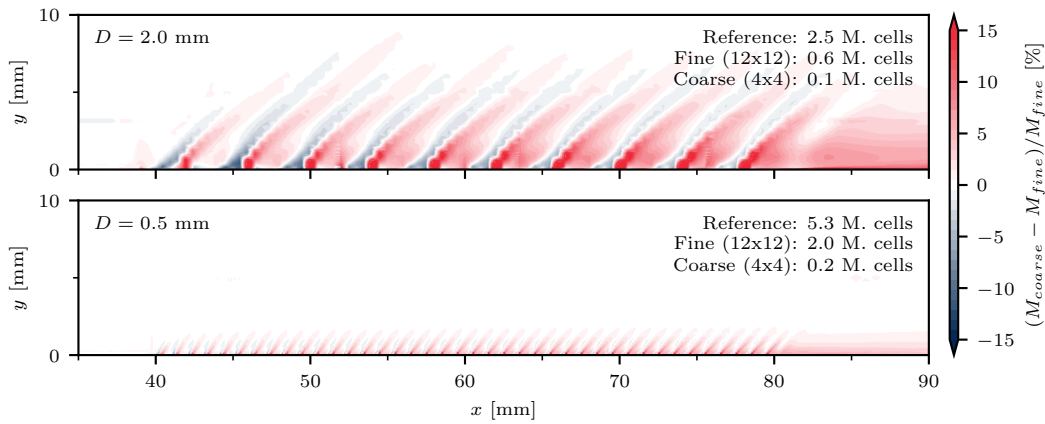


Figure 8.6: Relative deviation in the Mach number between coarse and fine mesh.

In Figure 8.5a, the external wall pressure distribution is presented. As discussed in Chapter 7, existing bleed models tend to overestimate the boundary-layer thinning, resulting in a lower wall pressure. In contrast, the new model shows a good agreement in both cases. At the beginning of the plate, the curves fit perfectly. Along the plate, the curves for reference simulations and the simulations with the new model diverge slightly.

Also, the prediction of the bleed mass flux is improved compared to the model of Slater [98], as shown in Figure 8.5b. However, the effect of the hole diameter on the mass flux does not entirely agree with the reference simulation. The model slightly overestimates the mass flux for large holes, leading to a similar trend for both plates.

The agreement of the wall shear stress for reference simulations and the new model is very good. For large holes, the values show only marginal differences to the reference, as illustrated in Figure 8.5c. The trend for small holes is also the same, but slightly below the reference.

The correct prediction of the boundary-layer profiles is essential in the case of SBLI control. As shown in Figure 8.5d, the agreement is perfect for small holes, while for larger holes the boundary layer is predicted to have a higher momentum. Nevertheless, this outcome is a significant improvement compared to the model of Slater [98].

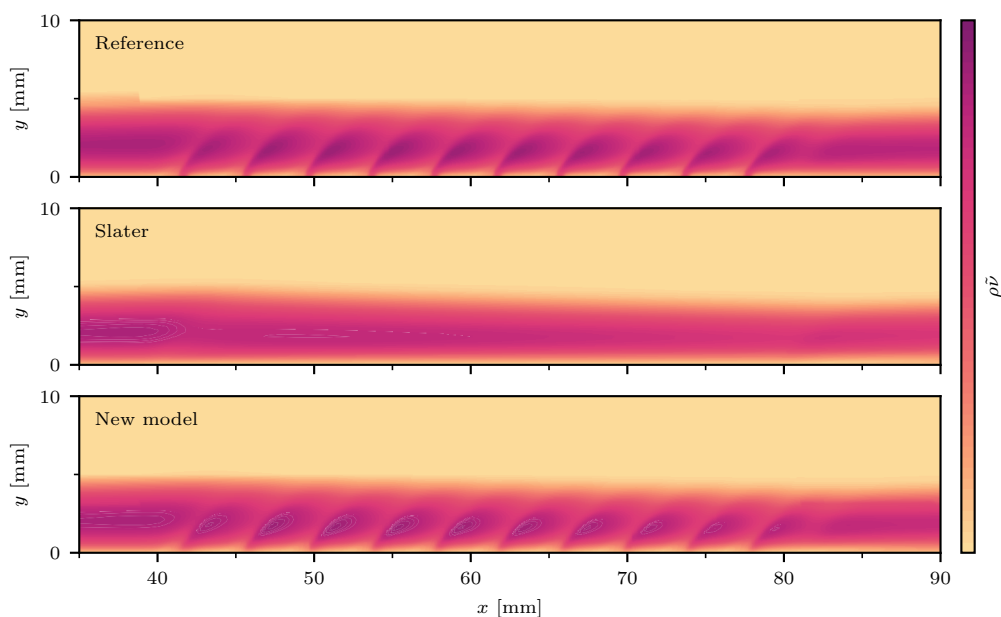


Figure 8.7: Influence of bleed models on Spalart-Allmaras non-dimensional turbulent viscosity.

As discussed in the previous section, an influence of the mesh on the effect of the bleed on the boundary layer is present. The presented results are based on simulations, where the hole was modeled by 12 x 12 cells. However, the simulations are also conducted with a coarse mesh of 4 x 4 cells per hole. Again, no influence on the bleed rate, as well as the physical quantities is found. However, an impact on the boundary layer is found, as visualized in Figure 8.6. Additionally, the mesh sizes are stated for the fine and the coarse mesh compared to the reference simulation.

A coarser mesh leads to an overestimation of the flow momentum in the vicinity of the holes. However, this effect is strongly dependent on the physical size of the holes with regard to the boundary layer. The larger the holes, the stronger the compressible effects. Thus, a larger amount of cells is required, which results in a reduction of cells of only a factor of 4 compared to the reference simulations. On the contrary, only a small number of cells is required for small holes, as the differences are in a negligible range. Thus, using the coarse mesh, the number of cells is reduced by more than 95 % compared to the reference simulation.

Generally, the mesh size is a trade-off between accuracy in the modeling and the computational costs. Moreover, the most essential savings in the application of the model are not made in terms of the computational size but the computational time, as the flow inside the holes and the cavity plenum is of low momentum and requires many iterations to converge. Thus, the savings in terms of CPU hours are in the order of hundreds.

Furthermore, the new model is compared to the reference simulation and the model of Slater [98] regarding the influence on the turbulence model. Therefore, the non-dimensional turbulent viscosity from the turbulence model [102] is extracted, as presented in Figure 8.7. Because of the barrier shocks, an increase in the turbulence near the holes is observed. The state-of-the-art modeling approaches do not capture the barrier shocks, resulting in an underestimation of turbulence, resulting in fuller boundary-layer profiles downstream of the bleed. In contrast, the new model captures the barrier shocks, which leads to a better prediction of the turbulence inside the boundary layer.

8.3.2 Subsonic Boundary-Layer Bleed

The next step is the application of the new model for subsonic conditions, using the same reference data as in Section 7.2. The flow field is visualized in Figure 8.8a for the reference simulation, the model of Poll et al. [85], and the new model. The model of Poll et al. [85] is selected as the benchmark as it showed the best fit with the reference data in this case in the previous chapter. The dashed lines illustrate the contour lines of $M = 0.6$. At first glance, the same flow field is apparent for all three simulations. The largest difference is found around the holes, where the flow is accelerated in the reference simulations and for the application of the new model. However, the impact on the boundary layer is less significant than for supersonic flows, as explained in earlier chapters.

Also, the deviations of the models from the reference simulations, as shown in Figure 8.8b, reveal only slight differences. The model of Poll et al. [85] overestimates the bleed rate, as described in Section 7.2, leading to a stronger upstream acceleration of the flow. Nevertheless, the differences in the flow field downstream are negligible. The application of the new model further minimizes the differences compared to the reference simulation. Only around the holes, tiny differences are notable.

The physical quantities along the bleed region are compared in Figure 8.9. The wall pres-

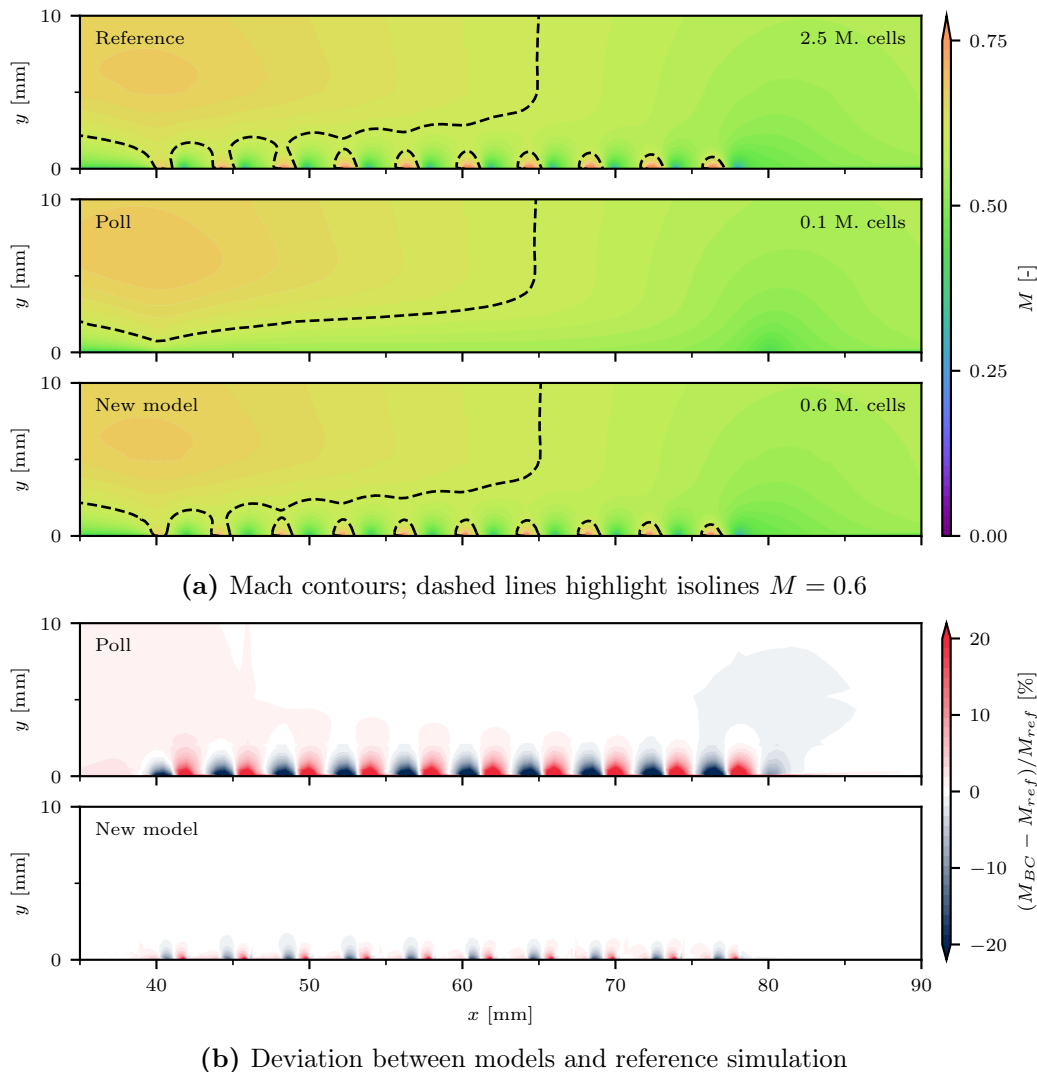


Figure 8.8: Flow field for new model compared to reference simulation and model of Poll et al. [85] for $D = 2.0$ mm.

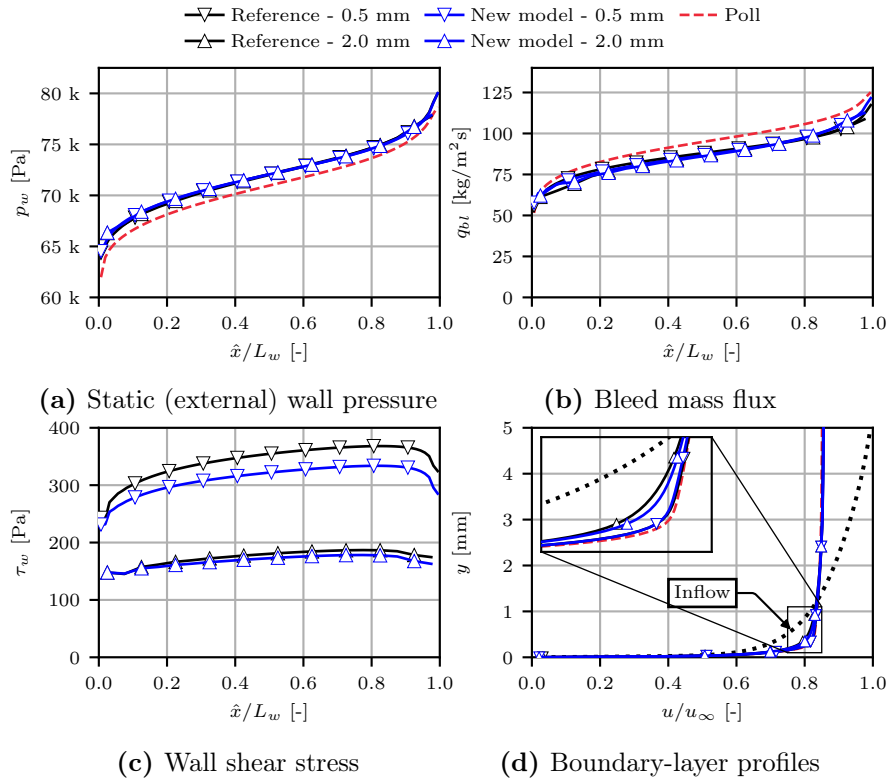


Figure 8.9: Applied boundary condition compared to the reference simulations.

sure along the plate agrees perfectly with the reference simulations, independently of the hole diameter (see Figure 8.9d). Also, the bleed mass flux is estimated with marginal deviations only, as shown in Figure 8.9b. However, the diameter influence seen for the first holes cannot be resolved in the prediction of the mass flux by using the new model, but the quality is significantly improved in comparison to the other implemented models.

Furthermore, the wall shear stress is predicted with a low deviation from the reference simulations. Figure 8.9c reveals only small deviations, which are larger for small holes, where the wall shear stress is slightly underestimated. The boundary-layer profiles downstream of the plate show a very good agreement with the reference simulations and in contrast to the model of Poll et al. [85], the diameter influence is correctly predicted.

As for the supersonic case, the influence of the mesh on the flow field is evaluated and illustrated in Figure 8.10 for both hole diameters. The impact of the mesh is similar, mean-

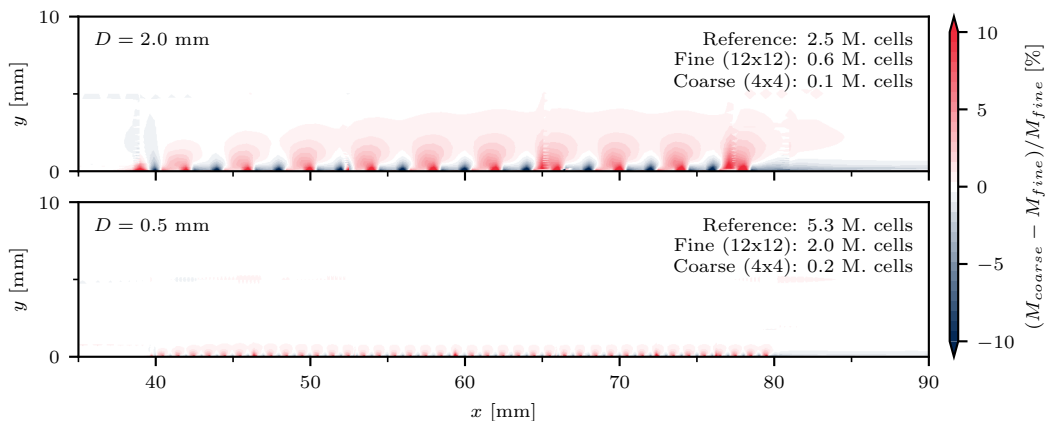


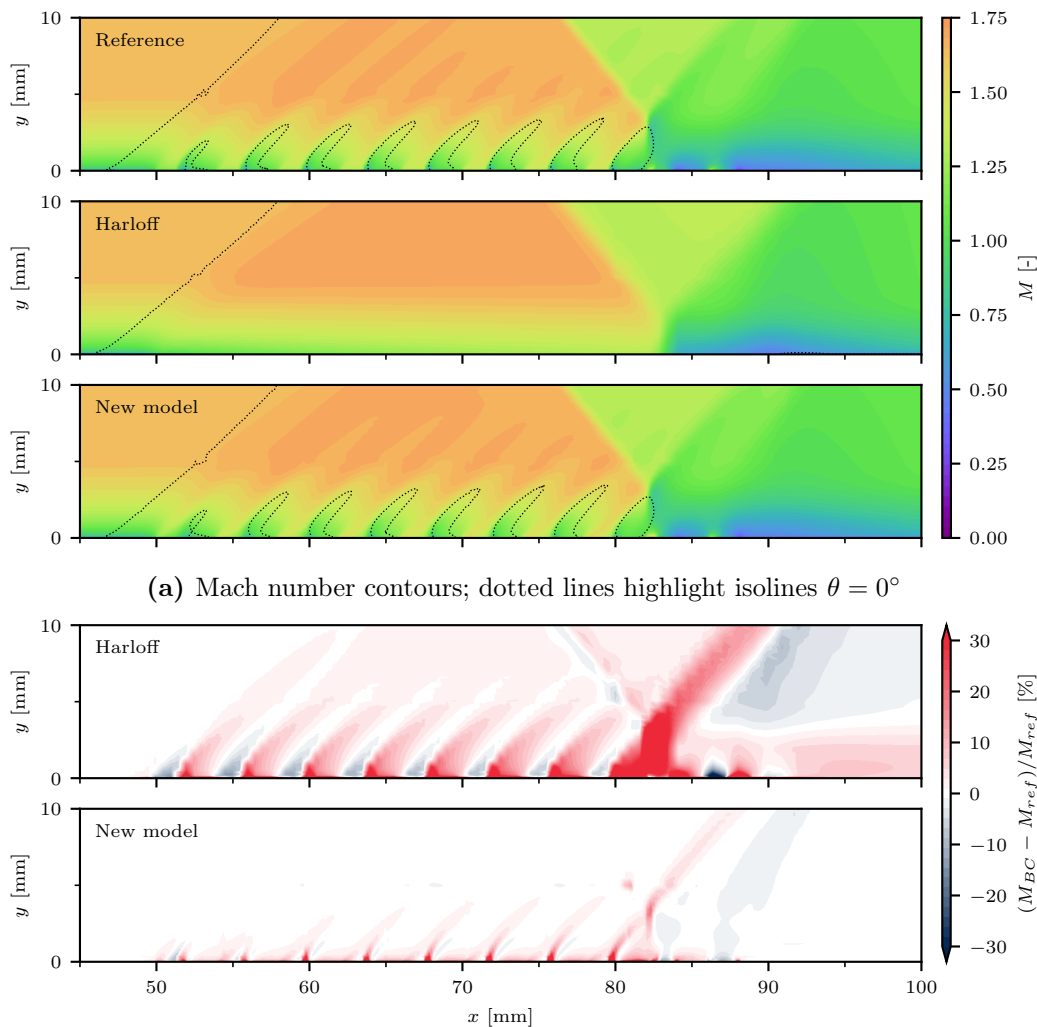
Figure 8.10: Relative deviation in the Mach number between coarse and fine mesh.

ing that the influence of the mesh on the accuracy is more important for larger holes. For $D = 0.5$ mm holes, the mesh is found to have a negligible influence. Altogether, the mesh has only a marginal influence on the simulation outcome for subsonic conditions. Thus, the mesh size can be reduced by more than 95% compared to the reference simulations.

The results also propose that the mesh size is not scaled with the hole size but the ratio from boundary-layer thickness to hole diameter δ/D of the perforated plate. Since large holes with respect to the boundary-layer thickness cause intense compressible effects, more cells are required to model the bleed roughness accurately. On the contrary, only a few cells are required for tiny holes.

8.3.3 Shock-Wave/Boundary-Layer Interaction Control

In the final step, the new bleed model is tested for SBLI control. The flow field obtained by using the new model as well as the model of Harloff and Smith [61], which is the only model distinguishing between supersonic and subsonic flows, are compared to the reference simulation in Figure 8.11a. As for the other flow cases, a very good agreement between the new model and the reference simulation is found. The isolines for the flow deflection angle $\theta = 0^\circ$ highlight the



(b) Relative deviation in the Mach number between models and reference simulation

Figure 8.11: Flow field of the reference simulation with $D = 2.0$ mm compared to the model of Harloff and Smith [61] and the new model.

excellent resolution of the flow patterns induced by the hole contours. While the shock position is located further downstream in the case of applying the model of Harloff and Smith [61], the shock location is identical by employing the new model, showcasing the good fit.

A deeper evaluation of the model is shown in Figure 8.11b, where the deviation from the reference simulation is illustrated. Thus, the low difference between the reference and the new model is visible. The main difference is again, like for supersonic conditions, the further downstream position of the barrier shocks. Also, the reflected shock is located slightly more downstream, which is a consequence of the interaction with the barrier shock. Downstream of the bleed region, no deviation can be noted. On the contrary, the model of Harloff and Smith [61] leads to an overestimation of the flow momentum inside the boundary layer and an underestimation of the external Mach number.

Also, the physical properties are accurately reproduced by using the new model. Wall pressure (Figure 8.12a), bleed mass flux (Figure 8.12b), and downstream boundary-layer profiles (Figure 8.12d) fit perfectly the reference simulations, independently of the hole diameter. The only deviation is found in the prediction of the wall shear stress along the bleed region, as seen in Figure 8.12c.

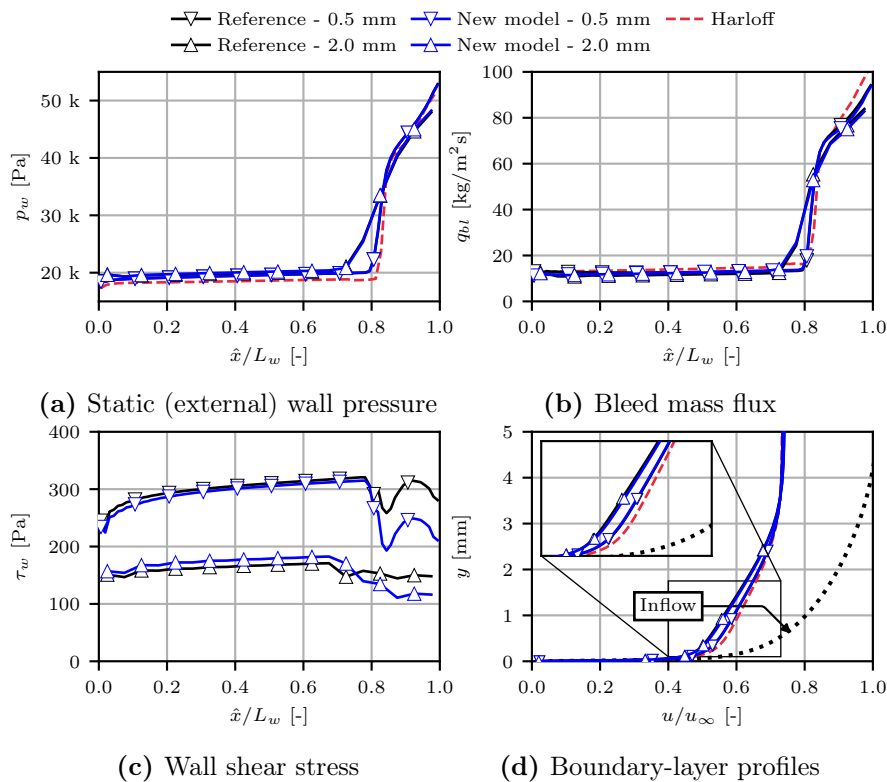


Figure 8.12: Relative deviation in the Mach number between coarse and fine mesh.

The influence of the mesh resolution is visualized in Figure 8.13. Again, the simulations are performed for 4×4 cells and 12×12 cells discretization of the holes. The contours show the deviation from the fine mesh by using a coarse mesh resolution. The mesh influence is found to be higher for large holes. The reason is the enhanced strength of the barrier shock, which interacts with the incident shock wave. The result is a slightly higher predicted flow momentum in the vicinity of the wall. However, this deviation is low with less than 5%.

For small holes, mesh coarsening results in a negligible deviation from the simulation with the fine mesh. The low penetration of the barrier shocks inside the boundary layer is the main reason. Thus, the correct prediction of the shock location is less significant for reproducing the flow field. It must be also stated that a finer mesh results in a more accurate prediction of the

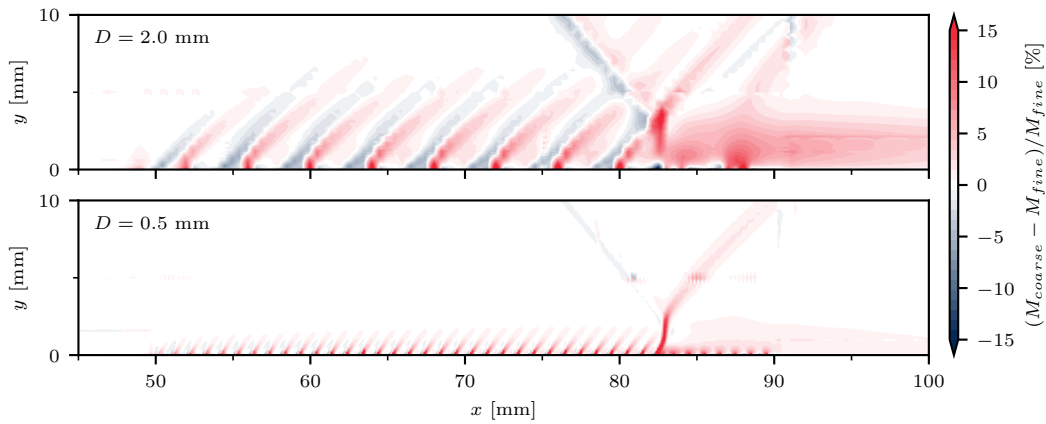


Figure 8.13: Influence of the mesh refinement on the flow field.

impingement location of the incident shock, which might increase the deviation between the coarse and the fine mesh.

Altogether, the new model is proven to be applicable for the control of SBLIs. The mass flux is correctly estimated for both supersonic and subsonic flows. Consequently, the effect of the bleed on the incident shock can be correctly modeled. Moreover, the distribution of the suction profile leads to the correct prediction of the flow field along and downstream of the bleed region. Deviations from the reference simulations are in a negligible range, and computational costs are significantly reduced as the bleed holes, as well as the cavity plenum, do not need to be modeled.

Chapter Summary

A novel bleed model was derived based on the data from the numerical parametric study in Chapter 6. The model was applied locally by discretely modeling the hole contour on a porous patch. Thus, the hole pattern was modeled in the mesh, and the tangential Mach number at the outflow boundary condition became extractable in the RANS solver. Hence, we can use the tangential hole Mach number and the pressure ratio from the cavity plenum to the external wall to assess the external flow condition. Thus, two separate regressions for supersonic and subsonic conditions were applicable based on the wall quantities extracted from the numerical database.

As a result of the two separate regression functions for supersonic and subsonic external flows, the model is superior compared to state-of-the-art bleed models. The prediction quality was proven to be significantly improved compared to the models tested Chapter 7, as shown by the lower modeling error computed on the numerical database.

The model was applied to the supersonic reference case and compared to the bleed model of Slater [98]. Capturing the barrier shocks resulted in a significant improvement in predicting the downstream boundary-layer profiles. Three-dimensional effects caused by the hole contour were observed using the boundary condition. Moreover, the physical quantities at the wall, like shear stress, were well predicted.

Similarly, the prediction quality for subsonic conditions was improved compared to the model of Poll et al. [85]. The deviations between the new model and reference simulations were in a negligible range, and all physical quantities showed excellent agreement.

As the final step, the new bleed model was applied to the complex case of the control of an SBLI. Only slight differences between the reference simulations and the new model were observed. One can then argue that the new model is the first bleed model that is applicable for the control of a shock-wave/boundary-layer interaction by considering the bleed geometry and external flow conditions sufficiently.

Key Points:**New bleed model**

- ❑ Model derived from the **comprehensive database** from Chapter 6
- ❑ Regression-based model → **low computational costs**
- ❑ Distinction between **supersonic** and **subsonic** conditions
- ❑ Only **wall quantities** used for computation
- ❑ **Low mesh influence** on the bleed rate
- ❑ **Spanwise variations** of the boundary layer resolved

Application in RANS solver

- ❑ **Supersonic conditions**
 - Modeling of **Barrier shocks** leads to **significant improvement** compared to state-of-the-art bleed models
 - **Good prediction** of the **boundary-layer profiles** downstream of the bleed region and the **bleed rate**
 - **Reduction** of the **mesh size** by more than 95 % for $D = 0.5$ mm and 75 % for $D = 2.0$ mm
- ❑ **Subsonic conditions**
 - **Very good agreement** in the prediction of the flow field
 - **Negligible deviation** from reference simulations
 - **Reduction** of the **mesh size** by more than 95 %
- ❑ **SBLI control**
 - Modeling of **Barrier shocks** leads to **significant improvement** in the prediction of the shock pattern
 - **Excellent prediction** of the **wall quantities** along the bleed region and **boundary-layer profiles** downstream of the bleed region
 - **Consideration** of hole diameter effect

Conclusions and Perspectives

*Alles Wissen und alles Vermehren unseres Wissens endet
nicht mit einem Schlußpunkt, sondern mit einem
Fragezeichen.*

HERMANN HESSE

Conclusions

The numerical and experimental studies performed in this thesis were dedicated to the control of turbulent flows with porous bleed. Porous bleed are a proven method for the control of SBLIs in supersonic air intakes to mitigate shock-induced flow separation, which may cause performance losses or unsteady oscillations, such as intake buzz. With the aim to optimize bleed systems, and simplify the design process, the following objectives were defined at the beginning of the thesis:

- ① Understanding the underlying flow physics of porous bleed
- ② Comprehensive evaluation and comparison of existing bleed modeling approaches
- ③ Derivation of a novel bleed model, applicable to a broad range of flow and geometrical characteristics, and suitable for the control of SBLIs

The complex flow case of controlling a (strong) SBLI with porous bleed was simplified by separating the problem into three subproblems:

- ① Bleed control of a supersonic boundary layer
- ② Bleed control of a subsonic boundary layer
- ③ Interaction of the incident shock with the bleed

Moreover, the distinction between **bleed efficiency** and **control effectiveness** was made. **Bleed efficiency** describes the ability to remove the highest possible mass for the lowest possible pressure losses. In contrast, **control effectiveness** is linked to control of the boundary

layer, i.e., the achievement of the fullest possible boundary-layer profile by removing as little mass as possible.

In the following, our approach of separating the problem into three subproblems is proven by summarizing step by step the path to achieve the defined objectives.

Understanding the Flow Physics

Supersonic Flow Control The first performed step was the study on the control of supersonic flows. A numerical parametric study was performed for a Mach number of $M = 1.6$ to examine the influence of the bleed geometry on bleed efficiency and control effectiveness. The generated data showed a significant spreading caused by the geometrical parameters. The bleed efficiency of the bleed was mainly influenced by the hole diameter and the thickness-to-diameter ratio. Large hole diameters were linked with a high momentum of the captured flow, resulting in high pressure losses caused by the barrier shock and the under-expanded jet streaming in the cavity plenum. The thickness-to-diameter ratio significantly affected the flow inside the hole depending on the pressure ratio. High friction losses appeared for thick plates and choked flows, while pressure losses dominated for low suction rates and thin plates. Plate length and porosity level influenced the bleed efficiency but were linked to the absolute bleed rate. Small plates with low porosity levels were more efficient, but the achievable bleed rate was too low for most applications.

The control effectiveness was mainly influenced by the hole diameter. Since the momentum of the captured flow was higher for large holes, the so-called barrier shock was of higher intensity, leading to a local thickening of the boundary layer downstream of the holes. Moreover, high porosity levels increased the control effectiveness of a porous bleed, as well as hole staggering.

Experiments in the S8Ch supersonic wind tunnel were performed for a Mach number of $M = 1.62$ to validate the numerically predicted effect on the boundary layer. Two different plate geometries were investigated for several bleed rates. The boundary-layer profiles acquired by LDV measurements validated the numerical findings. Moreover, the numerical parametric study revealed variations of the boundary-layer profiles along the spanwise directions for certain geometrical parameters (e.g., large hole diameters, low porosity levels, hole staggering). Acquisition of the spanwise boundary-layer profiles for a hole diameter of $D = 2.0$ mm confirmed the numerical findings.

Subsonic Flow Control Different behavior of porous bleed was observed for subsonic flows. Porous bleed, independently if applied in supersonic or subsonic flows, generated a diffuser effect, meaning that the external flow was deflected towards the wall. Consequently, the (external) flow was decelerated (or accelerated for supersonic conditions). Thus, two contradictory effects were present: the flow in the vicinity of the wall was accelerated, while the external flow velocity was decelerated. As a result, a quick saturation of the rise in the wall shear stress was achieved. On the contrary, unnecessary high bleed rates led to a deceleration of the external flow. This effect was validated by experiments conducted for a Mach number of $M = 0.5$. A consequence of the diffuser effect was also an increase in the bleed efficiency along the plate as the tangential velocity decreased. Thus, the separated region inside the holes decreased in size, resulting in an enlarged vena contracta area. The so-achieved bleed rates were significantly higher than for supersonic flows.

In contrast to supersonic conditions, the influence of the geometry on bleed efficiency and control effectiveness was small. The bleed efficiency was mainly influenced by the thickness-to-diameter ratio, which had an even more significant impact than for supersonic conditions. Hole diameter, porosity level, and hole diameter had an influence but were less significant than the

thickness-to-diameter ratio. Remarkably, high porosity levels were slightly more efficient while the opposite was the case for supersonic flows.

Also, the geometrical influence on the control effectiveness was relatively low. As for supersonic flows, small hole diameters were beneficial. Moreover, high porosity levels were found to be more effective.

Shock Interaction In the third step, the interaction of the incident shock with the porous bleed was investigated. Unfortunately, a (normal) shock wave is always linked to supersonic and subsonic flows, and thus, its control cannot be separated from the supersonic and subsonic flow control. However, after understanding the control mechanisms in both regimes, unforeseen behavior was linked to the adverse pressure gradient induced by the shock.

The first observed effect was linked to the different bleed rates upstream and downstream of the shock. The pressure rise due to the shock led to a higher wall pressure downstream of the shock, which resulted in higher suction rates. Additionally, the flow downstream of the shock was subsonic, leading to an increased bleed efficiency. Hence, the tangential flow velocity decreased along the shock, while the transpiration velocity increased. The consequence was a different flow angle downstream of the shock compared to the flow upstream. Thus, a deflection angle along the shock was generated, reducing the shock intensity. Simulations of the wind tunnel flow showed a significant reduction in the height of the Mach stem, which implied a "more regular" shock reflection. LDV measurements validated the numerically acquired velocity profiles along the bleed region, confirming the findings.

The bleed efficiency was found to behave analogously to supersonic and subsonic conditions. Upstream of the shock, the external flow was supersonic, resulting in the same trends as previously described. Downstream of the shock, where the flow was subsonic, the pressure ratio dropped and the sonic flow coefficient increased. Additionally, blowing occurred if the bleed rate was too low and the plenum pressure exceeded the wall pressure upstream of the shock.

The adverse pressure gradient was observed to significantly influence the control effectiveness. Again, effects upstream and downstream of the shock were known. As discussed before, large bleed holes generated an inhomogeneous boundary layer. Due to the adverse pressure gradient, this effect was enforced. The higher the sonic line height, the longer the separation length. Hence, the flow between the holes was more likely to separate in the case of large holes. Even though suction downstream of the shock led to a reattachment of the flow, the three-dimensionality of the flow remained and was even stronger than for the purely supersonic and subsonic boundary-layer bleed. Interestingly, low porosity levels were found to reach a higher effect on the boundary layer for the same bleed rate. It was expected to be a consequence of the lower pressure ratio upstream of the shock, and thus, better control of the supersonic boundary layer.

Benchmark of State-of-the-Art Bleed Models

Supersonic Flow Control A posteriori application of the bleed models revealed significant deviations between the different approaches and the data from the before-performed parametric study. As expected, models that were validated for supersonic flows performed better in this comparison. Models that do not consider tangential flow overestimated the bleed rate. The application of the models in the RANS solver revealed significant differences between definition and application. The homogeneous suction resulted in an overestimated thinning effect of the boundary layer. Hence, the boundary-layer profiles downstream of the bleed were observed to be significantly fuller. The consequently stronger expansion fan at the front of the plate resulted in a lower wall pressure, and hence a lower bleed rate than a priori expected. Moreover, the

effects of the hole geometry were not considered in the models.

Subsonic Flow Control The a posteriori comparison of the bleed models with the reference data revealed large deviations in all models. However, the application of the bleed boundary condition was observed to be less sensitive than for supersonic conditions. Even though the models overpredicted or underpredicted the bleed rate, a good agreement with the boundary-layer profiles downstream of the bleed region was found.

Shock Interaction None of the models was found to be accurate for the control of an SBLI. As discussed before, the effect on the boundary-layer profile upstream of the incident shock was overpredicted. Hence, the momentum of the boundary layer that interacted with the shock was too high to separate. Consequently, the pressure rise was found to be close to the inviscid theory.

Derivation of a Novel Bleed Model

Finally, a new bleed model was derived based on the data from the numerical parametric study. The model was applied locally by discretely modeling the hole contour. Thus, the hole pattern was modeled in the mesh, and the tangential Mach number at the outflow boundary condition became extractable. Using the tangential hole Mach number and the pressure ratio from the cavity plenum to the external wall, the external flow condition was detectable. Thus, two separate regressions for supersonic and subsonic conditions were applicable based on the wall quantities extracted from the numerical database. Consequently, the model was applicable to both supersonic and subsonic flow.

The model was applied to the supersonic reference case like the state-of-the-art bleed models before. Capturing the barrier shocks resulted in a significant improvement in predicting the downstream boundary-layer profiles. Moreover, the physical quantities at the wall were well predicted. Also, the prediction quality for subsonic conditions was improved.

Finally, the new bleed model was applied to the complex case of the SBLI. Only slight differences between the reference simulations and the new model were observed. Thus, the new model is the first bleed model that is applicable for the control of an SBLI and considers the bleed geometry sufficiently.

Perspectives

While many questions were answered, new topics arrived. In the following, possible steps to continue research on porous bleed systems are suggested.

Understanding of Flow Physics With the aim to further increase the knowledge about porous bleed systems, additional parameters may be studied:

- ❑ The hole inclination angle is another geometrical parameter, which is proven to significantly influence bleed efficiency and control effectiveness. In the current study, this parameter was excluded as its application below a normal shock seems to be not beneficial based on the literature research.
- ❑ With the aim to apply porous bleed systems for hypersonic applications, the research may be extended to higher supersonic or hypersonic Mach numbers. The study of Harloff and Smith [61] predicts a self-similarity for supersonic Mach number. However, research on Mach numbers higher than $M = 3.0$ is required to confirm this theory. Simulations performed for a Mach number of $M = 3.0$ have shown a notable degradation of the sonic flow coefficient. However, they were not shown since the numerical setup was only validated until $M = 2.5$.
- ❑ Additionally, alternative hole shapes might be interesting, especially since additive manufacturing enables the production of complex plate geometries. One idea could be the application of holes with chamfer to evaluate if a combination of normal and slanted holes is beneficial.

Model Improvement Also, the modeling may be improved by the following tasks:

- ❑ As stated, the hole inclination angle is an additional parameter to consider in the model. The inclination angle would be required to be added directly in the regression function, as the sonic flow coefficient is approximately three times higher for 20-degree holes compared to 90-degree holes. Moreover, it is unsure if there are interactions with the other geometrical parameters.
- ❑ A more complex regression function or the use of machine learning might increase the prediction accuracy of the sonic flow coefficient by considering all geometrical parameters. However, large computational resources might be required to extend the database for a relatively small improvement of the model.
- ❑ The flow in the cavity plenum is considered to be of constant pressure. However, small cavities or strong pressure gradients might result in secondary flows which lead to a variation of the plenum pressure inside the cavity plenum, and thus, different bleed rates. Hence, the model could be linked to an external domain modeling the cavity plenum. Moreover, in the modeling, the plenum pressure adjusts instantly. However, inertia might lead to a deferred response of the bleed on, for example, shock oscillations.

Different Model Concept The modeling approach of Laurendeau et al. [65] that manipulates the velocity scale in the turbulence model was introduced in Chapter 1. This approach might be interesting since it can be applied in two-dimensional simulations. The data generated in Chapter 6 may be used to estimate the bleed roughness. However, the model required the Mach number to obtain the associated trimming coefficient. Alternative approaches would

be required to obtain this value from wall quantities. Moreover, this model requires the manipulation of turbulence modeling, which is not easily applicable to all flow solvers. Also, three-dimensional effects are not considered using this approach.

Application of the New Model Moreover, the bleed model was tested only on basic academic cases. Other industrially relevant test cases are:

- The application to a supersonic air intake like the NASA 1507 air intake [101]. In this air intake, four different bleed regions consisting of eight patches are defined. Pressure data along the cowl interior and center body are available, as well as pressure rake data. A recent workshop [71] revealed significant differences between solvers and methods compared to the experimental data.
- The application of the bleed model to unsteady simulations to test the stability in the case of external flow variations.
- The testing of the model for shock oscillation control (e.g., air intake buzz).

Alternative Bleed Concepts Moreover, the findings of this thesis proved strong three-dimensional effects of the flow field downstream of the bleed for certain geometrical parameters. While fluidic vortex generators, which use blowing, are a topic of research, the application of suction to generate vortices in supersonic flows is by the author's knowledge not investigated. While blowing is impractical because of the required pressure, suction is relatively simple to apply.

Appendices

Implementation of the New Model Using Python

The implementation approach for the new model is presented in Section 2.6. The source code for the implementation in *Python* using the package *shapely* [51] is shown below (see Code A.1). In this example, a simplified mesh grid is generated and ϕ and ψ are computed for 2 mm holes with a porosity level of approximately 18%, from which the diameter of the extraction area A_o can be computed, called `diameter_o`. The variable `grid` describes the number of cells per hole, which is in this case 4. The variables `xh` and `yh` are the coordinates of the bleed hole centers.

The function `compute_phi_psi` is used to calculate ϕ and ψ from the given values. For every hole, the intersection of the cell areas with the hole and extractions areas is computed and scaled by the cell areas. Finally, ψ (variable `psi`) must be reduced by the value of ϕ (variable `phi`) to prevent extraction of the wall quantities from the hole. However, for $\phi < 0.5$ (`cut_phi`), the wall quantities are even on the outflow boundary condition extracted since the bleed mass flux on these cells is low.

```

1 import numpy as np
2 from shapely.geometry import Point, Polygon
3
4 # Constants
5 diameter = 4 # Bleed hole diameter
6 porosity = 0.18 # Porosity level of perforated plate
7 diameter_o = np.sqrt(diameter ** 2 / porosity) # Extraction diameter
8 grid = diameter / 4 # Grid resolution
9
10 # Coordinates of the mesh grid
11 x, y = np.meshgrid(
12     np.linspace(0, 25, int(25 / grid) + 1),
13     np.linspace(0, 7, int(7 / grid) + 1)
14 )
15
16 # Coordinates of the bleed hole centers
17 xh = np.array(((0, 10, 20), (5, 15, 25)))
18 yh = np.array(((0, 0, 0), (7, 7, 7)))
19
20 def compute_phi_psi(x, y, xh, yh, diameter, diameter_o, cut_phi=0.5):
21     grid_dimensions = np.array(x.shape) - 1
22     phi = np.zeros((*grid_dimensions, len(xh.flatten())))
23     psi = np.zeros((*grid_dimensions, len(xh.flatten())))
24
25     # Computation of the intersection areas
26     def compute_area(mask, dia, area_array, n):
27         bool_cells = np.array((mask[:-1, :-1], mask[1:, :-1], mask[:-1, 1:],
28             mask[1:, 1:]))
29         area_array[np.any(bool_cells, axis=0), n] = 0.5
30         area_array[np.all(bool_cells, axis=0), n] = 1.0
31         hole = Point(xn, yn).buffer(dia / 2)
32         for i0, i1 in np.argwhere(area_array[:, :, n] == 0.5):
33             pc = Polygon([
34                 (x[i0, i1], y[i0, i1]),
35                 (x[i0 + 1, i1], y[i0 + 1, i1]),
36                 (x[i0 + 1, i1 + 1], y[i0 + 1, i1 + 1]),
37                 (x[i0, i1 + 1], y[i0, i1 + 1])
38             ])
39             area_array[i0, i1, n] = hole.intersection(pc).area / pc.area
40
41     # Computation for every hole
42     for n, (xn, yn) in enumerate(zip(xh.flatten(), yh.flatten())):
43         dist = np.sqrt((x - xn) ** 2 + (y - yn) ** 2)
44         compute_area(dist <= (diameter / 2), diameter, phi, n)
45         compute_area(dist <= (diameter_o / 2), diameter_o, psi, n)
46
47     # Correction psi
48     psi -= phi
49     psi[phi > cut_phi] = 0
50
51     return phi, psi
52
53 phi, psi = compute_phi_psi(x, y, xh, yh, diameter, diameter_o)

```

Code A.1: Python code to compute ϕ and ψ for given mesh grid and hole positions.

Figure A.1 illustrates the outcome of Code A.1, where the hole is discretized using 4×4 cells. This corresponds to the coarse mesh resolution used in Chapter 8 for the new model.

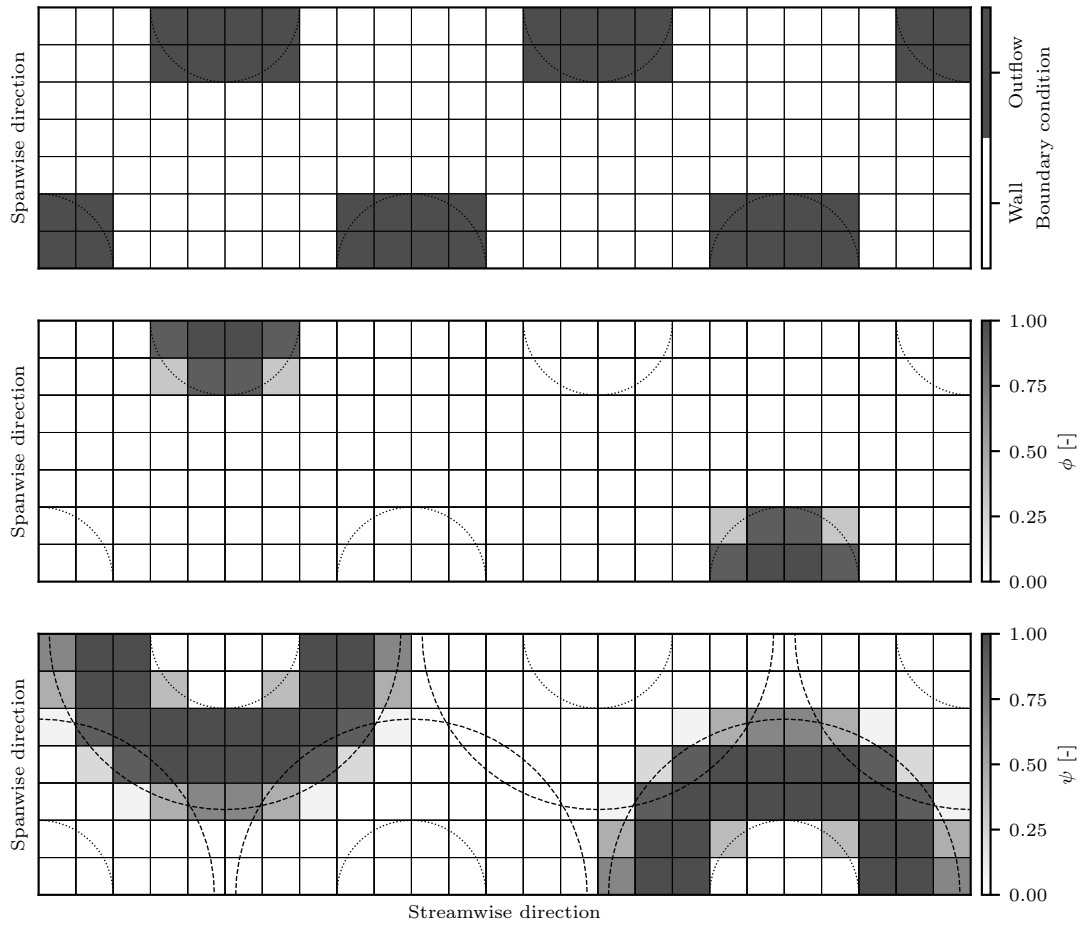


Figure A.1: Implementation of the new bleed model using 4×4 cells per hole; the location of outflow boundary conditions ($\phi > 0$) is shown at the top; ϕ (center) and ψ (bottom) are illustrated for two holes; dotted lines surround the hole area and dashed lines the extraction area.

Figure A.2 illustrates the outcome of Code A.1, where the hole is discretized using 12×12 cells. This corresponds to the fine mesh resolution used in Chapter 8 for the new model. In comparison to `fig:implementationCoarse`, the hole contour is significantly higher resolved.

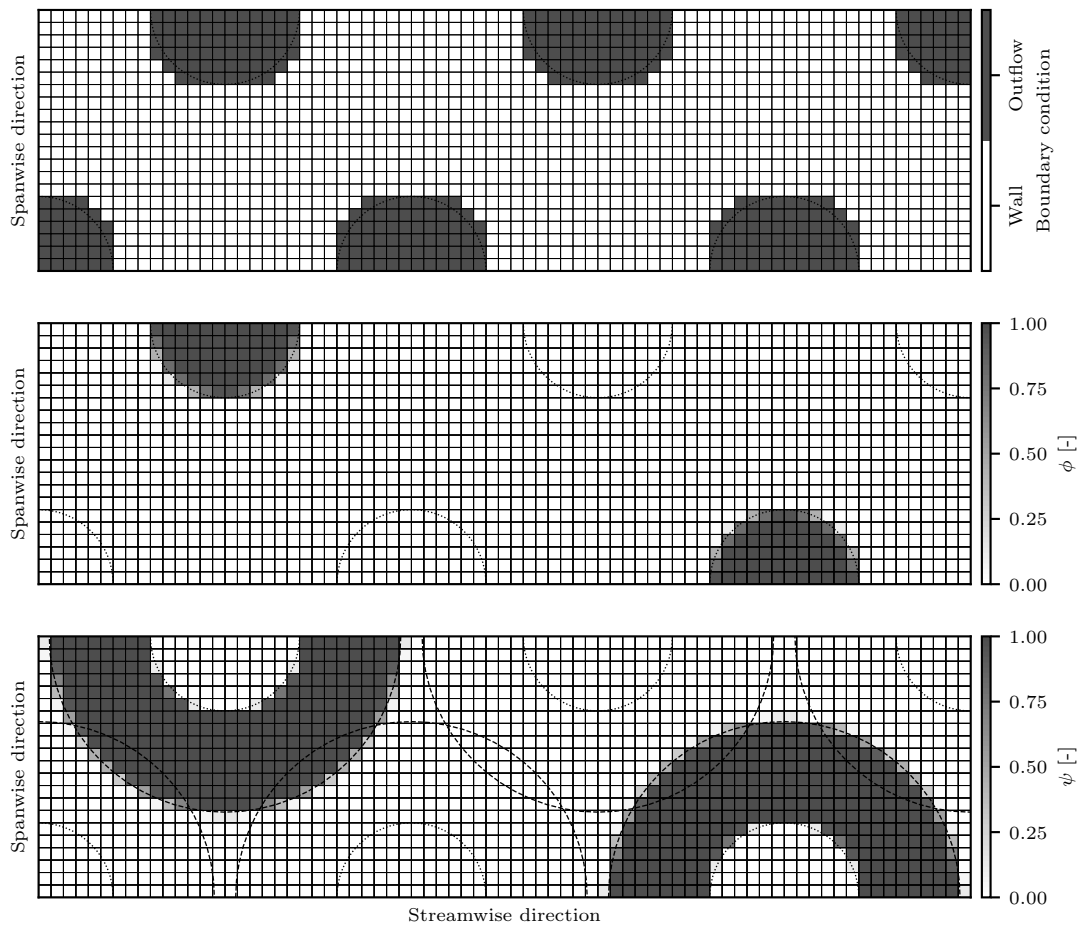


Figure A.2: Implementation of the new bleed model using 12×12 cells per hole; the location of outflow boundary conditions ($\phi > 0$) is shown at the top, ϕ (center) and ψ (bottom) are illustrated for two holes; dotted lines surround the hole area and dashed lines the extraction area.

Figure A.3 illustrates the outcome of Code A.1, where the hole is discretized using 4 x 4 cells. However, in this example, the bleed hole centers are not aligned with the mesh grid. Thus, no focus on the mesh generation concerning the hole pattern is required. Even for non-uniform meshes, the code can be applied.

Moreover, the code is written using the `Polygon` function of `shapely` to define the cell (lines 32 – 37 in Code A.1). Hence, the code can be modified to be applicable to unstructured computational meshes. Hence, a more accurate modeling of the hole contour is possible, which is thought to improve the prediction quality of the control effect induced by porous bleed using the new bleed model.

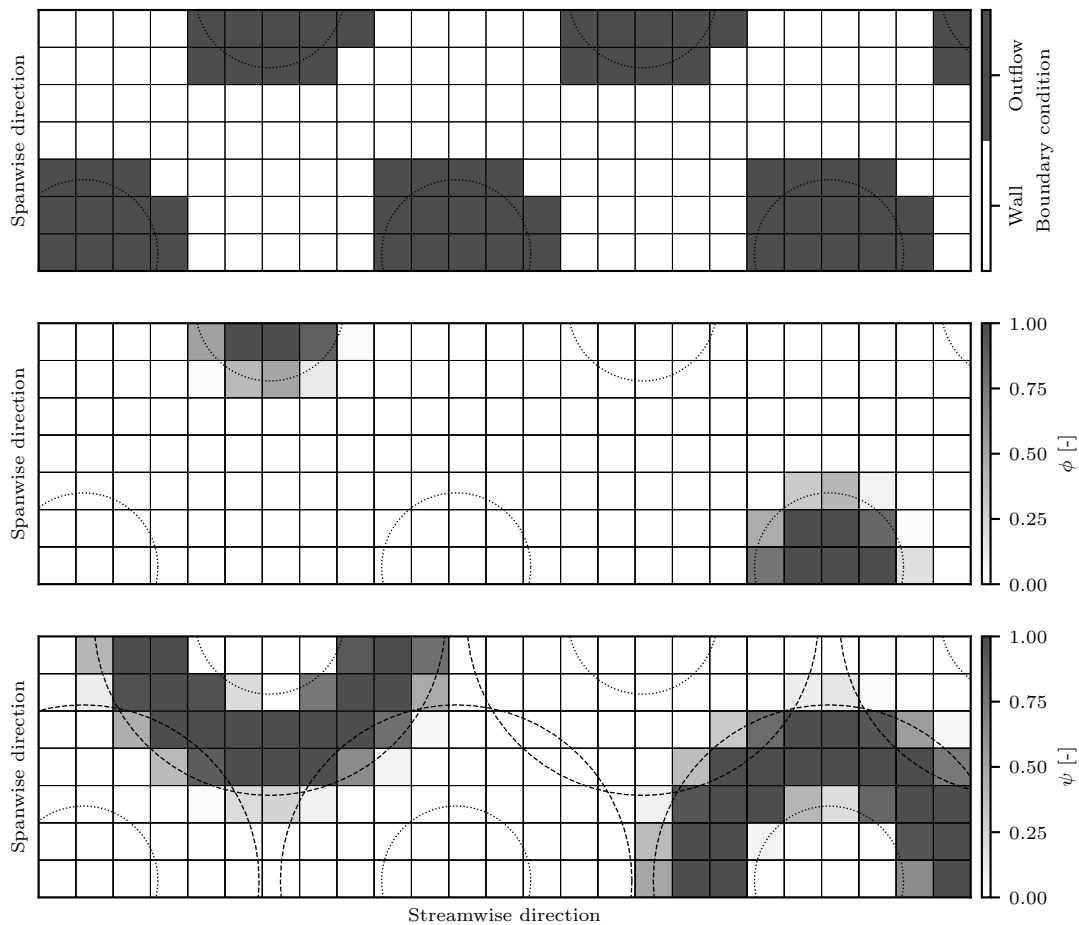


Figure A.3: Implementation of the new bleed model using 4 x 4 cells per hole unaligned with the bleed holes; the location of outflow boundary conditions ($\phi > 0$) is shown at the top, ϕ (center) and ψ (bottom) are illustrated for two holes; dotted lines surround the hole area and dashed lines the extraction area.

Turbulent Shear Stress in Experiments and Simulations

The two-component LDV measurements enabled the acquisition of the turbulent shear stress $u'v'$. Figure B.1 shows the turbulent shear stresses downstream of the bleed region for the equal measurements as shown in Figure 5.10. A good agreement is observed between RANS simulations and experiments. The lower the plenum pressure, the lower the shear stress inside the boundary layer because of the higher bleed rate removing most of the viscous flow. However, the turbulent shear stress increases for a very low suction rate because of the increased bleed roughness effect.

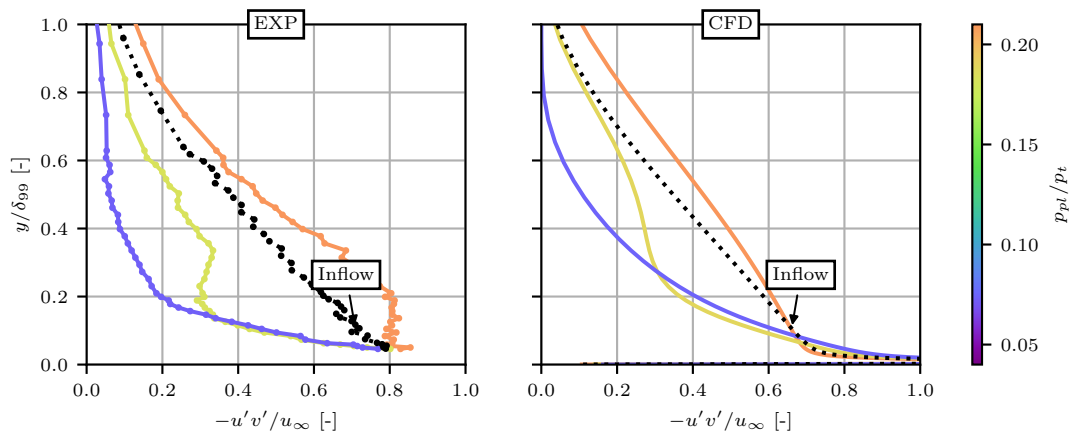


Figure B.1: Turbulent shear stress profiles normalized with free-stream (streamwise) velocity for the high-porosity plate HR.

Figure B.2 shows a comparison of the turbulent shear stresses for the flow fields shown in Figure 5.5. Again, a good agreement between experiments and simulations is observed. A decrease in the turbulent shear stress along the bleed region is apparent. The simulations reveal an increase caused by the barrier shocks, that is faintly visible in the experimental results. Moreover, the shear stresses drop with the expansion fan at the beginning of the bleed region and increase along the trailing shock.

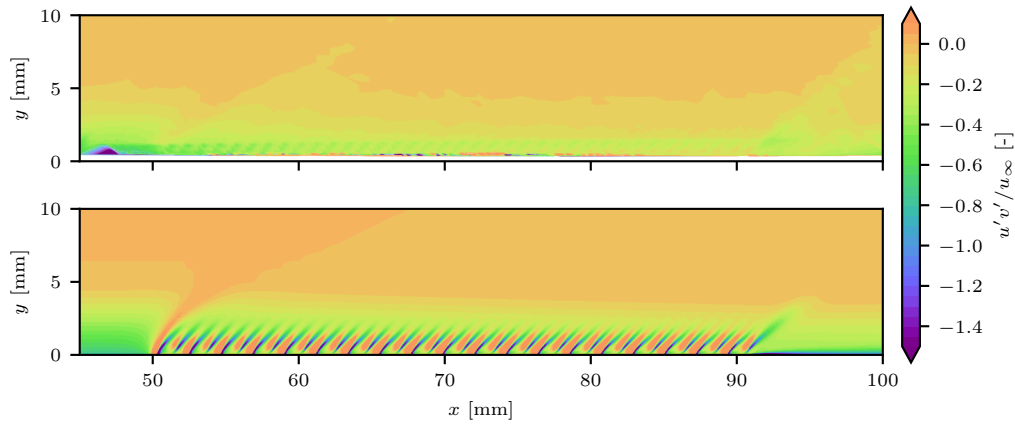


Figure B.2: Turbulent shear stress contours for low-porosity plate AR.

Résumé en français

Le simple est toujours faux. Ce qui ne l'est pas est inutilisable.

PAUL VALÉRY

Les études numériques et expérimentales réalisées dans cette thèse ont été dédiées au contrôle des écoulements turbulents avec des pièges poreux. Les pièges poreux sont une méthode éprouvée pour le contrôle des interactions onde de choc/couche limite dans les prises d'air supersoniques afin de réduire les décollements induits par le choc, qui peut entraîner une dégradation de performance ou des oscillations instables, phénomène appelé pompage supersonique. Dans le but d'optimiser les systèmes de pièges poreux et de simplifier le processus de conception, les objectifs suivants ont été définis au début de la thèse :

- ① Compréhension de la physique fondamentale des écoulements à travers des pièges poreux ;
- ② Évaluation et comparaison approfondies des approches existantes de modélisation des pièges poreux ;
- ③ Développement d'un nouveau modèle de piège poreux, applicable à un large éventail d'écoulement et de géométries, et adapté en particulier au contrôle des interactions onde de choc/couche limite.

Le cas d'écoulement complexe du contrôle d'une interaction d'un choc fort avec un piège poreux a été simplifié en séparant le problème en trois sous-problèmes plus simples :

- ① Contrôle de la couche limite supersonique, correspondant à l'état amont au choc ;
- ② Contrôle de la couche limite subsonique, correspondant à l'état aval au choc ;
- ③ Interaction onde de choc / couche limite sur le piège poreux.

De plus, la distinction entre **efficacité du piège** et **efficacité de contrôle** a été formellement établie. L'efficacité du piège décrit la capacité à aspirer le plus grand débit possible avec la différence de pression la plus faible entre la cavité et la face exposée à l'écoulement. En revanche, l'efficacité de contrôle est liée au contrôle de la couche limite, c'est-à-dire à l'obtention d'un profil de couche limite avec le plus de quantité de mouvement possible en aspirant le débit le plus faible possible.

Nous résumons ci-après les étapes franchies par rapport aux objectifs définis pour les trois sous-problèmes.

Compréhension de la Physique des Écoulements

Contrôle des Écoulements Supersoniques La première étape réalisée a été l'étude du contrôle des écoulements supersoniques. Une étude paramétrique numérique a été réalisée pour un nombre de Mach $M = 1.6$ afin d'investiguer l'influence de la géométrie de la plaque poreuse à la fois sur l'efficacité du piège et celle du contrôle. Les données obtenues ont montré une dispersion significative due aux paramètres géométriques. L'efficacité de piège est principalement influencée par le diamètre des trous et le rapport épaisseur sur diamètre. Pour les trous de grand diamètre, l'écoulement capturé possède une quantité de mouvement élevée entraînant des pertes de pression génératrices élevées dues aux chocs présents autour des trous (appelés barrier shocks) et au jet sous-détendu s'écoulant dans la cavité. Le rapport épaisseur de la plaque sur diamètre s'avère affecter significativement l'écoulement à l'intérieur du trou en fonction du rapport de pression. Des pertes de frottement élevées sont constatées pour les plaques épaisses et les écoulements amorcés. La longueur et le taux de porosité de la plaque influencent l'efficacité du piège en lien avec le débit aspiré. Les petites plaques avec de faibles taux de porosité s'avèrent efficaces. Le débit maximum d'aspiration reste cependant limité pour la plupart des applications.

L'efficacité de contrôle est principalement influencée par le diamètre des trous. Étant donné que le moment de l'écoulement capturé est plus élevé pour les grands trous, le barrier shock est d'une intensité plus élevée, entraînant un épaississement local de la couche limite en aval des trous. De plus, les niveaux de porosité élevés augmentent l'efficacité de contrôle du piège, de même que la mise en quinconce des trous.

Des expériences dans la soufflerie supersonique S8Ch ont été réalisées pour un nombre de Mach de $M=1.62$ afin de valider l'effet numériquement prédit sur la couche limite. Deux géométries de plaque différentes ont été étudiées pour plusieurs débits d'aspiration. Les profils de couche limite acquis par des mesures LDV ont permis de valider les observations numériques. De plus, l'étude paramétrique numérique a révélé des variations des profils de couche limite dans la direction transverse pour certains paramètres géométriques (par exemple, de grands diamètres de trou, des niveaux de porosité faibles, un décalage des trous). L'acquisition des profils dans cette direction pour un diamètre de trou de $D = 2.0$ mm a permis de confirmer les conclusions numériques.

Contrôle des Écoulements Subsoniques Différents comportements du piège poreux ont été observés pour les écoulements subsoniques. Le piège poreux, qu'il soit appliqué dans des écoulements supersoniques ou subsoniques, génère un effet de diffuseur, ce qui signifie que l'écoulement externe est dévié vers la paroi. Par conséquent, l'écoulement externe est décéléré (ou accéléré pour des conditions supersoniques). Ainsi, deux effets contradictoires étaient présents : l'écoulement à proximité de la paroi est accéléré, tandis que la vitesse de l'écoulement externe est décélérée. En conséquence, une saturation rapide de l'augmentation du frottement pariétal est observée. En revanche, des débits d'aspiration excessifs élevés entraînent une décélération de l'écoulement externe. Cet effet a été validé par des expériences en soufflerie menées pour un nombre de Mach $M=0.5$. Une conséquence de l'effet de diffuseur est l'augmentation de l'efficacité d'aspiration le long de la plaque à mesure que la vitesse tangentielle diminue. Ainsi, le décollement à l'intérieur des trous diminue en taille, ce qui résulte en une zone de vena contracta agrandie. Les débits aspirés ainsi obtenus sont significativement plus élevés que pour les écoulements supersoniques.

Contrairement aux conditions supersoniques, l'influence de la géométrie sur l'efficacité du piège et l'efficacité de contrôle est faible. L'efficacité du piège est principalement influencée par le rapport épaisseur sur diamètre, ce qui a un impact encore plus significatif que pour les conditions

supersoniques. Le diamètre des trous, le niveau de porosité et le diamètre des trous ont une influence, mais moins significative que le rapport épaisseur sur diamètre. Remarquablement, des niveaux de porosité élevés sont légèrement plus efficaces, tandis que c'est l'inverse pour les écoulements supersoniques.

De plus, l'influence de la géométrie sur l'efficacité de contrôle est relativement faible. Comme pour les écoulements supersoniques, les trous de petits diamètres sont bénéfiques. De plus, des niveaux de porosité élevés se sont révélés plus efficaces.

Interaction avec l'Onde de Choc Dans la troisième étape, l'interaction de l'onde de choc incidente avec le piège poreux a été étudiée. Une onde de choc (normale) sépare des écoulements supersoniques et subsoniques, et donc, son contrôle ne peut pas être séparé du contrôle des écoulements supersoniques et subsoniques. Cependant, après avoir successivement investigué les mécanismes de contrôle dans les deux régimes, un comportement particulier a été observé en lien avec le gradient de pression adverse induit par l'onde de choc.

Le premier effet observé est lié aux différents débits d'aspiration en amont et en aval de l'onde de choc. L'augmentation de pression due à l'onde de choc entraînait une pression pariétale plus élevée en aval de l'onde de choc, ce qui se traduit par des taux d'aspiration plus élevés. De plus, l'écoulement en aval de l'onde de choc est subsonique, ce qui entraîne une efficacité de piège accrue. Ainsi, la vitesse de l'écoulement tangentiel diminue le long de l'onde de choc, tandis que la vitesse de transpiration augmente. La conséquence est un angle de déviation le long de l'onde de choc, réduisant son intensité. Les simulations de l'écoulement en soufflerie ont montré une réduction significative de la hauteur de la réflexion irrégulière (Mach stem), ce qui implique une réflexion de l'onde de choc "plus régulière". Les mesures LDV ont validé les profils de vitesse acquis numériquement le long du piège.

L'efficacité du piège se comporte de manière analogue aux conditions supersoniques et subsoniques. En amont de l'onde de choc, l'écoulement externe était supersonique, ce qui entraîne les mêmes tendances que précédemment décrites. En aval de l'onde de choc, où l'écoulement est subsonique, le rapport de pression augmente et le coefficient sonique surfacique augmente. De plus, un soufflage se produit si le débit d'aspiration est trop faible et que la pression de plénum dépasse la pression pariétale en amont de l'onde de choc.

Le gradient de pression adverse s'est révélé influencer significativement l'efficacité de contrôle. Comme discuté précédemment, les trous de grands diamètres génèrent une couche limite inhomogène. En raison du gradient de pression adverse, cet effet était renforcé. Plus la hauteur de la ligne sonique est élevée, plus la taille de la zone décollée est importante. Ainsi, l'écoulement entre les trous est plus sensible au décollement dans le cas de grands trous. Bien que l'aspiration en aval de l'onde de choc entraîne un recollement de l'écoulement, la tridimensionnalité de l'écoulement subsiste et s'avère plus forte que pour les cas d'aspiration de couche limite purement supersonique et subsonique. Il a été constaté que les niveaux de porosité faibles provoquent un effet plus important sur la couche limite pour le même débit d'aspiration. Cela s'explique par un rapport de pression plus faible en amont de l'onde de choc, et donc, un meilleur contrôle de la couche limite supersonique.

Évaluation des Modèles de piège poreux de la littérature

Contrôle des Écoulements Supersoniques L'application a posteriori des modèles de pièges poreux issus de la littérature a révélé des écarts significatifs entre les différentes approches et les données de l'étude paramétrique précédemment réalisée. Comme prévu, les modèles validés pour les écoulements supersoniques se sont mieux comportés dans le cas de la couche limite supersonique. Les modèles qui ne tiennent pas compte de l'écoulement tangentiel surestiment

le débit d'aspiration. L'application des modèles dans le solveur RANS a révélé des différences significatives entre la définition et l'application. L'aspiration homogène provoque une surestimation de l'effet d'amincissement de la couche limite. Ainsi, les profils de couche limite en aval du piège présentent sont caractérisés par une quantité de mouvement plus importante à proximité de la paroi. L'onde de détente est par conséquent plus intense au début de la plaque, ce qui entraîne une pression pariétale plus faible et donc un débit d'aspiration inférieur à celui attendu a priori. De plus, les effets de géométrie des trous ne sont pas pris en compte dans les modèles.

Contrôle des Écoulements Subsoniques La comparaison a posteriori des modèles de piège poreux avec les données de référence a révélé de grands écarts pour tous les modèles. Cependant, il a été observé que l'application de la condition limite de piège poreux est moins sensible que pour les conditions supersoniques. Même si les modèles surestiment ou sous-estiment le débit d'aspiration, un bon accord avec les profils de couche limite en aval du piège a été trouvé.

Interaction avec l'Onde de Choc Aucun des modèles évalués n'a été jugé précis pour le contrôle d'une interaction onde de choc/couche limite. L'effet sur la modification d'un profil de couche limite en amont de l'onde de choc était surestimé. Par conséquent, la quantité de mouvement de la couche limite qui interagissait avec l'onde de choc est trop élevée, surestimant sa robustesse au décollement. En conséquence, le profil longitudinal de pression statique s'est avéré proche de celui prévu pour un écoulement non visqueux.

Développement d'un Nouveau Modèle de Piège Poreux

Dans l'étape finale, un nouveau modèle de piège poreux a été construit à partir des données de l'étude paramétrique numérique. Le modèle est appliqué localement en modélisant le contour des trous de manière discrète. Ainsi, le motif de trous est directement modélisé dans le maillage et le nombre de Mach tangentiel au niveau de la condition limite de sortie peut être extrait. En utilisant le nombre de Mach tangentiel du trou et le rapport de pression entre le plénum et la paroi externe, l'état de l'écoulement externe peut être quantifié. Ainsi, deux régressions analytiques différentes pour les conditions supersoniques et subsoniques ont été construites à partir des informations pariétales extraites de la base de données numérique, ce qui rend notre modèle applicable à la fois pour les écoulements supersoniques et subsoniques.

Notre modèle a été appliqué au cas de référence supersonique. La capture barrier shock a permis une amélioration significative de la prévision des profils de couche limite en aval du piège. De plus, les grandeurs physiques pariétales ont été bien prédites. De même, la qualité de prévision pour les conditions subsoniques a été améliorée.

Enfin, notre modèle a été appliqué au cas complexe de l'interaction onde de choc/couche limite. Seules de légères différences entre les simulations de référence et le nouveau modèle ont été observées. Ainsi, le nouveau modèle est le premier modèle de piège poreux applicable pour le contrôle d'une interaction onde de choc/couche limite à partir de grandeurs pariétales et prenant en compte la géométrie de la plaque poreuse de manière suffisante.

References

- [1] K. Abrahamson and D. Brower. An empirical boundary condition for numerical simulation of porous plate bleed flows. In *26th Aerospace Sciences Meeting*, Reston, Virginia, 1988. American Institute of Aeronautics and Astronautics.
<https://arc.aiaa.org/doi/10.2514/6.1988-306>.
Cited on pages 6, 31, 32, 35, 40, 41, 174, 175, 180, 183, 184, and 195.
- [2] G. Akar and S. Eyi. Computational Modelling and Analysis of Porous Bleed Holes at Supersonic Speeds. In *AIAA Propulsion and Energy 2020 Forum*, Reston, Virginia, 2020. American Institute of Aeronautics and Astronautics.
<https://arc.aiaa.org/doi/10.2514/6.2020-3721>.
Cited on pages 29 and 30.
- [3] J. Akatsuka, Y. Watanabe, A. Murakami, and S. Honami. Porous Bleed Model for Boundary Condition of CFD Analysis. In *3rd AIAA Flow Control Conference*, Reston, Virginia, 2006. American Institute of Aeronautics and Astronautics.
<https://arc.aiaa.org/doi/10.2514/6.2006-3682>.
Cited on pages XIV, 26, 27, 30, 32, 123, and 131.
- [4] H. Babinsky and J. K. Harvey. *Shock Wave-Boundary-Layer Interactions*. Cambridge Aerospace Series. Cambridge University Press, 2011.
<https://www.cambridge.org/core/books/shock-waveboundarylayer-interactions/1EC84B4EBF65B1B20C0CA60806B7DFF5>.
Cited on pages XIII, 7, 9, 10, 11, 12, and 101.
- [5] H. Babinsky and H. Ogawa. SBLI control for wings and inlets. *Shock Waves*, 18(2):89–96, 2008.
<http://link.springer.com/10.1007/s00193-008-0149-7>.
Cited on pages XIII and 7.
- [6] H. Babinsky, J. Oorebeek, and T. Cottingham. Corner effects in reflecting oblique shock-wave/boundary-layer interactions. In *51st AIAA Aerospace Sciences Meeting including the New Horizons Forum and Aerospace Exposition*, pages 1–10, Reston, Virginia, 2013. American Institute of Aeronautics and Astronautics.
<https://arc.aiaa.org/doi/10.2514/6.2013-859>.
Cited on page 79.

- [7] R. A. Baurle and A. T. Norris. A Source-Term Based Boundary Layer Bleed/Effusion Model for Passive Shock Control. *58th JANNAF Propulsion Meeting*, 2011.
<https://ntrs.nasa.gov/citations/20110011133>.
Cited on pages 39, 41, and 56.
- [8] G. Ben-Dor. *Shock Wave Reflection Phenomena*. Shock Wave and High Pressure Phenomena. Springer Berlin Heidelberg, Berlin, Heidelberg, 2007.
<http://link.springer.com/10.1007/978-3-540-71382-1>.
Cited on pages XIII and 8.
- [9] D. Benhachmi, I. Greber, and W. R. Hingst. Experimental and numerical investigation of an oblique shock wave/turbulent boundary layer interaction with continuous suction. In *27th Aerospace Sciences Meeting*, Reston, Virginia, 1989. American Institute of Aeronautics and Astronautics.
<https://arc.aiaa.org/doi/10.2514/6.1989-357>.
Cited on page 25.
- [10] C. Benoit, S. Péron, and S. Landier. Cassiopee: A CFD pre- and post-processing tool. *Aerospace Science and Technology*, 45:272–283, 2015.
<https://linkinghub.elsevier.com/retrieve/pii/S1270963815001777>.
Cited on page 51.
- [11] D. B. Benson, T. I.-P. Shih, D. O. Davis, and B. Willis. Boundary conditions for CFD simulations of supersonic boundary-layer flow through discrete holes. In *38th Aerospace Sciences Meeting and Exhibit*, Reston, Virginia, 2000. American Institute of Aeronautics and Astronautics.
<http://arc.aiaa.org/doi/10.2514/6.2000-888>.
Cited on pages 33, 58, and 191.
- [12] J. Bodner, I. Greber, D. O. Davis, and W. R. Hingst. Experimental investigation of the effect of a single bleed hole on a supersonic turbulent boundary-layer. In *32nd Joint Propulsion Conference and Exhibit*, Reston, Virginia, 1996. American Institute of Aeronautics and Astronautics.
<https://arc.aiaa.org/doi/10.2514/6.1996-2797>.
Cited on pages XIV, 17, 18, 23, and 96.
- [13] S. L. Bragg. Effect of Compressibility on the Discharge Coefficient of Orifices and Convergent Nozzles. *Journal of Mechanical Engineering Science*, 2(1):35–44, 1960.
http://journals.sagepub.com/doi/10.1243/JMES_JOUR_1960_002_007_02.
Cited on page 36.
- [14] P. J. K. Bruce, D. M. F. Burton, N. A. Titchener, and H. Babinsky. Corner effect and separation in transonic channel flows. *Journal of Fluid Mechanics*, 679:247–262, 2011.
https://www.cambridge.org/core/product/identifier/S0022112011001352/type/journal_article.
Cited on page 78.
- [15] R. Bur. Passive control of a shock wave/turbulent boundary layer interaction in a transonic flow. *Recherche Aerospatiale*, 6, 1992.
Cited on page 31.

- [16] R. Bush. Engine face and screen loss models for CFD applications. In *13th Computational Fluid Dynamics Conference*, pages 1161–1171, Reston, Virginia, 1997. American Institute of Aeronautics and Astronautics.
<https://arc.aiaa.org/doi/10.2514/6.1997-2076>.
Cited on page 38.
- [17] L. Cambier, S. Heib, and S. Plot. The Onera elsA CFD software: input from research and feedback from industry. *Mechanics & Industry*, 14(3):159–174, 2013.
<http://www.mechanics-industry.org/10.1051/meca/2013056>.
Cited on page 50.
- [18] F. Champagnat, A. Plyer, G. Le Besnerais, B. Leclaire, S. Davoust, and Y. Le Sant. Fast and accurate PIV computation using highly parallel iterative correlation maximization. *Experiments in Fluids*, 50(4):1169–1182, 2011.
<http://link.springer.com/10.1007/s00348-011-1054-x>.
Cited on page 70.
- [19] Q. Chanzy, E. Garnier, and R. Bur. Optimization of a Fluidic Vortex Generator’s Control in a Transonic Channel Flow. *AIAA Journal*, 58(12):5216–5227, 2020.
<https://arc.aiaa.org/doi/10.2514/1.J058873>.
Cited on page 51.
- [20] H. Chen, H.-j. Tan, Y.-z. Liu, and Q.-f. Zhang. External-Compression Supersonic Inlet Free from Violent Buzz. *AIAA Journal*, 57(6):2513–2523, 2019.
<https://arc.aiaa.org/doi/10.2514/1.J057811>.
Cited on pages XIII and 2.
- [21] Y. Choe, C. Kim, and K. Kim. Effects of Optimized Bleed System on Supersonic Inlet Performance and Buzz. *Journal of Propulsion and Power*, 36(2):211–222, 2020.
<https://arc.aiaa.org/doi/10.2514/1.B37474>.
Cited on pages XIV, 6, 32, 33, 39, 40, 41, 127, 175, 183, 184, 187, 188, and 195.
- [22] W. J. Chyu, G. W. Howe, and T. I.-P. Shih. Bleed-boundary conditions for numerically simulated mixed-compression supersonic inlet flow. *Journal of Propulsion and Power*, 8(4):862–868, 1992.
<https://arc.aiaa.org/doi/10.2514/3.23561>.
Cited on page 32.
- [23] W. J. Chyu, M. J. Rimlinger, and T. I.-P. Shih. Effects of bleed-hole geometry and plenum pressure on three-dimensional shock-wave/boundary-layer/bleed interactions. In *3rd Shear Flow Conference*, Reston, Virginia, 1993. American Institute of Aeronautics and Astronautics.
<https://arc.aiaa.org/doi/10.2514/6.1993-3259>.
Cited on pages XIV and 28.
- [24] W. J. Chyu, M. J. Rimlinger, and T. I.-P. Shih. Control of shock-wave/boundary-layer interactions by bleed. *AIAA Journal*, 33(7):1239–1247, 1995.
<https://arc.aiaa.org/doi/10.2514/3.12886>.
Cited on page 29.
- [25] D. Coles. The law of the wake in the turbulent boundary layer. *Journal of Fluid Mechanics*, 1(2):191–226, 1956.

- https://www.cambridge.org/core/product/identifier/S0022112056000135/type/journal_article.
Cited on pages XIII, 10, and 11.
- [26] W. G. Cornell. Losses in Flow Normal to Plane Screens. *Journal of Fluids Engineering*, 80(4):791–797, 1958.
<https://asmedigitalcollection.asme.org/fluidsengineering/article/80/4/791/1131920/Losses-in-Flow-Normal-to-Plane-Screens>.
Cited on page 38.
- [27] J. Cousteix. *Aérodynamique : couche limite laminaire*. Collection La Chevêche. Éd. Cépaduès, Toulouse, 1988.
Cited on page 12.
- [28] J. Cousteix. *Aérodynamique : turbulence et couche limite*. Collection La Chevêche. Cépaduès-éditions, Toulouse, 1989.
Cited on page 12.
- [29] R. W. Cubbison, E. T. Meleason, and D. F. Johnson. Effect of Porous Bleed in a High-Performance Axisymmetric, Mixed-Compression Inlet at Mach 2.50. Technical report, NASA-TM-X-1692, Washington, DC, 1968.
<https://ntrs.nasa.gov/citations/19690000963>.
Cited on page 16.
- [30] S. Dambara, M. Yamamoto, and S. Honami. Modeling of boundary condition for turbulent boundary layer bleed. In *36th AIAA Aerospace Sciences Meeting and Exhibit*, Reston, Virginia, 1998. American Institute of Aeronautics and Astronautics.
<https://arc.aiaa.org/doi/10.2514/6.1998-926>.
Cited on page 32.
- [31] H. Darcy. *Les fontaines publiques de la ville de Dijon : exposition et application des principes à suivre et des formules*. Victor Dalmont, éditeur, Paris, 1856.
<https://gallica.bnf.fr/ark:/12148/bpt6k624312>.
Cited on page 31.
- [32] D. O. Davis, M. Grimes, and M. Schoenenberger. Effect of Flow Misalignment and Multi-Hole Interaction on Boundary-Layer Bleed Hole Flow Coefficient Behavior. In *Fluids Engineering*, pages 323–328. American Society of Mechanical Engineers, 1996.
<https://asmedigitalcollection.asme.org/IMECE/proceedings/IMECE96/15502/323/1165742>.
Cited on page 17.
- [33] D. O. Davis, B. Willis, and M. Schoenenberger. Porous and microporous honeycomb composites as potential boundary-layer bleed materials. In *33rd Joint Propulsion Conference and Exhibit*, Reston, Virginia, 1997. American Institute of Aeronautics and Astronautics.
<https://arc.aiaa.org/doi/10.2514/6.1997-3260>.
Cited on pages XIV, 17, 18, 19, 21, 54, 131, and 133.
- [34] D. O. Davis, M. Vyas, and J. W. Slater. Research on Supersonic Inlet Bleed. In *50th AIAA Aerospace Sciences Meeting including the New Horizons Forum and Aerospace Exposition*, Reston, Virginia, 2012. American Institute of Aeronautics and Astronautics.
<https://arc.aiaa.org/doi/10.2514/6.2012-272>.
Cited on page 30.

- [35] J. M. Delery. Shock wave/turbulent boundary layer interaction and its control. *Progress in Aerospace Sciences*, 22(4):209–280, 1985.
<https://linkinghub.elsevier.com/retrieve/pii/0376042185900016>.
Cited on pages XIII, 12, 13, 14, and 54.
- [36] J. M. Délerly. Flow physics involved in shock wave/boundary layer interaction control. In G. E. A. Meier and P. R. Viswanath, editors, *IUTAM Symposium on Mechanics of Passive and Active Flow Control*, pages 15–22, Dordrecht, 1999. Springer Netherlands.
https://link.springer.com/chapter/10.1007/978-94-011-4199-4_3.
Cited on pages 7 and 13.
- [37] J. M. Délerly and J.-P. Dussauge. Some physical aspects of shock wave/boundary layer interactions. *Shock Waves*, 19(6):453–468, 2009.
<http://link.springer.com/10.1007/s00193-009-0220-z>.
Cited on pages XIII, 7, and 8.
- [38] P. P. Doerffer and R. Bohning. Modelling of perforated plate aerodynamics performance. *Aerospace Science and Technology*, 4(8):525–534, 2000.
<https://linkinghub.elsevier.com/retrieve/pii/S1270963800010634>.
Cited on pages XIV, 6, 21, 22, 32, 37, 40, 41, 56, 173, 174, 176, 178, 179, 181, 182, 183, 184, 186, 187, 188, and 195.
- [39] F. Durst, A. Melling, J. H. Whitelaw, and C. P. Wang. Principles and Practice of Laser-Doppler Anemometry. *Journal of Applied Mechanics*, 44(3):518–518, 1977.
<https://asmedigitalcollection.asme.org/appliedmechanics/article/44/3/518/385614/Principles-and-Practice-of-LaserDoppler-Anemometry>.
Cited on page 69.
- [40] M. Eichorn, P. Barnhart, D. O. Davis, M. Vyas, and J. W. Slater. Effect of Boundary-Layer Bleed Hole Inclination Angle and Scaling on Flow Coefficient Behavior. In *51st AIAA Aerospace Sciences Meeting including the New Horizons Forum and Aerospace Exposition*, Reston, Virginia, 2013. American Institute of Aeronautics and Astronautics.
<https://arc.aiaa.org/doi/10.2514/6.2013-424>.
Cited on pages XIII, XIV, XV, XXIII, 18, 19, 30, 89, 91, 92, 113, 115, 123, 131, and 133.
- [41] N. T. Frink, D. L. Bonhaus, V. N. Vatsa, S. X. S. Bauer, and A. F. Tinetti. Boundary Condition for Simulation of Flow Over Porous Surfaces. *Journal of Aircraft*, 40(4):692–698, 2003.
<https://arc.aiaa.org/doi/10.2514/2.3147>.
Cited on pages 6, 38, 40, 41, 173, 175, 178, 180, 183, 184, 187, 188, 191, and 195.
- [42] M. K. Fukuda, W. R. Hingst, and E. Reshotko. Bleed Effects on Shock/Boundary-layer Interactions in Supersonic Mixed Compression Inlets. *Journal of Aircraft*, 14(2):151–156, 1977.
<https://arc.aiaa.org/doi/10.2514/3.58756>.
Cited on page 16.
- [43] S. Ghosh, J.-I. Choi, and J. R. Edwards. Simulation of Shock/Boundary-Layer Interactions with Bleed Using Immersed-Boundary Methods. *Journal of Propulsion and Power*, 26(2):203–214, 2010.
<https://arc.aiaa.org/doi/10.2514/1.45297>.
Cited on pages 29, 30, and 84.

- [44] J. Giehler, P. Grenson, and R. Bur. Porous Bleed Boundary Conditions for Shock-Induced Boundary Layer Separation Control. In *56th 3AF International Conference on Applied Aerodynamics*, Paris, 2022. Association Aéronautique et Astronautique de France. Cited on pages III and 4.
- [45] J. Giehler, P. Grenson, and R. Bur. Parameter Influence on the Porous Bleed Performance with & without Shock-Boundary Layer Interaction. In *AIAA AVIATION 2022 Forum*, Reston, Virginia, 2022. American Institute of Aeronautics and Astronautics. <https://arc.aiaa.org/doi/10.2514/6.2022-3239>. Cited on pages III and 4.
- [46] J. Giehler, P. Grenson, and R. Bur. Porous Bleed Boundary Conditions for Supersonic Flows With & Without Shock-Boundary Layer Interaction. *Flow, Turbulence and Combustion*, 111(4):1139–1173, 2023. <https://link.springer.com/10.1007/s10494-023-00464-9>. Cited on pages III, 4, and 177.
- [47] J. Giehler, T. Leudiere, R. S. Morgadinho, P. Grenson, and R. Bur. Experimental and Numerical Investigation of Supersonic Turbulent Boundary Layer Bleeding. In *57th 3AF International Conference on Applied Aerodynamics*, Bordeaux, 2023. Association Aéronautique et Astronautique de France. Cited on pages III and 4.
- [48] J. Giehler, P. Grenson, and R. Bur. Parameter Influence on Porous Bleed Performance for Supersonic Turbulent Flows. *Journal of Propulsion and Power*, 40(1):74–93, 2024. <https://arc.aiaa.org/doi/10.2514/1.B39236>. Cited on pages III and 4.
- [49] J. Giehler, P. Grenson, and R. Bur. A New Approach of Using Porous Bleed Boundary Conditions - Application of Local Porosity. In A. Dillmann, G. Heller, E. Krämer, C. Wagner, and J. Weiss, editors, *New Results in Numerical and Experimental Fluid Mechanics XIV*, pages 361–371, Cham, 2024. Springer Nature Switzerland. https://link.springer.com/10.1007/978-3-031-40482-5_34. Cited on page III.
- [50] J. Giehler, T. Leudiere, R. S. Morgadinho, P. Grenson, and R. Bur. Experimental and numerical investigation of porous bleed control for supersonic/subsonic flows, and shock-wave/boundary-layer interactions. *Aerospace Science and Technology*, 147:109062, 2024. <https://linkinghub.elsevier.com/retrieve/pii/S1270963824001950>. Cited on pages III and 4.
- [51] S. Gillies et al. Shapely: manipulation and analysis of geometric objects, 2007–. <https://github.com/shapely/shapely>. Cited on page 215.
- [52] F. Gnani, H. Zare-Behtash, and K. Kontis. Pseudo-shock waves and their interactions in high-speed intakes. *Progress in Aerospace Sciences*, 82:36–56, 2016. <https://linkinghub.elsevier.com/retrieve/pii/S0376042116300094>. Cited on page 7.
- [53] K. P. Griffin, L. Fu, and P. Moin. General method for determining the boundary layer thickness in nonequilibrium flows. *Physical Review Fluids*, 6(2):024608, 2021.

- <https://link.aps.org/doi/10.1103/PhysRevFluids.6.024608>.
Cited on page 191.
- [54] J. Grzelak, P. Doerffer, and T. Lewandowski. The efficiency of transpiration flow through perforated plate. *Aerospace Science and Technology*, 110:106494, 2021.
<https://linkinghub.elsevier.com/retrieve/pii/S1270963821000067>.
Cited on pages XX, 6, 33, 40, 41, 122, 123, 139, 147, 150, 152, 157, 160, 161, 162, 173, 174, 175, 177, 178, 180, 183, 184, 185, 191, and 195.
- [55] A. Hamed and T. Lehnig. Investigation of oblique shock/boundary-layer bleed interaction. *Journal of Propulsion and Power*, 8(2):418–424, 1992.
<https://arc.aiaa.org/doi/10.2514/3.23494>.
Cited on pages XIV and 28.
- [56] A. Hamed and Z. Li. Simulation of Bleed-Hole Rows for Supersonic Turbulent Boundary Layer Control. In *46th AIAA Aerospace Sciences Meeting and Exhibit*, Reston, Virginia, 2008. American Institute of Aeronautics and Astronautics.
<http://arc.aiaa.org/doi/10.2514/6.2008-67>.
Cited on page 30.
- [57] A. Hamed, S. H. Shih, and J. J. Yeuan. An investigation of shock/turbulent boundary layer bleed interactions. In *28th Joint Propulsion Conference and Exhibit*, Reston, Virginia, 1992. American Institute of Aeronautics and Astronautics.
<https://arc.aiaa.org/doi/10.2514/6.1992-3085>.
Cited on page 28.
- [58] A. Hamed, S. H. Shih, and J. J. Yeuan. A parametric study of bleed in shock boundary layer interactions. In *31st Aerospace Sciences Meeting*, Reston, Virginia, 1993. American Institute of Aeronautics and Astronautics.
<https://arc.aiaa.org/doi/10.2514/6.1993-294>.
Cited on page 28.
- [59] A. Hamed, Z. Li, S. Manavasi, and C. Nelson. Flow Characteristics through Porous Bleed in Supersonic Turbulent Boundary Layers. In *47th AIAA Aerospace Sciences Meeting including The New Horizons Forum and Aerospace Exposition*, Reston, Virginia, 2009. American Institute of Aeronautics and Astronautics.
<http://arc.aiaa.org/doi/10.2514/6.2009-1260>.
Cited on page 30.
- [60] A. Hamed, S. Manavasi, D. Shin, A. T. Morell, and C. Nelson. Bleed Interactions in Supersonic Flow. *International Journal of Flow Control*, 3(1):37–48, 2011.
<http://multi-science.atypon.com/doi/10.1260/1756-8250.3.1.37>.
Cited on pages XIV, 30, 83, 100, and 128.
- [61] G. J. Harloff and G. E. Smith. Supersonic-inlet boundary-layer bleed flow. *AIAA Journal*, 34(4):778–785, 1996.
<https://arc.aiaa.org/doi/10.2514/3.13140>.
Cited on pages XIV, XX, 6, 27, 32, 36, 37, 40, 41, 44, 56, 68, 120, 123, 125, 139, 142, 173, 174, 175, 178, 183, 184, 187, 188, 191, 192, 194, 195, 202, 203, and 211.
- [62] W. R. Hingst and F. Tanji. Experimental investigation of a two-dimensional shock-turbulent boundary layer interaction with bleed. In *21st Aerospace Sciences Meeting*,

- Reno, Nevada, 1983. American Institute of Aeronautics and Astronautics.
<https://arc.aiaa.org/doi/10.2514/6.1983-135>.
Cited on pages XIV, 24, 25, 32, and 35.
- [63] G. Inger. Transonic shock - Turbulent boundary layer interaction and incipient separation on curved surfaces. In *14th Fluid and Plasma Dynamics Conference*, Reston, Virginia, 1981. American Institute of Aeronautics and Astronautics.
<https://arc.aiaa.org/doi/10.2514/6.1981-1244>.
Cited on pages XIII and 13.
- [64] G. Inger and H. Babinsky. Viscous compressible flow across a hole in a plate. *Journal of Aircraft*, 37(6):1028–1032, 1999.
<https://arc.aiaa.org/doi/10.2514/6.1999-3191>.
Cited on page 32.
- [65] E. Laurendeau, D. Russell, G. C. Paynter, and B. Willis. Insights on the bleed roughness effect. In *28th Fluid Dynamics Conference*, Reston, Virginia, 1997. American Institute of Aeronautics and Astronautics.
<https://arc.aiaa.org/doi/10.2514/6.1997-2019>.
Cited on pages 34 and 211.
- [66] M.-F. Liou. A Full Navier-Stokes Based Optimal Design of Bleed Flow for Supersonic Inlets. In *29th AIAA Applied Aerodynamics Conference*, Reston, Virginia, 2011. American Institute of Aeronautics and Astronautics.
<http://arc.aiaa.org/doi/10.2514/6.2011-3003>.
Cited on page 29.
- [67] D. W. Mayer and G. C. Paynter. Boundary conditions for unsteady supersonic inlet analyses. *AIAA Journal*, 32(6):1200–1206, 1994.
<https://arc.aiaa.org/doi/10.2514/3.12120>.
Cited on page 32.
- [68] D. K. McLaughlin and W. G. Tiederman. Biasing correction for individual realization of laser anemometer measurements in turbulent flows. *The Physics of Fluids*, 16(12):2082–2088, 1973.
<https://pubs.aip.org/pfl/article/16/12/2082/448446/Biasing-correction-for-individual-realization-of>.
Cited on page 70.
- [69] F. R. Menter. Two-equation eddy-viscosity turbulence models for engineering applications. *AIAA Journal*, 32(8):1598–1605, 1994.
<https://arc.aiaa.org/doi/10.2514/3.12149>.
Cited on page 50.
- [70] A. T. Morell and A. Hamed. Flow Expansion Based Model for 3-D Multi Bleed Hole Rows. In *51st AIAA Aerospace Sciences Meeting including the New Horizons Forum and Aerospace Exposition*, Reston, Virginia, 2013. American Institute of Aeronautics and Astronautics.
<https://arc.aiaa.org/doi/10.2514/6.2013-426>.
Cited on pages 32 and 34.

- [71] M. Moreno, P. K. Zachos, E. J. Gantt, L. Tobaldini Neto, D. Ferolla de Ambreu, N. D. Domel, and J. W. Slater. Summary of the 6 th Propulsion Aerodynamics Workshop: NASA 1507 Inlet. In *AIAA SCITECH 2024 Forum*, pages 1–33, Reston, Virginia, 2024. American Institute of Aeronautics and Astronautics.
<https://arc.aiaa.org/doi/10.2514/6.2024-0980>.
Cited on page 212.
- [72] F. Nicolas, V. Todoroff, A. Plyer, G. Le Besnerais, D. Donjat, F. Micheli, F. Champagnat, P. Cornic, and Y. Le Sant. A direct approach for instantaneous 3D density field reconstruction from background-oriented schlieren (BOS) measurements. *Experiments in Fluids*, 57(1):13, 2016.
<http://link.springer.com/10.1007/s00348-015-2100-x>.
Cited on page 70.
- [73] T. J. Nussdorfer. Some Observations of Shock-induced Turbulent Separation on Supersonic Diffusers. Technical Report May, NACA-RM-E51L26, Washington, DC, 1954.
<https://ntrs.nasa.gov/citations/19930087855>.
Cited on page 13.
- [74] L. J. Obery and C. F. Schueller. Effects of internal boundary-layer control on the performance of supersonic AFT inlets. Technical report, NACA-RM-E55L17, Washington, DC, 1956.
<https://ntrs.nasa.gov/citations/19930089032>.
Cited on page 15.
- [75] J. Oorebeek and H. Babinsky. Flow physics of a normal-hole bled supersonic turbulent boundary layer. In *51st AIAA Aerospace Sciences Meeting including the New Horizons Forum and Aerospace Exposition*, Reston, Virginia, 2013. American Institute of Aeronautics and Astronautics.
<https://arc.aiaa.org/doi/10.2514/6.2013-526>.
Cited on pages XIV, 23, 24, and 102.
- [76] J. Oorebeek, W. Nolan, and H. Babinsky. Comparison of Bleed and Micro-Vortex Generator Effects on Supersonic Boundary-Layers. In *50th AIAA Aerospace Sciences Meeting including the New Horizons Forum and Aerospace Exposition*, Reston, Virginia, 2012. American Institute of Aeronautics and Astronautics.
<https://arc.aiaa.org/doi/10.2514/6.2012-45>.
Cited on pages XIV, 20, 21, and 23.
- [77] J. Oorebeek, H. Babinsky, M. Ugolotti, P. D. Orkwis, and S. Duncan. Experimental and Computational Investigations of a Normal-Hole-Bled Supersonic Boundary Layer. *AIAA Journal*, 53(12):3726–3736, 2015.
<https://arc.aiaa.org/doi/10.2514/1.J053956>.
Cited on pages XIV, 22, 23, 30, 54, 83, 84, 100, 102, 120, 129, 130, and 132.
- [78] P. Orkwis, M. Turner, A. Apyan, K. Flenar, S. Duncan, and N. Wukie. Modeling and Simulation of Bleed Holes in the Presence of Shock Wave/Boundary Layer Interaction. In *51st AIAA Aerospace Sciences Meeting including the New Horizons Forum and Aerospace Exposition*, volume 19, Reston, Virginia, 2013. American Institute of Aeronautics and Astronautics.
<https://arc.aiaa.org/doi/10.2514/6.2013-425>.
Cited on pages XIV, 33, 34, and 58.

- [79] K. Oswatitsch. Der Druckrückgewinn bei Geschossen mit Rückstossantrieb bei hohen Überschallgeschwindigkeiten (Der Wirkungsgrad von Stoßdiffusoren). *Forschungen und Entwicklungen des Heereswaffenamtes*, 1005, 1944.
<https://ntrs.nasa.gov/citations/19990049423>.
Cited on pages XIII and 15.
- [80] G. C. Paynter, D. A. Treiber, and W. D. Kneeling. Modeling supersonic inlet boundary-layer bleed roughness. *Journal of Propulsion and Power*, 9(4):622–627, 1993.
<https://arc.aiaa.org/doi/10.2514/3.23666>.
Cited on page 20.
- [81] H. Pearcey. Introduction to Shock-Induced Separation and its Prevention by Design and Boundary Layer Control. In *Boundary Layer and Flow Control*, pages 1166–1344. Elsevier, 1961.
<https://linkinghub.elsevier.com/retrieve/pii/B978148321323150021X>.
Cited on page 13.
- [82] A. L. Philippou, P. K. Zachos, and D. G. MacManus. Aerodynamic Instabilities in High-Speed Air Intakes and Their Role in Propulsion System Integration. *Aerospace*, 11(1):75, 2024.
<https://www.mdpi.com/2226-4310/11/1/75>.
Cited on page 7.
- [83] P. Polivanov. Effect of blowing/suction through porous surfaces on boundary layer at supersonic Mach numbers. *MATEC Web of Conferences*, 115:02011, 2017.
<http://www.matec-conferences.org/10.1051/matecconf/201711502011>.
Cited on pages XIV and 24.
- [84] P. Polivanov, A. A. Sidorenko, and A. A. Maslov. The influence of the laminar–turbulent transition on the interaction between the shock wave and boundary layer at a low supersonic Mach number. *Technical Physics Letters*, 41(10):933–937, 2015.
<http://link.springer.com/10.1134/S1063785015100120>.
Cited on page 24.
- [85] D. I. A. Poll, M. Danks, and B. E. Humphreys. Aerodynamic Performance of Laser Drilled Sheets. In *First European Forum on Laminar Flow Technology*, Bonn, 1992. Deutsche Gesellschaft für Luft- und Raumfahrt - Lilienthal-Oberth e.V.
Cited on pages XX, 6, 32, 35, 40, 41, 55, 173, 175, 178, 180, 182, 187, 195, 200, 201, and 205.
- [86] M. J. Rimlinger, T. I.-P. Shih, and W. J. Chyu. Three-dimensional shock-wave/boundary-layer interactions with bleed through a circular hole. In *28th Joint Propulsion Conference and Exhibit*, Reston, Virginia, 1992. American Institute of Aeronautics and Astronautics.
<https://arc.aiaa.org/doi/10.2514/6.1992-3084>.
Cited on page 28.
- [87] M. J. Rimlinger, T. I.-P. Shih, W. J. Chyu, B. Willis, and D. O. Davis. Computations of shock-wave/boundary-layer interactions with bleed. In *34th Aerospace Sciences Meeting and Exhibit*, Reston, Virginia, 1996. American Institute of Aeronautics and Astronautics.
<http://arc.aiaa.org/doi/10.2514/6.1996-432>.
Cited on pages XIV and 29.

- [88] K. Sabnis and H. Babinsky. A review of three-dimensional shock wave–boundary-layer interactions. *Progress in Aerospace Sciences*, 143(February):100953, 2023.
<https://linkinghub.elsevier.com/retrieve/pii/S0376042123000696>.
Cited on page 79.
- [89] B. W. Sanders and R. W. Cubbison. Effect of Bleed-System Back Pressure and Porous Area on the Performance of an Axisymmetric Mixed-Compression Inlet at Mach 2.50. Technical report, NASA-TM-X-1710, Washington, DC, 1968.
<https://ntrs.nasa.gov/citations/19690004743>.
Cited on page 16.
- [90] H. Schlichting and K. Gersten. *Boundary-Layer Theory*. Springer Berlin Heidelberg, Berlin, Heidelberg, 2017.
<http://link.springer.com/10.1007/978-3-662-52919-5>.
Cited on page 11.
- [91] M. J. Schwartz, D. V. Gaitonde, and J. W. Slater. Effects of Bleed on Supersonic Turbulent Boundary Layers. In *AIAA AVIATION 2021 FORUM*, Reston, Virginia, 2021. American Institute of Aeronautics and Astronautics.
<https://arc.aiaa.org/doi/10.2514/6.2021-2885>.
Cited on page 30.
- [92] M. J. Schwartz, D. V. Gaitonde, and J. W. Slater. Structure and Dynamics of Bleed-Controlled Impinging Shock/Turbulent-Boundary-Layer Interactions. In *AIAA AVIATION 2022 Forum*, pages 1–21, Reston, Virginia, 2022. American Institute of Aeronautics and Astronautics.
<https://arc.aiaa.org/doi/10.2514/6.2022-3467>.
Cited on pages XIV and 29.
- [93] M. J. Schwartz, D. V. Gaitonde, and J. W. Slater. Uncertainty and Sensitivity Analysis of Bleed Modeling in Shock/Turbulent Interactions. *Journal of Propulsion and Power*, 39(1):106–120, 2023.
<https://arc.aiaa.org/doi/10.2514/1.B38785>.
Cited on pages 29 and 84.
- [94] T. I.-P. Shih. Control of Shock-Wave/Bound-Layer Interactions by Bleed. *International Journal of Fluid Machinery and Systems*, 1(1):24–32, 2008.
<http://koreascience.or.kr/journal/view.jsp?kj=OCGKEU&py=2008&vnc=v1n1&sp=24>.
Cited on pages 83 and 126.
- [95] T. I.-P. Shih, M. J. Rimlinger, and W. J. Chyu. Three-dimensional shock-wave/boundary-layer interactions with bleed. *AIAA Journal*, 31(10):1819–1826, 1993.
<https://arc.aiaa.org/doi/10.2514/3.11854>.
Cited on page 28.
- [96] T. I.-P. Shih, T. J. Benson, B. Willis, M. J. Rimlinger, and W. J. Chyu. Structure of shock-wave/boundary-layer interactions with bleed through rows of circular holes. In *35th Aerospace Sciences Meeting and Exhibit*, Reston, Virginia, 1997. American Institute of Aeronautics and Astronautics.
<http://arc.aiaa.org/doi/10.2514/6.1997-508>.
Cited on page 29.

- [97] P. C. Simon, D. W. Brown, and R. G. Huff. Performance of External-Compression Bump Inlet at Mach Numbers of 1.5 to 2.0. Technical report, NACA-RM-E56L19, Washington, DC, 1957.
<https://ntrs.nasa.gov/citations/19930089624>.
Cited on pages XIII and 15.
- [98] J. W. Slater. Improvements in Modeling 90-degree Bleed Holes for Supersonic Inlets. *Journal of Propulsion and Power*, 28(4):773–781, 2012.
<https://arc.aiaa.org/doi/10.2514/1.B34333>.
Cited on pages XIV, XV, XX, 6, 20, 30, 32, 33, 34, 39, 40, 41, 51, 53, 91, 92, 122, 123, 127, 137, 144, 147, 157, 160, 173, 174, 175, 177, 178, 180, 183, 185, 186, 187, 191, 192, 194, 195, 196, 197, 198, 199, and 205.
- [99] J. W. Slater and J. D. Saunders. Modeling of Fixed-Exit Porous Bleed Systems for Supersonic Inlets. *Journal of Propulsion and Power*, 26(2):193–202, 2010.
<https://arc.aiaa.org/doi/10.2514/1.37390>.
Cited on pages 57 and 127.
- [100] D. B. Smeltzer and N. E. Sorensen. Tests of a Mixed Compression Axisymmetric Inlet with Large Transonic Mass Flow at Mach Number 0.6 to 2.65. Technical report, NASA-TN-D-6971, Washington, DC, 1972.
<https://ntrs.nasa.gov/citations/19730005050>.
Cited on pages XIII, 16, and 32.
- [101] N. E. Sorensen and D. B. Smeltzer. Investigation of a Large-Scale Mixed-Compression Axisymmetric Inlet System Capable of High Performance at Mach Numbers 0.6 to 3.0. Technical report, NASA-TM-X-1507, Washington, DC, 1968.
<https://ntrs.nasa.gov/citations/19680007559>.
Cited on page 212.
- [102] P. Spalart. Strategies for turbulence modelling and simulations. *International Journal of Heat and Fluid Flow*, 21(3):252–263, 2000.
<https://linkinghub.elsevier.com/retrieve/pii/S0142727X00000072>.
Cited on pages 50 and 199.
- [103] P. Spalart and S. Allmaras. A one-equation turbulence model for aerodynamic flows. In *30th Aerospace Sciences Meeting and Exhibit*, pages 5–21, Reston, Virginia, 1992. American Institute of Aeronautics and Astronautics.
<https://arc.aiaa.org/doi/10.2514/6.1992-439>.
Cited on page 50.
- [104] E. Stanewsky. Euroshock i and ii: A survey. In G. E. A. Meier and P. R. Viswanath, editors, *IUTAM Symposium on Mechanics of Passive and Active Flow Control*, pages 35–42, Dordrecht, 1999. Springer Netherlands.
http://link.springer.com/10.1007/978-94-011-4199-4_6.
Cited on page 21.
- [105] E. Stanewsky, J. M. Détery, J. Fulker, and P. Matteis. *Drag Reduction by Shock and Boundary Layer Control*. Springer-Verlag, Berlin, Heidelberg, 2002.
<http://link.springer.com/10.1007/978-3-540-45856-2>.
Cited on page 37.

- [106] H. W. Stock and W. Haase. Determination of length scales in algebraic turbulence models for Navier-Stokes methods. *AIAA Journal*, 27(1):5–14, 1989.
<https://arc.aiaa.org/doi/10.2514/3.10087>.
Cited on page 56.
- [107] W. Sutherland. LII. The viscosity of gases and molecular force. *The London, Edinburgh, and Dublin Philosophical Magazine and Journal of Science*, 36(223):507–531, 1893.
<https://www.tandfonline.com/doi/full/10.1080/14786449308620508>.
Cited on page 50.
- [108] J. Syberg and T. E. Hickcox. Design of a Bleed System for a Mach 3.5 Inlet. Technical report, NASA-CR-2187, Washington, DC, 1973.
<https://ntrs.nasa.gov/citations/19730007094>.
Cited on pages 16, 32, and 123.
- [109] J. Syberg and J. L. Koncsek. Bleed System Design Technology for Supersonic Inlets. *Journal of Aircraft*, 10(7):407–413, 1973.
<https://arc.aiaa.org/doi/10.2514/3.60241>.
Cited on pages 37, 126, and 130.
- [110] J. Syberg and J. L. Koncsek. Experimental Evaluation of an Analytically Derived Bleed System for a Supersonic Inlet. *Journal of Aircraft*, 13(10):792–797, 1976.
<https://arc.aiaa.org/doi/10.2514/3.58712>.
Cited on page 16.
- [111] E.-J. Teh and T. I.-P. Shih. Reynolds-Averaged Simulations of Shock-Wave/Boundary-Layer Interactions with Bleed. In *51st AIAA Aerospace Sciences Meeting including the New Horizons Forum and Aerospace Exposition*, Reston, Virginia, 2013. American Institute of Aeronautics and Astronautics.
<https://arc.aiaa.org/doi/10.2514/6.2013-423>.
Cited on page 30.
- [112] N. Titchener and H. Babinsky. Microvortex Generators Applied to a Flowfield Containing a Normal Shock Wave and Diffuser. *AIAA Journal*, 49(5):1046–1056, 2011.
<https://arc.aiaa.org/doi/10.2514/1.J050760>.
Cited on page 111.
- [113] N. Titchener and H. Babinsky. Shock Wave/Boundary-Layer Interaction Control Using a Combination of Vortex Generators and Bleed. *AIAA Journal*, 51(5):1221–1233, 2013.
<http://arc.aiaa.org/doi/10.2514/1.J052079>.
Cited on pages 102 and 111.
- [114] C. Wang, Q. Eri, B. Kong, Y. Wang, and W. Ding. Novel Simplified Numerical Simulation Method for Modeling Bleed Holes in Supersonic Inlets. *AIAA Journal*, pages 1–14, 2022.
<https://arc.aiaa.org/doi/10.2514/1.J062150>.
Cited on pages XIV, 32, 34, 58, 59, and 191.
- [115] B. Willis and D. O. Davis. Boundary layer development downstream of a bleed mass flow removal region. In *32nd Joint Propulsion Conference and Exhibit*, Reston, Virginia, 1996. American Institute of Aeronautics and Astronautics.
<https://arc.aiaa.org/doi/10.2514/6.1996-3278>.
Cited on pages XIV, 17, 20, 21, 23, 29, 30, and 41.

- [116] B. Willis, D. O. Davis, and W. R. Hingst. Flowfield measurements in a normal-hole-bleed oblique shock-wave and turbulent boundary-layer interaction. In *31st Joint Propulsion Conference and Exhibit*, Reston, Virginia, 1995. American Institute of Aeronautics and Astronautics.
<https://arc.aiaa.org/doi/10.2514/6.1995-2885>.
Cited on pages XIV, 25, 26, 29, and 41.
- [117] B. Willis, D. O. Davis, and W. R. Hingst. Flow coefficient behavior for boundary layer bleed holes and slots. In *33rd Aerospace Sciences Meeting and Exhibit*, Reston, Virginia, 1995. American Institute of Aeronautics and Astronautics.
<https://arc.aiaa.org/doi/10.2514/6.1995-31>.
Cited on pages XIII, XIV, XV, 17, 18, 19, 25, 30, 32, 37, 39, 41, 89, 91, 92, 93, 113, 115, and 133.
- [118] N. A. Wukie, P. D. Orkwis, M. G. Turner, and S. Duncan. Simulations and Models for Aspiration in a Supersonic Flow Using OVERFLOW. *AIAA Journal*, 53(7):2052–2056, 2015.
<https://arc.aiaa.org/doi/10.2514/1.J053214>.
Cited on pages 30, 34, and 100.
- [119] X. Xiang and H. Babinsky. Corner effects for oblique shock wave/turbulent boundary layer interactions in rectangular channels. *Journal of Fluid Mechanics*, 862:1060–1083, 2019.
https://www.cambridge.org/core/product/identifier/S0022112018009837/type/journal_article.
Cited on page 79.
- [120] B.-h. Zhang, Y.-x. Zhao, J. Liu, and Q. Wang. Supersonic Bleed Rate Model for a Circular Orifice Based on Geometric Similarity. *AIAA Journal*, 58(6):2486–2493, 2020.
<https://arc.aiaa.org/doi/10.2514/1.J058495>.
Cited on pages 32, 34, and 41.

Titre : Caractérisation et modélisation de pièges poreux pour le contrôle de la couche limite avec et sans interaction d'une onde de choc

Mots clés : Contrôle de l'écoulement, Écoulements supersoniques, Interaction onde de choc/couche limite, Condition d'aspiration, Modélisation

Résumé :

Le contrôle de l'écoulement à l'aide de piège poreux est étudié à la fois numériquement et expérimentalement. On s'intéresse dans un premier temps au cas d'une couche limite turbulente en régimes supersonique puis subsonique. On traite en seconde partie du contrôle de l'interaction onde de choc/couche limite.

L'étude numérique se compose de deux parties. Tout d'abord, une étude paramétrique est réalisée afin d'identifier l'influence des paramètres géométriques et des conditions d'écoulement dans le but de générer une base de données exhaustive. Les concepts d'efficacité et d'effectivité d'un piège poreux sont introduits et évalués. L'efficacité décrit la capacité à assurer un niveau d'aspiration sans recourir à une pression trop basse dans la cavité. L'effectivité représente la capacité à augmenter la quantité de mouvement de l'écoulement de couche limite à proximité de la paroi en prélevant un débit minimal d'air. Dans la deuxième phase de l'étude, les modèles de pièges poreux issus de la littérature sont appliqués en tant que condition d'aspiration continue dans le solveur compressible structuré *elsA*. Une comparaison exhaustive de

ces modèles est conduite sur la base de données issue de l'étude paramétrique. Des écarts significatifs entre les modèles sont observés concernant la prévision de l'efficacité et de l'effectivité des pièges poreux.

Des expériences dans la soufflerie S8Ch à Meudon sont réalisées pour les nombres de Mach $M = 1.62$ et $M = 0.5$. Les mesures de pressions pariétales ainsi que de champs de vitesse par vélocimétrie laser à franges (VLF) ont permis de valider les conclusions des études numériques dans la mesure où un très bon accord entre les simulations et les expériences est observé.

Dans un dernier temps, nous avons élaboré un nouveau modèle de piège poreux en appliquant une condition d'aspiration distribuée. Le modèle est validé à la fois pour les écoulements supersonique et subsonique, à partir de grandeurs pariétales uniquement. L'efficacité et l'effectivité des pièges poreux issus de la base de données sont calculées finement avec une grande précision. Le modèle est finalement appliqué et validé au cas complexe du contrôle de l'interaction onde de choc/couche limite.

Title : Characterization & Modeling of Porous Bleed for Boundary-Layer Control with & without Shock-Wave Interaction

Keywords : Flow Control, Supersonic Flows, Shock-Wave/Boundary-Layer Interaction, Suction Boundary Condition, Modeling

Abstract :

Flow control by porous bleed systems is studied both numerically and experimentally. First, the control of the supersonic and subsonic turbulent boundary layer is investigated, followed by the control of a shock-wave/boundary-layer interaction.

The numerical study consists of two parts. First, a numerical parametric study is conducted to determine the influences of geometrical parameters and inflow conditions and to generate a comprehensive database. The concept of bleed efficiency and control effectiveness is introduced and evaluated. Bleed efficiency describes the ability to remove a high bleed rate with low pressure losses. Control effectiveness is the ability to generate a high momentum flow by removing only a small amount of bleed air. In the second step, state-of-the-art bleed models are applied as a suction boundary condition in the in-house flow

solver *elsA*. A comprehensive benchmark test is performed to evaluate the models based on the data from the parametric study. Significant model deficiencies regarding the prediction of the control effectiveness are observed.

Experiments in the S8Ch wind tunnel in Meudon are performed for the Mach numbers $M = 1.62$ and $M = 0.5$. The measurements serve as the validation of the numerical findings from the experimental study. A very good agreement between simulations and experiments is achieved.

Finally, a novel bleed model applying locally distributed suction is derived. The model is applicable for both supersonic and subsonic flow without requiring flow field quantities. Both bleed efficiency and control effectiveness are well predicted. Moreover, the model is applicable for the complex flow case of the control of a shock-wave/boundary-layer interaction.